12-2018

Engineering Soft Tissue Replacements and the Development of Novel Technologies to Heal these Wounds

Sarah Grace Dennis
Clemson University, sglittle16@gmail.com

ENGINEERING SOFT TISSUE REPLACEMENTS AND THE DEVELOPMENT OF NOVEL TECHNOLOGIES TO HEAL THESE WOUNDS

A Dissertation
Presented to
the Graduate School of
Clemson University

In Partial Fulfillment
of the Requirements for the Degree
Doctor of Philosophy
Bioengineering

---

by
Sarah Grace Dennis
December 2018

Accepted by:
Michael J. Yost, PhD, Committee Chair
Hai Yao, PhD
Ying Mei, PhD
Martine Laberge, PhD

ABSTRACT

The primary focus of tissue engineering is to develop biological substitutes capable of restoring, maintaining, or improving native tissue function. This field advances an exciting array of solutions for organ repair and wound healing. In the United States alone over 6.5 million people are affected by chronic wounds every year, which account for over $25 billion of healthcare expenses. Vascularization and fast anastomosis with the host are essential in engineering cellular constructs that survive once implanted. In the last decade, there has been extensive investigation into fabrication techniques to create tissue replacements that are rapidly perfused post-implantation to address this issue.

Three-dimensional bioprinting is a methodology used for generating 3D constructs of various sizes and shapes from a digital model using a layer-by-layer approach. These digital models can be derived from patient images, such as CT and MRI scans, to produce patient-specific tissue replacements. The fabrication of biomimetic constructs plays an essential role in the advancement of tissue engineering, and provides the ability to form 3D constructs that are able to recapitulate the *in vivo* structure and function of complex tissues. The Palmetto Printer, developed at the Medical University of South Carolina, is a custom-built multi-dispenser system that uses programmable robotic manufacturing methods to generate 3D heterogeneous tissue constructs. The assessment of the Palmetto bioprinter showed high cell viability (>95%) and significant cell proliferation within the printed constructs over 8 days. Therefore, this technique proves

its ability to generate scaffolds that allow cell growth, communication, and the formation of networks; each a requirement of vascularization.

Scaffold-free tissue engineering aims to produce physiologically-relevant 3D multicellular constructs through the process of cellular self-assembly. We have developed a scaffold-free prevascular implant model with dense endothelial networks surrounded by extracellular matrix, similar to capillary vasculature. Upon implantation, we found that the host rapidly endothelialized these constructs (<6hr), and were perfused by 72 hours post-implantation. We have demonstrated that this technology can be modified by growth factors and can be scaled up into larger, more complex geometries. Furthermore, bioprinter fabrication could allow the creation of personalized implants.

As an application for these fabrication techniques, we developed a novel wound dressing for the treatment of chronic wounds. The Smart Wound Dressing is a multi-component device made up of three separate layers that individually address different facets of the chronic wound environment. This combinatorial approach will provide an exciting new option for the treatment of these non-healing wounds.

DEDICATION

I have dedicated this work to my father, Timothy Dennis, who passed away this past March. When I was looking at colleges for my undergraduate studies, he told me I should be a biomedical engineer and has continuously pushed me to succeed. When I started my PhD, he was so proud and supportive of me along this journey. I wish he could be here to see me finally reaching our goal of becoming a doctorate in biomedical engineering, but he has been, and always will be with me in my spirit and my drive to succeed.

ACKNOWLEDGMENTS

I would like to acknowledge my PI, Dr. Michael Yost, who has supported and guided me for the past five years. He has been a wonderful mentor, and taught me well beyond the scope my dissertation. I would also like to thank Heather Bainbridge and Sanket Pattanaik for helping me throughout my graduate career, both with science and life. I would also like to acknowledge other members of the Yost lab, including Veronica, Matt, Ben, and John, as well as our collaborators, Caitlin, Dr. Fann, and members of the Mei lab, who have all contributed to this work. Finally, I would like to thank Dr. Foley for being a mentor to me, and for her help in guiding me over the last few years, as well as my friends and family without whom I could not have completed this work.

TABLE OF CONTENTS

Page

TITLE PAGE i

ABSTRACT ..... ii-iii

DEDICATION iv

ACKNOWLEDGMENTS v

LIST OF TABLES viii

LIST OF FIGURES ix

CHAPTER

I. OVERVIEW OF TISSUE ENGINEERING TECHNIQUES 1

1.1 Conventional Tissue Engineering Techniques 2
1.2 Biomaterials for Scaffold-based Tissue Engineering 3
1.3 Advances in Biofabrication Techniques for Engineering Soft Tissues: Three-dimensional Bioprinting 4
1.4 Scaffold-free Tissue Engineering 7
1.5 Limitations of Tissue Engineering 10
1.6 References 11

II. BIOMATERIALS AND THREE-DIMENSIONAL BIOPRINTING 13

2.1 Advanced Additive Manufacturing Bioprinting 14
2.2 Biomaterials for Extrusion-based, Direct-write Bioprinting 16
2.3 Modified Alginate as a Bioactive Scaffold 19
2.4 Mimicking the Complex *in vivo* Microenvironment 24
2.5 The Palmetto Bioprinter 25
2.6 Materials and Methods 32
2.7 Results 47
2.8 Discussion 66
2.9 References 70

Table of Contents (Continued) Page

III. SCAFFOLD-FREE TISSUE ENGINEERING 75

3.1 Scaffold-free Cellular Self-assembly 77
3.2 Prevascularization: Primary Network Formation 78
3.3 Development of Novel Scaffold-free Prevascularized Endothelial-fibroblast Constructs 81
3.4 Materials and Methods 83
3.5 Results 90
3.6 Discussion 105
3.7 References 113

IV. ANGIONESESIS AND TUBULOGENESIS: THE ANGIOGENIC POTENTIAL OF THE SPEC 116

4.1 Cord Hollowing Mechanism 117
4.2 Vascular Endothelial Growth Factor-A Signaling 120
4.3 Sphingosine-1-Phosphate Signaling 122
4.4 Materials and Methods 124
4.5 Results 126
4.6 Discussion 133
4.7 References 133

V. THE SMART WOUND DRESSING 135

5.1 Normal Wound Healing of Acute Wounds 135
5.2 The Chronic Wound Microenvironment 140
5.3 Pressure Ulcers 143
5.4 Traditional Wound Treatment 145
5.5 Modern Wound Treatment 147
5.6 The Smart Wound Dressing 149
5.7 Materials and Methods 153
5.8 Results 159
5.9 Discussion 170
5.10 References 175

LIST OF TABLES

Table Page

2.1 List of commands for use in JR-C software to control the Palmetto Bioprinter 31

5.1 Measurements taken from the scans of an infant patient suffering from craniosynostosis and of the model created using the MakerBot Replicator 2. 172

LIST OF FIGURES

Figure		Page
1.1	Organ shortage crisis facing the United States	1
1.2	Traditional Tissue Engineering Technique	2
1.3	Components of Inkjet, Microextrusion, and Laser-assisted Bioprinters	5
1.4	Indirect and Direct Bioprinting Techniques	6
1.5	Indirect Bioprinting to Form Tubular Structures	7
1.6	Scaffold-free tissue engineering method	8
1.7	Cell Sheet Engineering	10
2.1	Typical Workflow of Bioprinting	15
2.2	Bioprinting Techniques: Indirect and Direct Bioprinting	16
2.3	Alginate Copolymer Structure, where G represents Polyguluronate blocks, and M represents Polymannuronate blocks	20
2.4	Reaction scheme of peptide coupling to alginate molecules and an illustration of how cells bind and interact with the RGD-conjugated alginate	21
2.5	Chemical structure of partially oxidized alginate	22
2.6	Cell Viability assay of density and viscosity criterion-filtered samples	23
2.7	Palmetto Bioprinter at the Medical University of South Carolina	26
2.8	Palmetto Bioprinter at MUSC: Tool Nest, Optic Sensors, and Displacement Laser Components	28
2.9	Visual PathBuilder Software (CAD design) and bioprinted construct created from that design	30

List of Figures (Continued) Page

2.10 JR-C Points Software that is used to control deposition method, speed, distance between syringe tip and substrate surface, the allotted time for deposition, and the three-dimensional placement of droplets 30

2.11 Schematic representation of biodegradable oxidized alginate as bioink of bioprinting 40

2.12 Contact angle measurements for bioprinted droplets using 20G Micron-S Precision Tip 41

2.13 Bioprinted droplet with indications of how volume measurements were calculated.....42

2.14 Comparison of cell-laden, non-conjugated and RGD-conjugated alginates 48

2.15 Contact Angle measurements for bioprinted droplets using 20G Micron-S Precision Tip with ranging deposition volumes for three types of biomaterials: 30% Pluronic F-127, 5% LF10/60FT Alginate, and 5% LF20/40 Alginate 50

2.16 Volume analysis to characterize the effect of tip gauge-size on volume dispensed by the Palmetto Printer.....51

2.17 Resolution of the Palmetto Printer using a 30G Micron-S Precision Tip 52

2.18 Swelling properties of 2% and 4% LF20/40 alginate bioink over 7 days including Swelling Ratio, Q, the Equilibrium Mass Swelling Ratio, Q_m, and the Water Uptake Content,Q_W 53

2.19 Swelling properties of 4% LF10/60FT and 4% LF20/40 alginate bioink over 7 days including Swelling Ratio, Q, the Equilibrium Mass Swelling Ratio, Q_m, and the Water Uptake Content,Q_W 54

2.20 Effect of availability of gelation agent in the substrate used to produce 4% LF10/60FT alginate hydrogels on the swelling behavior.....55

2.21 Effect of availability of gelation agent in the substrate used to produce 2% LF20/40 alginate hydrogels on the swelling behavior....57

2.22 Bioprinted droplet analysis containing NHDFs in 5%LF20/40 bioink. Representation of droplets sectioned into quadrants and concentric circles with analyses of cells per area in each region of the bioprinted drops....59

2.23 Bioprinted droplet analysis containing NHDFs in 0.6% Collagen and 4% LF20/40 (1:1) blended bioink, sectioned into quadrants and concentric circles with analyses of cells per area in each region of the bioprinted drops....61

2.24 Bioprinted droplet analysis containing NHDFs in 5% LF10/60FT alginate bioink, sectioned into quadrants and concentric circles with analyses of cells per area in each region of the bioprinted drops....62

2.25 Quantified viabilities of bioprinted constructs on Day 0 and after 8 days of culture (Day 8)....64

2.26 Human adipose-derived stem cells in RGD-conjugated alginate on day 0 and day 8, stained with calcein AM and ethidium homodimer-1....66

3.1 Vascularization: An Issue of Time and Thickness....76

3.2 Vascularization Pipeline *in vivo*....77

3.3 Schematic of cellular self-assembly....78

3.4 The two principal vascularization strategies in tissue engineering: anastomosis and inosculation....80

3.5 Confocal projections of whole-mount rod tissue illustrating primary vascular networks with directional alignments....82

3.6 Schematic of computer-aided design used to generate the negative MakerBot mold and form the desired

shape of the non-adherent agarose gel that is subsequently seeded with cells 84

3.7 Process of creating scaffold-free prevascularized endothelial-fibroblast constructs 85

3.8 Experimental setup for determining the rate of endothelial cell migration out of the SPEC into an acellular environment 87

3.9 Schematic of animal model and where constructs will be implanted....89

3.10 Whole-mount immunofluorescence image of rod-shaped scaffold free prevascular endothelial fibroblast construct (SPEC) and fibroblast-only spheroids liberated from 2% agarose mold. Light microscopy images of Hematoxylin and Eosin stained rat hind limb tissue sections (10 μm) containing cross section of implanted SPEC (encircled) between vastus lateralis and biceps femoris muscles. 91

3.11 Endothelial Migration out of the SPEC was recorded to be ~250um per day. Rate was determined by tracking GFP-transduced HAMECs over the course of 24 hours using the LionHeartFX Live Cell Imager (Biotek). 92

3.12 Western Blot analysis of SPEC during formation looking at DLL4, VEGFR2, VE-cadherin, and vWF expression 93

3.13 Assessment of vascular structures within implanted constructs, including segmented tissue cross-section, microvessel area fraction, microvessel area fraction excluding capsule, and fraction of cords penetrating implants 95

3.14 Endothelial reorganization within implants was imaged through immunofluorescence imaging with Hoechst nuclear stain (Cyan) and anti-CD31 antibody stain for endothelial cells (Red) at 6, 12, and 24 hours post-implantation 96

3.15 Mural Cell Involvement at 6 and 12 hours post-implantation. Mural cells indicated by alpha-smooth

muscle actin 97

3.16 Lumen structures were present within the SPEC implants at 12-hours post-implantation, as indicated by polyclonal-CD31 (red)..... 98

3.17 Assessment of contributions to newly formed vasculature in and around implants at 6 and 12 hours post-implantation. Monoclonal anti-human CD31 antibody stain (red) and polyclonal anti-vWF antibody stain (green) colocalize in implant-derived human endothelial structures (yellow)..... 99

3.18 At 12-hours post-implantation, invading host endothelial branches (vWF, red) inosculate with Cell Tracker+ cells (blue) indicative of both host and implant contribution to vascular network (magenta)..... 100

3.19 Light microscopic images of hematoxylin-eosin–stained tissue sections of a prevascular tissue xenograft 3 days after implantation in an immune-competent rat. Immunofluorescence images of tissue sections of a prevascular tissue xenograft 3 days after implantation showing activated satellite cells migrating into the xenograft..... 101

3.20 Prevascularized Bioartificial Pancreas. Incorporation of islet cells in the SPECs did not alter vascular network formation..... 102

3.21 Tissue-engineered Scaffold-free Renal Segment Construct..... 103

3.22 Potential for Scalability of the SPEC. A honeycomb structure was formed around a non-adherent agarose mold, and retained the dense endothelial cord networks (CD31), as well as extracellular matrix production (Phalloidin staining for F-actin)..... 104

3.23 SPECs fuse together under perfusion, and retain endothelial networks (CD31), as well as the extracellular matrix components required for stability (Phalloidin staining for F-actin)..... 105

3.24 SPEC and FOS cryosections (10um) harvested at 6, 12, 24h were stained with Tdt dUTP Nick-End Labeling Assay (green) and counterstained with Hoechst nuclear stain (blue). A significant increase in TUNEL+ cells was observed between 6h and 24 h for FOS and SPEC implants (n=4, $p<0.01$) compared to the surrounding rat host muscle 111

3.25 Red blood cell presence within implants at 24hours is inconsistent, indicating implants have not been thoroughly perfused by this time point. 112

4.1 Vascularization Pipeline..... 117

4.2 Cord Hollowing Mechanism 118

4.3 Vascular Endothelial Growth Factor-A Signaling..... 122

4.4 Sphingosine-1-Phosphate Signaling 123

4.5 Dosing Regimen of SPECs During Formation..... 125

4.6 VEGFA-treated SPECs have lumens present..... 127

4.7 Assessment of endothelial networks in untreated SPECs and VEGFA-treated SPECs..... 128

4.8 Sphingosine-1-Phosphate-treated SPECs..... 129

4.9 Comparison of S1P-treated SPECs and the untreated SPEC control 130

4.10 Western Blot analysis for PODXL in VEGF-treated and untreated SPEC controls..... 131

4.11 Western Blot analyses for vWF, Cdc42, N-cadherin, and loading control (GAPDH) in VEGF-treated and untreated SPEC controls..... 132

4.12 Western Blot analysis for Laminin in VEGF-treated and untreated SPEC controls..... 132

5.1 Stages of Normal Wound Healing..... 136

5.2 Before and after images of a patient treated at MUSC with traditional therapies, where the wound healed, but the resultant tissue was non-functional and disfigured 139

5.3 Normal-healing wound microenvironment and the Chronic, non-healing wound microenvironment, as well as clinical images of patients treated at MUSC 140

5.4 Key players contributing to impaired wound healing 142

5.5 Progression and classification of pressure ulcers 143

5.6 Traditional Wound Dressings 145

5.7 TriTec Silver®, by Milliken, Wound Dressing 146

5.8 Apligraf®, by Organogenesis, Wound Dressing 147

5.9 Schematic of the Smart Wound Dressing 149

5.10 Scaffold-free Prevascularized Endothelial-fibroblast Construct explants from hind limb of rat at 6-hours post-implantation 151

5.11 Electrospinning apparatus developed by the Yost Lab at the Medical University of South Carolina 153

5.12 JM-2 Peptide 157

5.13 Invasion Assay setup for mock wound assay 158

5.14 Image of 1.5% reaction electrospun collagen fibers with Scanning Electron Microscopy and Transmission Electron Microscopy images 159

5.15 Scanning electron microscopy images of woven polyester sputter-coated with silver and the hydrophilic 0.1μm PTFE membranes taken at 3,000X 160

5.16 Contact angle measurements of silver-coated woven polyester membrane 161

5.17 Bulk Absorption measurements 162

5.18 Bacterial Colonization assay with silver-coated woven polyester on MSSA, MRSA, and E.Coli bacteria....163

5.19 Cell Toxicity analysis of woven polyester membrane with and without silver-coating on days 2,8, and 14....164

5.20 Moisture content of reaction electrospun collagen fibers of varying concentrations....165

5.21 Confocal image projection of whole-mount rod-shaped SPEC in 1.4% collagen....166

5.22 JM-2 release kinetics from reaction electrospun collagen fibers....167

5.23 Invasion assay results....168

5.24 Assembled Smart Wound Dressing....169

5.25 Two wound models being investigated by our lab for assessing the properties of the Smart Wound Dressing *in vivo*....170

5.26 Reconstruction of the skull of a MUSC patient suffering from craniosynostosis....172

5.27 Utilizing the Palmetto Bioprinter to develop patient-Specific wound dressings....173

5.28 Novel scanning technology for recreating architecture of soft tissue wounds with high fidelity....174

5.29 Smart Wound Dressing Production Timeline....175

CHAPTER ONE

OVERVIEW OF TISSUE ENGINEERING TECHNIQUES

The primary focus of tissue engineering is to bridge the gap between organ shortages and transplantation needs by developing biological substitutes capable of restoring, maintaining, or improving native tissue function (1-2). As of 2017, in the United States alone, there were almost 116,000 patients on the organ transplant waiting list at years end, and only 16,473 recovered donors (3). The number of people on the waiting list has been rapidly increasing, while the number of donors and transplants has remained relatively constant since 1990 (**Figure 1.1,** 3). There is a significant disproportion between the supply and demand for organ transplants that must be improved.

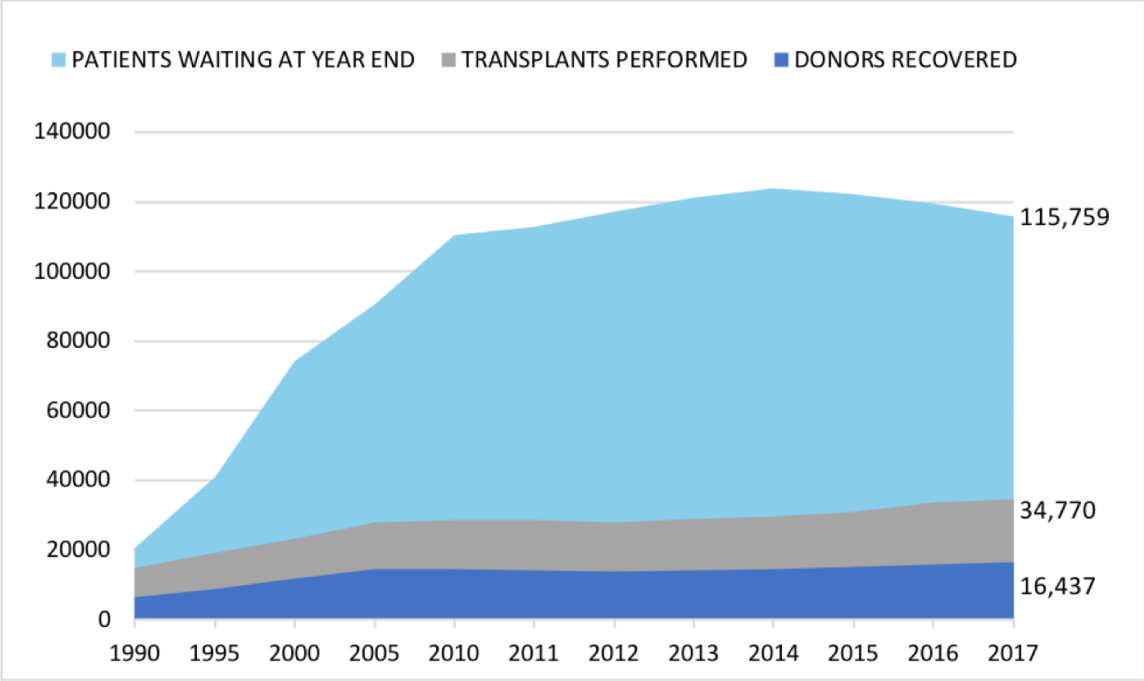

Figure 1.1. Organ shortage crisis facing the United States. As of 2017, there were almost 116,000 patients on the transplant waiting list at year's end, while only 34,770 transplants were performed and only 16,437 recovered donors.

Tissue engineering and regenerative medicine aims to alleviate this organ shortage crisis through the fabrication of functional tissue replacements. The typical process of tissue engineering starts with harvesting cells from a patient, typically through a biopsy (**Figure 1.2**). The cells are then expanded in vitro, and seeded onto scaffolds, which are materials that support cells to grow on. The cellularized scaffolds are then cultured and allowed to mature before implanting the construct back into the patient (4).

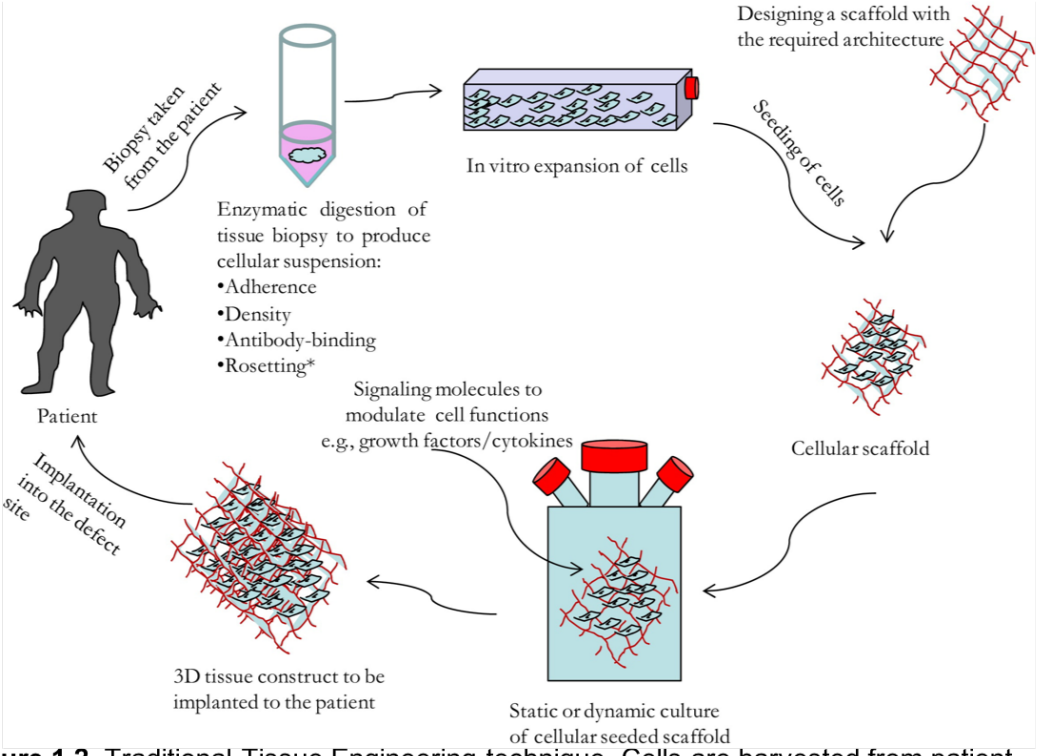

Figure 1.2. Traditional Tissue Engineering technique. Cells are harvested from patient, expanded *in vitro,* and seeded onto a scaffold. The cellularized construct is allowed to mature in culture, and then re-implanted back into the patient. Fig adapted from ref Abou, NEA, et. al. (2014) *Journal of Dentistry* **42**(8): 915-928.

1.1 CONVENTIONAL TISSUE ENGINEERING TECHNIQUES

The conventional tissue engineering approach involves the creation of acellular porous sacrificial scaffolds that are seeded with cells post-fabrication (5). The classical tissue engineering approach involves the isolation and seeding of organ-specific cells or

multipotent stem cells on different scaffold biomaterials (**Figure 1.2**; 6). Many techniques have been employed, such as fiber bonding, solvent casting, and melt molding, but proved to be minimally successful for tissue engineering applications. Fiber bonding methods allow fibers to be aligned in specific shapes, but they are only capable of producing very thin scaffolds (7). Solvent casting methods produced highly porous constructs, however the largest produced membrane was only 3-mm thick (8). Therefore, creating larger, organ-sized three-dimensional constructs is not feasible using these techniques. Melt molding techniques proved successful in producing three-dimensional scaffolds, but the high temperatures are required that biological materials cannot be incorporated during the production process (7). Scaffolds seeded post-fabrication are limited in their ability to meet the requirements of tissue engineering to produce three-dimensional scaffolds with predefined or controllable microstructures and macrostructures (9). Another major issue with solid scaffold seeding technologies is the deficiency of vascularization and poor mechanical integrity (10-11).

1.2 BIOMATERIALS FOR SCAFFOLD-BASED TISSUE ENGINEERING

Biomaterials used to create the scaffolds for the development of cellular constructs must satisfy multiple requirements. The scaffold serves as a temporary foundation for cell attachment and proliferation, so it must be constructed from materials with sufficient mechanical properties, a timed biodegradability to non-toxic products, and a controllable porosity (10,12-15). Additionally, the scaffold materials should not be cytotoxic or create an adverse response from the host. The materials must allow for a uniform cell

distribution within the bioprinted constructs, so that encapsulated cells are able to migrate, communicate, and form intercellular connections for tissue maturation.

1.3 ADVANCES IN BIOFABRICATION TECHNIQUES FOR ENGINEERING SOFT TISSUES: THREE-DIMENSIONAL BIOPRINTING

Bioprinting has since been extended to three dimensions through the use of nontoxic, biodegradable, thermo-reversible or chemically crosslinked hydrogels to overcome the disadvantages of conventional methods (16,17).

Types of Three-dimensional Bioprinters

A few of the solid freeform fabrication techniques currently being employed are laser-assisted bioprinting and inkjet printing. Laser-assisted bioprinting techniques use a pulsed laser source, a target plate, and a receiving substrate to generate three-dimensional scaffolds (**Figure 1.3**; 18). However, this technique is limited due to low throughput, low cell viability, and can only produce limited arrangements of fabricated structures because only photo-crosslinkable prepolymers can be used to form a crosslinked hydrogel network (15,19). Inkjet printing was developed as a non-contact methodology that reproduces digital image data on a substrate by depositing picoliter ink droplets (**Figure 1.3**; 20,21). However, inkjet printing does not produce a high-resolution construct, the fabricated constructs experience rapid protein denaturation, and many of the cells are lysed during the deposition process (22-23). Microextrusion bioprinters utilize syringe printer heads that deposit bioink in a drop-by-drop or layer-by-layer build-up approach. The biomaterials used as bioink for extrusion printing must be structurally stable or

include an *in situ* crosslinking mechanism to generate three-dimensional tissue constructs.

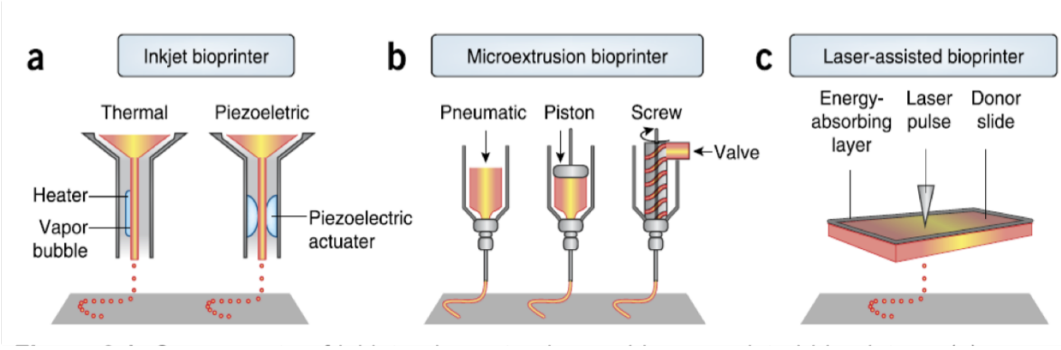

Figure 1.3. Components of (A) Inkjet, (B) Microextrusion, and (C) Laser-assisted Bioprinters. (A) Thermal inject printers electrically heat the printhead to produce air-pressure pulses that force droplets from the nozzle. (B) Microextrusion printers use pneumatic or mechanical (piston or screw) dispensing systems to extrude continuous beads of materials and/or cells. (C) Laser-assisted printers use lasers focused on absorbing substrate to generate pressures that propel cell-containing materials onto a collector substrate. Figured adapted from ref. Murphy, S.V. and Atala, A. *Nature Biotechnol.* **32:**773-785, (2014).

Direct and Indirect Bioprinting Techniques

Bioprinting technologies typically utilize two methods for fabricating cellular constructs. Indirect bioprinting involves the deposition of an acellular scaffold, shown here in blue, that is first created to determine the geometry of the desired construct (**Figure 1.4;** 24). This acellular mold is subsequently seeded with cells (red) to have them assemble in the set architectures. Once the construct has matured, the acellular blue scaffold is sacrificed leaving a cell-only construct. Direct bioprinting involves the deposition of cell-laden bioink in specific geometries to fabricate tissue constructs in cellularized patterns.

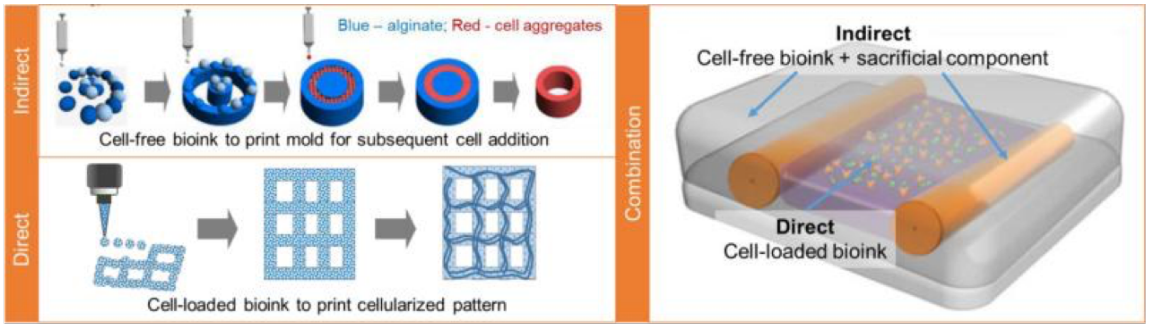

Figure 1.4. Indirect printing involves printing of a mold or sacrificial component for subsequent cell seeding. Direct printing is performed with cell-loaded or cell-only bioink for desired bioprinted patterning. Additionally, a combination of indirect and direct bioprinting can be used. Figure adapted from ref. Richards, D., et. al. *Ann Biomed Eng.* **45**(1):132-147 (2017).

Norotte, C., et. al. investigated the possibility of creating bioprinted constructs with embedded vascular patterns via indirect bioprinting (**Figure 1.5A-E;** 17). They created the sacrificial scaffold using non-adherent agarose (purple rods), and were able to create tubes with various dimensions. The smallest tube created was 900μm in diameter and had a wall thickness of 300μm. The seeded cells (orange) fused into multicellular spheroids within 5 and 7 days of culture to produce a tubular construct. This group was able to develop tubular structures with varying diameters and wall thicknesses, indicating an ability to tailor this technology to specific vascular constructs.

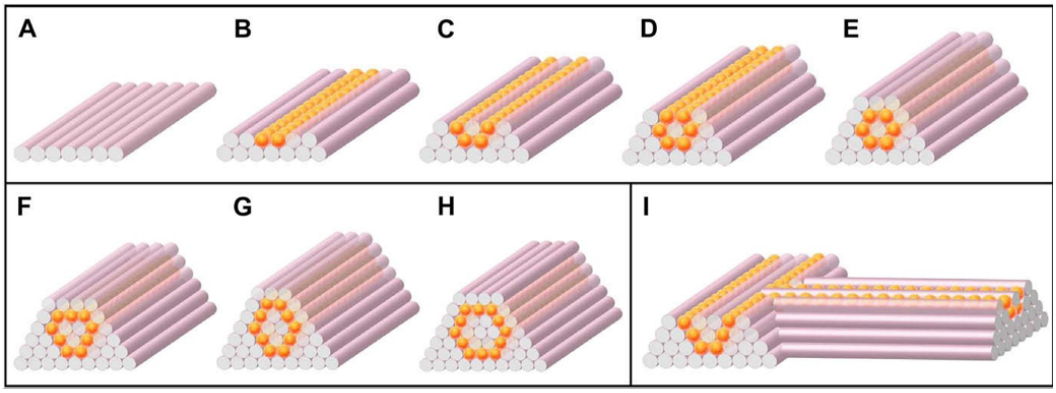

Figure.1.5. Design template for tubular structures. (A–E) Deposition scheme for the smallest diameter tube that can be built of agarose rods (pink) and multicellular spheroids (orange) of the same diameter. (F–H) More complex tubular structures. (I) Scheme for a branching structure. Fig adapted from ref Norotte, C., et. al. *Biomat* **30:**5910-5917, (2009).

The creation of tubular cell constructs is an exciting achievement, but there were many deficiencies observed with these constructs. The time to create larger constructs was very time consuming as fusion of spheroids can take up to a week and may result in non-uniform tubular surfaces. Additionally, the formed constructs indicated positive for apoptotic cells, likely due to the limited diffusion of oxygen and nutrients to these constructs.

1.4 SCAFFOLD-FREE TISSUE ENGINEERING

Scaffold-free tissue engineering aims to produce physiologically-relevant three-dimensional multicellular constructs without the use of a scaffold. These methods have been developed as ways to avoid the issues associated with scaffold materials, such as toxicity of by-products, uncontrolled mechanical properties, and others, as well as to develop more physiologically-relevant constructs that rely on the mechanisms driving tissue development *in vivo*.

Generation of Multicellular Spheroids

The creation of multicellular spheroids relies on the use non-adherent molds, which means that the cells are unable to interact with or adhere to the material used (**Figure 1.7**). Cells are expanded on cell culture dishes, and then harvested using enzymatic digestion, typically trypsinization (**Figure 1.7B**). The suspended cells, shown in blue, are then seeded into the non-adherent mold, and cultured. Cellular constructs are formed in the dimensions of the non-adherent mold with time in culture.

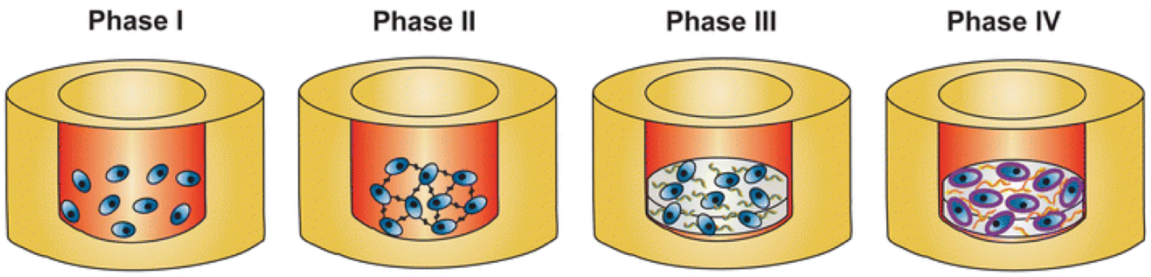

Figure 1.6. Scaffold-free tissue engineering method. Cells (blue) are seeded into non-adherent mold (yellow), and allowed to culture. During this culture period, the cells undergo self-assembly to form three-dimensional tissues in the shape of the non-adherent mold. Figure adapted from ref DuRaine, G.D., et. al. Annals of Biomed Eng **43**(3):543-54, (2015).

During the culture period, the cells undergo the process of cellular self-assembly, which relies on the inherent capability of cells to migrate and for intercellular connections (25). Adherent cells depend on the formation of these intercellular as well as cell-matrix connections for survival. When adherent cells are placed in an environment that lacks a surface for adhesion, the cells will aggregate and undergo the process of self-assembly. During this process, suspended cells form three-dimensional multi-cellular spheroids. The produced multicellular spheroids have similar architectural and functional characteristics of native tissues.

Cell Sheet Engineering

Another emerging technique for generating scaffold-free constructs, is cell sheet engineering. Harvesting cells via enzymatic digestion, trypsinization, cell-cell junctional proteins and deposited extracellular matrix are disrupted and degraded for cell recovery (**Figure 1.7B**). To overcome this limitation Yang, J., et. al. developed temperature-responsive cell culture dishes to create scaffold-free cellular sheets (26). The temperature-responsive cell culture dish is created by covalently attaching a thermo-responsive polymer, poly(N-isopropylacrylamide) (PI-PAAm). During normal culture conditions, 37℃ and 5% CO_2, the surface is hydrophobic and allows cell attachment, migration, and proliferation. Once a confluent monolayer has been established on the culture plate, the temperature is reduced to 32℃, or the PI-PAAm lower critical solution temperature, which causes the dish surface to become hydrophilic and swell (**Figure 1.7C**). A hydrated layer forms between the cells and the culture plate, which permits their spontaneous detachment without the need for enzymatic digestion. This retains essential cell surface proteins like ion channels, growth factor receptors, and cell-cell junctional proteins within the cell sheet constructs. Additionally, the deposited extracellular matrix is harvested with the cellular sheets, allowing for the reconstruction of multiple tissues and organs using this technique.

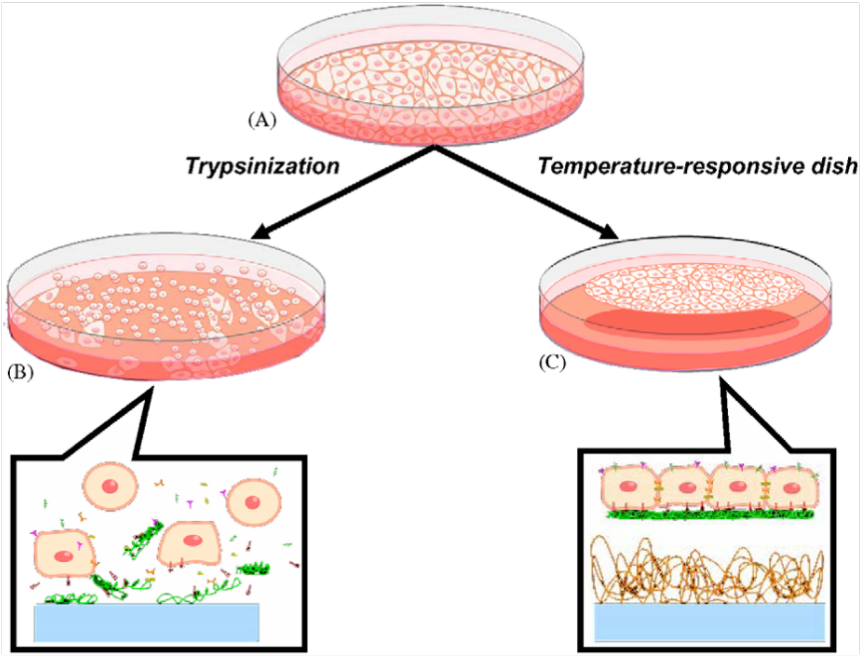

Figure 1.7. Cell sheet engineering. (A) During cell culture, cells deposit extracellular matrix molecules and form cell-cell junctions. (B) With proteolytic harvest by trypsinization, both ECM and cell-cell junction proteins are degraded for cell recovery. (C) In contrast, cells harvested from temperature-responsive dishes are recovered as intact sheets along with their deposited ECM, by simple temperature reduction. Figure adapted from ref Yang, J., et. al. *Biomat* **26:**6415-6422, (2005).

1.5 LIMITATIONS IN TISSUE ENGINEERING

The field of tissue engineering advances an exciting array of solutions for organ repair and wound healing. However, to realize this potential, several hurdles must be overcome. Vascularization is arguably the most important practical limitation in tissue engineering, imposing both dimensional and time constraints on the technology. Vascularization and fast anastomosis with the host are essential in engineering cellular constructs that survive once implanted, as well as tissue maintenance and regeneration. Endothelial cell migration and physiological growth of new blood vessels *in vivo* has been reported to occur at ~5 um/hour due to the availability of oxygen, which is limited to a diffusion distance of $150 - 200\mu m$ from a supplying blood vessel (27-28).

With the clinical need being for larger engineered tissues, a major focus in the tissue engineering field has been on designing constructs with pre-existing vascular architectures (**Figure 1.5**) or, more recently, prevascularized constructs. This dissertation focuses on the integration of scaffold-based and scaffold-free techniques to develop novel technologies for engineered tissue replacements and wound dressings that address the limitations described in this chapter.

1.6 REFERENCES

1. Smith, C.M., Christian, J.J., Warren, W.L., & Williams, S.K. Characterizing Environmental Factors that Impact Viability of Tissue-Engineered Constructs Fabricated by a Direct-Write Bioassembly Tool. *Tissue Engineering.* **13** (2), 373-383, (2007).
2. Ozbolat, I. and Yu, Y. Bioprinting Towards Organ Fabrication: Challenges and Future Trends. *IEEE Trans Biomed Eng.* **60** (3), 691-699, (2012).
3. Derakhshanfar, S., Mbeleck, R., Xu, K., Zhang, X., Zhong, W., and Xing, M. 3D bioprinting for biomedical devices and tissue engineering: a review of recent trends and advances. *Bioactive Materials.* **3:**144-156, (2018).
4. Abou Neel, E.A., Chrzanowski, W., Salih, V., et. al. Tissue Engineering in Dentistry. *Journal of Dentistry* **42**(8): 915-928, (2014).
5. Yeong, W.Y., Chua, C.K., Leong, K.F., & Chandrasekaran, M. Rapid Prototyping in Tissue Engineering: Challenges and Potential. *Trends Biotechnol.* **22** (12), 643-652, (2004).
6. Laschke, M.W. and Menger, M.D. Vascularization in Tissue Engineering: angiogenesis versus inosculation. *Eur Surg Res.* **48**(2):85-92, (2012).
7. Lu, L. and Mikos, A.G. The Importance of New Processing Techniques in Tissue Engineering. *MRS Bull.* **21**(11), 28-32, (1996).
8. Wake, M.C., Gupta, P.K., Mikos, A.G. Fabrication of pliable biodegradable polymer foams to engineer soft tissues. *Cell Transplant*. **5**(4), 465–473, (1996).
9. Yang, S., Leong, K.F., Du, Z., & Chua, C.K. The Design of Scaffolds for Use in Tissue Engineering. Part II. Rapid Prototyping Techniques. *Tissue Engineering.* **8** (1), 1-11, (2002).
10. Sachlos, E. & Czernuszka, J.T. Making Tissue Engineering Scaffolds Work. Review on the Application of Solid Freeform Fabrication Technology to the Production of Tissue Engineering Scaffolds. *European Cells and Materials.* **5**, 29-40 (2003).
11. Mironov, V., Visconti, R.P., Kasyanov, V., Forgacs, G., Drake, C.J., & Markwald, R.R. Organ Printing: Tissue Spheroids as Building Blocks. *Biomaterials.* **30** (12), 2164-2174, (2009).

12. Landers, R., Pfister, A., Hubner, U., John, H., Schmelzeisen, R., and Mulhaupt, R. Fabrication of Soft Tissue Engineering Scaffolds by means of Rapid Prototyping Techniques. *Journal of Materials Science.* **37** (15), 3107-3116, (2002).
13. Murphy, S.V., Skardal, A., and Atala A. Evaluation of Hydrogels for Bio-Printing Applications. *Journal of Biomedical Materials Research Part A.* **101A** (1), 272-284, (2013).
14. Burg, K.J.L. & Boland, T. Minimally Invasive Tissue Engineering Composites and Cell Printing. *IEEE Eng Med Biol Mag.* **22** (5), 84-91, (2003).
15. Billiet, T., Vandenhaute, M., Schelfhout, J., Van Vlierberghe, S., & Dubruel, P. A Review of Trends and Limitations in Hydrogel-Rapid Prototyping for Tissue Engineering. *Biomaterials.* **33** (26), 6020-6041, (2012).
16. Gruene, M., *et al.* Laser Printing of Three-Dimensional Multicellular Arrays for Studies of Cell-Cell and Cell-Environment Interactions. *Tissue Eng.* **17** (10), 973-982, (2011).
17. Norotte, C., Marga, F.S., Niklason, L.E., & Forgacs, G. Scaffold-free Vascular Tissue Engineering Using Bioprinting. *Biomaterials.* **30** (30), 5910-5917, (2009).
18. Devillard, R., *et al.* Cell Patterning by Laser-Assisted Bioprinting. *Methods Cell Biol.* **119**: 159-174, (2014).
19. Ferris, C.J., Gilmore, K.G., Wallace, G.G., & Panhuis, M. Biofabrication: An Overview of the Approaches Used for Printing of Living Cells. *Appl. Microbiol. Biotechnol.* **97** (10), 4243-4258, (2013).
20. Binder, K.W., Allen, A.J., Yoo, J.J, & Atala, A. Drop-on-Demand Inkjet Bioprinting: a Primer. *Gene Ther Reg.* **6** (1), 33-, (2011).
21. Murphy, S.V. & Atala, A. 3D Bioprinting of Tissues and Organs. *Nat Biotech.* **32** (8), 773-785, (2014).
22. Xu, T., *et al.* Viability and Electrophysiology of Neural Cell Structures Generated by the Inkjet Printing Method. *Biomaterials.* **27** (19), 3580-3588, (2006).
23. Calvert, P. Inkjet Printing for Materials and Devices. *Chem Mater.* **13** (10), 3299-3305, (2001).
24. Jia, J., *et al.* Engineering Alginate as Bioink for Bioprinting. *Acta Biomaterialia.* **10** (10), 4323-4331, (2014).
25. Czajka, C. and Drake, C.J. Self-assembly of prevascular tissues from endothelial and fibroblast cells under scaffold-free, non-adherent conditions. *Tissue Eng Part A.* **21**(1-2):277-287, (2015).
26. Yang, J., Yamato, M., et. al. Cell sheet engineering: recreating tissues without biodegradable scaffolds. *Biomaterials* **26**:6415-6422, (2005).
27. Grimes, D.R., Kelly, C., Bloch, K., and Partridge, M. A Method for Estimating the Oxygen Consumption Rate in Multicellular Tumour Spheroids. *J. Royal Society Interface* **11**(92): 1-11, (2014).
28. Matthias, W., Laschke, M.W., Vollmar, B., Menger, M.D. Inosculation: Connecting the Life-Sustaining Pipelines. *Tiss Eng: Part B* **15**(4):455-462, (2009).

CHAPTER TWO

BIOFABRICATION AND BIOMATERIALS

Organ transplantation has been limited by two major factors: a critical shortage in donors and a high risk of graft rejection (58). With over 120,000 patients on the organ waiting list as of 2017, transplantation is not a feasible option for many of these people (54). Tissue engineering utilizes the principles of biology and engineering to develop functional substitutes that serve to maintain, restore, or enhance native tissues and organs (1). The traditional tissue engineering techniques involve the creation of a solid, porous scaffold that is seeded with cells post-fabrication. The scaffold is designed to try to encourage cells to form the desired tissue by the incorporation of specific cell types, growth factors, or other signaling molecules (55). However, these techniques have been met with limited success due to the lack of organization and hierarchy within the constructs that is typically seen in native tissues. Additionally, under these conditions the cells are unable to grow in favored three-dimensional orientations, which is often accompanied by loss of tissue-specific function (3-5).

The capability of generating three-dimensional biomimetic constructs on demand would facilitate scientific and technological advances in tissue engineering as well as in cell-based sensors, drug/toxicity screening, tissue or tumor models, and other areas (2). This has led to the direct fabrication of scaffolds with a complex, anatomically correct external geometry, and precise control over the internal geometry (9). Three-dimensional bioprinting is a methodology used for generating three-dimensional constructs of various sizes and shapes from a digital model using a layer-by-layer approach (34). The

fabrication of three-dimensional biomimetic constructs plays an essential role in the advancement of tissue engineering, and the bioprinting process restores the ability to form three-dimensional constructs that are able to recapitulate the *in vivo*-like structure and function of complex tissues.

2.1 ADVANCED ADDITIVE MANUFACTURING BIOPRINTING

As an additive manufacturing technique, three-dimensional bioprinting involves the deposition of either cell-laden biomaterials, or acellular biomaterials that are seeded post-fabrication (54). Extrusion bioprinters have been developed as an expansion of inkjet printing in order to deposit more viscous materials with higher local cell densities (54). The versatility of these machines permits the deposition of almost all types of hydrogel pre-polymer solutions with varying ranges of viscosity and cell aggregates (53). These bioprinters are also able to deposit concurrent lines of cell-laden materials as opposed to independent droplets in traditional techniques.

The typical workflow of extrusion bioprinting of cell-laden materials is shown in Figure 2.1, and involves the isolation and expansion of human cells *in vitro,* mixing these cells into a printable material, and finally, depositing cell-laden scaffolds in a layer-by-layer fashion (53; **Figure 2.1**). In these systems cells, proteins, growth factors, and others can be integrated into the matrix materials during the fabrication process and concurrently deposited using computer-controlled actuators to generate three-dimensional cell-laden scaffolds that closely mimic the microarchitecture of native tissue (12,28,45). The produced scaffolds can be used as therapeutic devices themselves (i.e. implant the

generated constructs), as a testing platform for drug screening and discovery, as well as an *in vitro* model for disease (53).

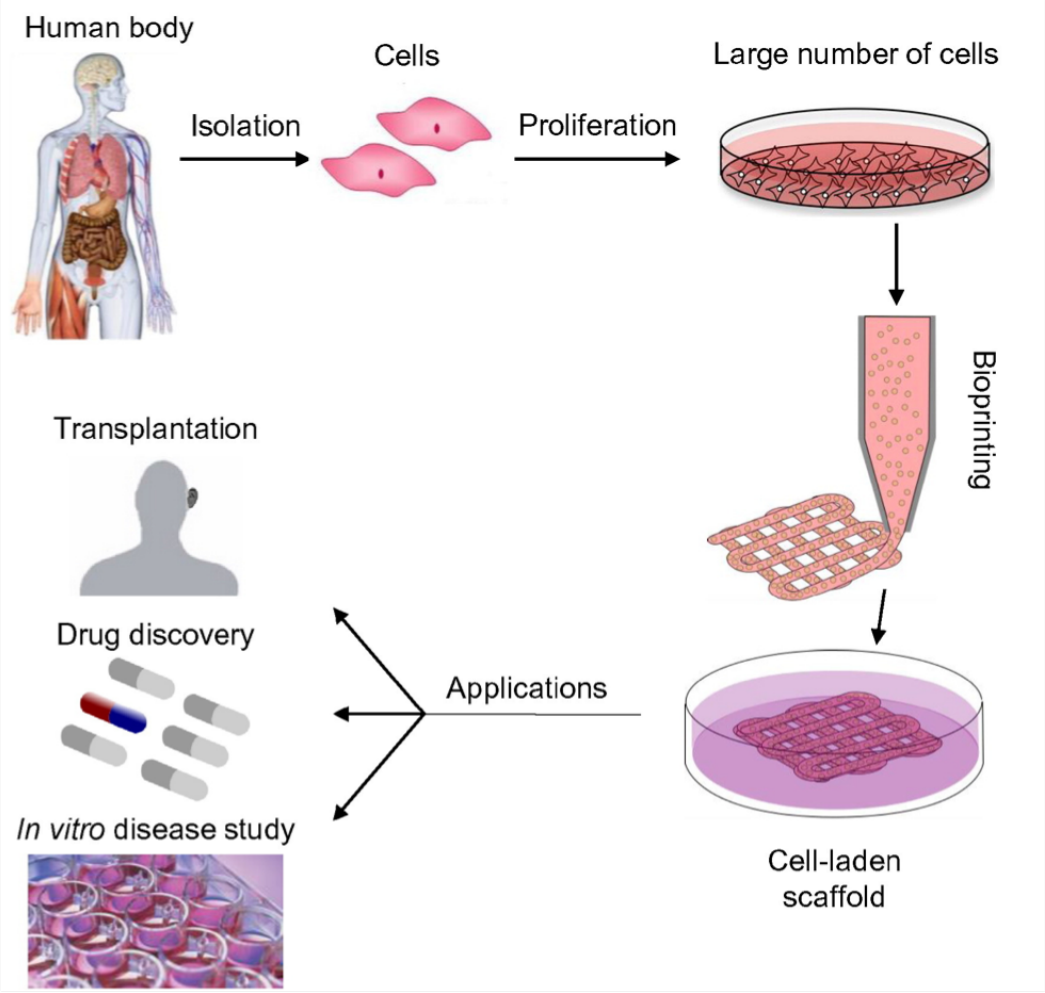

Fig. 2.1. The typical workflow of bioprinting. First, human cells are isolated and expanded *in vitro* prior to bioprinting the desired cell-laden scaffold. These scaffolds could then be used as therapeutic devices themselves (i.e. implants), as a testing platform for drug screening and discovery, or as an *in vitro* model system for disease.
Fig adapted from ref Mandrycky, C., et. al. *Biotechnol Adv* **34:**422-434, (2016).

Bioprinting typically utilizes two methods for creating three-dimensional constructs: direct and indirect printing. Direct bioprinting techniques have cells, as well as other factors (i.e. growth factors, peptides, etc.), loaded in a cytocompatible bioink that

are deposited together to generate cellularized scaffolds. Constructs generated with this technique rely on a fast gelation/crosslinking in order to sustain the stable structure (44; Figure 2.2). Indirect printing methods generate an acellular negative structure that serves as a scaffold for cell-seeding post-fabrication (44; Figure 2.2).

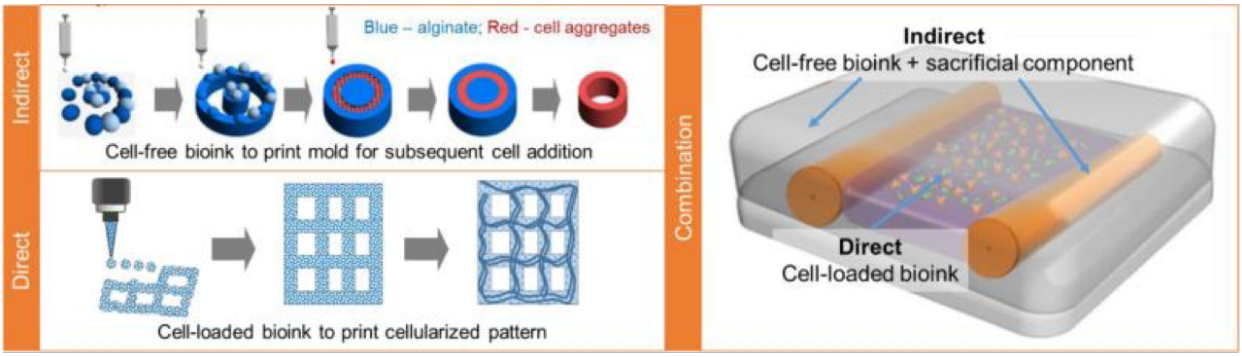

Figure 2.2. Indirect printing involves printing of a mold or sacrificial component for subsequent cell seeding. Direct printing is performed with cell-loaded or cell-only bioink for desired bioprinted patterning. Additionally, a combination of indirect and direct bioprinting can be used. Figure adapted from ref. Richards, D., et. al. *Ann Biomed Eng.* **45**(1):132-147 (2017).

2.2 BIOMATERIALS FOR EXTRUSION-BASED, DIRECT-WRITE BIOPRINTING

Human tissue biology is heavily regulated by specific interactions and cross-talk between different resident cell populations. The three-dimensional organization of tissue-engineered constructs is a fundamental component of the fabrication method because the produced constructs must closely mimic the highly organized interaction of cells and extracellular matrix in native tissue. The materials in which the cells are embedded directly influences the mechanical and biological properties of the produced scaffold, as well as subsequent cell behaviors within that scaffold. Therefore, the two most critical factors for bioprinting functional tissue replacements are the biomaterials used to create

scaffolds and the cell types incorporated within those scaffolds in order to adequately recapitulate these complex microenvironments *in vitro* (53,54).

Each technique for bioprinting has different requirements for the materials used to create scaffolds, as discussed in chapter 1. Bioinks are typically comprised of cell-laden pre-polymer solutions (53). The ideal bioink must satisfy specific material and biological requirements because it serves as a temporary foundation of cell attachment and proliferation. Important material properties include tunable mechanical properties, printability, crosslinking mechanism, biocompatibility, and controlled degradation into non-toxic by-products (4,6-9,47).

Extrusion-based bioprinters used for printing cell-laden materials are able to incorporate higher cell densities than other techniques, and are able to print materials with viscosities ranging from $30 - 60 \times 10^7 \mathrm{mPa}$ (54). Cell-laden bioprinting requires the material used for encapsulation has a high-water content and adequate porosity for cells to receive nutrients and oxygen from the environment, and remove waste to sustain viability within the scaffold (54). Hydrogels, both natural and synthetic, have been frequently employed in bioprinting due to their structural similarity to the macromolecular-based components of the body, and their tissue-mimetic properties (52). These hydrophilic materials are able to absorb large amounts of water within their three-dimensional networks, and retain this water in their swollen state (56).

The mechanical properties of hydrogels are significantly important for tissue engineering applications where the gel must create and maintain a space for cell infiltration and tissue development (52). The mechanical properties of the scaffolds post-

polymerization must be adequate to sustain a suitable environment for cell attachment, proliferation, and differentiation (53). These properties include shear stress, strain, compressive modulus, and the mass swelling ratio (7).

Printability refers to the interaction between the deposited bioink and the printing substrate that allows for the formation of high-quality, geometrically accurate constructs. This property is related to the surface tension between the bioink and substrate, which can be measured by the contact angles between the two materials, as well as the resolution of the bioprinter (53). The deposited pre-polymeric bioink solution should have a large contact angle with the substrate, which is produced when the bioink solution maintains tension in the vertical direction (53). Bioprinters in the literature have reported resolutions ranging from $10 - 10{,}000\mu$m (54). The wide range of resolutions is due to the fact that many labs are developing novel in-house bioprinter setups for applications that have specific requirements within this range. In general, bioprinters have a resolution on the micron-scale, which is relevant on a cellular level (54). The crosslinking mechanism of the bioink also has a large effect on its printability. In order to deposit cell-laden solutions, the materials must be polymerized post-printing. Therefore, the mechanism for gelation must be gentle on cells and not impact cell viability. There are three dominant methods of crosslinking frequently used for bioprinting applications: 1) photo-crosslinking, 2) physical crosslinking, and 3) chemical crosslinking (53). Photo-crosslinking utilizes the polymerization of light-sensitive polymers, however, many of these techniques require the use of ultraviolet (UV) light, which can be toxic to encapsulated cells, as well as degrade the matrix in which the cells are embedded (54).

Chemical crosslinking leads to the formation of permanent junctions, while transient/reversible three-dimensional polymer networks are formed via physical crosslinking, such as thermal crosslinking techniques (56).

Biocompatibility is determined by how the biomaterial performs with the host response in a specific situation. *In vitro,* it is required that the material is not harmful to cell survival, proliferation, and provides proper binding sites for cells embedded within it (53). *In vivo,* it is additionally required that the biomaterial can be degraded or incorporated into the native extracellular matrix without producing toxic by-products or resulting in destructive interactions with host cells (53). Once implanted, biodegradable hydrogels can be broken down into lower-molecular weight, water-soluble fragments that can be resorbed or excreted by the body once the function of the gel has been completed (52). This makes these materials promising choices for releasing drugs or other factors in a clinically-relevant timeline.

2.3 MODIFIED ALGINATE AS A BIOACTIVE SCAFFOLD

More recently, the engineering of "smart", or bio-functional, and composite materials have evolved due to the limitations of using a single material for various bioprinting applications (53). Native alginate, which is arguably the most frequently used bioink in bioprinting applications due to its biocompatibility and gentle gelation mechanism (30,59). Alginate is a natural polysaccharide derived from seaweed, and is comprised of alternating chains of polyguluronate (G) and polymannuronate (M) (**Figure 2.**, 60). The mechanical properties, pore size, and crosslinking density of the alginate polymers can be controlled by varying the M:G monomers ratio (60). It has been shown

that alginates containing a high fraction of polyguluronate blocks produces gels with superior strength compared to those with high amounts of polymannuronate (60). Alginate is polymerized in the presence of divalent cations, like calcium, that ionically crosslink the carboxylate groups in the polyguluronate blocks of the copolymer structure (30,60). However this material is bioinert, i.e. lacks cell-binding sites, contains minimal cell-activating properties, and only gets minimally degraded *in vivo* (54). The *in vivo* degradation of native alginate is caused by the loss of divalent cations in an uncontrolled manner, and results in the release of both low- and high-molecular weight strands. The resultant high-molecular weight strands are not easily broken down and may take long periods of time to be cleared from the body, if at all.

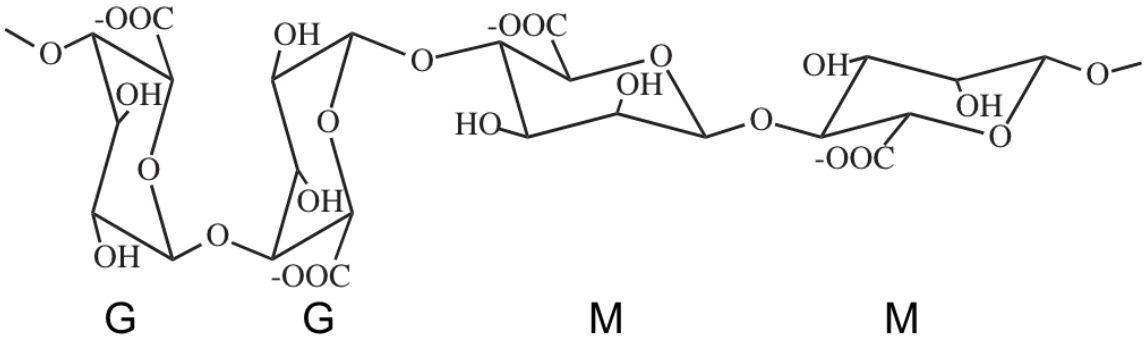

Figure 2.3. Alginate copolymer structure, where G represents polyguluronate blocks, and M represents polymannuronate blocks. The properties, including strength, pore size, and crosslinking density of the polymerized structure can be manipulated by varying M:G ratios within the chains. Fig adapted from ref Drury, J.L., et. al. *Biomat* **24,** (2003).

To expand on this material for regenerative applications, alginates functionalized with RGD-binding sites have been frequently used as bioink to provide a matrix scaffold that will direct a specific 3D cell growth (37). Scaffolds made using RGD-conjugated

alginate were shown to be capable of forming robust cell-compatible hydrogels in physiological conditions (7,14,17,44).

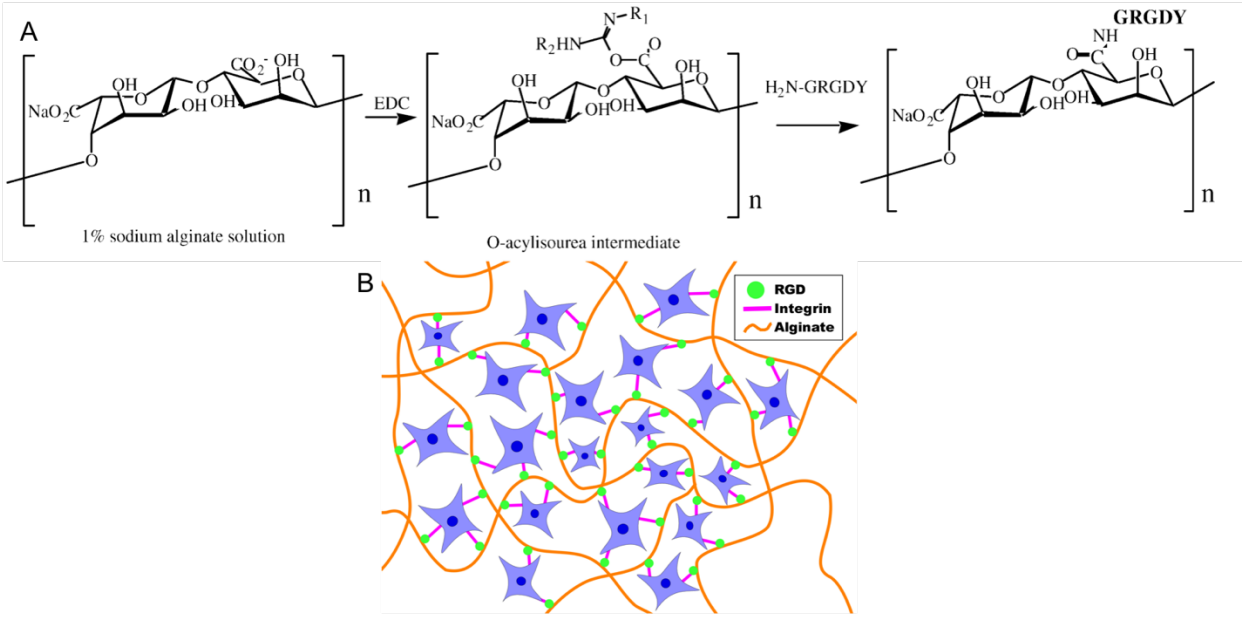

Figure 2.4. (A) Reaction scheme of peptide coupling to alginate molecules. Amide bond formation is mediated by the carbodiimide through the carboxyl group of the polymannuronate blocks on the alginate and the N-terminal amine of the GRGDY pentapeptide. Fig adapted from ref Rowley, J.A., et. al. *Biomat* **20**, (1999). (B) Illustration of how cells bind and interact with the RGD-conjugated alginate via integrin linkages.

Additionally, chemically modifying the alginate through oxidation has been demonstrated in the literature to produce scaffolds with controllable degradation rates (37). Partial oxidation using sodium periodate alters the conformation of the uronate residues into an open-chain adduct, which are vulnerable to hydrolysis (**Figure 2.5**, 61).

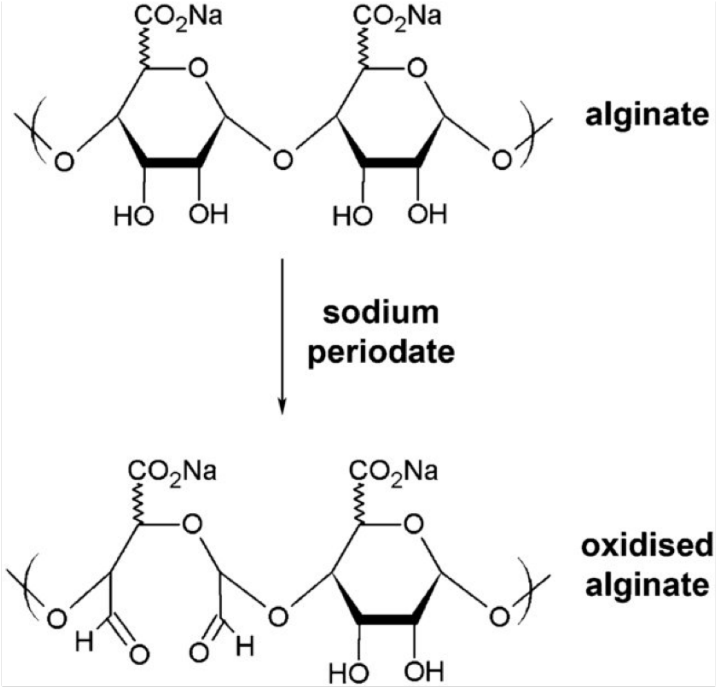

Figure 2.5. Chemical structure of partially oxidized alginate, showing the conformation change that occurs from a closed to open state with oxidation. Fig adapted from ref Wright, B., et. al. *J Biomed Mater Res A.* **102**(10), (2014).

By changing the polymeric chain to an "open" state the pore size of the resultant hydrogel is less dense as well as the stiffness, which has been reported to enhance cell viability in implanted constructs (37, 61). For example, Jia, et. al. showed that varying the degree of oxidation and concentration of the alginate used effected the viability human Adipose-derived stem cells in bioprinted constructs (Figure 2.3; 37). High viabilities (>90%) were associated with alginate bioinks with medium viscosities ($\sim 400 \mathrm{mm}^2\mathrm{s}^{-1}$), while low viabilities were observed in high viscosity bioinks ($\sim 3{,}000 \mathrm{mm}^2\mathrm{s}^{-1}$). The differences seen in cell viability between the materials was attributed to the denser polymeric environment associated with high viscosity alginates, which diminished nutrient transport to the cells embedded in these constructs (37). Therefore, when using modified alginate as a vehicle for cell encapsulation and transplantation, it is essential to

determine the appropriate environment required for the specific application and to modify the materials to meet those demands.

(a)

Viability after printing (day 0)

Ox. \ Conc.	2	5	8	10	15	20
0	-	>95%	>95%	~70%	-	-
1	-	-	>95%	>90%	-	-
3	-	-	>95%	>95%	<20%	-
5	-	-	-	>95%	>95%	<20%
10	-	-	-	-	>95%	>90%

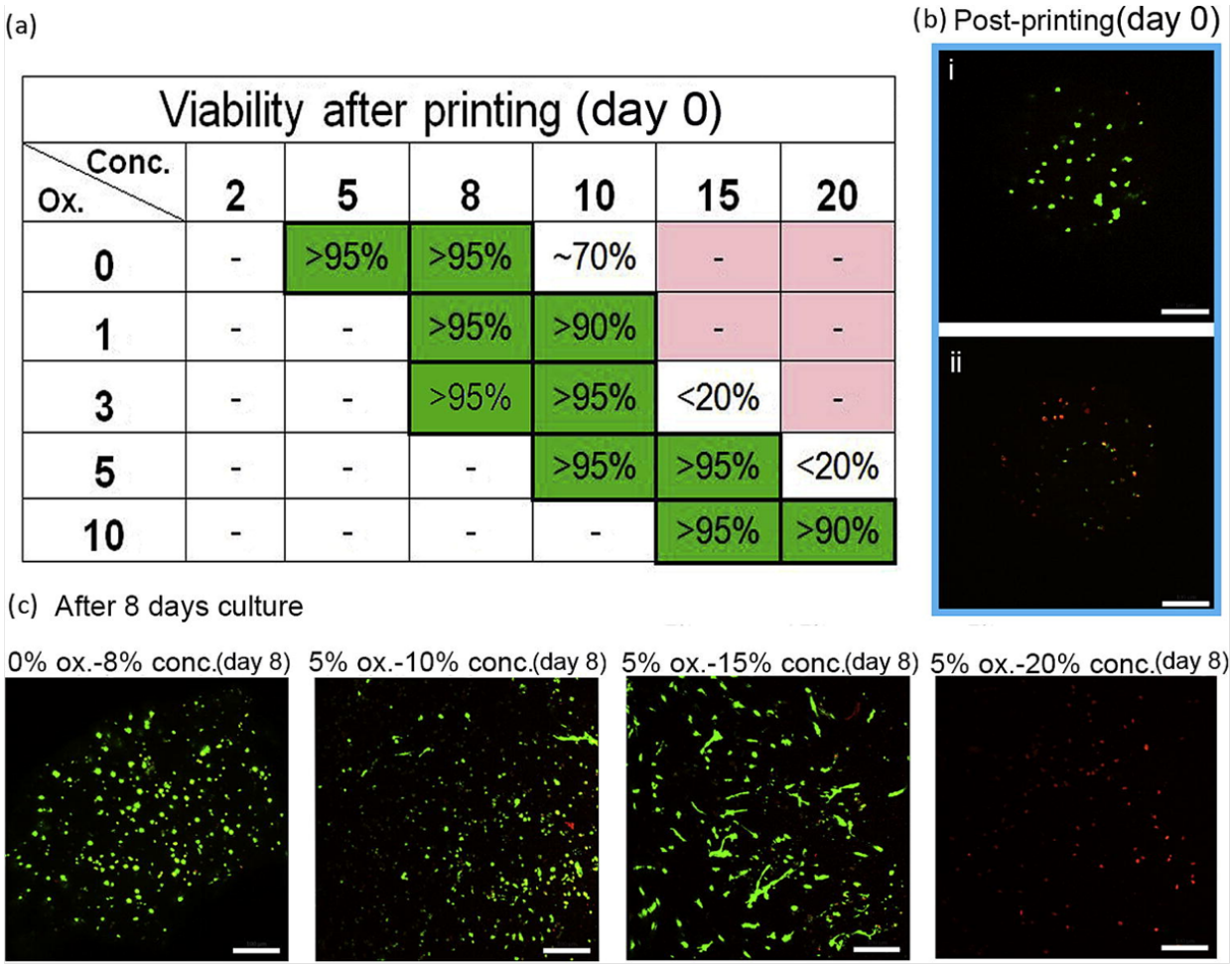

Fig. 2.6. Cell viability assay of density and viscosity criterion-filtered samples. (a) Samples of high viability (>90%) after printing (green). (b) The fluorescent pictures of live–dead assay after printing: (i) high cell viability sample (e.g. 5% ox.–15% conc.); (ii) low cell viability sample (e.g. 5% ox.–20% conc.) (scale bar = 100 μm). (c) Cell viability assay at day 8. Except for the 5% ox.–20% conc. sample (0% viability), the remaining four samples showed high viabilities (>95%) after 8 days in culture (scale bar = 100 μm). Fig adapted from ref Jia, J., et. al. *Acta Biomaterialia* **10**(10):4323-4331, (2014).

Another avenue for material modification is the combination of multiple materials to produce a heterogeneous scaffold. Through the combination of different hydrogels, the synthesized scaffold's properties are modifiable to meet distinct application requirements.

To further expand alginate as a useful material for regenerative tissue engineering applications it could be combined with collagen to provide structural and cell-adhesive properties. Collagen is the most abundant protein in mammalian tissues and is the main component of natural extracellular matrix (46). It inherently contains RGD cell-binding sites, and provides structural support and mechanical strength to tissues *in vivo* (46,57). Additionally, collagen is known to permit cell adhesion, chemotaxis, and migration, making it a good candidate for bioprinting applications. We have developed collagen/alginate blend hydrogels that, in collaboration with other labs at the Medical University of South Carolina, have been explored for applications including timed drug release of vancomycin for surgical implant sites (provisional patent submitted), as well as for the attachment, migration, and subsequent release of regulatory T-cells for *in vivo* applications (provisional patent submitted). The incorporation of additional materials or chemical modifications could expand the use of this material to a multitude of different applications, such as wound healing and fabricating soft tissue replacements.

2.4 MIMICKING THE COMPLEX *IN VIVO* MICROENVIRONMENT

Every tissue in the body is composed of multiple cells types positioned relative to each other in specific, complex orientations and patterns. To replicate this on a cellular level *in vitro,* the hydrogels that constitute the bioink can be heterogeneous, i.e. consisting of multiple cell types and/or materials, or homogeneous, depending on the tissue being replicated. Additive manufacturing systems deposit these multicellular building blocks, or the bioink, drop-by-drop or layer-by-layer via disposable syringes and

tips onto a computer-controlled stage capable of moving in the x, y, and z directions. Through computer software, the architecture of printed scaffolds can be easily manipulated to mimic tissue-specific patterns depending on the requirements of the application. Unlike conventional techniques, three-dimensional medical technologies (i.e. magnetic resonance imaging, computer tomography) can be incorporated into the designs, which enables the possibility of generating patient-specific constructs (10).

2.5 THE PALMETTO BIOPRINTER

The Palmetto Printer is a custom built three-dimensional multi-dispenser system that uses programmable robotic manufacturing methods to generate three-dimensional heterogeneous tissue constructs (**Figure 2.4**). It allows the use of a plurality of materials in unique combinations to produce heterogeneous structures. The initialization of the bioprinter is one of the most important steps in bioprinting because it allows you to set a variety of parameters to optimize the printability of the bioprinted constructs.

Figure 2.7. Palmetto Bioprinter at Medical University of South Carolina.
(A) Programmable Logic Controller coordinates the actions of all printer functions. An airtight containment chamber (B) with filtered intake (C) and exhaust (C) maintains a regulated internal positive pressure to reduce the chance of contamination. Dual UV lights (D) mounted in the chamber ceiling can be programmed to operate at safe intervals. A Janome 2300N XYZ Robot (E) is programmed and controlled by an integrated computer (I). Three dispenser controllers (G) are programmed to regulate the output of dispenser guns (F) available to be loaded onto the robot Z-axis arm (H) under computer control. The temperature of the robot sample holder (J) is set between 4 and 40 °C by a water bath controller (K). Dual digital cameras (L) are available to monitor printer activity and sample formation. One camera is mounted onto the robot Z-axis arm and provides a magnified image of the dispenser tip of the loaded gun.

The bioprinter comprises a batch type process with startup, operation and shutdown sequences controlled by a programmable logic controller (PLC), which the user

operates through an interactive touch screen control panel (**Figure 2.4, A**). To prevent contamination of biological materials the bioprinter is enclosed in a positively-pressured poly(methyl methacrylate) (PMMA) chamber with a high-efficiency particulate arrestance (HEPA)-filtered air circulation system (**Figure 2.4, B,C**). The interior of the printer can be sterilized using the built-in ultraviolet light sources (**Figure 2.4, D**). The central component of the bioprinter is a fully programmable positioning robot that can reproducibly place a dispenser tip with an accuracy of 10 micrometers (**Figure 2.4, E**). There are three dispensers, which are able to deposit volumes as small as 230 nanoliters using a rotary screw (**Figure 2.4, F**). They are independently programmable using separate computers that govern printing parameters for each dispenser (**Figure 2.4, G**). Rotary-screw dispensing utilizes the rotation of a motor-driven screw to move bioink down a syringe and out of the syringe tip. These dispensers are mounted onto a pneumatically controlled Tool Nest (**Figure 2.5, A, B**), allowing the robot to switch dispenser mounted onto the Z-axis robotic arm under programmed control (**Figure 2.4, H**).

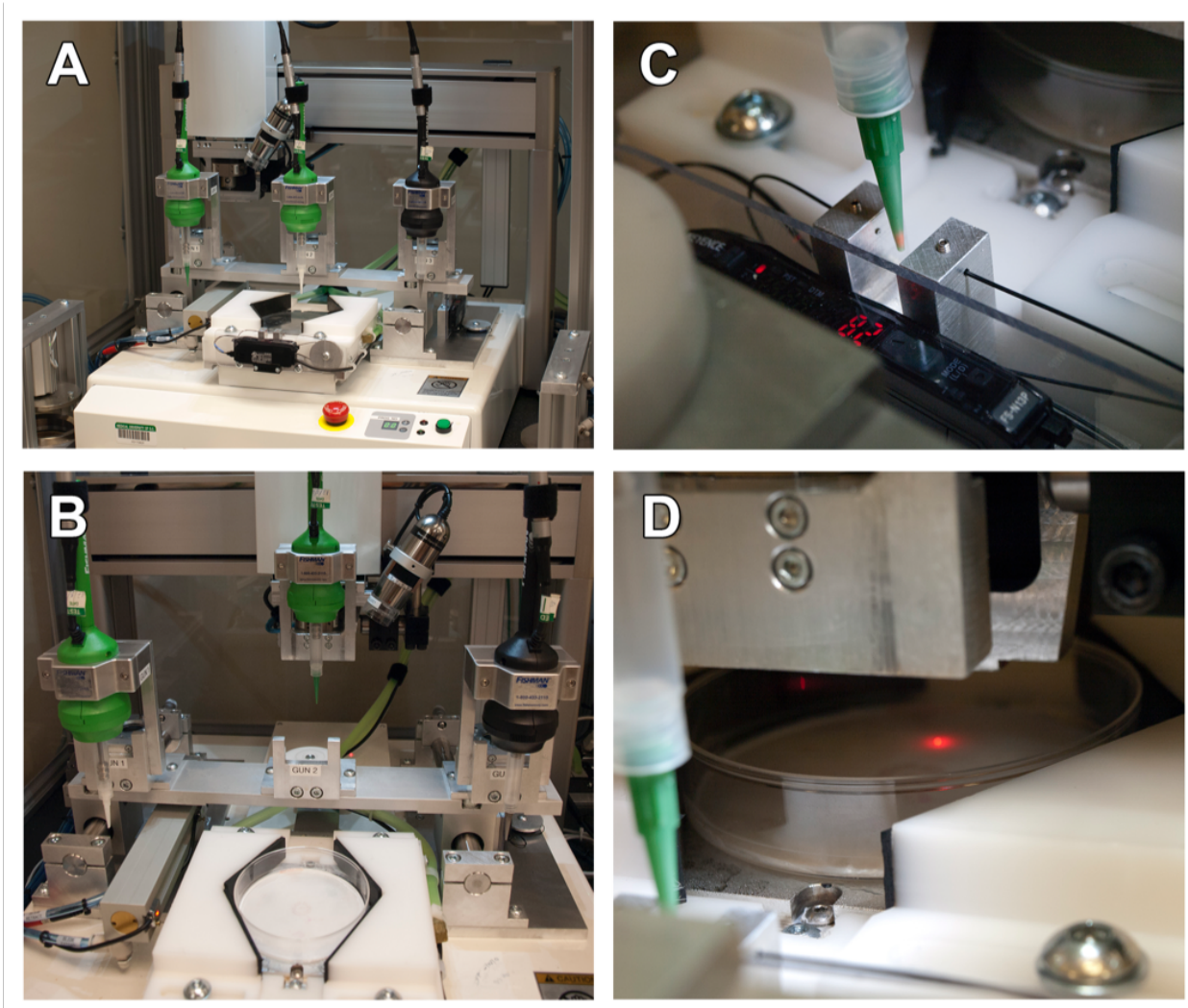

Figure 2.8. Palmetto Bioprinter at Medical University of South Carolina: Tool Nest, Optic Sensors, and Displacement Laser of Bioprinter. (A) Unloaded tool nest view from the front. (B) Loaded tool nest view from the front. (C) Optic Sensors measuring the dispensing tip end in three-dimensional space. (D) Distance laser measuring the Z coordinate of the printing surface.

The XYZ robot receives printing instructions from a computer running design software (**Figure 2.4, I**). Each program contains dispensing locations, calibration routines, and dispenser-changing protocols. The design of generated constructs primarily consists of the XYZ coordinates where each dispenser will deposit material. The bioprinter comprises two optical light sensors (**Figure 2.5, C**) that determine the XYZ

coordinates of the syringe tip end. These sensors send coordinate information to the robot, which uses these to calculate positions of the dispenser tip ends. There is an additional displacement laser (**Figure 2.4, D**) that projects a 633 nm diode red laser beam of spot size 30 x 100 micrometers to measure distance with an accuracy of 0.1 micrometers. When the beam is highly focused the robot determines the Z distance of the printing surface. This measurement, and the optical light sensors measurement of the tip end in Z, allows calculation of accurate Z coordinates used to place the dispenser tip in relation to the printing surface. The dispenser tips move laterally and vertically through the X-axis oriented optical light sensor to find the Y and Z centers, and laterally through a Y-axis sensor to find the center of the X-axis. The printing surface is mapped using the formula for a flat plane in xyz space: ax + by +cz = d to determine where the surface is relative to the position of the dispensing tip end. The printer stage (**Figure 2.4, J**) holds a sample Petri dish up to 80 mm in diameter and uses a recirculating water bath to maintain the set temperature (**Figure 2.4, K**). Stage temperature can be set within a range of -20 and remains stable within a range of -20-100 degrees Celsius and remains stable within 0.5 degrees Celsius. There is a USB camera mounted onto the robot Z-arm to provide a magnified view of the dispensing tip during the printing process (**Figure 2.4, L**). There is a second camera mounted towards the top of the chamber interior that provides a complete view of the bioprinter during the printing process (**Figure 2.4, L**).

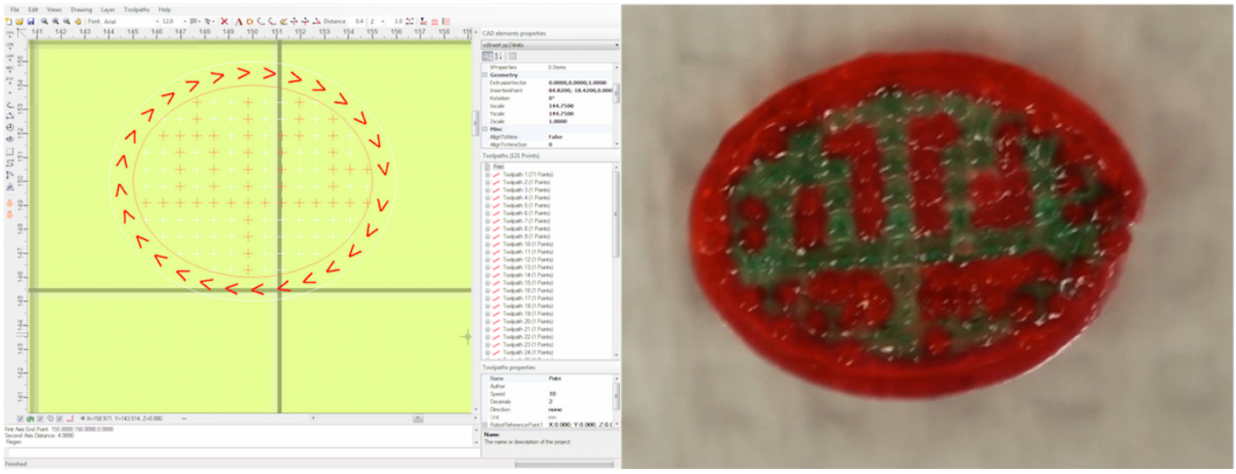

Figure 2.9. Visual PathBuilder Software. (A) Image of computer-aided design drawing software used for designing the external architecture of bioprinted constructs. This program provides the ability to generate incrementally spaced droplets and complex geometries. (B) Bioprinted construct portrayed in A using the Palmetto Printer.

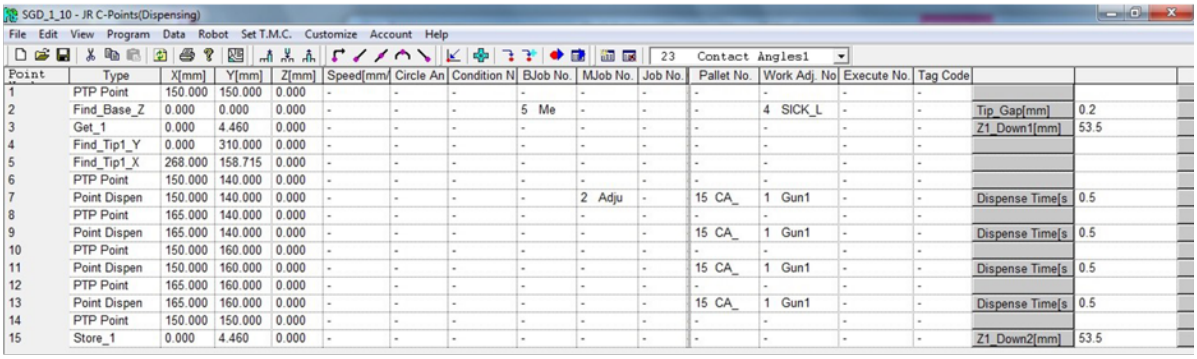

SGD_1_10 - JR C-Points(Dispensing)

File Edit View Program Data Robot Set T.M.C. Customize Account Help

23 Contact Angles1

Point	Type	X[mm]	Y[mm]	Z[mm]	Speed[mm/	Circle An	Condition N	BJob No.	MJob No.	Job No.	Pallet No.	Work Adj. No	Execute No.	Tag Code		
1	PTP Point	150.000	150.000	0.000	-	-	-	-	-	-	-	-	-	-		
2	Find_Base_Z	0.000	0.000	0.000	-	-	-	5 Me	-	-	-	4 SICK_L	-	-	Tip_Gap[mm]	0.2
3	Get_1	0.000	4.460	0.000	-	-	-	-	-	-	-	-	-	-	Z1_Down1[mm]	53.5
4	Find_Tip1_Y	0.000	310.000	0.000	-	-	-	-	-	-	-	-	-	-		
5	Find_Tip1_X	268.000	158.715	0.000	-	-	-	-	-	-	-	-	-	-		
6	PTP Point	150.000	140.000	0.000	-	-	-	-	-	-	-	-	-	-		
7	Point Dispen	150.000	140.000	0.000	-	-	-	-	2 Adju	-	15 CA_	1 Gun1	-	-	Dispense Time[s	0.5
8	PTP Point	165.000	140.000	0.000	-	-	-	-	-	-	-	-	-	-		
9	Point Dispen	165.000	140.000	0.000	-	-	-	-	-	-	15 CA_	1 Gun1	-	-	Dispense Time[s	0.5
10	PTP Point	150.000	160.000	0.000	-	-	-	-	-	-	-	-	-	-		
11	Point Dispen	150.000	160.000	0.000	-	-	-	-	-	-	15 CA_	1 Gun1	-	-	Dispense Time[s	0.5
12	PTP Point	165.000	160.000	0.000	-	-	-	-	-	-	-	-	-	-		
13	Point Dispen	165.000	160.000	0.000	-	-	-	-	-	-	15 CA_	1 Gun1	-	-	Dispense Time[s	0.5
14	PTP Point	150.000	150.000	0.000	-	-	-	-	-	-	-	-	-	-		
15	Store_1	0.000	4.460	0.000	-	-	-	-	-	-	-	-	-	-	Z1_Down2[mm]	53.5

Figure 2.10. JR-C Points Software. Screenshot of the printer-compatible design software. This program allows the user to control the deposition method (*i.e.* single drop deposition or continuous pathway deposition), deposition speed, distance between syringe tip end and printing substrate surface, the allotted time for deposition of each drop, and the three-dimensional placement of droplets (refer to Table 1).

Command	Robot Response
PTP Point	Robotic arm moves to indicated point in X, Y, Z space.
Find_Base_Z	Uses the SICK laser to measure the printing surface of the substrate; The distance between the syringe tip end and substrate surface is manually set.
Work Adj. No.	Commands robot to use SICK laser (for determining substrate surface), Gun 1, Gun 2, or Gun 3.
Get_1	Commands robot to retrieve and load Gun 1.
Find_Tip1_YZ	The robot finds the tip end of Gun 1 in the Y and Z directions.
Find_Tip1_X	The robot finds the tip end of Gun 1 in the X direction.
Point Dispense	The robot will dispense one droplet of bioink in the determined X, Y, Z position.
Pallet No.	Incorporates a manually coded design for printing, e.g. an array.
Dispense Time	Is the time allotted for the deposition of each individual drop.
Store_1	Commands the robot to return Gun 1 to the toolnest, and return to home position: (0,0,0).

Table 2.1. List of commands for use in JR-C Points software to control the Palmetto Bioprinter.

A computer-aided design drawing software determines the deposition pattern and permits the user to generate incrementally spaced droplets and complex structures (**Figure 2.6**). Three- dimensional pathways can be manually coded into the printer-compatible design software or imported from a separate computer-aided design drawing software (**Figure 2.7, Table 2.1**). The printer-compatible software allows variations of printing parameters such as the deposition method (single droplet deposition or continuous pathway deposition), three-dimensional geometry of the pathways, deposition

rate, distance between the syringe tip end and substrate printing surface, the amount of time to deposit an individual drop, and the height and speed the syringe is lifted between deposition of the drops. Each program contains XYZ dispensing locations, tip calibration routines, and dispenser-changing protocols to provide a sterile environment, without operator intervention, during printing. The programmable logic controller (PLC) of the robot receives instructions from the computer running the design software and controls the timing of events from the external controllers (e.g. the dispensers). To do this, the PLC uses a looping mechanism to control the dispensers, robotic positioning device, and environmental factors.

In this study we aimed to characterize a variety of materials that could function as vehicles for the transplantation of cell-laden constructs by analyzing different material properties and cell behaviors within these biomaterials. We hypothesize that the Palmetto Printer, developed at MUSC, is capable of depositing viable cell-laden structures in biomimetic geometries that accurately replicate the *in vivo* environment with respect to mechanical properties and cellular functions.

2.6 MATERIALS AND METHODS

Collagen Extraction

Collagen was extracted from the hide of an 18-month-old bovine steer following the methods of Yost, et al. (50). The superficial epidermis, including the hair and follicle pits, was first removed using a scalpel. The hide was then cut into 4 × 6 cm strips and was washed three times in deionized water for 1 hour per wash, with the second wash

including 0.2% $NaHC)_3$. The leftover follicles and non-collagenous proteins were removed by washing in a solution of 0.6% $NaHCO_3$, 2% $Ca(OH)_2$, and 4.3% NaHS for 30 minutes at $20℃$. The hides were then washed three times in deionized water and soaked in 2% $Ca(OH)_2$ at $4℃$ overnight. The fat and epidermis remaining after the overnight wash was trimmed, and the strips were placed in a 2M sodium chloride (NaCl) solution and neutralized with hydrochloric acid (HCl) to pH 6.8-7.0. The hide strips were then washed three times in deionized water, and cut into smaller 0.5×2 cm pieces and placed into a solution of 0.5Nacetic acid, containing pepsin (1:100 based on hide weight), and incubated overnight at 4℃. The strips were then mixed with ice and emulsified into a gel dispersion using a Kitchen-Aid food processor (model FP500WH; Kitchen-Aid, St. Joseph, MD). The suspension was centrifuged at $9950 \times g$ for 35 minutes, resuspended in deionized water, and neutralized to pH 7.2 with NaOH. The collagen suspension was then dialyzed versus phosphate-buffered saline overnight, and then versus deionized water for three changes over 24 hours. The resulting collagen gel was centrifuged at $9950 \times g$ for 35 minutes to remove excess water, and the collagen concentration was adjusted to $25\ {}^{mg}/_{mL}$ by adding deionized water. The collagen was then aliquoted into 50mL tubes and stored at $-20℃$ until ready for use.

Synthesis of Collagen Bioinks

When ready for use, the collagen was thawed, diluted to the appropriate concentration using deionized water, and the pH was adjusted to pH 2.5-3.0 with concentrated HCl. Once acidified, the collagen was diluted to the desired concentration using cold, 4℃,

deionized water. The pH was then checked again, and if it was not pH ~3.0, the collagen was again acidified using concentrated HCl.

Synthesis of Alginate Bioinks

Sodium Alginates, Protanal LF 20/40 and Protanal LF 10/60 FT, were generously provided by FMC BioPolymer (Philadelphia, PA). The alginate powder was sterilized via gamma irradiation (at 1200cGy for X minutes) followed by UV exposure for two hours in a cell culture hood. To make 50 mL of 5% (weight-to-total volume) alginate bioink, 2.5 grams of sodium alginate was mixed with 50 mL sterile ddH_2O. It was then kept in the cell culture hood until use.

Oxidation of Alginate Hydrogels

Sodium alginate was oxidized following the method for partially oxidized alginate by Bouhadir, et. al. (30). To make a 5% oxidized alginate solution 1 gram of sodium alginate was dissolved in 100mL of distilled water. An aqueous solution of sodium periodate (0.25M, 0.25 mmol), the oxidizing reagent, was added to produce a 5% oxidation solution. The solution was stirred for 19 hours at room temperature. Finally, at the 24 hour time point, 40 mL of ethylene glycol was added to the solution to end the reaction. 2.5 grams of sodium chloride was added to the solution, as well as an excess amount of ethyl alcohol (2:1) in order to precipitate the oxidized alginate. The solution was centrifuged at 1000xg to collect the precipitates, which were then re-dissolved in distilled water. The ethanol wash was then repeated. The pellets were freeze-dried and stored at $-20℃$ until ready for use. The degree of oxidation was determined by measuring the

percentage of sodium periodate consumed before being terminated by the ethylene glycol. This was accomplished by preparing a potassium iodide solution (20% w/v, pH 7.0 sodium phosphate buffer) and a thyodene solution (10% w/v, pH 7.0 sodium phosphate buffer). The two solutions were mixed with the oxidized alginate at room temperature. The reacted alginate and sodium periodate solution were gradually dropped into the mixed potassium iodide and thyodene solutions. The absorbance of the mixture was measured spectrophotometrically at 426nm. When the maximum absorbance was reached, the used volume of the alginate and sodium periodate solution was recorded as V_1. The reaction is $IO_4^- + 2I^- = I_2 + IO_3^-$, and the amount of unreacted sodium periodate was calculated using the following formula: $20\% \left(\frac{w}{v}\right) \times 10mL \times 100 \frac{mL}{V_1}$. The amount of unreacted sodium periodate was subtracted from the original concentration to determine the amount of sodium periodate consumed during the reaction and the degree of oxidation of the alginate.

RGD-conjugation onto Alginate Hydrogels

Ligands with an exposed arginine-glycine-aspartate sequence (G_4RGDSP peptide) were conjugated onto the previously oxidized alginate by following the RGD-Alginate conjugation method described by Rowley, et. al. in order to promote cell attachment and spreading (31). Aqueous carbodiimide chemistry with G_4RGDSP was used to conjugate the RGD peptide onto the alginate polymer. 1 g of 5% oxidized alginate was dissolved in a 0.1 M 2-(N-morpholino) ethanesulfonic acid (MES) buffer, pH = 4. 1-ethyl-(dimethylaminopropyl) carbodiimide (EDC, 0.54 mmol) and N-Hydroxysuccinimide

(NHS, 0.27 mmol) were added at 2:1 ratio to form amide intermediate. 0.28 mmol G_4RGDSP peptide was added, which couples to the backbone of the alginate polymer via the terminal amine, and stirred overnight. The coupling reaction was terminated by adding 2.5 g sodium chloride to the solution. An excess amount of ethyl alcohol (2:1) was added to precipitate the RGD-conjugated oxidized alginate. The mixture was centrifuged at 4,000xg for five minutes to collect the precipitates. The supernatant was aspirated in the cell culture hood, and the precipitates were re-dissolved in distilled water. The ethanol wash was then repeated. The samples were then freeze-dried and stored at $-20℃$ for later use.

RGD Peptide Conjugation Analysis

The success of RGD peptide conjugation on the alginate was determined by comparing RGD-alginate and non-conjugated alginate. This was done by imaging the printed constructs using (4', 6-Diamidino-2-Phenylindole, Dihydrochloride) (DAPI) and phalloidin stains. The phalloidin working solution was created by diluting 5μL of the methanolic stock solution with 200μL of DPBS++. A 300μM stock solution of the DAPI stain was made following the equation: $\frac{0.10509\,^{g}/_{L}}{350.3\,^{g}/_{mol}} = 3 \times 10^{-4}\text{M} = 0.0003\text{M} = 0.300\text{mM} = 300\mu\text{M}$. The DAPI working solution was made by diluting the stock solution 1:100 in DPBS++ to obtain 3μM solution. The samples were completely submerged in $37℃$, 4% paraformaldehyde, and incubated for one hour at room temperature. The samples were then washed three times with DPBS++, and the solution

was allowed to sit for 5 minutes each wash. The gel samples were then transferred from the well to a glass slide, and the gel was flipped over in the process. The samples were then immersed in 0.1% Triton X-100 ($\frac{0.1\text{g}}{100\text{mL}}$) in DPBS++ for ten minutes. Each sample was washed three times in DPBS++ for five minutes per wash. The bioprinted constructs were stained with phalloidin by immersing them in the working solution in the dark for four hours. The phalloidin stain was removed and the samples were washed three times. The first wash was fast (~45 seconds), while the latter washes were for 5 minutes each. The bioprinted constructs were stained with DAPI by immersing them in the DAPI working solution in the dark for thirty minutes. The samples were washed three times for 5 minutes per wash. The samples were imaged on a confocal microscope system and analyzed.

Preparation of Ca^{2+}-Contatining Gelatin Substrate for 3-D bioprinting of Alginate Hydrogels

The calcium substrate was prepared following the methods by Pataky et al in order to avoid reduced viability associated with high concentrations of Ca^{2+} (11). Briefly, calcium chloride dehydrate, sodium chloride (0.9 wt.%), and porcine gelatin (2 wt.%) were combined in distilled water and boiled for 2 minutes to form a 100mM $CaCl_2$ gelatin solution. To increase the opacity of the surface, titanium dioxide (0.3 wt.%) was added to the gelatin solution and stirred for 10 minutes. 5 ml of gelatin/TiO_2 mixture was put into standard petri dishes and left to gel in the 4℃ refrigerator overnight to be used within 3 days.

Cell Culture

Human adipose tissue stromal cells (hADSC's) were cultured in 75 cm treated cell culture flasks (T75 flasks), covered with 15 mL low glucose DMEM with 10% fetal bovine serum and 1% penicillin-streptomycin, 1% glutamine, and 1% antimycin. Media was changed every two days until the cells reached confluence (80-90%). Once confluent, the cells were suspended via trypsin enzyme digestion method.

Normal Human Dermal Fibroblasts (NHDF) were cultured in 175-cm treated cell culture flasks (T175), covered with 25 mL of Fibroblast Growth Medium-2 (FGM-2, Lonza). The media was changed every two days until the cells reached ~85% confluence. Once confluent, the cells were suspending using trypsin enzyme digestion.

Human Adipose Microvascular Endothelial Cells (HAMEC) were cultured in 75 cm treated cell culture flasks covered with 15 mL of Endothelial Growth Medium-2 (EGM-2, Lonza). Media was changed every two days until the cells reached 80% confluence. Once confluent, cells were suspended via trypsin enzyme digestion method.

Bioprinter Setup

First, the bioprinter was turned on, as well as each of the dispenser computers and the recirculating water bath. The recirculating water bath temperature was set to 4℃ in order to maintain the gelatin substrate solution in a solid state. The printing parameters were manually set for each dispenser on the correlating dispenser computer, including the dispense volume, back-off steps, and the dispense rate. The JR-C points design software was opened, and additional printing parameters were set, including the distance between

the tip end and the substrate surface, the distance the syringe is lifted between depositions, and the amount of time per deposition. The program was saved and then sent to the robot. The gelatin/TiO_2-containing Petri dish was placed on the 4℃ printer stage, and the chamber door was closed and locked. The PLC was used to initialize the ultraviolet light sources for 90 seconds in order to sterilize the chamber. Once the sterilization was complete, the chamber door was briefly opened, and the syringes are loaded into their appropriate gun location. The PLC was then used to turn on the fan system, which takes 30 seconds to reach equilibrium internal pressure within the chamber. Finally, on the computer the appropriate program containing the geometrical pathway and printing parameters was run.

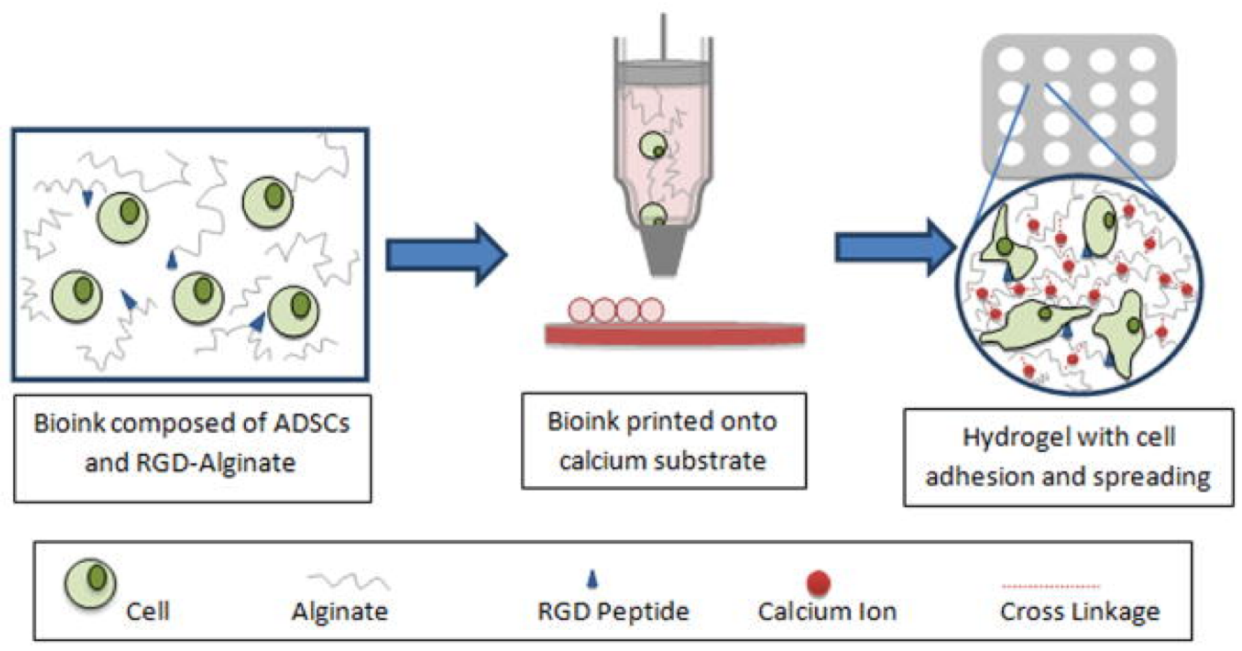

Figure 2.11. Schematic representation of biodegradable oxidized alginate as bioink for bioprinting. A bioink consisting of RGD-modified oxidized alginate hADSCs was printed in a define lattice structure on a gelatin substrate to crosslink the hydrogel. The constructs were then evaluated over an 8-day period for cellular behavior (i.e., cell proliferation and spreading). Fig adapted from ref Jia, J., et. al. *Acta Biomaterialia* **10**(10):4323-4331, (2014).

Contact Angles of Bioprinted Droplets

Contact angle measurements were taken to determine the printability of different materials and analyze the surface interactions during deposition. Assuming compatible surface adhesion properties, the contact angle should be high. It is valuable to predict the droplet dimension at different system configurations and process conditions for planning the printing sequences (49). The contact angle measurements were calculated using the formula in **Figure 2.8**.

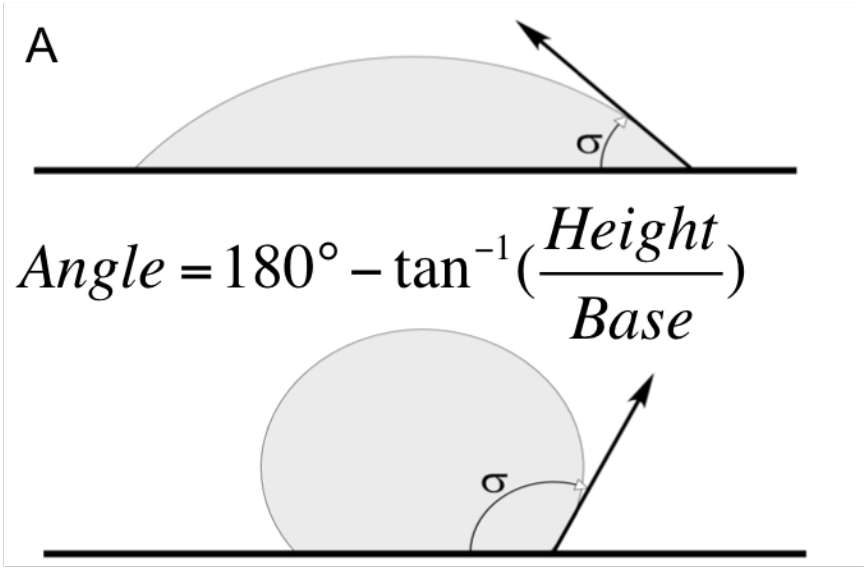

Figure 2.12. Contact angle measurements for bioprinted droplets using a 20G Micron-S Precision Tip. (A) Schematic for measuring contact angles. (B) Image of bioprinted Protanal LF 10/60FT 0.00045cc droplets used for measuring contact angles in CellSens.

A 20G Micron-S tip with 0.00023cc, 0.00045cc, and 0.00135cc deposition volumes, 0 back-off steps, 0.25mm tip height was used for all experiments. Contact angle measurements for 30% Pluronic F-127, 5% Protanal LF 10/60 FT, 5% Protanal LF 20/40 were compared (n=10).

Volume Analysis of Bioprinted Droplets

To determine the actual volume deposited by the bioprinter for different set dispense volumes, bioprinted droplets were measured in CellSens. The droplets were irregular in shape, so they were divided into two sections to accurately calculate the dispensed volume (**Figure 2.9**). The top half of the droplets were hemispherical in shape, and the volume for this portion of the drop, V_1, was calculated as $V_1 = \frac{2}{3}\pi r^3$. The bottom half of the drops, V_2, were cylindrical in shape, and the volume was calculated as $V_2 = \frac{(D_1+D_2)\times\pi\times H2}{4}$. The total volume for each drop was found by summing the two volumes, $\text{Total Volume} = V_1 + V_2$.

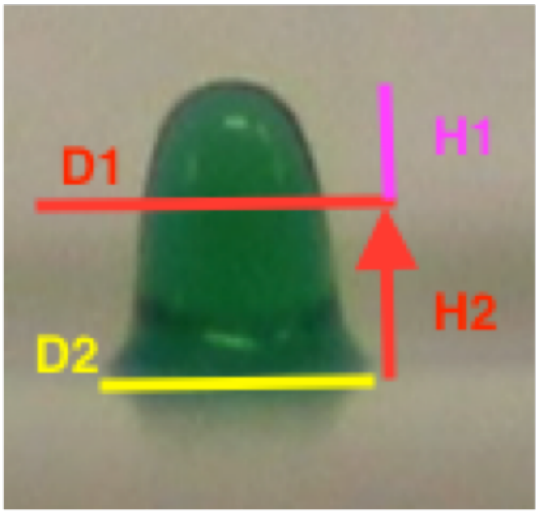

Figure 2.13. Bioprinted droplet with indications of how volume measurements were calculated.

Resolution of the Palmetto Bioprinter

To determine the accuracy and reproducibility of the Palmetto bioprinter, droplets were sequentially deposited on top of a previously deposited droplet and the offsets were

measured. Using a 30G Micron-S Precision tip, the green droplets are deposited first with a dispense volume of 0.00135cc. The red droplets were deposited after gelation of the first droplets at a dispense volume of 0.00023cc, so the offsets from the center of the droplets can be quantified. Offsets were calculated as: Offsets = Green(X,Y)-Red(X,Y).

Swelling Characteristics of Alginate Hydrogels

Hydrogels are composed of hydrophilic polymer networks that are biodegradable and contain pores and void space between the polymer chains, which act to provide an enhanced supply of nutrients and oxygen to the cells contained within them. To characterize the polymer volume fraction in the swollen state, i.e. the amount of water that can be imbibed by the hydrogel, the swelling properties of alginate hydrogels were analyzed. Two experiments were performed to determine swelling properties of alginate hydrogels.

The first experiment was designed to determine if the concentration of alginate, as well as its molecular weight, have an effect on the swelling properties of the hydrogels. This portion of the experiment includes the comparison of 2% and 4% LF20/40 alginate bioinks, as well as 4% LF20/40 and 4% LF10/60FT. LF20/40 is a high molecular-weight alginate, while LF10/60FT has a low molecular-weight, indicating the chain densities between these two polymers are different, and therefore, may have different effects on the materials printability and cell viability within it (54).

To determine the effect of the concentration, and therefore availability, of the gelation agent, Ca^{2+}, three different solutions were used in the substrates to form alginate

hydrogels: (1) 200 mM, (2) 300 mM, and (3) 400 mM CaCl2. Each gelation solution also included 0.9%(w/v) NaCl dissolved in deionized water. Gels were created in 12-well plates, with 0.5mL of calcium solution deposited on the bottom, followed by ~2.8mL of alginate.

The alginate hydrogels were created by plating 0.5mL of $300\text{mM } CaCl_2$ and 0.9% NaCl in deionized water at the bottom of each well of a 12-well plate. Approximately 3mL of alginate hydrogel was then added to each well and allowed to gel overnight at room temperature. The next day, the gels were weighed for initial wet weights, and transferred to wells in a 6-well plate with 8mL of PBS (made from tablet) in each well, and placed in the incubator at 37℃. The gels were pulled out of the incubator on days 1, 2, 5, 6, and 7 for weight analyses. On day 7, the swollen (wet) gels were weighed, then the gels were dried to determine the air-dried weight for each sample.

The swelling properties of hydrogels include the swelling ratio, Q, the mass loss percentage, the equilibrium mass swelling ratio, Q_m, and the water uptake content, Q_w. The swelling ratio, Q, is defined as the fractional increase in the weight of the hydrogel due to water absorption, and is calculated by $Q = \frac{m_{WT}}{m_{w_0}}$, where m_{WT} is the mass of the hydrogel at time T, and m_{w_0} is the mass of the hydrogel at time 0. The equilibrium mass swelling ratio, Q_m, is the mass of the hydrogel immediately post-fabrication compared to the mass of air-dried and calculated as $Q_m = \frac{m_{WT}}{W_d}$, where W_d is the air-dried weight. Finally, the water uptake content, $Q_w = \frac{m_{WT} - W_d}{W_d} \times 100\%$.

Cell Distribution Within Bioprinted Droplets

A homogeneous cell distribution within bioprinted droplets is crucial for cell communication, proliferation, and interconnectivity. High local cell densities are required for successful cell differentiation and generation of extracellular matrix. To date, achieving a uniform distribution of cells within bioprinted droplets has been a challenge in bioprinting. Current technologies typically have an aggregation of cells towards the innermost region of the droplet, which can inhibit cell-cell communication and subsequent activities, such as migration. To demonstrate the Palmetto Printer is unique in its ability to produce three-dimensional scaffolds with uniform cell distributions throughout, multiple cell types and materials were analyzed post-printing.

A 0.62% Collagen and 4% LF 20/40 (1:1) blend bioink was seeded with Human Adipose Microvascular Endothelial Cells (HAMEC) and Normal Human Dermal Fibroblasts (NHDF) at a 1:4 ratio with a cell density of 1,000,000 cells/mL (n=5). A 5% LF 20/40, high molecular-weight alginate, was seeded with NHDF only at 1,000,000 cells/mL (n=9). Additionally, 5% LF 10/60 FT, low molecular-weight alginate, was seeded with HAMECs at 1,000,000 cells/mL (n=7).

The bioink was then loaded into printer syringes, transported to the printer, and printed in a 5 x 2 dot array onto a gelatin/TiO_2 substrate. The following printing parameters were used: deposition volume of 0.00045 ml, deposition rate of $0.010\ \frac{\mathrm{mL}}{\mathrm{s}}$, tip height of 0.1 mm, 10 backsteps, stage temperature of 4℃, a height of 15 mm the syringe was lifted between depositions, and a 22-gauge plastic tip (Fishman). The constructs were allowed

to gel for 40 minutes. While the constructs were gelling, a fluorescent-based stain (Invitrogen Life Technologies) was made following the protocol of the kit. The cell-laden hydrogels were then immersed in the stain for 15 minutes, in the dark, prior to imaging. All of the fluorescent images were taken on a Leica TCS SP2 AOBS confocal microscope system using Z-stack parameters of 103 optical slices over a 326.40μm depth. Pictures of each droplet were taken individually. These images were then imported into CellSens software and each was sectioned into quadrants and concentric circles. Cells were manually counted for the entire droplets and each section within the droplets.

Cell Viability in Bioprinted Constructs

To quantify the viability of the constructs, stain them using a fluorescent-based viability/cytotoxicity assay, and image using confocal microscopy. Following the kit instructions, prepare a staining solution containing calcein AM and ethidium homodimer-1. To make 10 mL of staining solution, add 20 microliters of the ethidium homodimer-1 and 5 microliters of the calcein am to 10 mL of sterile, tissue culture-grade Dulbecco's Phosphate-Buffered Saline (+magnesium, +calcium; DPBS++). Image the stained constructs using a confocal microscope system at days 0 and 8. Take multiple pictures of each bioprinted construct, using Z-stack parameters of 30 optical slices over a 300μm depth, and manually count the cells. If cells appear yellow or green they are counted as alive, and if red, they are counted as dead.

Cell viability was calculated using the following formula:

$$\text{Viability} = \frac{\#\text{ live cells (green+yellow)}}{\#\text{ total cells (green+yellow+red)}} \times 100\%.$$

Cell Proliferation in Bioprinted Constructs

To quantify the amount of cell proliferation within the bioprinted constructs, they were stained with a fluorescent-based viability/cytotoxicity assay on day 0 and 8, and imaged using confocal microscopy. Multiple pictures were taken of each bioprinted construct with Z-stack parameters of 30 optical slices over a 300μm depth, and the cells were manually counted. The amount of cell proliferation in bioprinted constructs over 8 days was calculated using the following equation:

$$\text{Proliferation} = \frac{\#\text{ live cell count on day 8}}{\#\text{ live cell count on day 0}} \times 100\%.$$

2.7 RESULTS

RGD Peptide Conjugation Analysis

To analyze the success of RGD peptide conjugation on the alginate bioink, a comparison experiment was performed using cell-laden, RGD-conjugated 15% concentration, 5% oxidation alginate bioink and cell-laden, non-conjugated 15% concentration, 5% oxidation alginate bioink. DAPI staining for nuclei and phalloidin staining for actin were used to analyze the cell spreading in printed constructs on day 8. Images of each sample (at least three random pictures per sample) were taking using a confocal microscope system using Z-stack parameters of 30 optical slices over a 300μm depth (**Figure 2.14 A,B**).

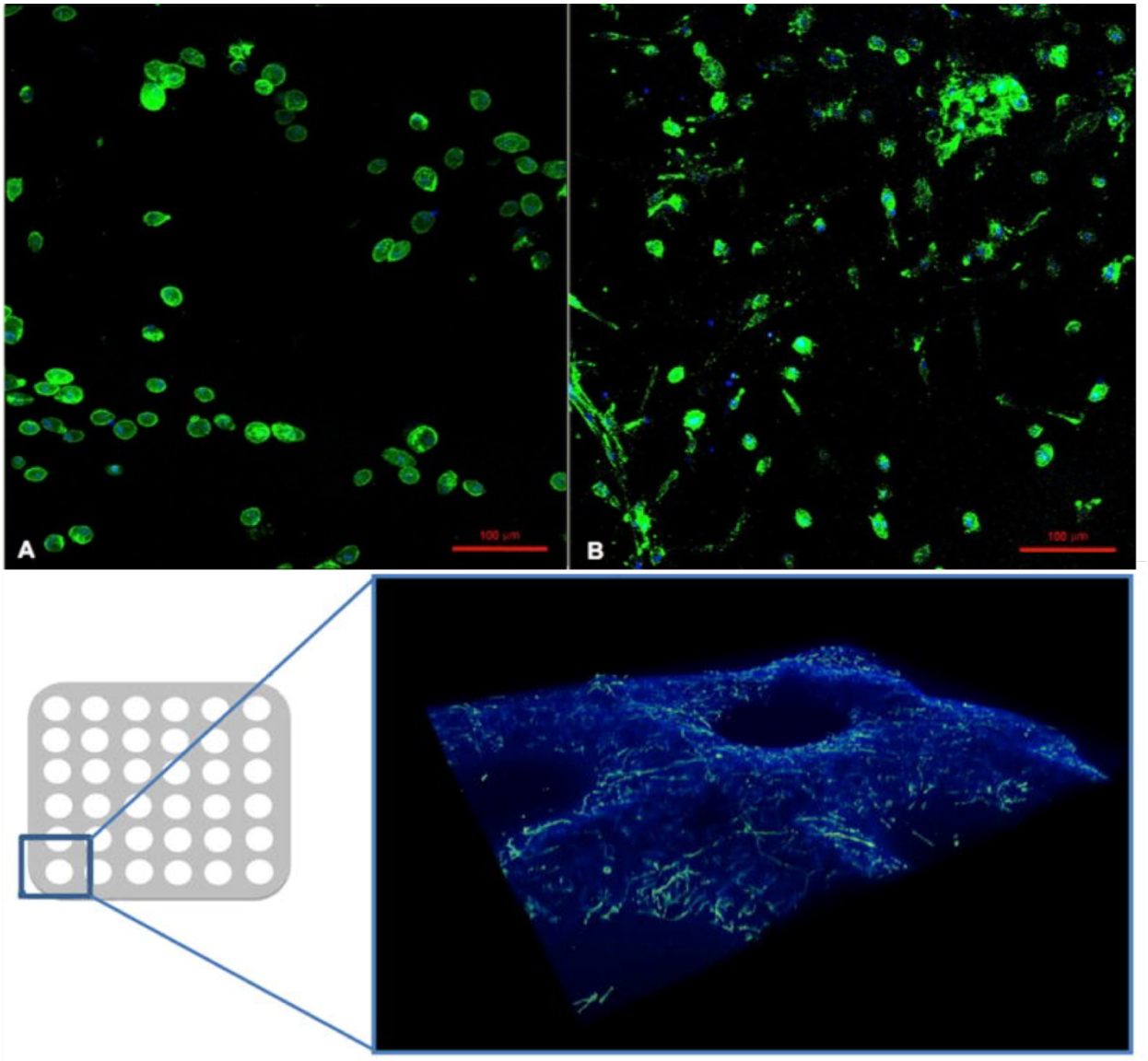

Figure 2.14. Comparison of Cell-Laden, Non-Conjugated and RGD-Conjugated Alginates. Fluorescent images of bioprinted hADSC's in (A) non-conjugated, and in (B) RGD-conjugated 15% concentration 5% oxidation alginate bioink taken using a confocal microscope system (Z-stack parameters of 30 optical slices over a 300 μm depth). The hADSC's were stained with phalloidin and DAPI stains to analyze the cell spreading in each of the constructs. (C) A computer-rendered 3D picture of a portion of the printed lattice structure made by the best supporting hADSC material, 5% ox.-15% conc. oxidized alginate, showing multiple layers of spreading cells within the hydrogel. Fig C adapted from ref Jia, J., et. al. *Acta Biomaterialia* **10**(10):4323-4331, (2014).

The cell spreading shown in the sample with RGD-conjugated alginate proves the successful incorporation of the peptide on the alginate. Additionally, Jia, et. al., who we

worked in collaboration with for this project, previously demonstrated that the cell adhesive and migratory properties were not limited to certain regions of the construct, but occurred throughout (**Figure 2.14C**, 37). Cell migration is an important step in tissue development, therefore the conjugation of RGD peptides on alginate improves the likelihood of *in vivo* application using this bioink.

Contact Angles of Bioprinted Droplets

A 20G Micron-S tip with 0.00023cc, 0.00045cc, and 0.00135cc deposition volumes, 0 back-off steps, 0.25mm tip height was used for all experiments. Contact angle measurements for 30% Pluronic F-127, 5% Protanal LF 10/60 FT, 5% Protanal LF 20/40 were compared (n=10; **Figure 2.15**).

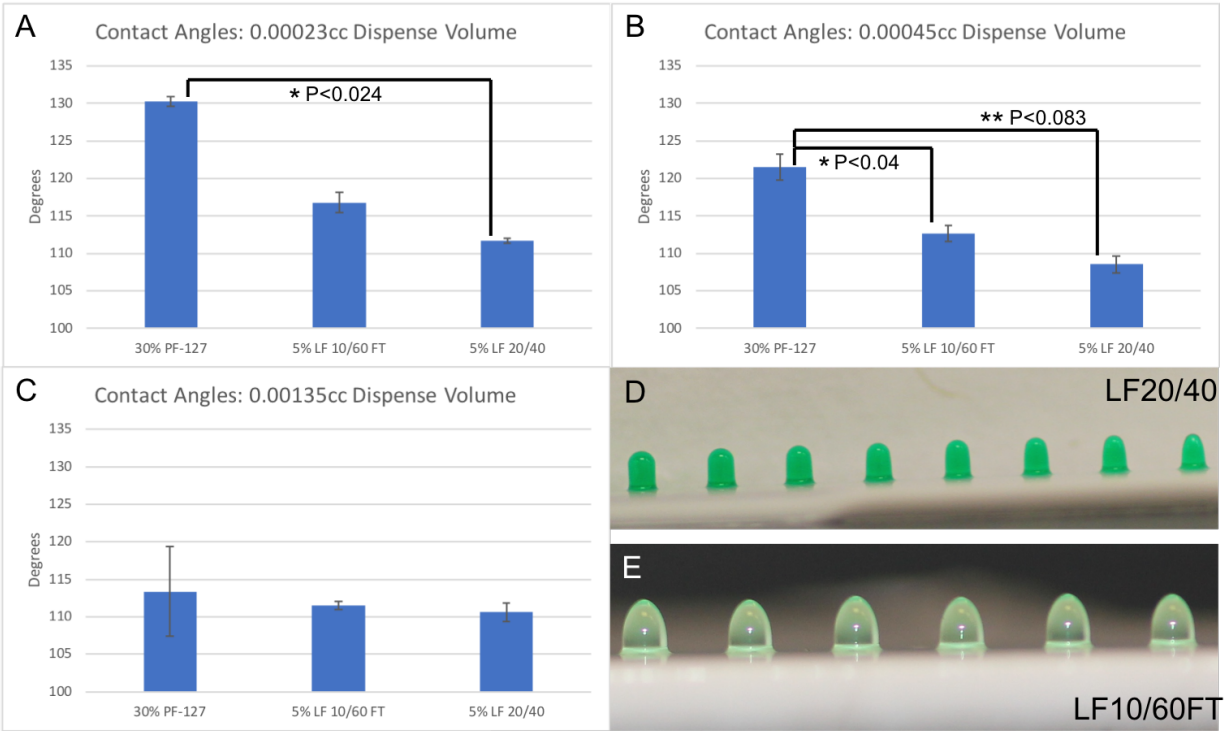

Figure 2.15. Contact angle measurements for bioprinted droplets using a 20G Micron-S Precision Tip with ranging deposition volumes for three types of biomaterials: 30% Pluronic F-127, 5% LF10/60FT, and 5% LF20/40. Contact angle measurements for (A) 0.00023cc, (B) 0.00045cc, and (C) 0.00135cc dispense volumes. (D, E) Images of bioprinted droplets used to calculate contact angles for 0.00023cc dispense volume for 5% LF20/40 (D) and 5% LF10/60FT (E).

For the smaller dispense volumes, 230 nL and 450 nL, there were significant differences between the materials tested. However, all of the materials tested had appropriate contact angles ($> 90°$), indicative of maintained tension in the vertical direction, a requirement for the printability of these materials. Therefore, all three of these biomaterials could serve as vehicles for the construction of cell-laden constructs based on this requirement.

Volume Analysis of Bioprinted Droplets

Dispense volumes for acellular 5% LF20/40 alginate were measured using CellSens (n=10). A dispense volume of 0.00135cc with a 0.30mm tip height and 0 back-off steps was used to compare the volumes dispensed when using a 27G versus 30G Micron-S

Precision Tip. The two tips were shown to deposit significantly different volumes ($P<0.006$), which highlights the decreasing volume with increase of tip gauge size, i.e. decreased diameter with increasing gauge size of the tip (**Figure 2.16**). This suggests that the volume of deposited droplets is dependent on gauge size, and that due to the increased surface tension in the smaller diameter tips they dispense a smaller volume than the larger diameter tips.

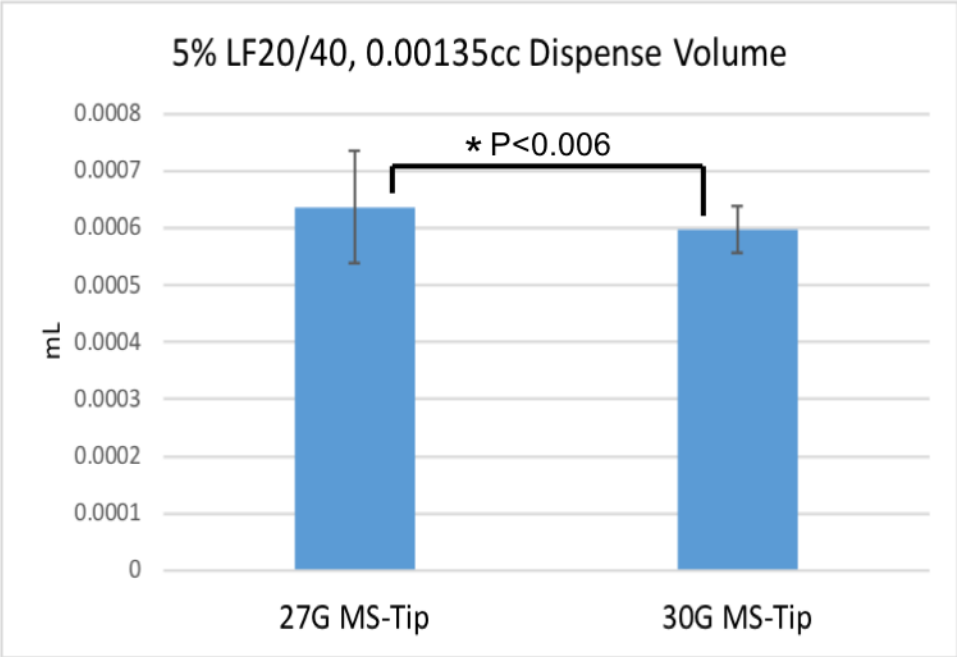

Figure 2.16. Volume analysis to characterize the effect of tip gauge-size on volume dispensed by the Palmetto Printer.

Resolution of the Palmetto Bioprinter

The resolution of the Palmetto Printer was found to be 10 nanometers (**Figure 2.17**). The results demonstrate the bioprinter is capable of depositing cell-laden hydrogels in specific three-dimensional locations accurately and consistently using computer-aided software. The software determines the placement of each droplet and controls many of the

parameters for dispensing (Figure 2.5). The repeatability of the bioprinter to appropriately deposit biomaterials is fundamental to its success in tissue engineering applications.

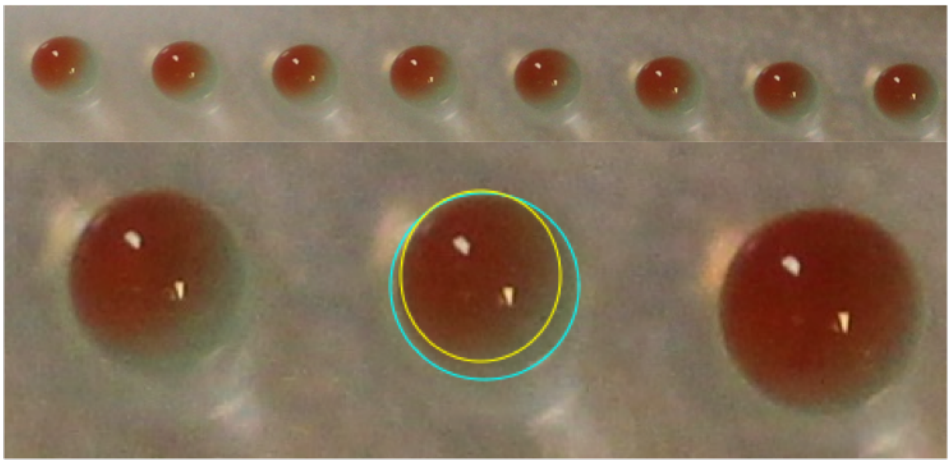

Figure 2.17. Resolution of the Palmetto Printer. Using a 30G Micron-S Precision Tip, the green droplets were printed first with a 0.00135cc dispense volume, and allowed to gel for 10 minutes on gelatin substrate. Red droplets were then deposited in the same geometric locations as the green droplets with a smaller 0.00023cc dispense volume, so that the circumference of each droplet could be measured and the offsets calculated.

Swelling Characteristics of Alginate Hydrogels

The day 1 swelling ratio, Q, was analyzed because that was the time point at which the most mass increase was observed in all hydrogels compared to any other time in culture over 7 days.

Independent t tests were used to compare 2% LF20/40 and 4% LF20/40 over 7 days (n=8), and determine the impact of alginate concentration, i.e. polymer density, on the swelling properties of the hydrogels (**Figure 2.18**). The day 7 swelling ratio, Q, between the two group was not different ($P<0.461$). Additionally, the water uptake content, Q_w,

for the two hydrogels was not different (P<0.336). There were no significant differences between these two groups, which suggests that the concentration of the alginate has minimal effect on the materials' water absorption properties.

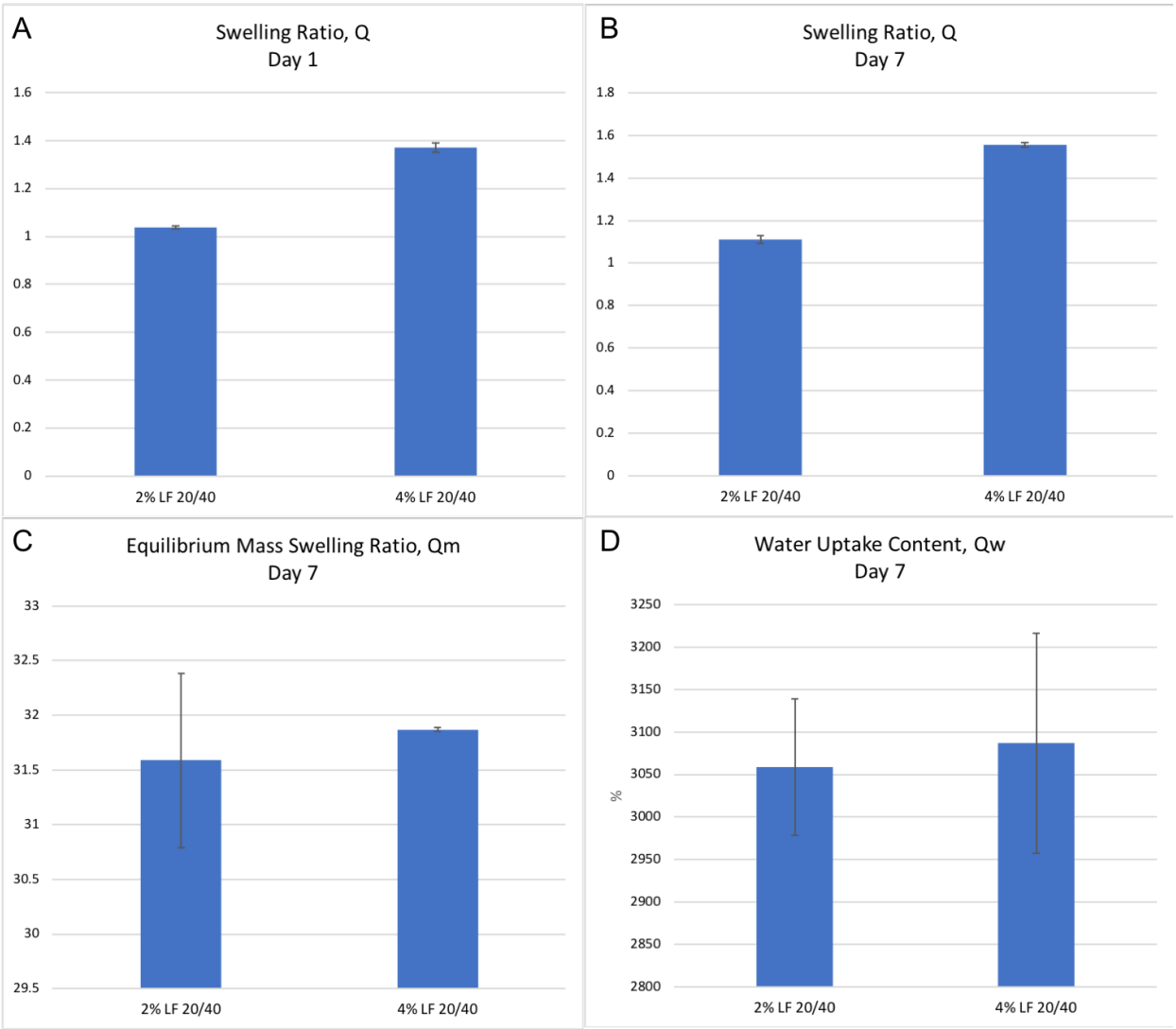

Figure 2.18. Swelling properties of 2% and 4% LF20/40 alginate bioink over 7 days including Swelling Ratio, Q, on days (A) 1 (P<0.093) and (B) 7 (P<0.461), the Equilibrium Mass Swelling Ratio , Q_m (P<0.336), and the (D) Water Uptake Content, Q_W (P<0.336).

LF 20/40 is a high molecular weight alginate, and LF 10/60FT is a low molecular weight. To determine the effect of polymer network density, the two materials were compared (**Figure 2.19**).

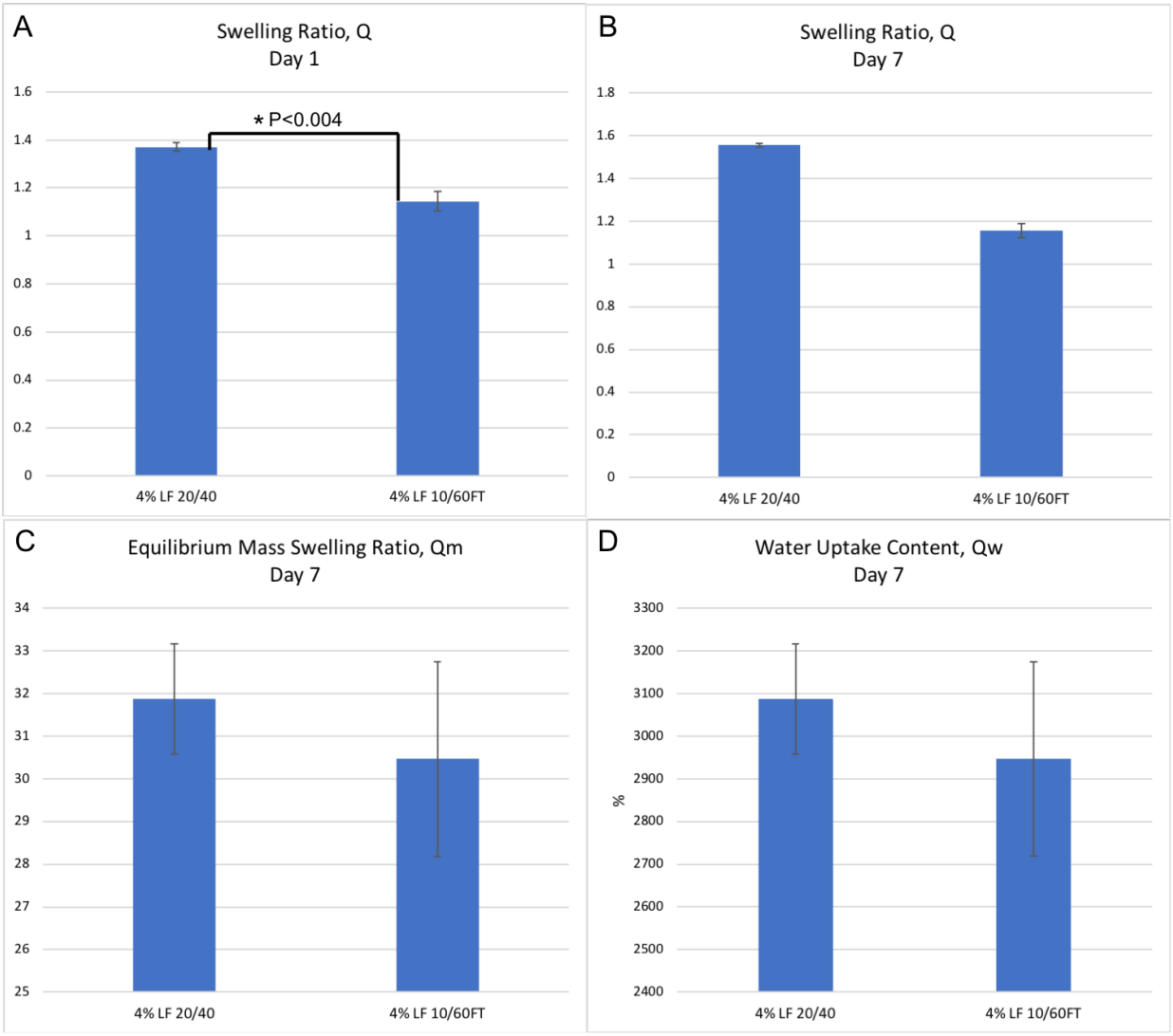

Figure 2.19. Swelling properties of 4% LF20/40 and 4% LF10/60FT alginate bioinks over 7 days including Swelling Ratio, Q, on days (A) 1 (P<0.004*) and (B) 7 (P<0.110), the Equilibrium Mass Swelling Ratio , Q_m (P<0.059), and the (D) Water Uptake Content (Q_W , P<0.059).

The second half of this experiment aimed to discern whether the availability of the gelation agent, in this case Ca^{2+}, in the substrate has an effect on the swelling properties

of alginate hydrogels. 4% LF10/60FT gels made with three different concentrations of calcium in the substrate were compared in **Figure 2.20**. Interestingly, there were no significant differences between any of the groups for the varying concentrations of Ca^{2+}.

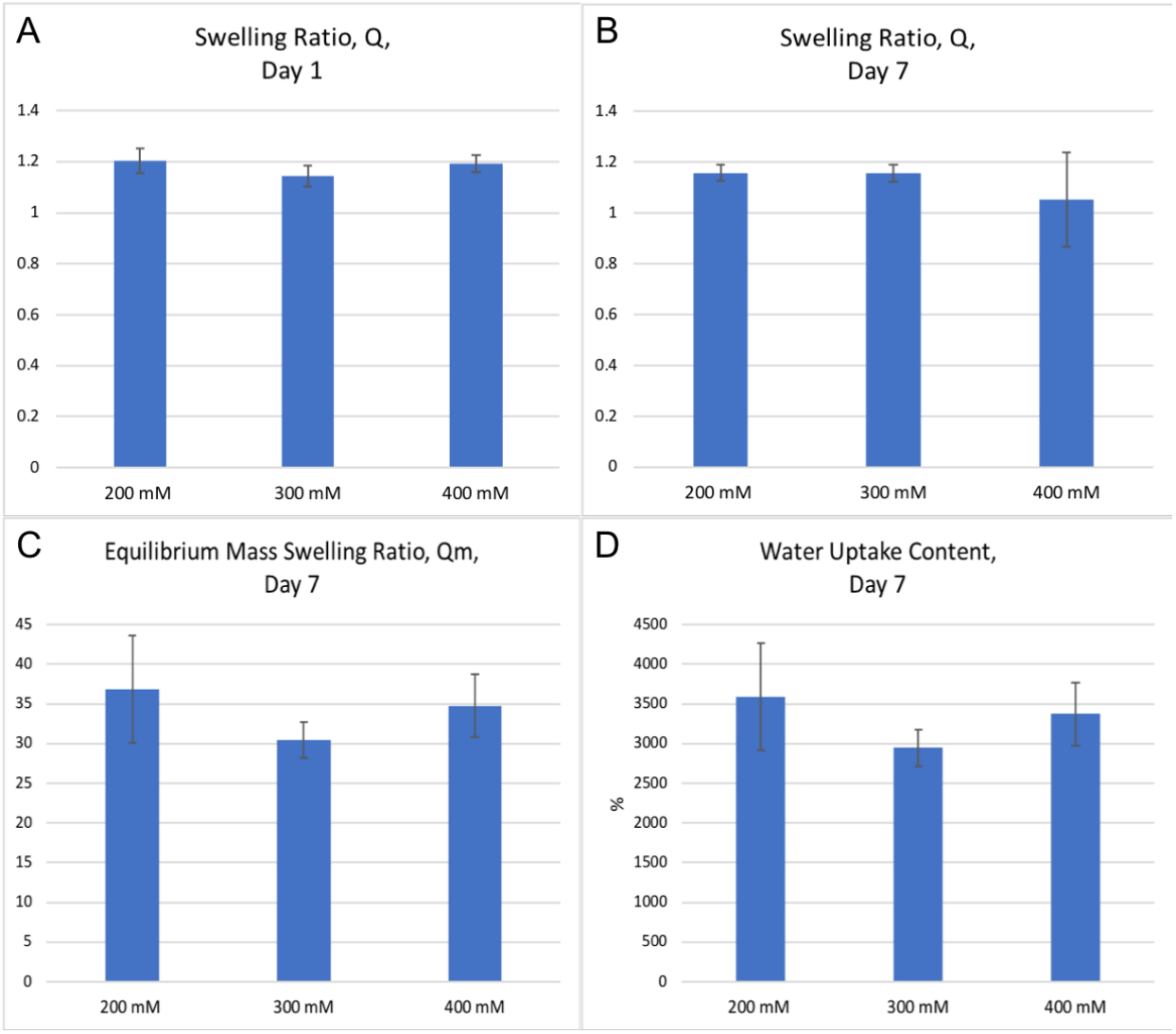

Fig. 2.20. Effect of the availability of the gelation agent in the substrate used to produce 4% LF10/60FT alginate hydrogels on their swelling behavior. A) Day 1 swelling ratio (P<0.169), B) Day 7 swelling ratio (P<0.396), C) Day 7 equilibrium mass swelling ratio (P<.198), and D) water uptake content on Day 7 (P<0.198).

2% LF20/40 alginate hydrogels created in varying concentrations of calcium were compared in **Figure 2.21**. The day 1 swelling ratios, Q, were significantly different for all Ca^{2+}concentrations when analyzed with independent t-tests. However, there was no difference between the day 7 swelling ratios. This indicates that at earlier time points the hydrogels are more susceptible to ion exchange with their surrounding media, and eventually reach an equilibrium by day 7.

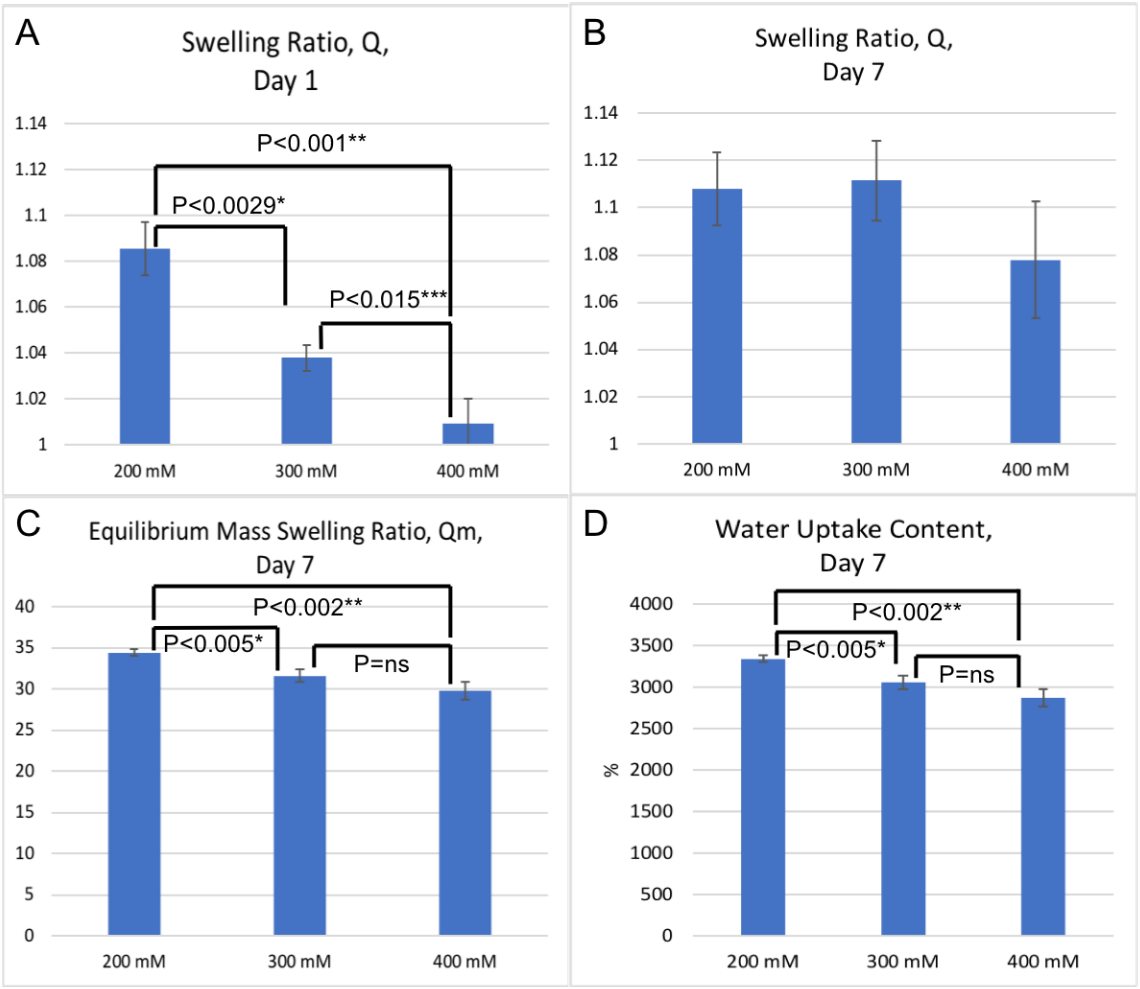

Fig. 2.21. Effect of the availability of the gelation agent in the substrate used to produce 2% LF20/40 alginate hydrogels on their swelling behavior. A) Day 1 swelling ratio, B) Day 7 swelling ratio (F=2.672, P<0.148), C) Day 7 equilibrium mass swelling ratio, and D) water uptake content on Day 7.

The significant differences seen in the higher molecular weight alginate, but not in the lower molecular weight, imply that the density of the polymer network does have an effect on the water-absorption capacity of the hydrogel. These studies suggest that as the density of the polymer network increases, so do the water absorptive properties of the material. This was further validated by the comparisons of the high- and low-molecular weight alginates in **Figure 2.19**.

Cell Distribution Within Bioprinted Droplets

Cell homogeneity was determined by sectioning the bioprinted droplets into quadrants, as well as concentric circles to evaluate the distribution of cells within different biomaterials after the bioprinting process. The cell distributions were then analyzed in SPSS Statistics software using ANOVA to determine if there was any difference with respect to cell density in the different areas.

For the NHDFs suspended in 5% LF20/40 alginate (**Figure 2.22**) bioprinted droplets sectioned into quadrants (n=10) the calculated F value was 1.572 ($P<0.215$), which was less than the critical value of F (2.901). Therefore, there was no difference between cell distribution in the different quadrants indicating a homogeneous cell distribution throughout the bioprinted droplet.

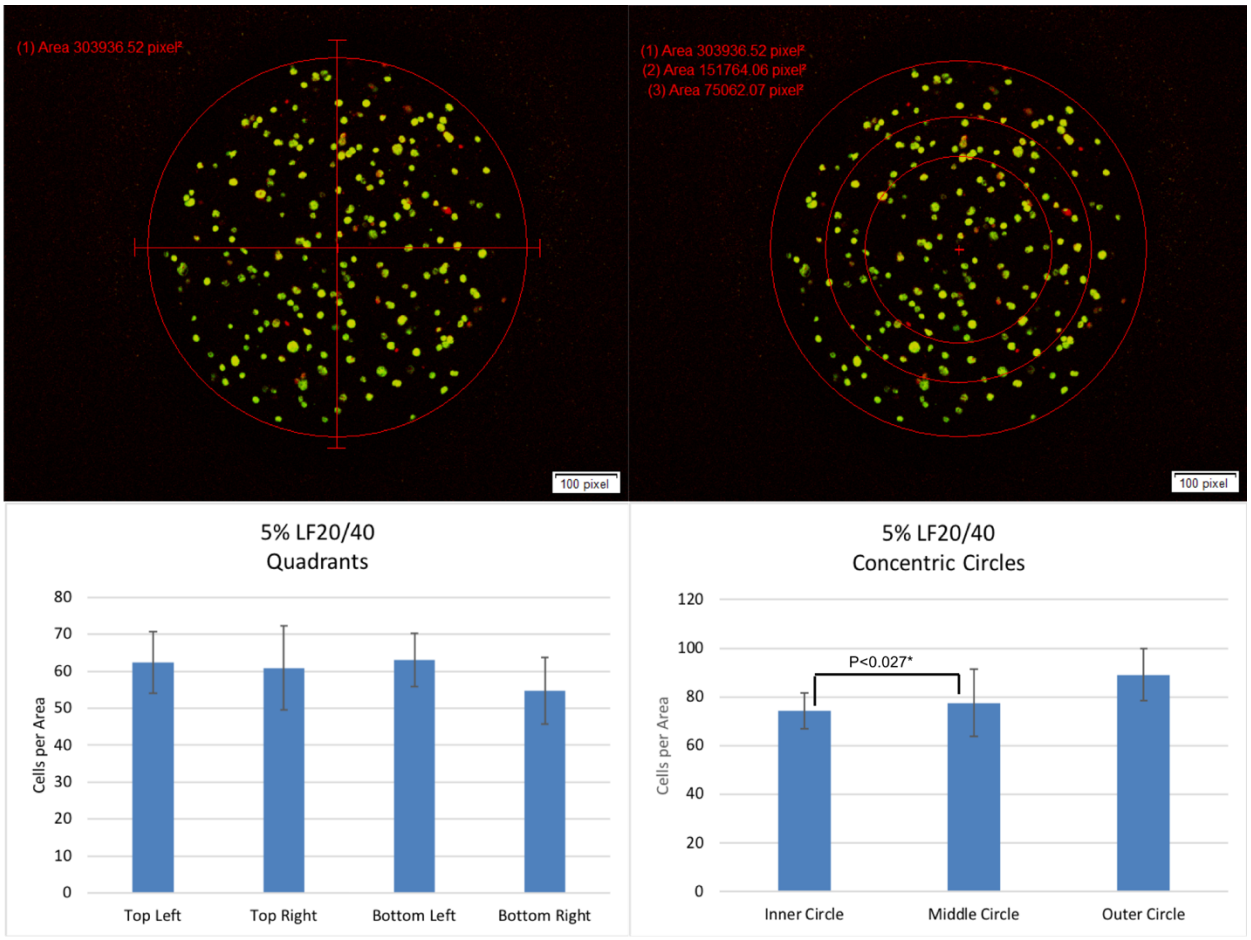

Figure 2.22. Bioprinted droplet analysis containing NHDFs in 5% LF 20/40 (high-molecular weight alginate) bioink. Representation of the bioprinted droplets sectioned into (A) quadrants and (B) concentric circles. Analysis of the cells per area in each region of the bioprinted droplet sectioned into (C) quadrants (P<0.215) and (D) concentric circles (P<0.005*).

For the droplets sectioned into concentric circles (n=10) the calculated F value was 6.463, P<0.005, which indicates there is a difference in cell distribution between the different concentric regions. To determine which regions were different from one another, independent t tests were performed in SPSS statistics to compare all of the groups. When the outer and middle rings were compared, the calculated P value was P<0.234, which suggests there was no difference in number of cells between these two groups. When the outer and inner concentric rings were compared, the calculated P value was P<0.332

indicating no difference between these groups. Finally, when the middle and inner concentric rings were compared, the P value was found to be $P<0.027$. Therefore, there is a significant trend of a denser cell population within the middle concentric ring as compared to the inner-most portion of the bioprinted droplet for this bioink.

For the 0.62% collagen and 4% LF20/40 alginate blend (1:1; n=5; **Figure 2.23**) sectioned into quadrants the calculated F value was 2.101 ($P<0.140$), which was less than the critical value of F for $P<0.05$. For the droplets sectioned into concentric circles the calculated F value was 1.083 ($P<0.369$), which was also less than the critical value of F for $P<0.05$. Therefore, there was no difference in the distribution of cells between the different quadrants or concentric circles of the bioprinted droplets using the collagen/alginate blend bioink.

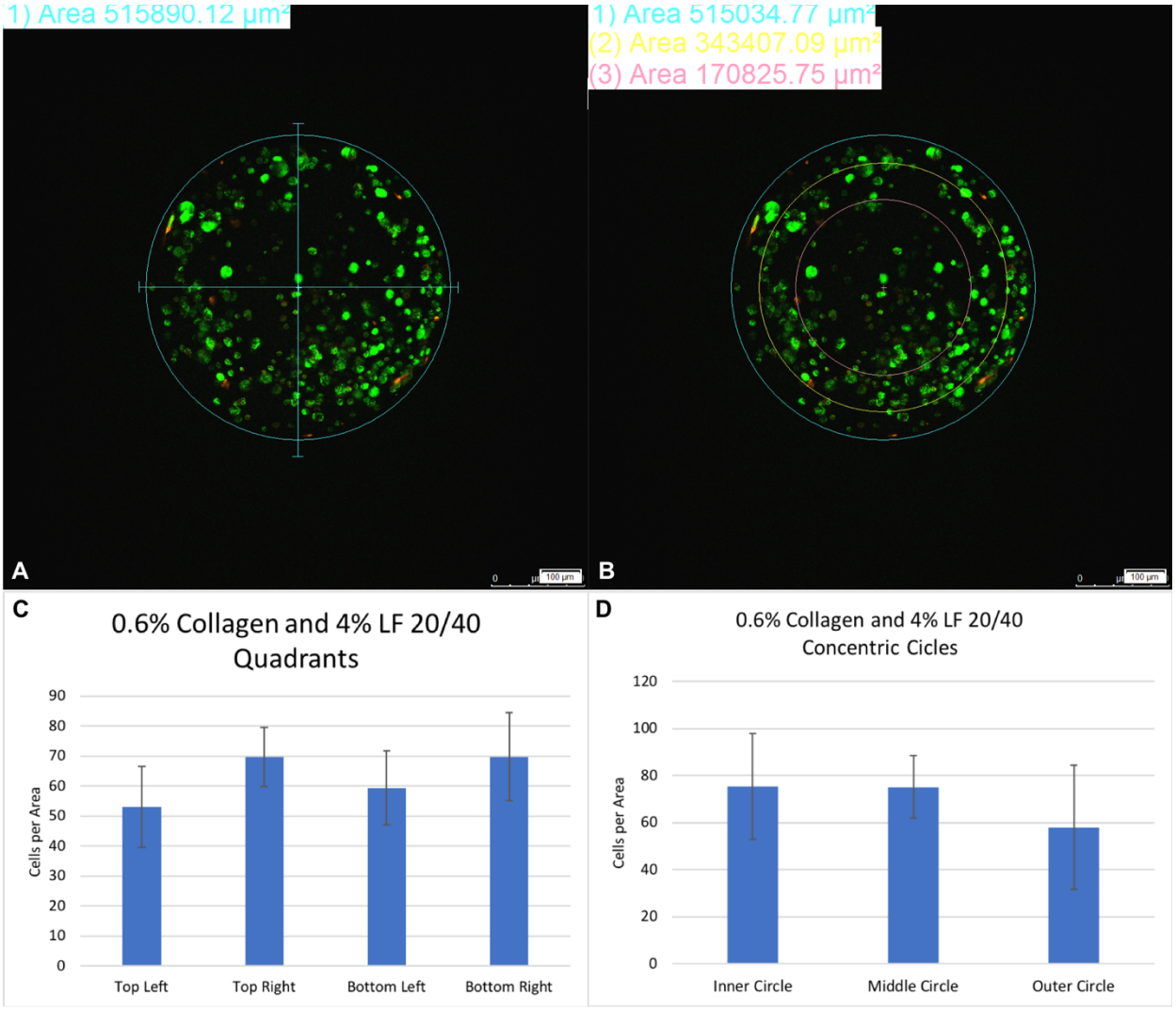

Figure 2.23. Bioprinted droplet analysis containing NHDFs in 0.62232% Collagen and 4% LF 20/40 (1:1) blended bioink. Representation of the bioprinted droplets sectioned into (A) quadrants and (B) concentric circles. Analysis of the cells per area in each region of the bioprinted droplet sectioned into (C) quadrants ($P<0.14$) and (D) concentric circles ($P<0.369$).

The F value calculated for NHDFs suspended in 5% LF10/60FT alginate (n=9; **Figure 2.24**) bioprinted droplets sectioned into quadrants was 1.963 ($P<0.139$), which was less than the critical value of F for $P<0.05$, indicating there was no difference in cell distribution between the different quadrants of the bioprinted droplets. For the NHDFs suspended in 5% LF10/60FT alginate sectioned into concentric circles, the calculated F

value was 23.084, which was greater than the critical value of F, 19.45, for P<0.05. Therefore, there was a difference in cell distribution between the different regions of the bioprinted droplet. To determine which regions were significantly different from one another, independent t tests were run in SPSS statistics.

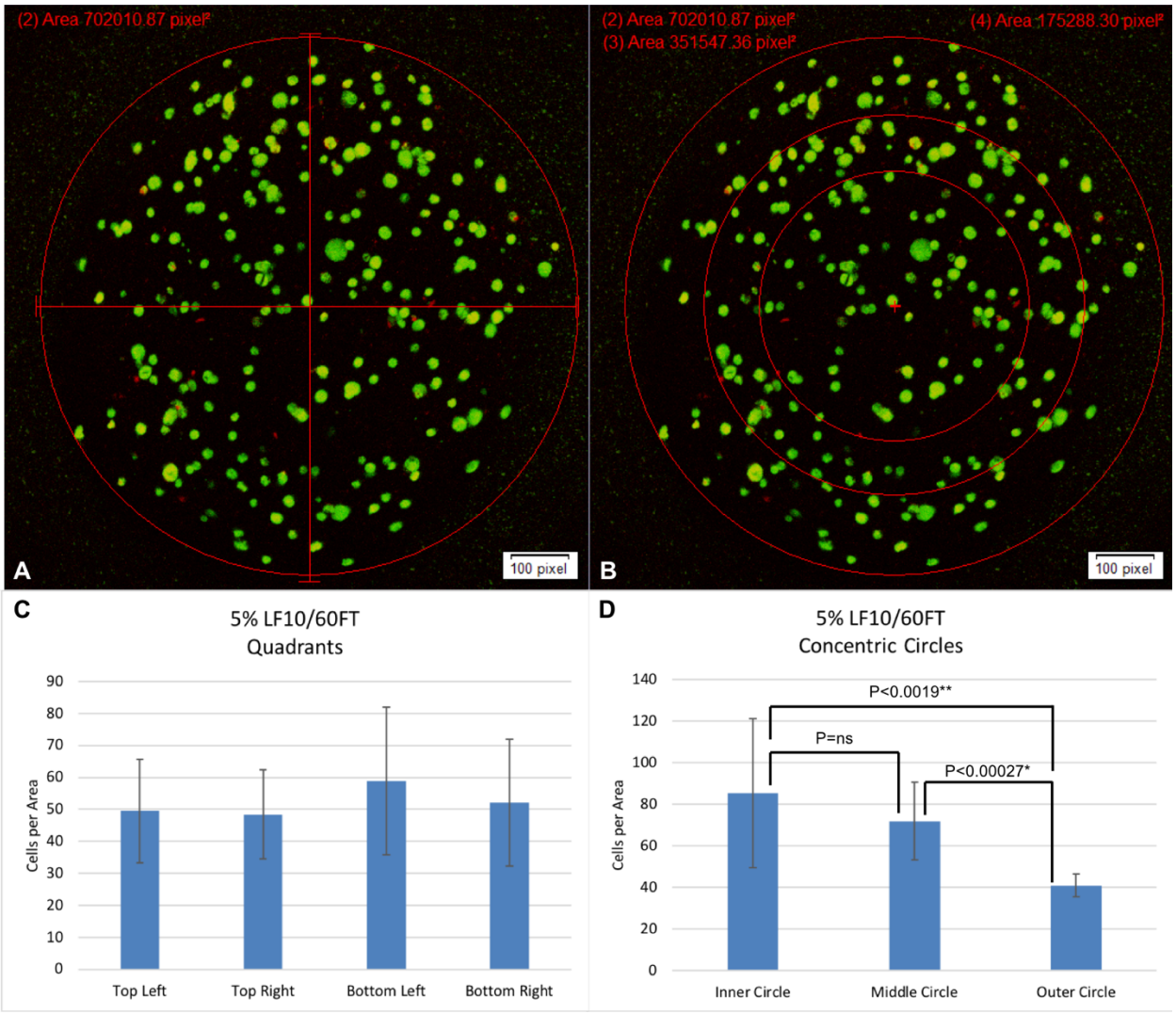

Figure 2.24. Bioprinted droplet analysis containing NHDFs in 5% LF10/60FT (low-molecular weight alginate) bioink. Representation of the bioprinted droplets sectioned into (A) quadrants and (B) concentric circles. Analysis of the cells per area in each region of the bioprinted droplet sectioned into (C) quadrants (P<0.139) and (D) concentric circles (P<0.05*).

When the inner and outer rings were compared, the significance was $P<0.001925$ with a definite trend of more cells being located in the inner concentric circle as compared to the outer. When the outer and middle rings were compared, the significance was $P<0.000267$ with more cells being located in the middle ring than the outer. Finally, when the middle and inner rings were compared the significance was $P<0.180344$ indicating there was no difference in the cell distribution between these two regions. Therefore, for the 5% LF10/60FT bioink there is a trend of cell distribution towards the interior of the bioprinted droplets.

Cell Viability in Bioprinted Constructs

Cell viability, one of the requirements of a successful bioprinting technique, was analyzed 1 hr and 8 days post-printing. High cell viability is essential for fabricating biomimetic constructs and is a direct representation of an adequate bioink. RGD peptide conjugation improves cell viability over extended periods of time by promoting cell spreading. Fluorescent microscopy was used to quantify cell viability in constructs after the printing process. Alginate bioink with a concentration of 15% and oxidation of 5% had average day 0 viability of 98%, day 4 of 96%, and day 8 of 95% (**Figure 2.25**). An independent t test was performed to determine the significance of the difference between cell viabilities on days 0 and 8, and a P-value of $P<0.002$ suggests the viability significantly increased over the culture time period.

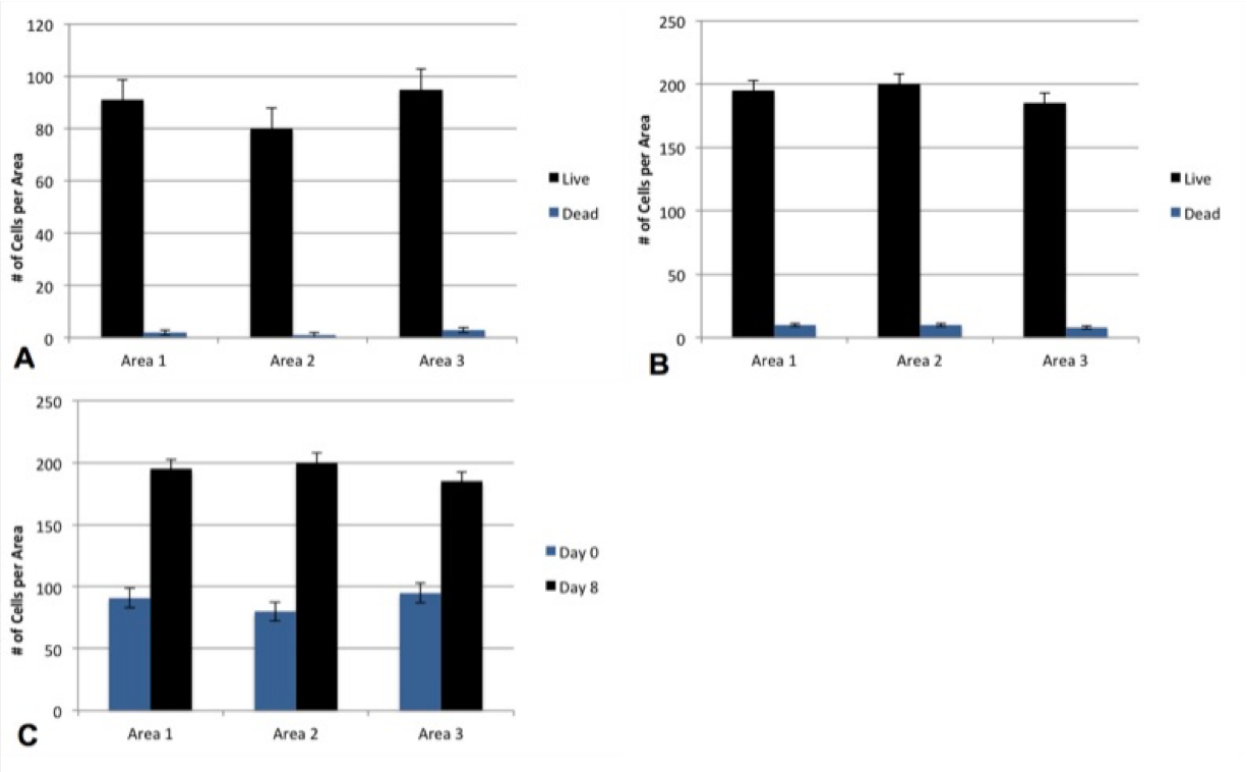

Figure 2.25. Quantified Viabilities of Bioprinted Constructs. The number of live and dead cells was quantified using a viability/cytotoxicity assay. The live/dead cell counts for Day 0 are shown in (**A**), and the counts for Day 8 in (**B**). The number of live cells counted for each area on days 0 and 8 are shown in (**C**) and were used to quantify cell proliferation.

These results indicate the deposition technique of the direct-write bioprinter extrudes cells gently enough to produce constructs that remain viable during and after the printing process. The high cell viability shows the 5% oxidation and 15% concentration alginate bioink was a suitable vehicle for cell deposition and provided an adequate environment for cell-survival. Similar cell counts in each of the areas showed a homogeneous cell distribution in the alginate bioink, a fundamental aspect of printing resolution.

Cell Proliferation in Bioprinted Constructs

Most tissues have complex combinations and gradients of extracellular matrix constituents, each with specific biological and mechanical influences. A biomaterial should be biomimetic of the native environment and facilitate cellular functions. The high porosity of the alginate scaffold allows the cells to communicate and network with each other, and may also facilitate the flux of nutrients and metabolites between the scaffold and its surrounding environment. Cell adhesion to the extracellular matrix is a preliminary phase of tissue formation that happens before cell proliferation and the organization of extracellular matrix molecules into functional tissue. The proliferation of cells plays a vital role in wound healing and tissue growth, and is therefore a very important factor when analyzing bioprinted constructs for tissue engineering applications. The RGD-conjugated alginate enhanced cell attachment in printed constructs, leading to improved cell spreading and proliferation. The proliferation of cells in the printed scaffolds was quantified by counting three separate areas on days 0 and 8 (**Figure 2.26**).

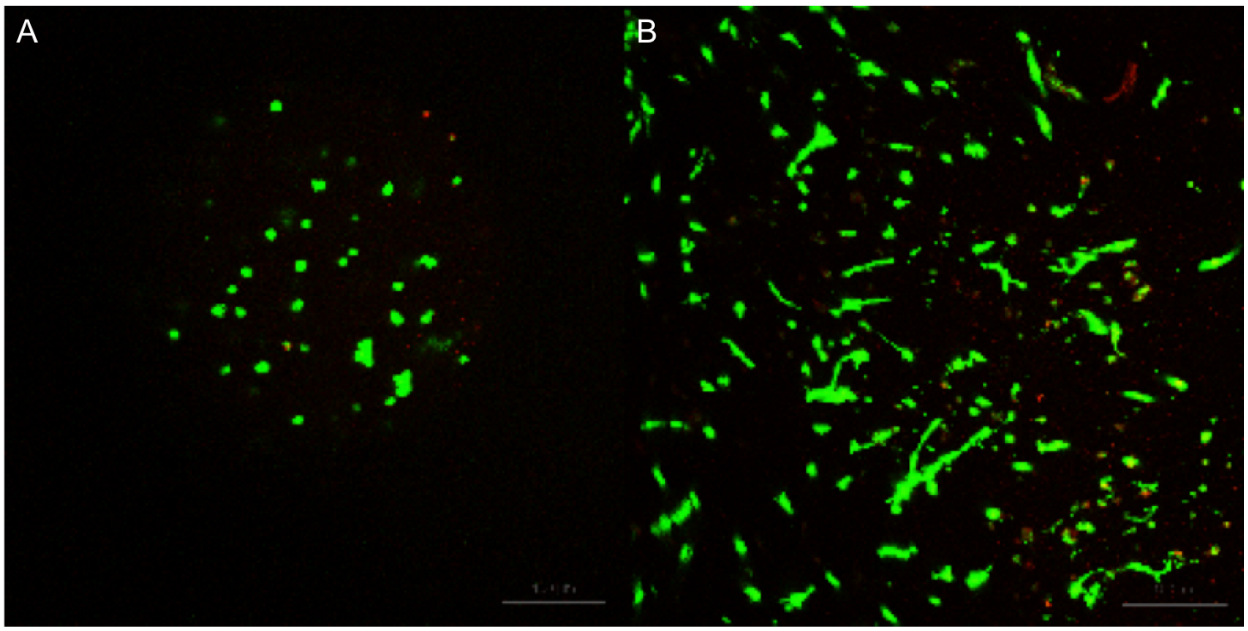

Figure 2.26. Human adipose-derived stem cells in RGD-conjugated alginate on (A) day 0 and (B) day 8 stained with calcein AM (live, green) and ethidium homodimer-1 (dead, red).

The overall cell proliferation was found to be 219.674% after 8 days of culture. These results signify the scaffold has adequate biocompatibility to be used as a synthetic extracellular matrix for delivering cells to repair damaged or nonfunctional tissue.

2.8 DISCUSSION

Presented here is a 3D robotic bioprinter that reliably and consistently dispenses homogenous drops of individual cells or cells mixed with biomimetic hydrogels (37). There are critical aspects of the design process that impact the generated construct's biomimetic function (35,36). The ability to control the temperature of the biomaterial and substrate is essential for the gelling mechanism of the hydrogels and the maintenance of their mechanical properties, therefore influencing cell distribution, proliferation, and differentiation within the hydrogel. Organs consist of many cell types, so the multiple

dispensers are critical for producing heterogeneous, tissue-like structures. The computer-aided design of the external architecture allows the production of custom tissue substitutes for distinct wounds or tissues. This is essential for the development of patient-specific replacements. The internal architecture is equally important because it affects the cell-cell relationships within the structure by placing the proper cells in intimate contact with each other and allowing them to form *in vivo*-like cell-cell junctions. Precise placement of cells determines how the cells communicate and network with each other to form vascular networks and mimic their bioactivity in native tissues. Three-dimensional bioprinting provides homogeneously dispersed cells within the bioink, as well as excellent precision on spatial placement of the cells themselves (33). Generated scaffolds also have high local cell densities, which is essential for cell differentiation and the formulation of extracellular matrix.

The bioprinter implemented here comprises a unique temperature-controlled environment in which the cells and cell-hydrogel mixtures are not limited by the necessity of pre-fusion. Under these conditions, the bioprinter is not solely reliant on the differential adhesion hypothesis. The inclusion of hydrogel materials can help guide the cell distribution and allow the cells to fuse, or not, depending on the properties desired for specific experimentation. The selection of biomimetic hydrogels for cell-encapsulation also has a profound effect on cell phenotype. Materials are known to have an effect on cell attachment, as well as cell size and morphology (36). The rheological characteristics, such as viscosity, of hydrogels dictate their influence on the cellular microenvironment (35). Native alginate is inert and does not readily communicate with

cells participating in the control of phenotype. However, using alginates that are chemically modified via peptide conjugation and oxidation, produces constructs with controlled degradability and increased cell attachment, migration, and proliferation (39). Altering the physiochemical properties of a biomaterial can influence tissue development *in vivo* (35,41).

Three-dimensional bioprinting using a fluid-dispensing, direct-write machine is limited by the degree of resolution of printed constructs, the availability of hydrogel materials, initial cell death post-printing, and the ability to vascularize the biomimetic scaffolds (32,41,42). An important feature of the bioprinting is its resolution. Every printing method is defined by the lower technical limit size of the smallest achievable details. There is a dynamic relationship between the lower limit size and attainable scale of the printed construct: the higher the resolution of the minute details, the smaller maximum construct size (9). The bioprinter is capable of depositing volumes as small as 230 nL in highly specific and organized patterns, giving it a higher resolution than similar machines. Hydrogels have been commonly used in bioprinting due to their hydrophilicity, biocompatibility, structural similarity to the extracellular matrix, and ease of modification (10-16). The high-water content of hydrogels improves their biocompatibility, but greatly reduces their mechanical strength and printability (33). There is a lack of optimal hydrogels with the appropriate mechanical properties for fluid delivery during bioadditive-manufacturing extrusion. Therefore, there is a large demand for developing hydrogels that are immunologically inert, have cytocompatible gelation mechanisms that can be successfully extruded using fluid delivery, and also produce a

cell-laden matrix with an optimal range of mechanical properties (2). Before the printing process, the cell-laden hydrogel bioink must be stored in the syringes for an amount of time, compromising the cell's viability (33). During the printing process, the shear stress induced on cells during extrusion can also be harmful to their viability (2,43). The bioprinter is able to produce highly viable (>90%) constructs, therefore overcoming the issue of initial cell death.

Vascularization plays a vital role in transmitting, supporting, or preserving the biomimetic function of bioprinted constructs (43). The diffusion of oxygen is $100 - 200\mu$m; therefore, in larger bioprinted constructs hypoxia is a concern (9). Conventional techniques are incapable of producing constructs with embedded vasculature, greatly limiting the size of producible scaffolds. The cell viability assessment of the bioprinter showed significant cell proliferation in the printed constructs over 8 days. Therefore, the technique proves its ability to generate scaffolds that allow cell growth, communication, and the formation of networks, requirements of vascularization.

The bioprinter provides the ability of using a variety of materials to quickly deposit cell-laden hydrogels in specific patterns. While this technique produces heterogeneous constructs with tunable properties, it is incapable of concurrent deposition, i.e. multiple syringes depositing at once, and reactive mixing, such as core-shell bioprinting discussed in chapter one. For some biomaterials, this deposition method would enhance the gelation mechanism and shorten the time for scaffold production (35). The addition of a multi-syringe dispenser could allow a broader range of biomaterials for the biofabrication technique. Investigation of cell activity in bioprinted constructs over a

longer period of time would provide more information about hydrogel characteristics, cell network formation, and vascularization of the constructs. These methods provide the possibility of producing vascularized replacements for future applications because the constructs are produced with high local cell densities and allow cell-cell interactions, which improves the likelihood of post-implantation survival (12,29).

The bioprinter's deposition method described can further involve robotically positioning and driving the three dispensers to deposit a plurality of biological materials on top of previously deposited materials in a predetermined pattern. This step can be repeated using ascending patterns until a three-dimensional organ or tissue is produced. Therefore, the Palmetto Printer is suitable for reliably dispensing cell-laden hydrogels to create a three-dimensional construct that is capable of retaining vasculature and high cell viability, and could be used in a variety of future tissue engineering applications.

2.9 REFERENCES

1. Langer, R. & Vacanti, J.P. Tissue Engineering. *Science*. **260** (5110), 920-926, (1993).
2. Derby, B. Review: Printing and Prototyping of Tissues and Scaffolds. *Science*. **338** (6109), 921-926, (2012).
3. Kachurin, A.M., *et al*. Direct-Write Construction of Tissue-Engineered Scaffolds. *Mat. Res. Soc. Symp. Proc.* **698**, , (2002).
4. Sachlos, E. & Czernuszka, J.T. Making Tissue Engineering Scaffolds Work. Review on the Application of Solid Freeform Fabrication Technology to the Production of Tissue Engineering Scaffolds. *European Cells and Materials.* **5**, 29-40 (2003).
5. Yeong, W.Y., Chua, C.K., Leong, K.F., & Chandrasekaran, M. Rapid Prototyping in Tissue Engineering: Challenges and Potential. *Trends Biotechnol.* **22** (12), 643-652, (2004).
6. Landers, R., Pfister, A., Hubner, U., John, H., Schmelzeisen, R., and Mulhaupt, R. Fabrication of Soft Tissue Engineering Scaffolds by means of Rapid Prototyping Techniques. *Journal of Materials Science.* **37** (15), 3107-3116, (2002).
7. Murphy, S.V., Skardal, A., and Atala A. Evaluation of Hydrogels for Bio-Printing Applications. *Journal of Biomedical Materials Research Part A.* **101A** (1), 272-284, (2013).

8. Burg, K.J.L. & Boland, T. Minimally Invasive Tissue Engineering Composites and Cell Printing. *IEEE Eng Med Biol Mag.* **22** (5), 84-91, (2003).
9. Billiet, T., Vandenhaute, M., Schelfhout, J., Van Vlierberghe, S., & Dubruel, P. A Review of Trends and Limitations in Hydrogel-Rapid Prototyping for Tissue Engineering. *Biomaterials.* **33** (26), 6020-6041, (2012).
10. Khalil, S., Nam, J., and Sun, W. Multi-Nozzle Deposition for Construction of 3D Biopolymer Tissue Scaffolds. *Rapid Prototyping Journal.* **11** (1), 9-17, (2005).
11. Pataky, K., Braschler, T., Negro, A., Renaud, P., Lutolf, M.P., & Brugger, J. Microdrop Printing of Hydrogel Bioinks into Three-Dimensional Tissue-Like Geometries. *Adv Mater.* **24** (3), 391-396, (2011).
12. Pati, F., Shim, J.H., Lee, J.S., & Cho, D.W. Three-Dimensional Printing of Cell-Laden Constructs for Heterogeneous Tissue Regeneration. *Manufacturing Letters.* **1** (1), 49-53, (2013).
13. Gruene, M., *et al.* Laser Printing of Three-Dimensional Multicellular Arrays for Studies of Cell-Cell and Cell-Environment Interactions. *Tissue Eng.* **17** (10), 973-982, (2011).
14. Khalil, S. and Sun, W. Bioprinting Endothelial Cells With Alginate for 3D Tissue Constructs. *J Biomed Eng.* **131** (11), 1-8, (2009).
15. Xu, T., *et al.* Hybrid Printing of Mechanically and Biologically Improved Constructs for Cartilage Tissue Engineering Applications. *Biofabrication.* **5** (1), 1-10, (2012).
16. Zhang, T., Yan, K.C., Ouyang, L., and Sun, W. Mechanical Characterization of Bioprinted *in vitro* Soft Tissue Models. *Biofabrication*. **5** (4), 1-10, (2013).
17. Chung, J.H.Y, *et al*. Bio-ink Properties and Printability for Extrusion Printing Living Cells. *J. Biomater. Sci., Polym. Ed.* **1** (7), 763-773, (2013).
18. Yang, S., Leong, K.F., Du, Z., & Chua, C.K. The Design of Scaffolds for Use in Tissue Engineering. Part II. Rapid Prototyping Techniques. *Tissue Engineering.* **8** (1), 1-11, (2002).
19. Ferris, C.J., Gilmore, K.G., Wallace, G.G., & Panhuis, M. Biofabrication: An Overview of the Approaches Used for Printing of Living Cells. *Appl. Microbiol. Biotechnol.* **97** (10), 4243-4258, (2013).
20. Lu, L. and Mikos, A.G. The Importance of New Processing Techniques in Tissue Engineering. *MRS Bull.* **21**(11), 28-32, (1996).
21. Wake, M.C., Gupta, P.K., Mikos, A.G. Fabrication of pliable biodegradable polymer foams to engineer soft tissues. *Cell Transplant*. **5**(4), 465–473, (1996).
22. Mironov, V., Visconti, R.P., Kasyanov, V., Forgacs, G., Drake, C.J., & Markwald, R.R. Organ Printing: Tissue Spheroids as Building Blocks. *Biomaterials.* **30** (12), 2164-2174, (2009).
23. Norotte, C., Marga, F.S., Niklason, L.E., & Forgacs, G. Scaffold-free Vascular Tissue Engineering Using Bioprinting. *Biomaterials.* **30** (30), 5910-5917, (2009).
24. Devillard, R., *et al.* Cell Patterning by Laser-Assisted Bioprinting. *Methods Cell Biol.* **119** (), 159-174, (2014).
25. Binder, K.W., Allen, A.J., Yoo, J.J, & Atala, A. Drop-on-Demand Inkjet Bioprinting: a Primer. *Gene Ther Reg.* **6** (1), 33-, (2011).

26. Xu, T., *et al.* Viability and Electrophysiology of Neural Cell Structures Generated by the Inkjet Printing Method. *Biomaterials.* **27** (19), 3580-3588, (2006).
27. Calvert, P. Inkjet Printing for Materials and Devices. *Chem Mater.* **13** (10), 3299-3305, (2001).
28. Chang, C.C., Boland, E.D., Williams, S.K., & Hoying, J.B. Direct-Write Bioprinting Three-Dimensional Biohybrid Systems for Future Regenerative Therapies. *J Biomed Mater Res B Appl Biomater.* **98** (1), 160-170, (2011).
29. Li, M.G., Tian, X.Y., & Chen, X.B. A Brief Review of Dispensing-Based Rapid Prototyping Techniques in Tissue Scaffold Fabrication: Role of Modeling on Scaffold Properties Prediction. *Biofabrication.* **1** (3), 1-10, (2009).
30. Bouhadir, K.H., Lee, K.Y., Alsberg, E., Damm, K.L., Anderson, K.W., & Mooney, D.J. Degradation of Partially Oxidized Alginate and its Potential Application for Tissue Engineering. *Biotechnol Prog.* **17** (5), 945-950, (2001).
31. Rowley, J.A., Madlambaya, G., & Mooney, D.J. Alginate Hydrogels as Synthetic Extracellular Matrix Materials. *Biomaterials.* **20** (1), 45-53, (1999).
32. Smith, C.M., Christian, J.J., Warren, W.L., & Williams, S.K. Characterizing Environmental Factors that Impact Viability of Tissue-Engineered Constructs Fabricated by a Direct-Write Bioassembly Tool. *Tissue Engineering.* **13** (2), 373-383, (2007).
33. Ozbolat, I. & Yu, Y. Bioprinting Towards Organ Fabrication: Challenges and Future Trends. *IEEE Trans Biomed Eng.* **60** (3), 691-699, (2012).
34. Peltola, S.M., Melchels, et. al. A Review of Rapid Prototyping Techniques for Tissue Engineering Purposes. *Annals of Medicine.* **40** (4), 268-280, (2008).
35. Malda, J., *et al.* 25th Anniversary Article: Engineering Hydrogels for Biofabrication. *Adv Mat.* **25** (36), 5011-5028, (2013).
36. Murphy, S.V. & Atala, A. 3D Bioprinting of Tissues and Organs. *Nat Biotech.* **32** (8), 773-785, (2014).
37. Jia, J., *et al.* Engineering Alginate as Bioink for Bioprinting. *Acta Biomaterialia.* **10** (10), 4323-4331, (2014).
38. Forty, R.A. & Steinberg, M.S. The Differential Adhesion Hypothesis: a Direct Evaluation. *Developmental Biology.* **278** (1), 255-263, (2005).
39. Wang, L., Shansky, J., Borselli, C., Mooney, D., & Vandenburgh, H. Design and Fabrication of a Biodegradable, Covalently Crosslinked Shape-Memory Alginate Scaffold for Cell and Growth Factor Delivery. *Tis Eng Part A.* **18** (19-20), 2000-2007, (2012).
40. El-Sherbiny, I.M. & Yacoub, M.H. Hydrogel Scaffolds for Tissue Engineering: Progress and Challenges. *Global Cardiology Science & Practice.* **3** (38), 316-342, (2013).
41. Smith, C.M., *et al.* Three-Dimensional BioAssembly Tool for Generating Viable Tissue-Engineered Constructs. *Tissue Engineering.* **10** (9-10), 1566-1576, (2004).
42. Ozbolat, I.T., Chen, H., & Yu, Y. Development of a 'Multi-arm Bioprinter' for Hybrid Fabrication of Tissue Engineering Constructs. *Robotics and Computer-Integrated Manufacturing.* **30** (3), 295-304, doi: 10.1016/j.rcim.2013.10.005 (2014).

43. Kolesky, D.B., Truby, R.L., Gladman, A.S., Busbee, T.A., Homan, K.A., & Lewis, J.A. Three-Dimensional Bioprinting of Vascularized, Heterogeneous Cell-Laden Tissue Constructs. *Adv Mater*. **26**(19), 3124-3130, (2014).
44. Richards, D.J., Jia, J., Yost, M.J., Markwald, R., and Mei, Y. 3D Bioprinting for Vascularized Tissue Fabrication. *Ann Biomed Eng.* **45**(1), 132-147, (2017).
45. Dennis, S.G., Trusk, T., Richards, D., Jia, J., Tan, Y., Mei, Y., Fann, S., Markwald, R., and Yost, M.J. Viability of Bioprinted Cellular Constructs Using a Three-dispenser Cartesian Printer. *Journal of Visualized Experiments.* **103,** e53156, (2015).
46. Lee, S.J., Yoo, J.J., Lim, G.J., Atala, A., and Stitzel, J. In Vitro Evaluation of Electrospun Nanofiber Scaffolds for Vascular Graft Application. *Journ Biomed Mat Res A*. **83**(4)**:**999-1008, (2007).
47. Ji, S. and Guvendiren, M. Recent advances in Bioink Design for 3D Bioprinting of Tissues and Organs. *Front Bioeng Biotechnol.* **5**(23):1-8, doi:10.3389/fbioe.2017.00023 (2017).
48. Laschke, M.W., Rucker, M., Jensen, G., Carvalho, C., Mulhaupt, R., Gellrich, N.-C., and Menger, M.D. Incorporation of Growth Factor Containing Matrigel Promotes Vascularization of Porous PLGA Scaffolds. *J Biomed Mater Res A.* **85**(2): 397-407, doi:10.1002/jbm.a.31503 (2008).
49. Han, Y., Wei, C., and Dong, J. Droplet Formation and Settlement of Phase-change Ink in High Resolution Electrohydrodynamic (EHD) 3D Printing. *Journal of Manufacturing Processes.* **20**(3): 485-491, (2015).
50. Yost, M.J., Baicu, C.F., Stonerock, C.E., Goodwin, R.L., Price, R.L., Davis, J.M., Evans, H., Watson, P.D., Gore, C.M., Sweet, J., Creech, L., Zile, M.R., and Terracio, L. A Novel Tubular Scaffold for Cardiovascular Tissue Engineering. *Tissue Engineering.* **10**(1/2):273-284, (2004).
51. Datta, P., Ayan, B., and Ozbolat, I.T. Bioprinting for Vascular and Vascularized Tissue Biofabrication. *Acta Biomaterials.* **51:**1-20, doi: 10.1016/j.actbio.2017.01.035 (2017).
52. Wong, J.Y. and Bronzino, J.D. (2007). Biodegradable Hydrogels: Tailoring Properties and Function through Chemistry and Structure. In *Biomaterials* (pp 5.1-5.13). Boca Raton, FL: Taylor & Francis Group, LLC.
53. Mandrycky, C., Wang, Z., Kim, K., and Kim, D. 3D Bioprinting for Engineering Complex Tissues. *Biotechnol Adv.* **34**:422-434, (2016).
54. Derakshanfar, S., Mbeleck, R., Xu, K., Zhang, X., Zhong, W., and Xing, M. 3D Bioprinting for Biomedical Devices and Tissue Engineering: A Review of Recent Trends and Advances. *Bioactive Mat.* **3:**144-156, (2018).
55. Pan, C., Bruyas, A., and Yang, Y.P. Bioprinting for Tissue Engineering and Regenerative Medicine. *Material Matters.* **11**(2), (2016).
56. Ahmed, E.M. Hydrogel Preparation, Characterization, and Applications: A Review. *Journal of Adv Res.* **6:**105-121, (2015).
57. Tracy, L.E., Minasian, R.A., and Caterson, E.J. Extracellular Matrix and Dermal Fibroblast Function in the Healing Wound. *Adv Wound Care.* **5**(3):119-136, (2014).

58. Yang, J., Yamato, M., Kohno, C., Nishimoto, A., Sekine, H., Fukai, F., and Okano, T. Cell Sheet Engineering: Recreating Tissues without Biodegradable Scaffolds. *Biomaterials.* **26:**6415-6422, (2005).
59. Axpe, E. and Oyen, M.L. Applications of Alginate-based Bioinks in 3D Bioprinting. *Int J Mol Sci.* **25**(17):E1976, (2016).
60. Drury, J.L. and Mooney, D.J. Hydrogels for Tissue Engineering: Scaffold Design Variables and Applications. *Biomaterials.* **24**:4337-4351, (2003).
61. Wright, B., De Bank, P.A., Luetchford, K.A., Acosta, F.R., and Connon, C.J. Oxidized Alginate Hydrogels as Niche Environments for Corneal Epithelial Cells. *J Biomed Mater Res A.* **102**(10):3393-3400, (2014).

CHAPTER THREE

SCAFFOLD-FREE TISSUE ENGINEERING

The field of tissue engineering advances an exciting array of solutions for organ repair and wound healing. However, to realize this potential, several hurdles must be overcome. Vascularization is arguably the most important practical limitation in tissue engineering, imposing both dimensional and time constraints on the technology. Vascularization and fast anastomosis with the host are essential in engineering cellular constructs that survive once implanted, as well as tissue maintenance and regeneration. Endothelial cell migration and physiological growth of new blood vessels *in vivo* has been reported to occur at ~5 um/hour due to the availability of oxygen, which is limited to a diffusion distance of $150 - 200\mu$m from a supplying blood vessel (**Figure 3.1**) (42-43). This diffusion limit is relative to the distance between mammalian cells and an adjacent vascular bed (Lovett). With the clinical need being for larger engineered tissues, a major focus in the tissue engineering field has been on designing constructs with pre-existing vascular architectures or, more recently, prevascularized constructs.

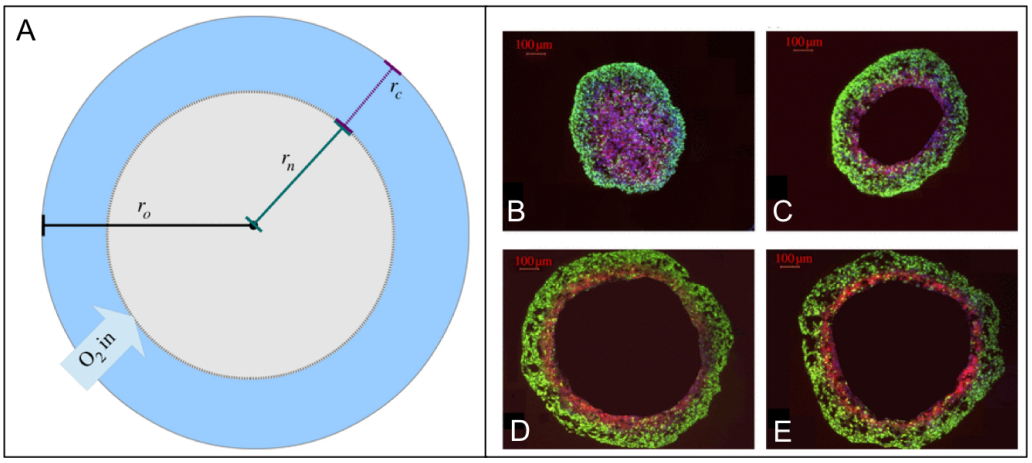

Figure 3.1. (A) Cross section of a tumor spheroid of radius r_o. Oxygen partial pressure is non-zero in the region r_c. This region comprises all viable cells both hypoxic and oxic. Oxygen cannot penetrate into region r_n, which is anoxic. (B-E) Development of hypoxia and anoxia in tumour spheroids. Tissue sections taken from tumour spheroids grown over 17 days were stained for the proliferation marker Ki-67 (green) and hypoxia (red). A distinct progression was observed: (B) day 4 of growth, with central hypoxia; (C) day 6 with beginnings of an anoxic core; (D) day 15 of growth, with distinct core; (E) day 17 of growth, distinct core and the degradation of spheroid integrity apparent. Fig adapted from ref Grimes, *et al*. (2014) *J. Royal Society Interface* **11**(92).

Vascularization of an avascular tissue, or a tissue graft, can be modeled by a well-ordered series of events (**Figure 3.2)**, starting with (1) endothelial cell activation, (2) migration of endothelial cells and remodeling of the implant stroma, (3) Primitive network formation (4) anastomosis of host/implant endothelial structures, (5) Network remodeling (6) Lumen formation within the endothelial architecture, and (7) maturation of vessels through recruitment of mural cells. This leads to formation of a blood-perfused vascular pedicle in an implant. Depicted is the expected entry point of different implant types, with preceding development either occurring *in vitro* or supplied by donor.

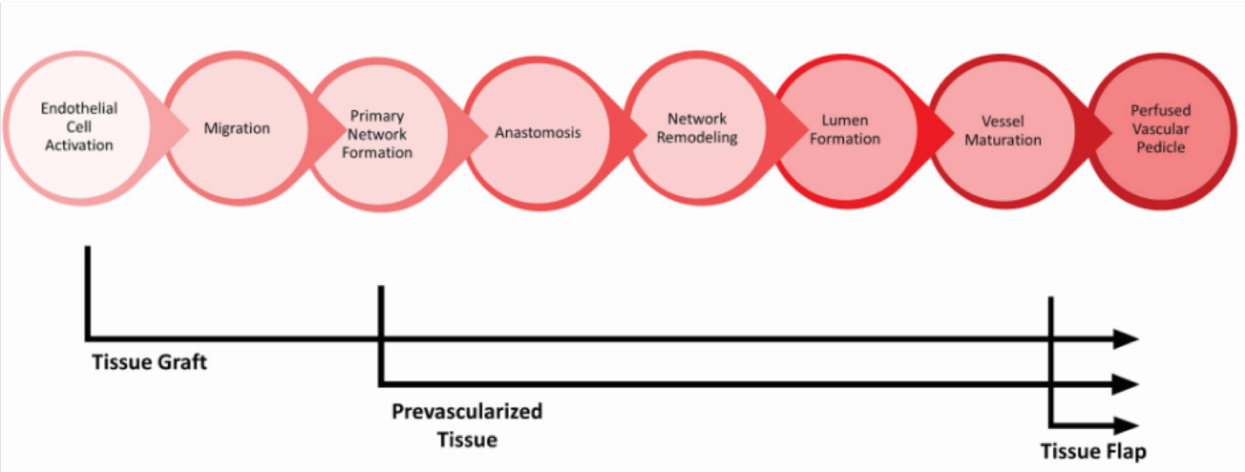

Figure 3.2. Proposed Vascularization Pipeline. The process of vascularization *in vivo* starts with endothelial cell activation, migration, network formation, tubulogenesis, and ends with anastomosis and blood flow.

Current engineered grafts, such as the bioprinted constructs discussed in chapter 2, are absent of any vascular architecture, forcing them to enter the vascularization pipeline at the earliest time point. Rather than incorporating intricate microvessel architectures into our bioprinted constructs, we began investigating scaffold-free fabrication methods. Scaffold-free tissue engineering aims to produce physiologically-relevant three-dimensional multicellular constructs without the use of a scaffold.

3.1 SCAFFOLD-FREE CELLULAR SELF-ASSEMBLY

Scaffold-free engineering techniques rely on the inherent capacity of cells to migrate and form intercellular connections. Adherent cells, like endothelial cells and fibroblasts, depend on the formation of these intercellular as well as extracellular matrix-cellular connections for survival. When adherent cells are placed in an environment that lacks a surface for adhesion or a substrate, the cells will aggregate and undergo the process of self-assembly. During the process of self-assembly, suspended cells form three-dimensional multicellular spheroids. This process mimics processes known to occur

during embryogenesis, morphogenesis, and organogenesis *in vivo* (Achilli, 2012). The produced multicellular spheroids have similar architectural and functional characteristics of native tissues.

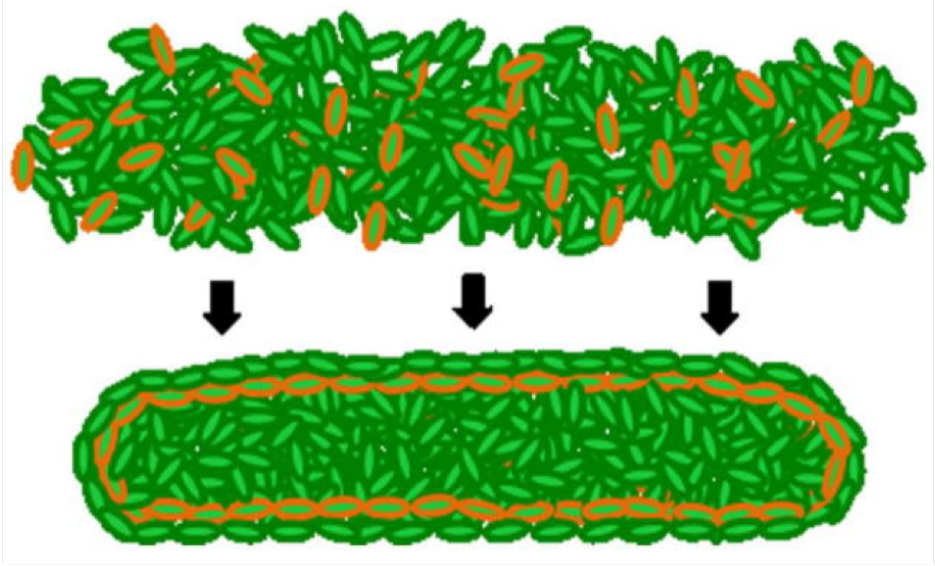

Figure 3.3. Schematic of cellular self-assembly . In the generation of linear tissue constructs from cell suspension under the non-adherent linear constrained conditions, cell-cell adhesions and organization of cellular cortical cytoskeletons results in the generation of a linear tissue construct with a shape-appropriate cortical cytoskeleton. Fig adapted from ref Czajka, C.A., et. al. (2014). *Annals of Biomed Eng.* **24**(5):1049-1061.

3.2 PREVASCULARIZATION: PRIMARY NETWORK FORMATION

To sustain larger tissue engineered constructs, an intact vascular pedicle consisting of an inlet, outlet, and a perfusable capillary bed, must either pre-exist or form rapidly upon implantation. Prevascularization has recently been explored in tissue engineering in attempts to accelerate the acceptance of implanted cellular constructs. These techniques aim to produce implants with a preformed microvasculature prior to implantation. Prevascularization refers to the *in vitro* assembly of primitive endothelial networks resembling a capillary bed.

In recent years two strategies for vascularization of tissue engineered constructs have been explored: angiogenesis and inosculation. The angiogenesis approach relies on the ingrowth of vascular sprouts from the host microvasculature (indicated by the red vessels in **Figure 3.4A**) into the implanted construct, which overtime fuse together to form a new microvascular network (12). This process is highly dynamic and must progress through the entire vascularization pipeline depicted in **Figure 3.1**. The inosculation approach incorporates a preformed microvascular network prior to implantation (depicted by the blue vessels in **Figure 3.4B**) that forms interconnections, or inosculates, with the host vasculature to get a fully blood-perfused vessel within a short amount of time (12).

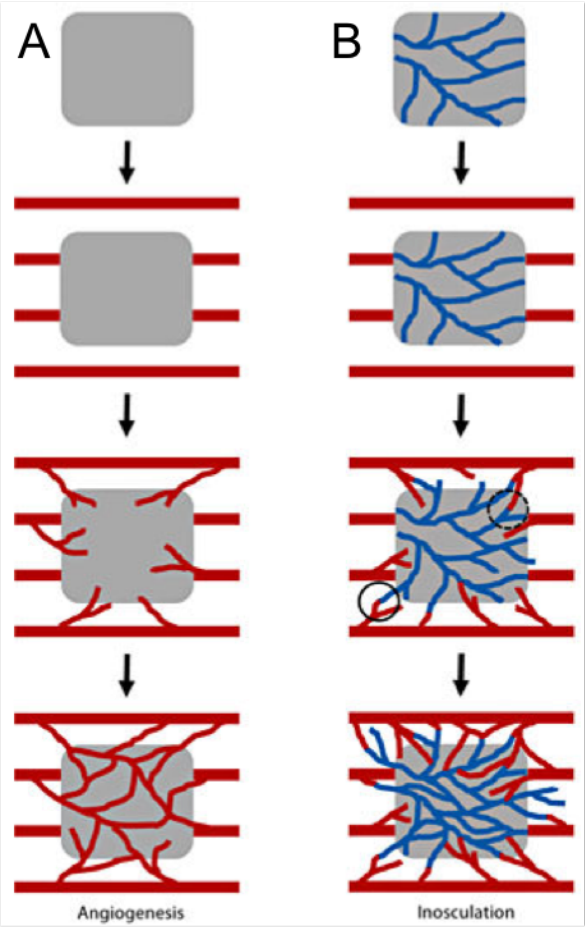

Figure 3.4. Schematic drawing of the two principal vascularization strategies in tissue engineering, i.e. (A) angiogenesis and (B) inosculation. Fig adapted from ref Laschke, M.W. and Menger, M.D. *Eur Surg Res* **48**:85-92.

Laschke and Menger make a useful distinction between angiogenesis and inosculation that explains the utility of prevascularization: angiogenic sprouting, while potentially faster than de novo vasculogenesis, is still a slow process, whereas inosculation, or the merging of existing microvessels into larger diameter vessels, occurs more rapidly (12,14,43-44). Specifically, *in vivo* microvessel growth occurs at a peak rate of $5\ {}^{\mu m}/_{hr}$ (12). Therefore, spanning an entire implant exceeding dimensions of a few

hundred micrometers at this rate is too slow to prevent ischemic damage, as hypoxia peaks in skeletal muscle at approximately eight hours (9,12).

3.3 DEVELOPMENT OF NOVEL SCAFFOLD-FREE PREVASCULARIZED ENDOTHELIAL-FIBROBLAST CONSTRUCTS

Engineering these vascularized implants *in vitro* requires the use of multiple cell sources to form the multiple components of vessels including the lining of the vessels, which is predominantly made up of endothelial cells, and the supporting cellular network (41). We have developed and previously reported on the anastomotic potential of a scaffold-free prevascular implant model that is formed from the coculture of human adipose microvascular endothelial cells (HAMECs) and normal human dermal fibroblasts (NHDFs) (5,23,25-26). We use primary human adipose derived endothelial cells to ensure clinical translatability, where an autologously derived population of cells can be re-implanted in a patient with minimal morbidity due to immune compatibility complications. The adult fibroblasts create the extracellular-rich stroma necessary to support a vascular bed and provide additional proangiogenic stimuli (22). Mature endothelial cells, while capable of forming spontaneous capillary like tubes *in* vitro, appear to require consistent input of proangiogenic environmental signaling. Fibroblasts, through constitutive expression of vascular endothelial factor (VEGF), basic fibroblast growth factor (bFGF) and angiopoitin-1 (Ang-1), address this basic need (22). The presence of fibroblasts corresponds to an increased microvessel density within an implant and stabilization of vessels by signaling endothelial cell to express smooth muscle actin

(16). Other exctacellular matrix proteins deposited by the fibroblasts such as laminin, collagen type I and collagen type IV are needed for vessel maturation (10).

We have previously reported that a specific 1:4 ratio of human microvascular endothelial cells and fibroblasts maximizes the density of endothelial cords when allowed to self-assemble in a scaffold-free non-adherent environment. Increasing the density of fibroblasts resulted in endothelial clusters without cords, and increasing density of endothelial cells resulted in structures lacking avascular stromal areas consistent with a vascular bed (23). Additionally, these endothelial cords were shown to organize into vascular networks with distinct directional orientations that reflect self-assembly-mediated tension (25; **Figure 3.5**).

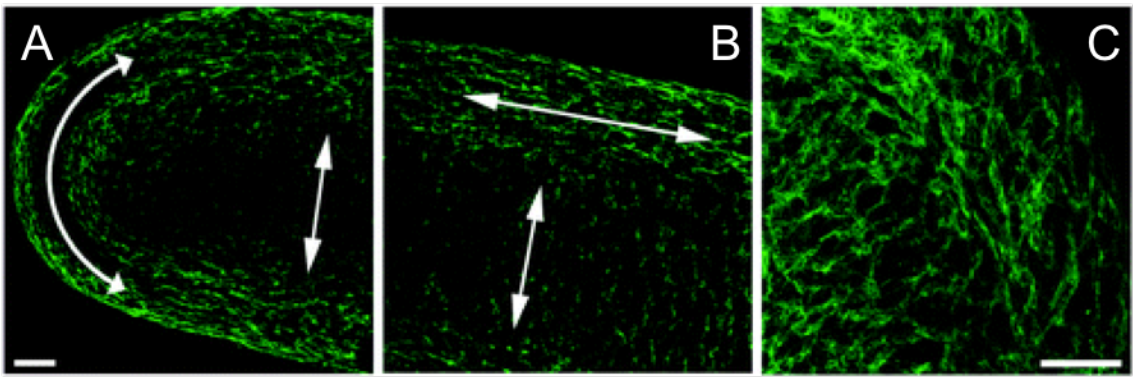

Figure 3.5. Confocal projections of whole-mount rod tissue illustrating primary vascular networks (CD31, green). Arrows indicate directional alignments. (A) and (B) are 10X, (C) is 20X image. Scale bars 100 μm. Figure adapted from ref Czajka, C.A., et al. *Ann Plastic Surg* **75**(3):371-375, 2015.

Within 3 days of *in vitro* culture in an agarose mold, the coculture generated an extracellular matrix containing laminin, type I collagen, and fibronectin. The interplay between ECM components, such as laminins and fibrillar collagen, and cell surface integrins play a key role in vascular lumen formation (24).

Due to the diffusional limits of oxygen and nutrients to the interior of implanted constructs, we wanted to take a more systematic approach to investigate the vascularization process and how engineered constructs get perfused once implanted. The literature reports findings from later time points post-implantation, spanning from a few days to even more than a week post-implantation, to assess graft acceptance. However, this data is incomplete as it does not evaluate the dynamics of vascularization at early time points following implantation. Additionally, ischemic damage to tissues occurs within a time span of hours rather than days, necessitating a focus on processes impacting vascularization within a 24-hour post-implantation window. Therefore, we wanted to investigate the early temporal kinetics of vascularization, i.e. <24 hours post-implantation, of implanted cellular constructs, in order to discern the immediate events happening post-implantation. Specifically, we hypothesized that the existing self-assembled primitive network of the Scaffold-free Prevascularized Endothelial-fibroblast Constructs (SPECs) will allow earlier host-implant anastomosis and increased presence of lumen containing vessels in the interior of the implants by 24 hours compared to avascular grafts, such as fibroblast spheroids.

3.4 MATERIALS AND METHODS

Formation of Non-adherent Agarose Molds

A 2% (w/v) agarose solution is made by dissolving the agarose in deionized water. To sterilize the solution, it is autoclaved on the liquid cycle for thirty minutes. The geometry of the agarose mold is determined by the computer-aided design used to create the

negative in which the agarose is gelled around. This provides the opportunity for using patient-specific images to create physiologically-relevant SPECs in the future.

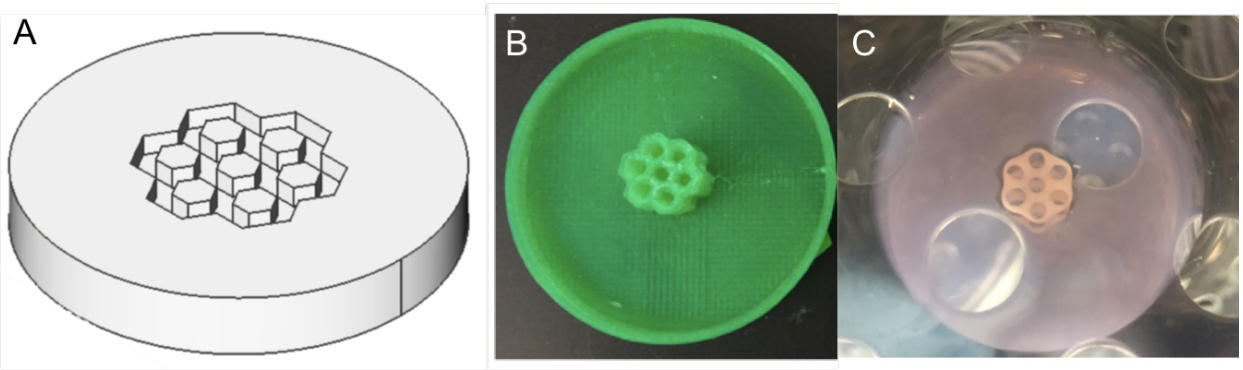

Figure 3.6. Schematic of computer-aided design (A) used to generate MakerBot negative (B) and form the desired shape of the non-adherent Agarose Mold that is subsequently seeded with cells (C).

Cell Culture

Human adipose microvascular endothelial cells (HAMEC) (ScienceCell, Carlsbad, CA, 7200) were cultured in T75 cell culture flasks with endothelial growth medium-2 (EGM-2) (Lonza, Allendale, NJ, CC-3156 & CC-4176) until reaching 80% confluence. Normal human dermal fibroblasts (NHDF-Ad) (Lonza, CC-2511) were cultured in Fibroblast growth media-2 (FGM-2) (Lonza, CC-3131 & CC-4126). Cells were collected between passages for use in experiments.

Formation of Scaffold-free Prevascularized Endothelial-fibroblast Constructs

We have developed and previously reported on the anastomotic potential of a scaffold-free prevascular construct that is formed from the coculture of human adipose microvascular endothelial cells (HAMECs) and normal human dermal fibroblasts (NHDFs) (5). In previous work, Czajka, et. al. determined the appropriate ratio of

fibroblast to endothelial cells to be 4:1 (5,23,25-26). The scaffold-free prevascularized endothelial-fibroblast constructs (SPECs) were modifications of the protocol established by Czajka and Drake (23). Rod-shaped troughs of 0.9 cm length by 0.1 cm width by 0.5 cm depth were constructed in 2% UltraPure Agarose (Invitrogen, Carlsband, CA, 16500-100) and high density 4:1 mixtures of 720,000 NHDF-Ad cells and 180,000 HAMECs were pipetted into the troughs of the agarose mold. Cells were then cultured in a 2:1 mixture of FGM-2 and EGM-2 for 3 days. Implants were either collected in Dulbecco's Phosphate Buffered Saline for use in surgical implantation or collected and fixed in 4% paraformaldehyde for histology. Fibroblast-only spheroids (FOS) were constructed similarly with 900,000 NHDF-Ad and no HAMECs. Silicone fragments of rectangular box dimensions of 0.6 cm by 0.1 cm by 0.1 cm (to match the eventual dimensions of the cell-based rods) were autoclaved and stored in DPBS in preparation for implantation.

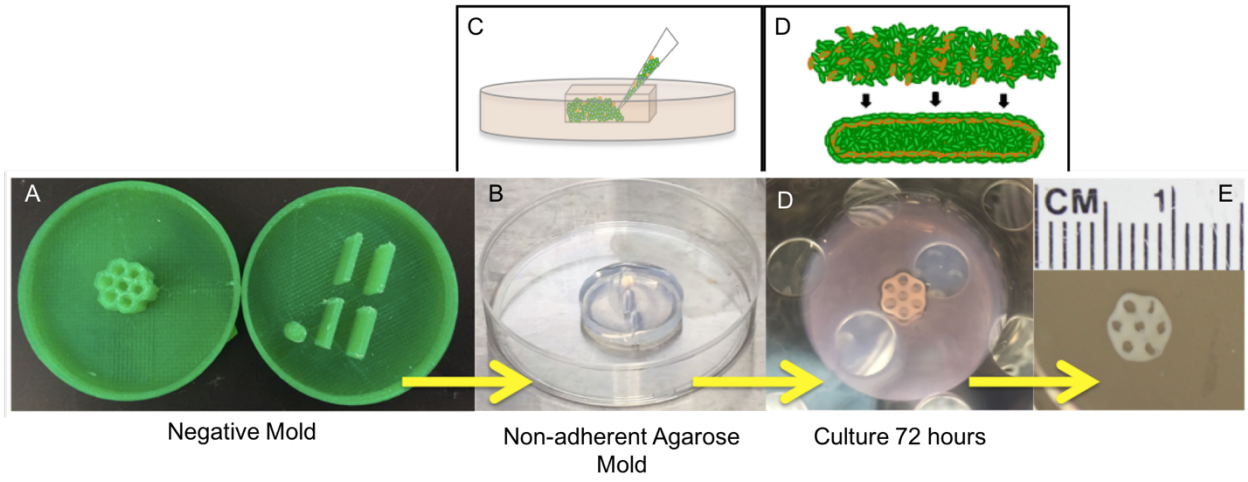

Figure 3.7. SPEC Formation Process. (A) A negative mold of the desired tissue shape is created using computer-aided design software and a MakerBot Replicator 3D printer. (B) The non-adherent agarose mold is generated by placing the molten agarose around the negative stamp. (C) Cells are seeded into the troughs, and incubated for three days. (D) During their incubation, cells undergo cellular self-assembly to form a three-dimensional tissue (E).

Immunohistochemistry Analysis of SPEC

Tissue sections were fixed in 4% paraformaldehyde solution for thirty minutes and subjected to hematoxylin and eosin staining, direct or indirect immunofluorescence labeling. Tissue sections were directly labeled with Hoescht 33342 nuclear stain (Molecular Probes, 1:10,000), and Alexa Fluor™ phalloidin 488 (ThermoFisher Scientific A12379, 1:500) for F-actin. Selected sections were stained with primary antibodies to von Willebrand Factor (Abcam, Catalog# ab6994, 1:1000), CD31 (Abcam ab28364, 1:50), human CD31 (monoclonal antibody) (R&D Systems BBA7, 1:25), smooth muscle actin (ThermoFisher Scientific PA5-19465, 1:1000). Primary antibodies were fluorescently tagged with the secondary antibodies Alexa Fluor™ goat anti-mouse 488, goat anti-rabbit 546, goat anti-mouse 546, and goat anti-rabbit 633 (ThermoFisher Scientific, A-11001,11035,11030,21070, 1:500). Sections were mounted on Colormark Plus microscope slides in Prolong Gold antifade reagent (Molecular probes P36934).

Western Blot Analysis

SPECs and FOS were collected after 1, 2, and 3 days of culture in 2% linear agarose molds as previously described. Samples were snap frozen, and mechanically homogenized in RIPA lysis buffer with protease inhibitor cocktail. Samples were maintained in constant agitation for 2h at 4°C, centrifugated for 20 min at 16,000 g at 4°C. Supernatant was stored in fresh tube at -20°C. Pierce™ BCA Protein Assay kit (Thermofisher Scientific 23227) was used to estimate protein concentration for samples as per manufacturer's instructions. Prior to gel electrophoresis, samples were diluted in RIPA buffer to attain 20 ug of protein in 20 uL solution, and further diluted 1:1 in 2x

Laemmli Sample buffer to attain 40 uL loading volumes. Samples were loaded onto Any kD™ Mini-Protean® TGX™ Precast Protein Gels. Following protein separation and overnight transfer onto PVDF membranes, western blots were performed using antibodies towards GAPDH (loading control) (CalBioChem CB1001, 1:1000), VEGFR2 (Abcam ab39256, 1:900), VE-Cadherin (ThermoFisher Scientific 36-1900, 1:250), vWF (Abcam, ab6994, 1:500), and DLL4 (Abcam ab7280, 1:1000).

Endothelial Cell Migration out of the SPEC in vitro

To investigate whether the SPEC could promote vascularization, we looked at the behavior of the embedded endothelial cells when placed in an acellular environment. Endothelial cells were tagged with GFP following the protocol. In this study, the SPEC was placed in the center of a well of a cell culture dish and monitored using the LionHeartFX Live cell imager (Biotek) over 7 days (**Figure 3.8**).

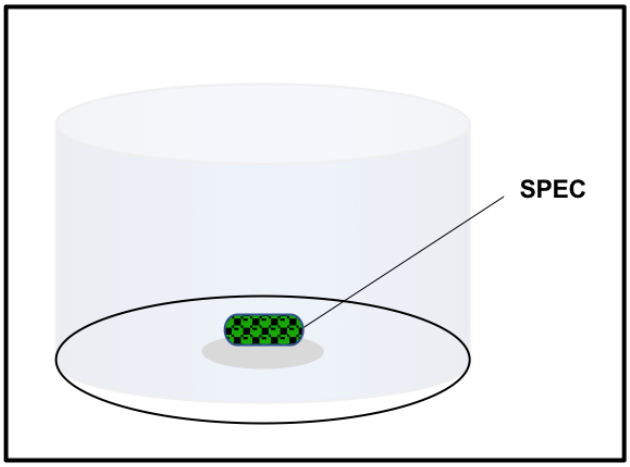

Figure 3.8. Experimental setup for determining rate of endothelial cell migration out of the SPEC into an acellular environment.

Microscopy and Quantitative Analysis of Endothelial Cord Organization

Confocal images were acquired using Leica TCS SP5 AOBS Confocal Microscope system (Leica Microsystems Inc., Buffalo Grove, IL) and collected as average projected z-stacks at 20x and 40x magnifications. Stitching was performed using LAS AF v2.6.3 Build 8173 and encompassed the entire visible cross section of each implant. Images were auto-enhanced and analyzed using ImageJ (NIH, Bethesda, MD). To analyze endothelial cord organization, stitched 40x (512x512) confocal images of sections stained with antibodies for vWF and CD31 were segmented as follows. Average projected images (10um depth) were auto-thresholded in ImageJ (Otsu auto threshold; 29), and binarized. Perimeter of the implants and endothelial capsule around implants were drawn freehand. Binary images were used to calculate microvessel area fractions of the implant. Binary images were skeletonized using an ImageJ plugin, provided by Arganda-Carreras *et al*, with branches pruned by lowest intensity voxel (30). Resulting images was used to calculate number of junctions and vessel branch lengths.

Animal Model Development

Animal procedures were conducted following the approval by Institutional Care and Animal Use Committee (IACUC) of the Medical University of South Carolina. Fifty-four Sprague Dawley rats (Charles River Labs, Wilmington, MA) were divided into three groups: SPECs (n=15), FOS (n=15), and silicone implants (n=15). Nine rats were set aside for sham surgeries. Surgeries were performed as described by Calder, et al. Implants were placed in submuscular pocket, with the long axis oriented parallel to the hind limb running proximal to distal. Five rats within each implant group were sacrificed at 6hr, 12hr, and 24 hours with muscle excised from the left hind limb *en bloc* with

implant or sham surgery, placed in O.C.T. Compound (Tissue-Tek 4853, Torrance, CA) and frozen at −80℃ for cryosectioning. Muscle from the right hind limb was harvested for comparison.

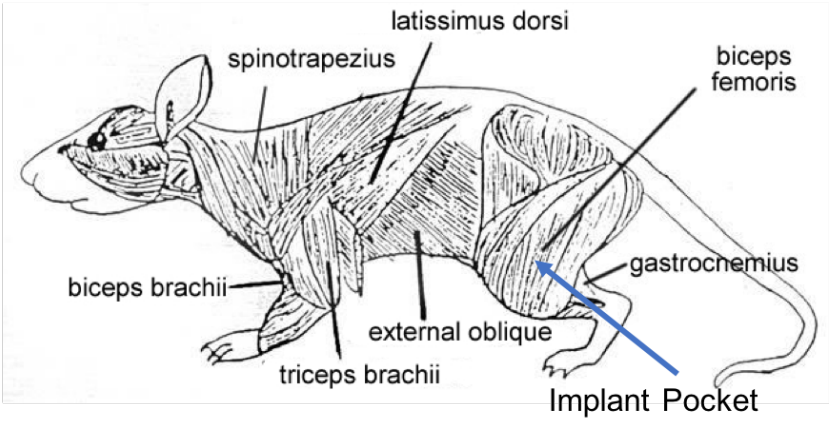

Figure 3.9. Schematic of animal model and where SPEC will be implanted.

Statistical Analysis

Statistical Analysis was performed using IBM SPSS for Windows Version 24.0 (Released 2017, Chicago, SPSS Inc). Levene's test for homogeneity of variance was used to determine equality of variances (α=0.05). For data with equal variance between groups, One-way ANOVA was performed with post hoc application of Bonferroni's t test used to compare microvessel density, degree of penetrance of vessels, and branching density among the three implant types at each time point. For data with unequal variances, Welch's one-way ANOVA was performed with Dunnett T3 post-hoc corrections.

Scalability of the SPEC Technology

The most important part of developing cellular technologies for tissue engineering, is the feasibility of scaling these constructs to physiologically-relevant sized tissues. To assess

the possibility of scaling this technology to larger, more complex geometries, we created a honeycomb structure consisting of the cells equivalent to nine SPECs, including 6.48 million NHDFs and 1.6 million HAMECs.

3.5 RESULTS

In vitro Analysis of Scaffold-free Prevascularized Endothelial-fibroblast Constructs

When we analyzed the SPECs *in vitro,* we observed a high abundance of primary vascular networks, indicated by CD31. The minimum requirements for primary network formation are endothelial cells and synthetic cells, like fibroblasts, that together secrete extracellular matrix. As indicated here by CD31 there are dense endothelial networks within these scaffold-free constructs, surrounded by extracellular matrix, indicated by Phalloidin staining for F-actin (**Figure 3.10**).

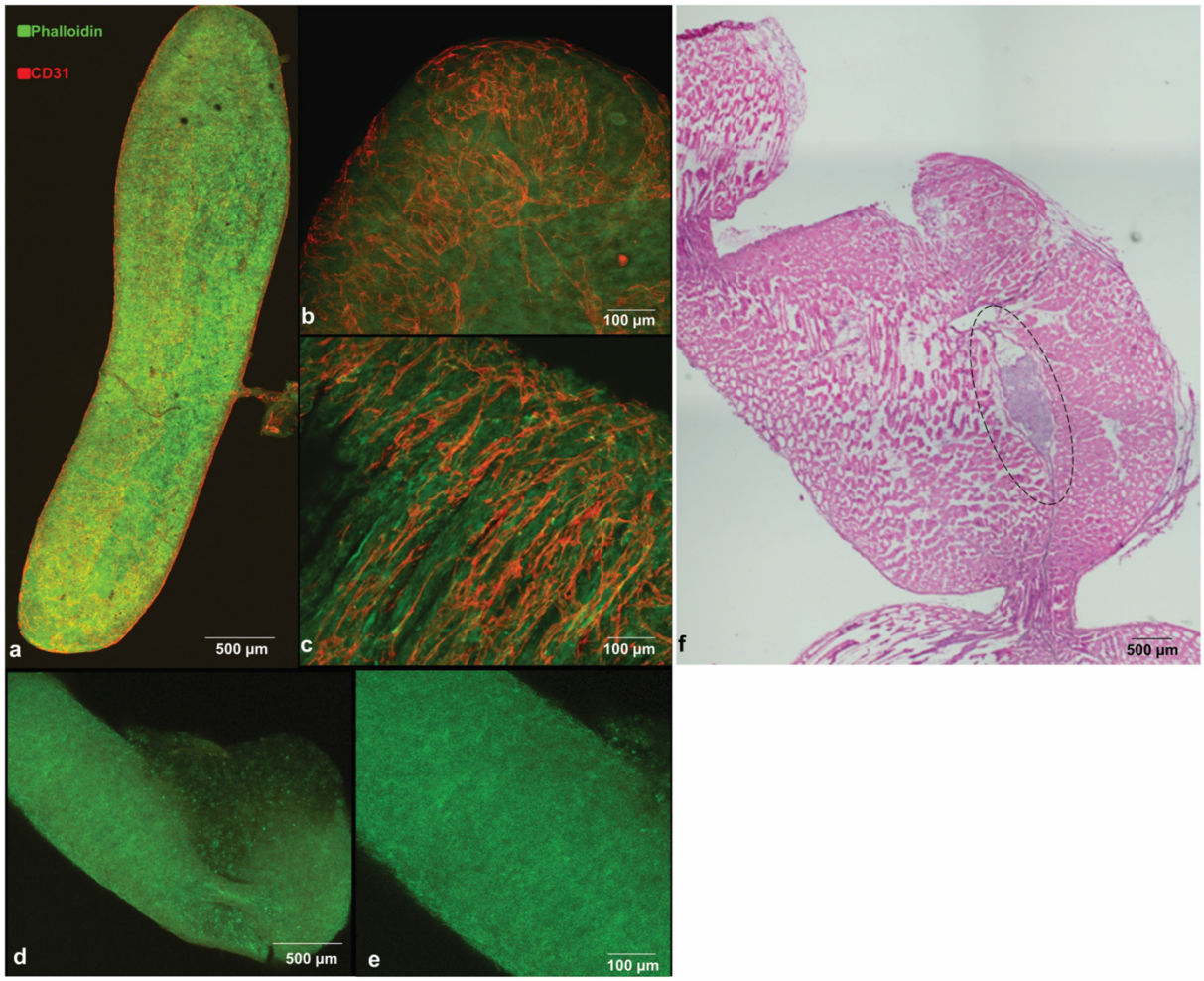

Figure 3.10. (a-c) Whole-mount immunofluorescence image of rod-shaped scaffold free prevascular endothelial fibroblast construct (SPEC) liberated from 2% agarose mold. F-actin fibers present in fibroblasts labelled with Phalloidin 488 (green) represent the stromal components of the implant, and CD31-labeled structures (red) represent capillary-like cords of endothelial cells. (d,e) Whole-mount immunofluorescence images of rod-shaped fibroblast-only spheroids (FOS) similarly presented with F-actin fibers in fibroblasts labelled with Phalloidin 488 (green). However, these constructs lack presence of CD31-labeled structures (red) (f) Light microscopy images of Hematoxylin and Eosin stained rat hind limb tissue sections (10 µm) containing cross section of implanted SPEC (encircled) between vastus lateralis and biceps femoris muscles. Fig adapted from Pattanaik, S., Dennis, SG, et.al. (in submission), 2018.

Rate of Endothelial Cell Migration out of the SPEC in vitro

A time-series image of GFP-tagged HAMECs within the SPECs placed on a tissue culture plate demonstrated a high degree of motility of the endothelial cells following

three days of culture, with some cells tracked as traveling over 400 µm in distance within a 24h time series (**Figure 3.11**).

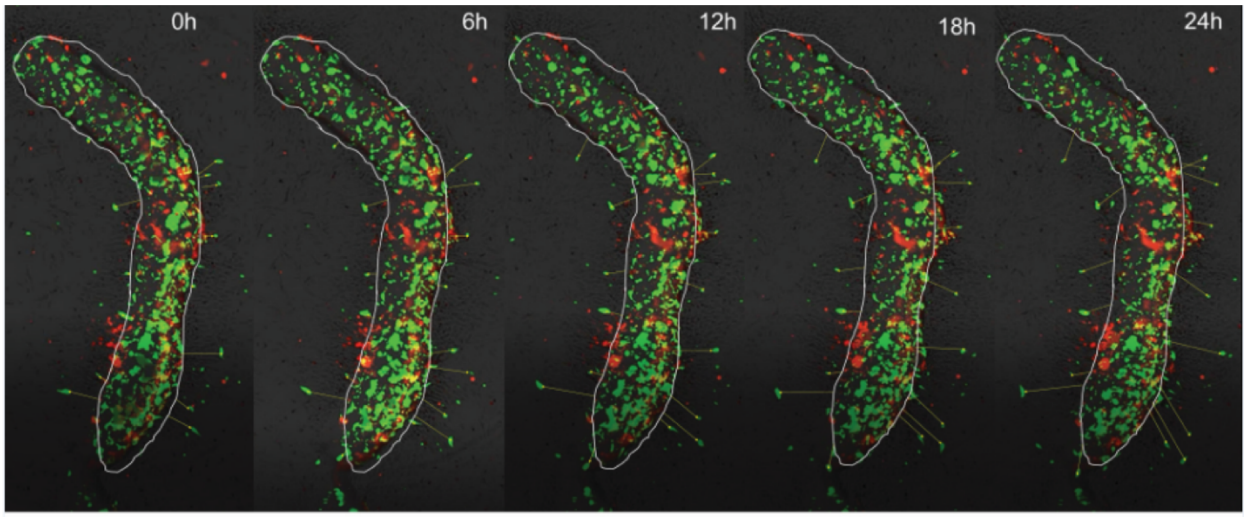

Average 24 hr Displacement of HAMECs	247 µm
Range	62-494 µm

Figure 3.11. Endothelial Migration out of the SPEC was recorded to be ~250um per day. Rate was determined by tracking GFP-transduced HAMECs over the course of 24 hours using the LionHeartFX Live Cell Imager (Biotek).

Western Blot Analysis

Prior to implantation, the SPECs presented with vWF, VEGFR2 and VE-cadherin as indicated by **(FIGURE 3.12)**. Control FOS implants displayed negligible levels of these vascular markers. Western blotting for DLL4, a marker of endothelial tip cell phenotype showed increased levels at days 1 and 2 of SPEC incubation but decrease by day 3 compared to FOS controls.

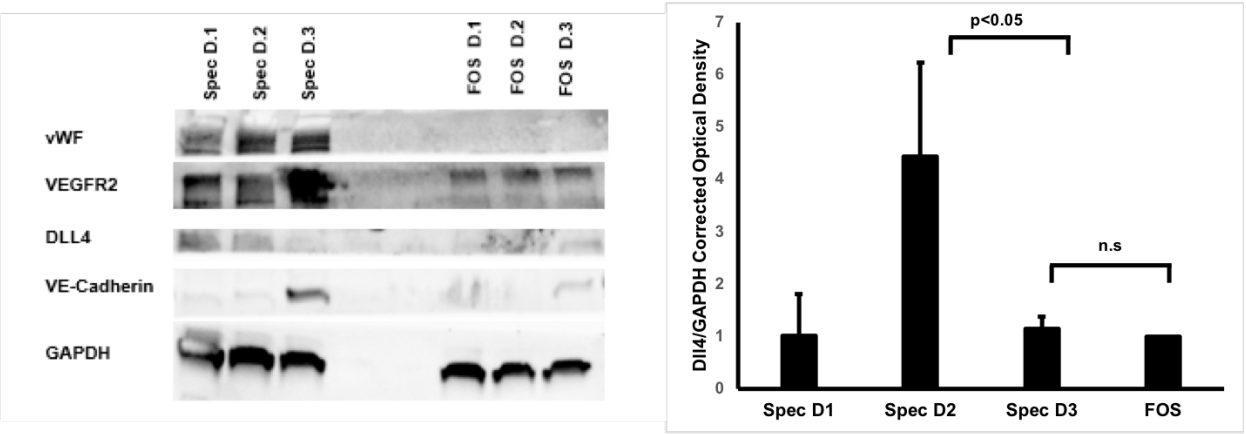

Figure 3.12. Western Blot analysis of SPEC during formation. Interestingly, expression of DLL4, a tip cell phenotype, was highest at day 2 during formation. This indicates the SPEC may have the highest angiogenic potential at this time point during formation.

Quantitative Analysis of Endothelial Cord Organization

Implant vascular structures (CD31 or vWF+) were segmented based on immunofluorescent images of tissue cross sections (10 μm depth) containing the entire implant cross section as well as an intact muscle/implant interface (**Figure 3.13A**). Endothelial structures in direct connection with this interface and the endothelial capsule surrounding the implant were segmented separately (green) from the vascular structures found within the interior of the implants (yellow). Total microvessel area fraction, or the percentage of the implant cross sectional area containing vascular elements, was calculated for each implant, with comparisons made between implant types at the 6h, 12h, an 24h time points (**Figure 3.13B**). Microvessel area fraction excluding the endothelial capsule at the muscle/implant interface was calculated for each implant (**Figure 3.13C**). The fraction of endothelial cords that penetrate the implant interior was calculated by dividing the length of the cords found excluding the capsule vessels by the total length of the vascular network (**Figure 3.13D**). This fraction is a surrogate marker

of the invasiveness of the vessels within and surrounding each implant within the host. Junction density was calculated as the number of vessel branch points found per um^2 of the implant cross sectional area (**Figure 3.13E-F**). Similarly branching density was calculated as the number of branches per um^2. These two metrics assess the branching complexity of the developing vascular networks in each implant type across time. Microvessel area, junction density, and branch density of SPECs remain significantly elevated compared to other implants at all time points. Fibroblast spheroids demonstrated the most growth in terms of microvessel area and penetrating tubule fraction between 12 and 24h with branch density resembling the SPECs at 24h.

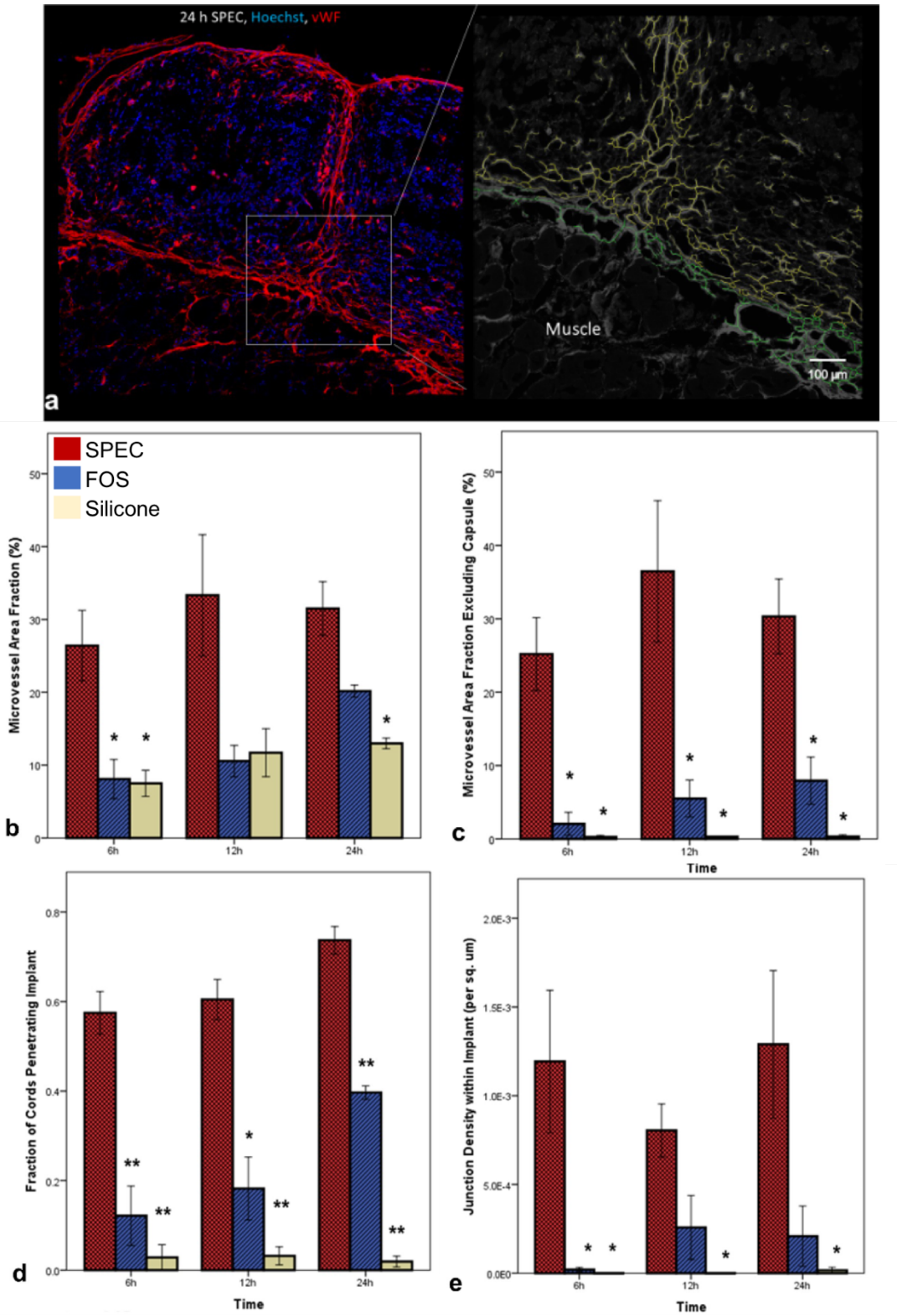

Figure 3.13. Assessment of vascular structures within implanted constructs. (A) Segmented tissue cross-section. (B) Microvessel area fraction. (C) Microvessel Area Fraction Excluding Capsule as a percent. (D) Fraction of cords penetrating implant. (E) Junction density within implant.

Assessment of Short-term SPEC Implants (<24 hours)

All three implant types developed a CD31 and vWF-positive capsule as early as 6h post-implantation, indicating early endothelialization of the host-implant interface (**Figure 3.14)**. The SPECs showed this capsule interdigitating with internal vascular elements at 6h; however, neither the FOS, nor the silicone showed endothelial cords within the implant interior at the 6h time point. By 12h, the SPECs displayed larger vessel-like bands composed of smaller cords penetrating through the implants, some of which bisected the implants (**Figure 3.14**). By 24h, many small lumen-like structures were present at the periphery of the implant connecting with the thicker endothelial capsules (**Figure 3.14**).

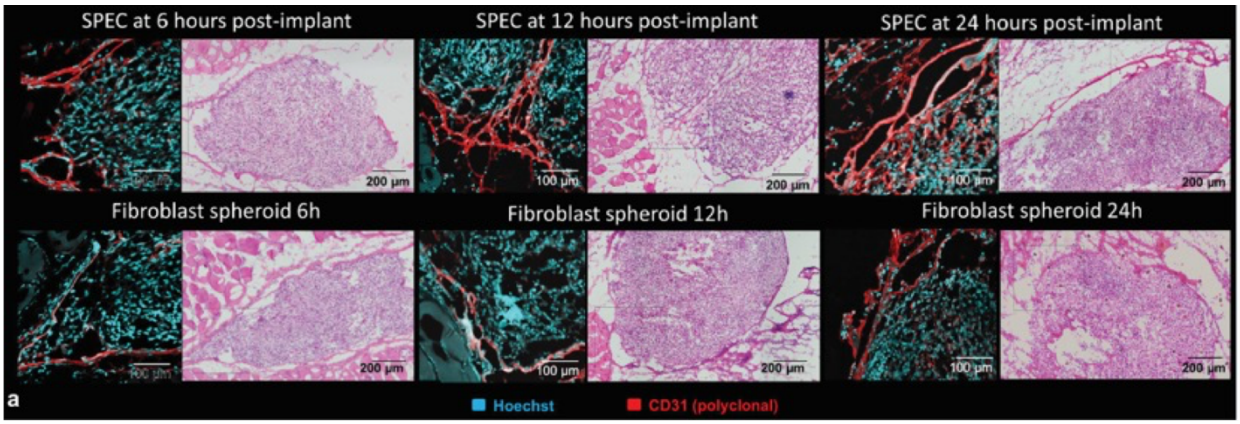

Figure 3.14. Endothelial reorganization within implants was imaged through immunofluorescence imaging with Hoechst nuclear stain (Cyan) and anti-CD31 antibody stain for endothelial cells (Red). A capsule-like layer of endothelial cells surrounds both construct types at 6h. The internal endothelial structures in the SPEC interdigitate with this capsule, resulting in a lacy layer of cords. By 12h, coalesced bands of endothelial cords penetrate SPEC interior, while fibroblast spheroids still lack internal endothelial structures. At 24h, both fibroblast spheroids and SPECs are invaded by endothelial cords, with SPECs containing a more complex branching structure at the implant/muscle interface.

Mural Cell Involvement

Mural cells improve vessel stability and reduce vessel turnover. They are recruited later in the vascularization pipeline, and stabilize vessels by forming connections with the endothelial cells toward the periphery of the vessels. At the 6 hour time point, there was very low mural cell involvement. However, by 12 hours there was a significant increase in mural cell recruitment indicated by the alpha-smooth muscle actin stain (yellow) in **Figure 3.15**.

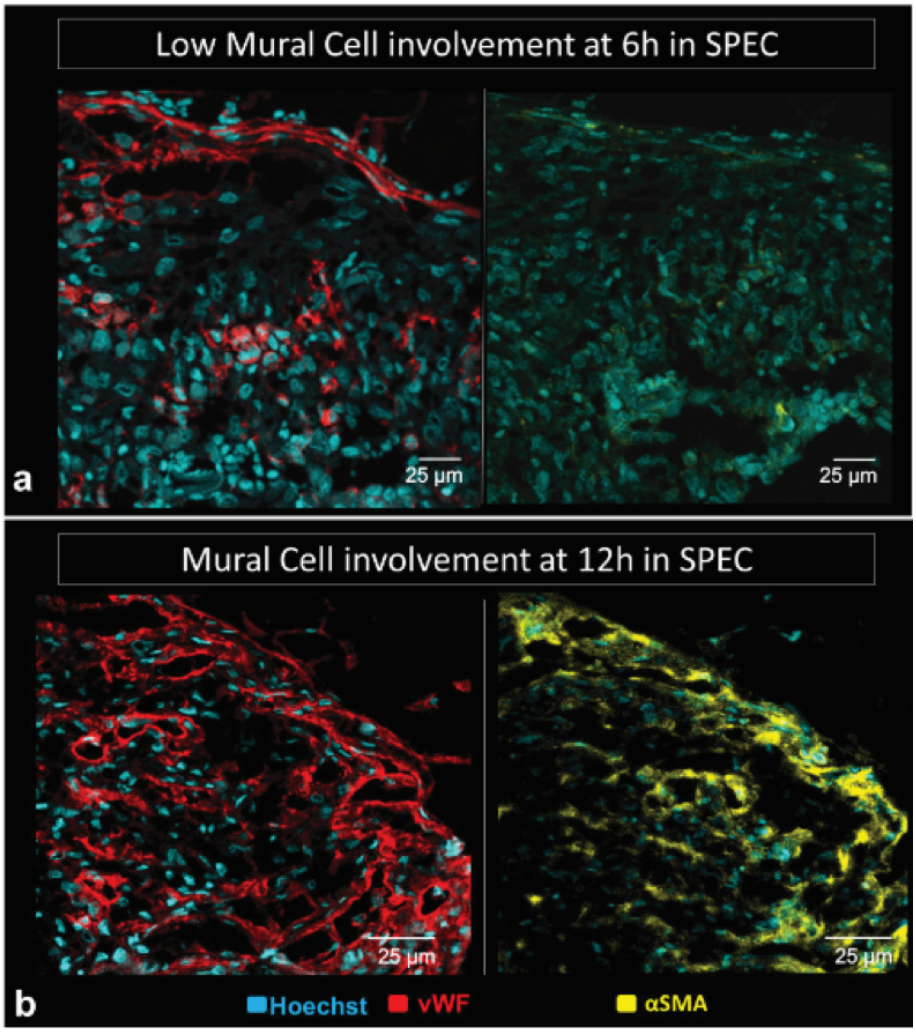

Figure 3.15. Mural Cell Involvement at 6 and 12 hours post-implantation. Mural cells indicated by alpha-smooth muscle actin (yellow).

Lumen Formation Within Implants

Implanted cells were labeled with CellTracker Blue to distinguish them from the host. Cd31+structures (red) with apparent lumens are visible within implanted SPEC cells labeled with Cell Tracker (Blue) at 12 hrs post-implantation (**Figure 3.16**). These lumens were not present in the FOS or the silicone implants.

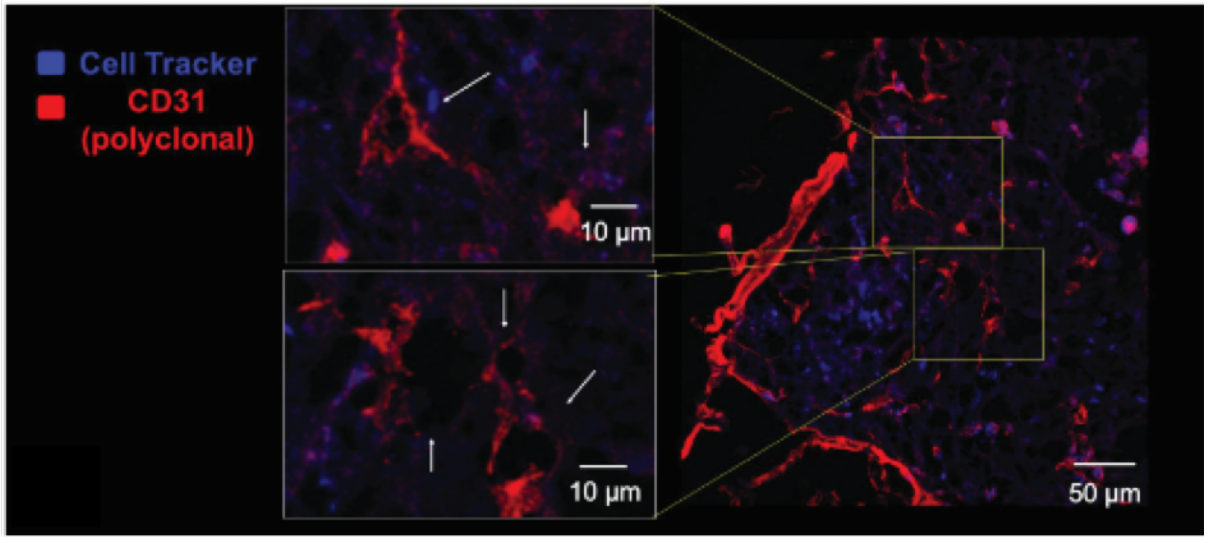

Figure 3.16. Lumen structures were present within the SPEC implants at 12-hours post-implantation, as indicated by polyclonal-CD31 (red).

Contributions to the Formed Vascular Networks

Monoclonal anti-human CD31 antibody stain (red) and polyclonal anti-vWF antibody stain (green) were used to distinguish implant-derived networks from the host to determine the contributions of each to the vasculature seen **(Figure 3.17**). Host-derived vascular networks only stain for anti-vWF, while implant-provided vasculature is tagged by a colocalization resulting in a yellow label. The internal vasculature of the SPECs was largely implant derived, as indicated by the monoclonal human CD31 stain (**Figure 3.17A**). By contrast, the endothelial capsule components in the SPEC and FOS only

express polyclonal vWF, which labels both rat and human endothelial cells, indicating derivation from the rat hosts. Vessels in control sections of muscle without a surgical pocket similarly solely express vWF in their lumens (**Figure 3.17B**). Host-derived vascular networks only stain for anti-vWF stain and are visible at the external capsule surrounding the SPECs and in vessels distal to the implant site in the opposite host hind limb muscle (**Figure 3.17C**).

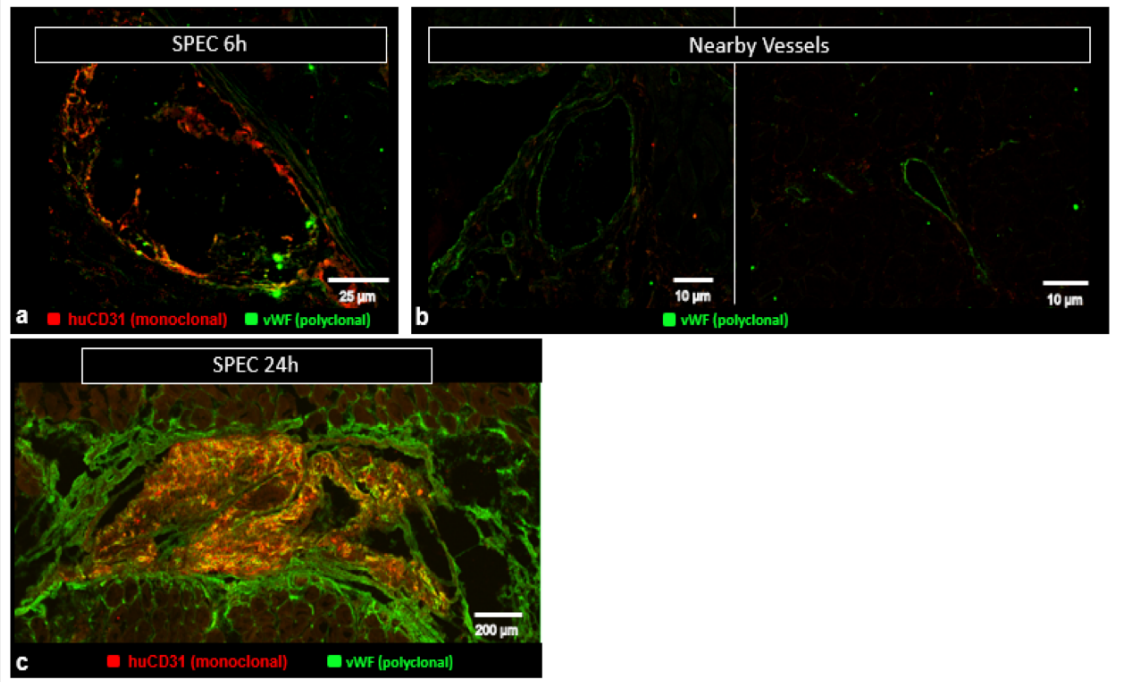

Figure 3.17. (a-c). Monoclonal anti-human CD31 antibody stain (red) and polyclonal anti-vWF antibody stain (green) colocalize in implant-derived human endothelial structures (yellow). These structures are limited to the interior component of the implanted SPECs at both 6h and 24h. Host-derived vascular networks only stain for anti-vWF stain and are visible at the external capsule surrounding the SPECs and in vessels distal to the implant site in the opposite host hind limb muscle.

Additionally, at 12-hours post-implantation, penetrating host-derived cords within the SPECs colocalized with the implant-derived components, indicated by cell tracker (blue) (**Figure 3.18**), indicating implant contribution to these endothelial structures.

Invading von Willebrand factor+ endothelial branches from the endothelial capsule inosculate with cell tracker positive endothelial cords (magenta) indicating both host and implant contribution to SPEC vascular network.

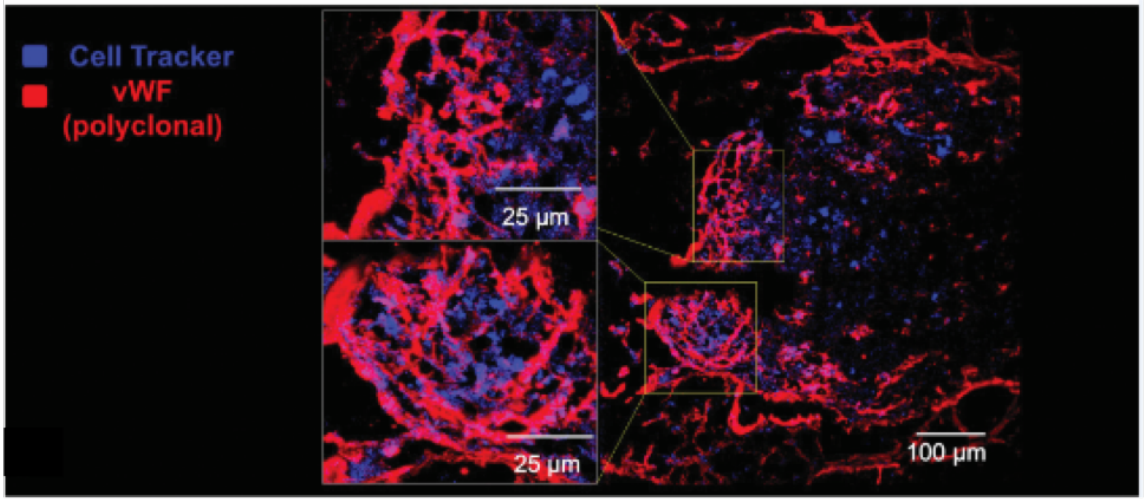

Figure 3.18. At 12-hours post-implantation, invading host endothelial branches (vWF, red) inosculate with Cell Tracker+ cells (blue) indicative of both host and implant contribution to vascular network (magenta).

Assessment of Long-term SPEC Implants (72 hours)

Implanted constructs show early signs of anastomosis in a rat hind limb muscle. Within 3 days, there was evidence of red blood cell perfusion in the implants with vascular structures that persisted out to 2 weeks (25). The SPECs were implanted in hind limb defects, and excitingly by three days post-implantation neighboring satellite cells had been activated and were migrating towards the muscle defect site (**Figure 3.19**).

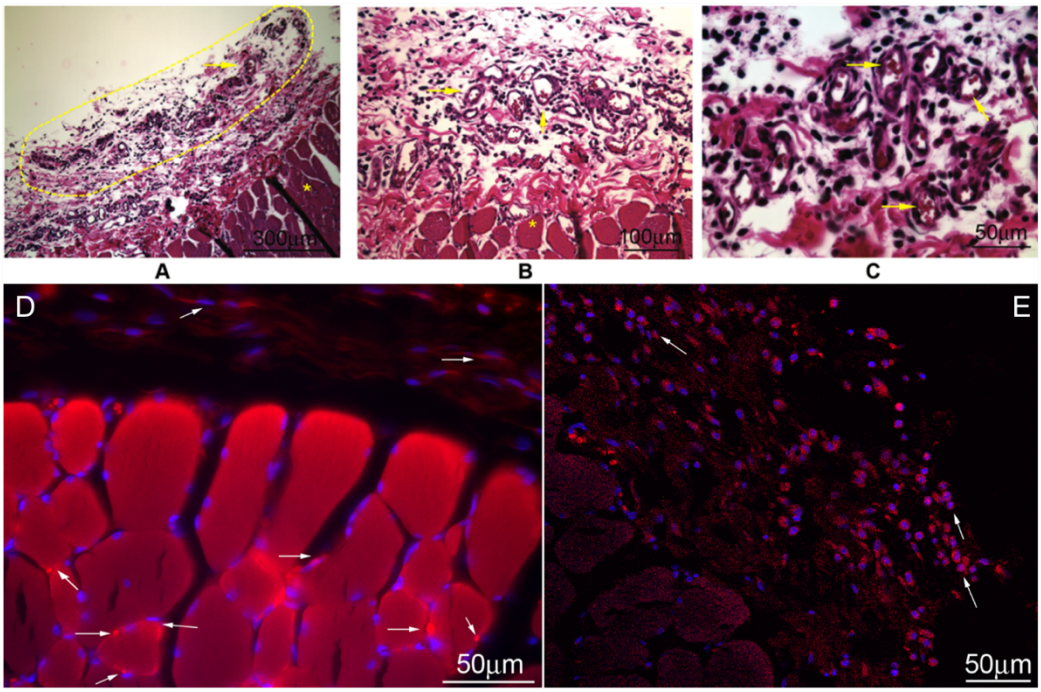

Figure 3.19. (A-C) Light microscopic images of hematoxylin-eosin–stained tissue sections of a prevascular tissue xenograft 3 days after implantation in an immune-competent rat. Xenograft is outlined with dashed yellow line (A); host muscle is oriented to the bottom region of the images (yellow asterisks). Presence of red blood cells in the lumens of vessels (yellow arrows) indicates the xenograft anastomosed to the host vasculature. Image in C shows a higher magnification region from the middle of the xenograft, distal from the implant-host border zone. (A) 10X;(B) 20X;(C) 40X**.** (D-E) Immunofluorescence images of tissue sections of a prevascular tissue xenograft 3 days after implantation in a hind limb muscle defect in an immune-competent rat showing activated satellite cells migrating into the xenograft. (D) Pax-7 (red), Hoechst (blue); 20 . (E) MyoD (red), Hoechst (blue); 20 confocal image projection. Arrows indicate activated satellite cells (D) and nascent myotubes (E). Fig adapted from ref Czajka, C.A., et. al. *Ann Plastic Surg* **74**(3):371-375, (2015).

Applications of the SPEC Technology

To investigate the potential for creating tissue-specific SPECs that are function as the tissue they are designed to be, Rhett, JM, et. al. incorporated islet cells to see if a prevascularized bioartificial pancreas could be created (28). Immunoconfocal microscopy images demonstrated the islet-containing constructs expressed insulin and retained the microvascular network seen in constructs without islets (**Figure 3.20**). Note the dense,

web-like pattern of endothelial cells in both constructs, indicating a robust vascular network. Importantly, the vascular network surrounds the embedded islets. These results indicate that the prevascularized bioartificial pancreas is a potential tool for improving long-term survival of implanted islet cells *in vivo*.

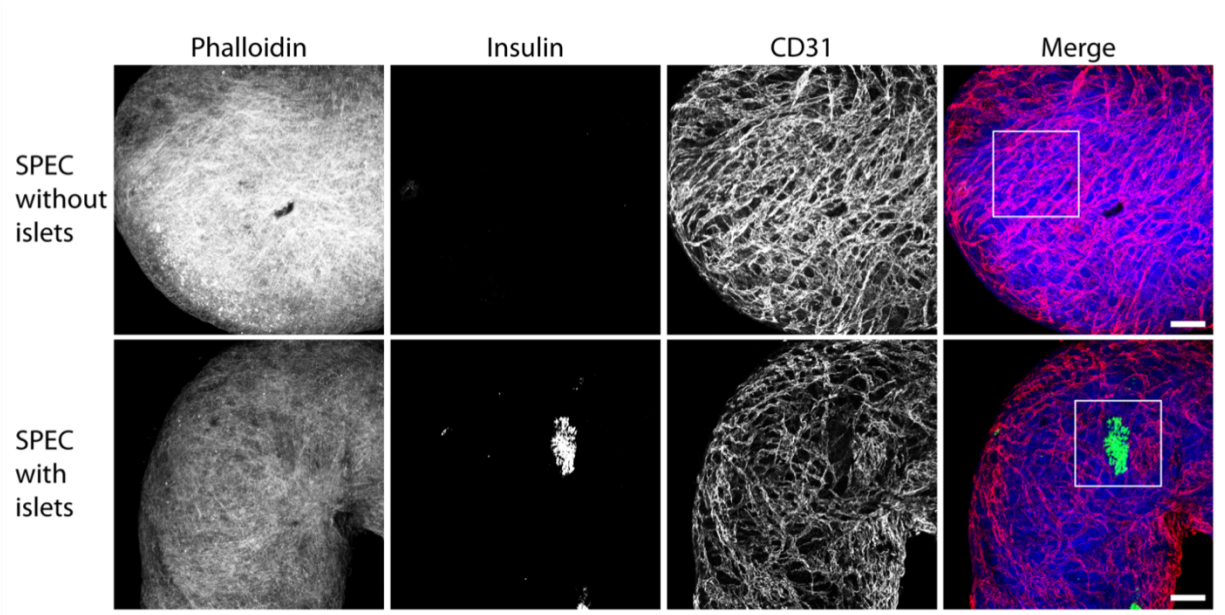

Figure 3.20. Prevascularized Bioartificial Pancreas. Incorporation of islet cells in the SPECs did not alter vascular network formation. SPECs with and without islets were generated, fixed, and whole-mount-labeled for actin (phalloidin, blue), islets (insulin, green), and endothelial cells (CD31, red). The images are maximum projections of z-stacks acquired by confocal microscopy under 20x magnification. Scale bars represent 100um.

As another application, we investigated the possibility of creating prevascularized renal tissue. Murine kidneys were micro-dissected and isolated for living corticomedullary renal segments (27). These segments were capable of rapid incorporation into the SPEC and form intact structures (**Figure 3.21A**). The constructs retained their prevascularized network shown by labeling with von Willebrand Factor for endothelial cells (**Figure 3.21E**). However, unlike in the bioartificial pancreas, the prevascular network did not appear to invade the renal cellular material. Renal epithelial cells were labeled with

Cytokeratin-18 (green, **Figure 3.21B**). The constructs were incubated with FITC-labeled albumin (gray in **Figure 3.21C**) to test *in vitro* renal functionality. While there was resident albumin found away from the segments of embedded renal tissue, there are "hot spots" in the area of the renal tubular epithelial cells, which are known to take up albumin that traverses intra-luminally. Therefore, there was successful albumin reuptake in the renal segment SPEC construct.

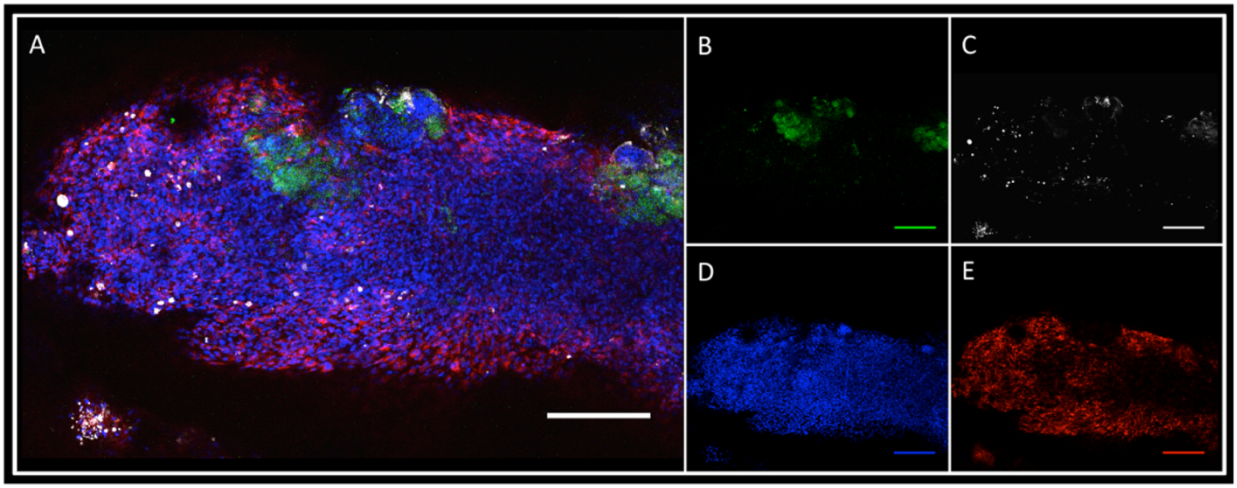

Figure 3.21. Tissue-engineered Scaffold-free Renal Segment Construct. (A) Merged image showing incorporation of renal segments into the SPEC. (B) Cytokeratin-18-positive renal tubular epithelial cells (green). (C) FITC-labeled albumin. (D) Hoescht stain for nuclei. (E) von-Willebrand Factor (vWF) positively highlighting the prevascular network. 10X images, scale bar = 200um.

Scalability of the SPEC Technology

The most important part of developing cellular technologies for tissue engineering, is the feasibility of scaling these constructs to physiologically-relevant sized tissues. Here, we have demonstrated the SPEC can be scaled up into larger, more complex geometries, and the use of the bioprinter, described in chapter 2, to fabricate these constructs could allow the creation of much larger and even more complex constructs, including patient-image derived implants.

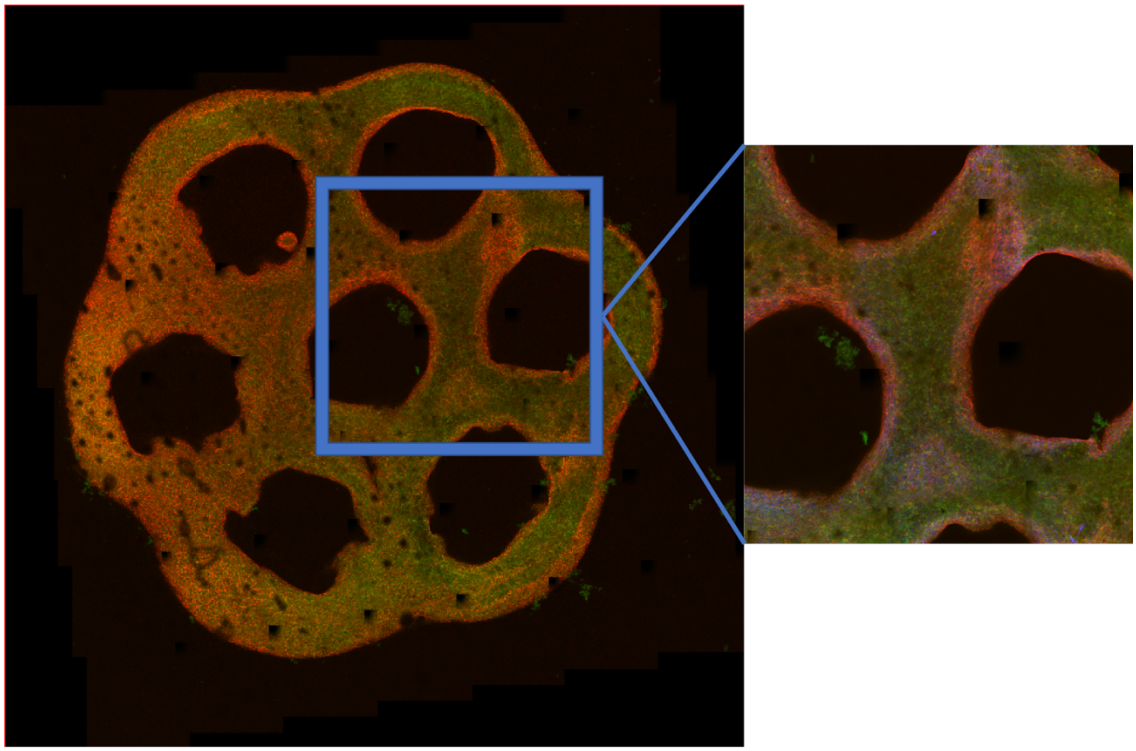

Figure 3.22. Potential for Scalability of the SPEC. A honeycomb structure was formed around a non-adherent agarose mold, and retained the dense endothelial cord networks (CD31, red), as well as extracellular matrix production (Phalloidin staining for F-actin, green).

Additionally, in preliminary work investigating the effects of perfusion on SPECs during their formation *in vitro* we found that the SPECs were able to readily fuse together to form larger constructs (**Figure 3.23**), which retained their vascular networks (CD31, red) and extracellular matrix components. This offers another potential technique for expanding this technology to the much-desired larger implants required for tackling the organ deficiency crisis.

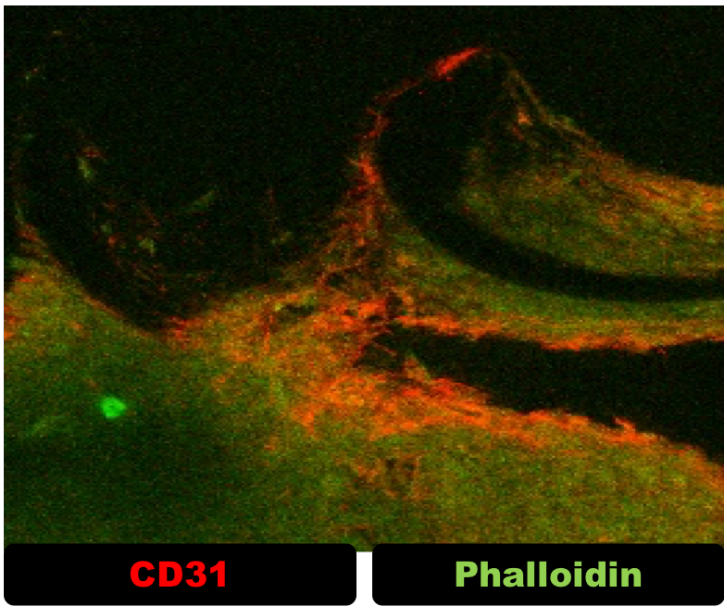

Figure 3.23. SPECs fuse together under perfusion, and retain endothelial networks (CD31, red), as well as the extracellular components required for stability (Phalloidin staining for F-actin, green).

3.6 DISCUSSION

The timeline of vascular events (**Figure 3.2**) immediately following implantation of prevascular tissue is critical to evaluating the success of implant technology. The observation windows selected in this study were designed to dissect the components of endothelial organization, cord sprouting, anastomosis, network remodeling, lumen formation and, ultimately, vessel maturation that occurred early in the *in vitro* development of our implant and shortly following implantation. The 6-12h post-implantation window is particularly important as it contains the time points associated with a peak in markers of hypoxic stress found within autologous full-thickness muscle flap transplants in prior studies by our laboratory (9).

In vitro SPEC development was consistent with non-random organization of a proangiogenic vascular network

The endothelial cord formation within the SPECs is a non-random process, with the initial dispersed endothelial cells coalescing into cords throughout the 3-day incubation period. This migration stands contrary to the popular theory of cellular behavior termed the differential adhesion hypothesis (32). If the rearrangement was entirely driven by passive cell adhesion behavior rather than active vascular development processes, a single interface between endothelial cells within the core and fibroblasts on the periphery would be observed. This behavior would optimize interfacial energy based on cell-type specific expression of adhesion molecules such as cadherins (33). Further evidence of active vessel formation within the implant is provided by western blot data, through expression of vascular markers such as VEGFR2, VE-cadherin, and vWF. Dll4 expression in implants is consistent with angiogenic and anastomotic potential of endothelial cells as reported in literature (**Figure 3.12**; 34-35).

Early 6hr post-implantation period demonstrates rapidity of endothelial capsule formation around implants, and rapid inosculation of scaffold-free prevascular constructs to host

One of the major goals of vascular tissue engineering is near instantaneous perfusion of well-organized cords either by spontaneous *in vivo* inosculation or surgical anastomosis (1). While these constructs were not well perfused during the 24h observation time, endothelial structures extended continuously from the host to the interior of the SPEC implants within 6h, indicating rapid mobilization of endothelial cells

to and from the implant. Notably, the SPEC internal structures are derived from human endothelial cells (**Figure 3.17**), suggesting that this anastomotic network contains, at least in part, the preformed primitive network that was developed *in vitro*.

Additionally, the microvessel vascular area of the SPECs 6h post-implantation is 26±5% which is comparable to the vascular density of the implant prior to implantation and only approximately 1.2-fold lower than the average microvessel vascular area fraction throughout the 24h time point (**Figure 3.13**). The filamentous net-like primordial form of the network prior to implantation is preserved at 6h post-implantation, with a high branch point density of approximately $1.2x10^5$ per mm^2 implant tissue, resembling the pre-implantation average branching density of $1.12x10^5$ per mm^2. The FOS, on the other hand, show a significantly lower presence of branching endothelial structures within the implant stroma, with most of the 8 ± 3% microvessel area confined to the external capsule. As such, the fraction of the vascular area that includes internally penetrating tubules in the SPEC is 4.7-fold higher than the fraction within fibroblast-only spheroids.

The 6 to 12-hour window shows increase in microvessel area in fibroblast only spheroids and silicone implants but not in SPECs; SPECs show remodeling and fusion of existing branches

The 6-12-hour window is a period of remodeling in both the SPEC and FOS implant models. Notably, the band of host-derived endothelial structures around the implant appear to thicken with a small but significant increase of internally penetrating branches within some of the FOS. However, the mean microvessel area of the fibroblast

spheroids, including the capsular components, remains 3.2-fold lower than the SPEC implants and comparable to that of the silicone implants (**Figure 3.13**). In other words, the lack of an existing internal endothelial network in the FOS results in a 12-hour latency in vascular development of these implants compared to SPECs. The SPECs, on the other hand, maintain a nearly constant mean vascular area; however, there is a 1.5-fold decrease in junctions within the implant and a 2-fold decrease in junctions within the endothelial capsule. This may be attributed to increased condensation of endothelial branches to larger structures, an example of which is seen in (**Figure 3.14**), where a denser band of endothelial structures appears to pass through the center of the implant and lumen like structures begin to appear within the SPEC implant cross sections. This cohesion of existing endothelial cords to form larger multicellular structures is most consistent with formation of the early vascular tree during embryological vasculogenesis (36)**.**

Parity between SPEC and FOS angiogenic development by the 24-hour timepoint

By 24h, SPECs and FOS begin to resemble each other in terms of endothelial organization and mean vascular area, with a greater preponderance of penetrating endothelial cords in the fibroblast- only spheroids than at previous time points. The advantage in anastomosis provided by the SPECs, thus, seems to lessen at the 24h time point, as cords from the peripheral endothelial capsule appear to reach the center of the FOS. This rapid invasion of vessels in a previously avascular space is itself a surprising finding. Vascular network can invade on its own as a part of foreign body response, but

the process has been cited to take a few days to a week (1). The presence of a branching vascular architecture, however, still seems largely limited to the SPECs.

Evidence of maturation of SPECs at 12-24-hour without perfusion

In angiogenesis, maturation of vessels follows anastomosis and usually occurs concurrent with perfusion of vascular networks (37). However, in the absence of consistent perfusion, the SPECs show some indication of vessel maturation. Smooth-muscle actin presenting cells, representing mural, stabilizing cells such as pericytes around capillaries, or smooth muscle cells around larger arterioles and arteries, are recruited in the latter stages of angiogenesis, involving a careful interplay between basolateral elements of endothelial cells such as Tie-2, macrophages, and pericytes.[38, 39] The SPECs, which present with an apparently disorganized SMA+ cells at the early 6hr time points show SMA+ cells more fully organized around lumen like structures in the SPEC at the 12 and 24 hour timepoints (**Figure 3.15)**.

Conclusion

The SPECs retain a set of properties that have inherent therapeutic value when incorporated into replacement tissue technologies. SPEC spheroids can readily fuse to form larger spheroids in unconstrained nonadherent conditions and can reshape their cytoskeletal structures to assume patterns dictated by linear confinements such as agarose mold.[26] This scalability and shapeable nature, coupled with the primary cord networks of the SPECs makes them ideal analogues to a vascular stroma or artificial vascular bed that is inherent to the function of most tissues. The SPECs readily incorporate renal segments[27] and pancreatic islet cells[28], paving the way for rapidly vascularizable

artificial renal grafts and bioratifical pancreas. The incorporation of these other cell types leads to the creation of tissue-specific implants, and could be extended to a multitude of other tissue-types, as the SPEC serves as the foundation building block of most functional tissues.

As past studies have reported inosculation of prevascular implants at 2-5 days[40], vascularization dynamics in literature have not focused on early time points preceding a few days following implantation. Our study reveals that an earlier observation window informs us on the relative rapidity of endothelialization around cellular constructs and reveals that the crucial advantages to a prevascular network might be best seen within 6 to 12 hours of implantation. By this period, the groundwork for a vascular pedicle feeding the implants has already been laid, with evidence of reorganization towards a more mature host-implant vascular network. Vascular tissue engineering strategies that proceed from this point should promote lumen formation and patency of the existing vascular architecture.

Unmet Challenges of the SPEC Technology

When implanted SPECs and FOS were examined for cell death at 6-hours and 24-hours post-implantation, it was evident that the prevascular network in the SPEC did not alter the viability of implanted cells, as indicated by Tdt dUtp Nick-End Labeling Assay (TUNEL; green in **Figure 3.24A**) There was a significant increase in TUNEL+ cells between the 6 hour and 24 hour time points in both the SPEC and FOS implants compared to the surrounding rat host muscle (**Figure 3.24B**).

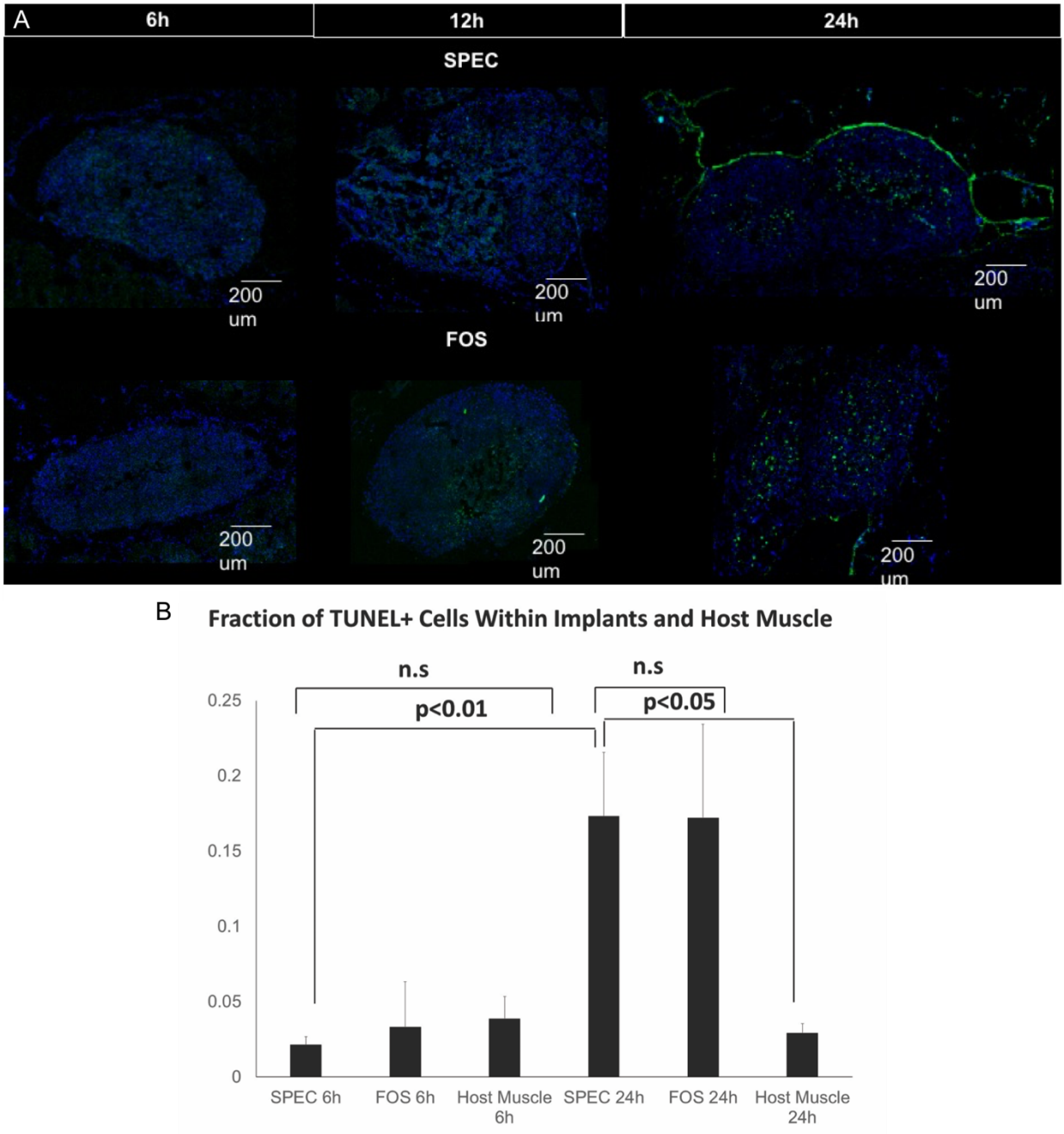

Figure 3.24. (A) SPEC and FOS cryosections (10um) harvested at 6, 12, 24h were stained with Tdt dUTP Nick-End Labeling Assay (green) and counterstained with Hoechst nuclear stain (blue). (B) A significant increase in TUNEL+ cells was observed between 6h and 24 h for FOS and SPEC implants (n=4, $p<0.01$) compared to the surrounding rat host muscle.

Additionally, while these implants get thoroughly perfused by 72-hours (**Figure 3.19A-C**), there was inconsistent red blood cell presence within the 24-hour window we were examining (**Figure 3.25**).

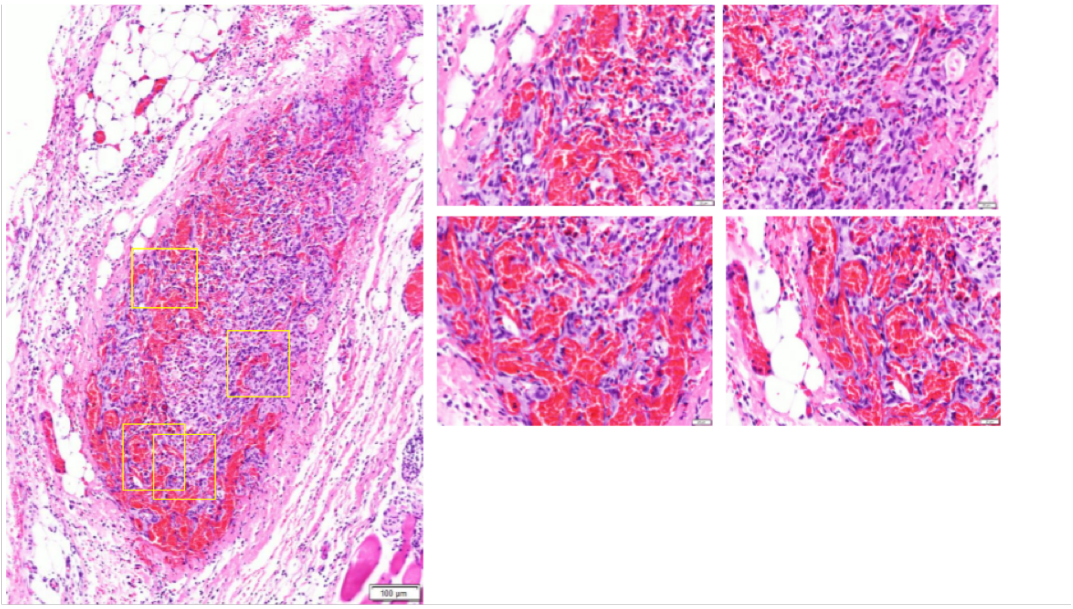

Figure 3.25. Red blood cell presence within implants at 24hours is inconsistent, indicating implants have not been thoroughly perfused by this time point.

The upregulation of DLL4-expression in SPECS at day 2 is consistent with increased vascularization of the implant; in contrast, the comparative downregulation at day 3 of incubation, coinciding with when the implant finishes resolving into a solid structure, is consistent with quiescence of the prevascular networks. This period of quiescence may contribute to the latency between anastomosis and *in vivo* tubulogenesis. While ideally anastomosis of prevascular implants should only involve inosculation of externally located cords to the nearby host vasculature, the need to ramp up the angiogenic machinery of the construct cells might delay further morphogenesis of these tubes and delay perfusion through the resulting networks. Therefore, further investigation

into how to drive the SPEC further down the vascularization pipeline should be done to see if these challenges can be met.

3.7 REFERENCES

1. Rouwkema, J. and A. Khademhosseini, *Vascularization and Angiogenesis in Tissue Engineering: Beyond Creating Static Networks.* Trends Biotechnol, 2016. **34**(9): p. 733-45.
2. Tanaka, Y., et al., *Generation of an autologous tissue (matrix) flap by combining an arteriovenous shunt loop with artificial skin in rats: preliminary report.* British Journal of Plastic Surgery, 2000. **53**(1): p. 51-57.
3. Lovett, M., et al., *Vascularization Strategies for Tissue Engineering.* Tissue Engineering. Part B, Reviews, 2009. **15**(3): p. 353-370.
4. Wang, Z., et al., *Rapid vascularization of tissue-engineered vascular grafts in vivo by endothelial cells in co-culture with smooth muscle cells.* Journal of Materials Science: Materials in Medicine, 2012. **23**(4): p. 1109-1117.
5. Czajka, C.A., et al., *Implanted scaffold-free prevascularized constructs promote tissue repair.* Ann Plast Surg, 2015. **74**(3): p. 371-5.
6. Stosich, M.S., et al., *Vascularized Adipose Tissue Grafts from Human Mesenchymal Stem Cells with Bioactive Cues and Microchannel Conduits.* Tissue engineering, 2007. **13**(12): p. 2881-2890.
7. Sun, X., W. Altalhi, and S.S. Nunes, *Vascularization strategies of engineered tissues and their application in cardiac regeneration.* Advanced Drug Delivery Reviews, 2016. **96**: p. 183-194.
8. van Amerongen, M.J., et al., *Neovascularization and vascular markers in a foreign body reaction to subcutaneously implanted degradable biomaterial in mice.* Angiogenesis, 2002. **5**(3): p. 173-80.
9. Propst, J.T., et al., *Focused in vivo genetic analysis of implanted engineered myofascial constructs.* J Invest Surg, 2009. **22**(1): p. 35-45.
10. Naderi, H., M.M. Matin, and A.R. Bahrami, *Review paper: Critical Issues in Tissue Engineering: Biomaterials, Cell Sources, Angiogenesis, and Drug Delivery Systems.* Journal of Biomaterials Applications, 2011. **26**(4): p. 383-417.
11. Song, D.H., et al., *Chapter 2: Grafts and Flaps*, in *Plastic Surgery: Essentials for Students*. 2012, American Society of Plastic Surgeons: Arlington Heights, IL. p. 9-15.
12. Laschke, M.W. and M.D. Menger, *Vascularization in tissue engineering: angiogenesis versus inosculation.* Eur Surg Res, 2012. **48**(2): p. 85-92.
13. Zarem, H.A., *The microcirculatory events within full-thickness skin allografts (homografts) in mice.* Surgery, 1969. **66**(2): p. 392-397.
14. Laschke, M.W., et al., *Improvement of vascularization of PLGA scaffolds by inosculation of in situ-preformed functional blood vessels with the host microvasculature.* Ann Surg, 2008. **248**(6): p. 939-48.

15. Daley, W.P., S.B. Peters, and M. Larsen, *Extracellular matrix dynamics in development and regenerative medicine.* Journal of Cell Science, 2008. **121**(3): p. 255-264.
16. Levenberg, S., et al., *Engineering vascularized skeletal muscle tissue.* Nat Biotech, 2005. **23**(7): p. 879-884.
17. Carmeliet, P., *Mechanisms of angiogenesis and arteriogenesis.* Nat Med, 2000. **6**(4): p. 389-395.
18. Tan, A.R. and C.T. Hung, *Concise Review: Mesenchymal Stem Cells for Functional Cartilage Tissue Engineering: Taking Cues from Chondrocyte-Based Constructs.* Stem Cells Transl Med, 2017. **6**(4): p. 1295-1303.
19. Tasso, R., et al., *Development of sarcomas in mice implanted with mesenchymal stem cells seeded onto bioscaffolds.* Carcinogenesis, 2009. **30**(1): p. 150-7.
20. Baiguera, S. and D. Ribatti, *Endothelialization approaches for viable engineered tissues.* Angiogenesis, 2013. **16**(1): p. 1-14.
21. Freiman, A., et al., *Adipose-derived endothelial and mesenchymal stem cells enhance vascular network formation on three-dimensional constructs in vitro.* Stem Cell Research & Therapy, 2016. **7**: p. 5.
22. Baldwin, J., et al., *In vitro pre-vascularisation of tissue-engineered constructs A co-culture perspective.* Vascular Cell, 2014. **6**: p. 13-13.
23. Czajka, C.A. and C.J. Drake, *Self-Assembly of Prevascular Tissues from Endothelial and Fibroblast Cells Under Scaffold-Free, Nonadherent Conditions.* Tissue Engineering. Part A, 2015. **21**(1-2): p. 277-287.
24. Rivron, N.C., et al., *Sonic Hedgehog-activated engineered blood vessels enhance bone tissue formation.* Proceedings of the National Academy of Sciences, 2012. **109**(12): p. 4413-4418.
25. Czajka, C.A., et al., *Implanted scaffold-free prevascularized constructs promote tissue repair.* Annals of plastic surgery, 2015. **74**(3): p. 371-375.
26. Czajka, C.A., et al., *Scaffold-free Tissue Engineering: Organization of the Tissue Cytoskeleton and its Effects on Tissue Shape.* Ann Biomed Eng, 2014. **42**(5): p. 1049-61.
27. Au - Arbra, C.A., et al., *Microdissection of Primary Renal Tissue Segments and Incorporation with Novel Scaffold-free Construct Technology.* JoVE, 2018(133): p. e57358.
28. Rhett, J.M., et al., *Connexin-Based Therapeutics and Tissue Engineering Approaches to the Amelioration of Chronic Pancreatitis and Type I Diabetes: Construction and Characterization of a Novel Prevascularized Bioartificial Pancreas.* J Diabetes Res, 2016. **2016**: p. 7262680.
29. Otsu, N., *A Threshold Selection Method from Gray-Level Histograms.* IEEE Transactions on Systems, Man, and Cybernetics, 1979. **9**(1): p. 62-66.
30. Arganda-Carreras, I., et al., *3D reconstruction of histological sections: Application to mammary gland tissue.* Microscopy Research and Technique, 2010. **73**(11): p. 1019-1029.
31. Avolio, E., et al., *Perivascular cells and tissue engineering: Current applications and untapped potential.* Pharmacology & Therapeutics, 2017. **171**: p. 83-92.

32. Foty, R.A., et al., *Surface tensions of embryonic tissues predict their mutual envelopment behavior.* Development, 1996. **122**(5): p. 1611-20.
33. Foty, R.A. and M.S. Steinberg, *The differential adhesion hypothesis: a direct evaluation.* Dev Biol, 2005. **278**(1): p. 255-63.
34. Blanco, R. and H. Gerhardt, *VEGF and Notch in Tip and Stalk Cell Selection.* Cold Spring Harb Perspect Med, 2013. **3**(1).
35. Hellstrom, M., et al., *Dll4 signalling through Notch1 regulates formation of tip cells during angiogenesis.* Nature, 2007. **445**(7129): p. 776-80.
36. Herwig, L., et al., *Distinct cellular mechanisms of blood vessel fusion in the zebrafish embryo.* Curr Biol, 2011. **21**(22): p. 1942-8.
37. Jain, R.K., *Molecular regulation of vessel maturation.* Nat Med, 2003. **9**(6): p. 685-93.
38. Imhof, B.A. and M. Aurrand-Lions, *Angiogenesis and inflammation face off.* Nat Med, 2006. **12**(2): p. 171-2.
39. Reiss, Y., A. Scholz, and K.H. Plate, *The Angiopoietin—Tie System: Common Signaling Pathways for Angiogenesis, Cancer, and Inflammation*, in *Endothelial Signaling in Development and Disease*, M.H.H. Schmidt and S. Liebner, Editors. 2015, Springer New York: New York, NY. p. 313-328.
40. Tremblay, P.L., et al., *Inosculation of tissue-engineered capillaries with the host's vasculature in a reconstructed skin transplanted on mice.* Am J Transplant, 2005. **5**(5): p. 1002-10.
41. Park, K.M. and Gerecht, S. *Harnessing Developmental Processes for Vascular Engineering and Regeneration*. Development. **141**(14):2760-2769, (2014).
42. Grimes, D.R., Kelly, C., Bloch, K., and Partridge, M. *A Method for Estimating the Oxygen Consumption Rate in Multicellular Tumour Spheroids*. J. Royal Society Interface **11**(92): 1-11, (2014).
43. Matthias, W., Laschke, M.W., Vollmar, B., Menger, M.D. *Inosculation: Connecting the Life-Sustaining Pipelines.* Tiss Eng: Part B **15**(4):455-462, (2009).
44. Laschke, M.W. and Menger, M.D. *Prevascularization in Tissue Engineering: Current Concepts and Future Directions.* Biotechnol Adv **34**:112-121, (2016).
45. Pattanaik, S., Arbra, C.A., Dennis, S.G., Bainbridge, H.A.,

CHAPTER FOUR

THE ANGIOGENIC POTENTIAL OF SCAFFOLD-FREE PREVASCULARIZED ENDOTHELIAL-FIBROBLAST CONSTRUCTS

Vasculature is required for tissue maintenance and regeneration *in vivo.* During normal tissue development, new vasculature is formed through vasculogenesis and angiogenesis. These processes are highly dynamic and regulated at multiple levels, including transcriptional hierarchies and the interactions of proteins, as well as signal inputs from the extracellular environment (1). In previous work, the Scaffold-free Prevascularized Endothelial-fibroblast Construct (SPEC) was shown to organize into vascular networks with distinct directional orientations that reflect self-assembly mediated tension, and was later shown to quickly anastomose with the host and promote vascularization upon implantation (2-4). While these cellular constructs have exhibited successful integration with the host vasculature, they have not reached the phase of tubulogenesis *in vitro.* To overcome the unmet challenges of the SPEC seen from our *in vivo* studies, we wanted to investigate ways to accelerate the SPEC along the vascularization pipeline *in vitro* (**Figure 4.1**). Specifically, we wanted to investigate methods for inducing lumen formation, and subsequent tubulogenesis, in the SPEC pre-implantation. The ability to drive the SPEC further down the vascularization pipeline *in vitro* should improve its engraftment *in vivo.*

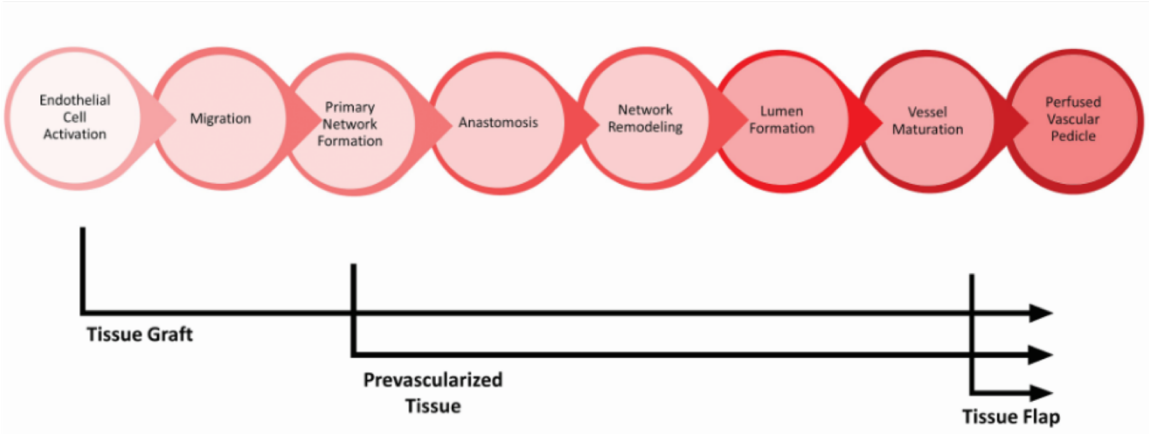

Figure 4.1. Proposed Vascularization Pipeline. The process of vascularization *in vivo* starts with endothelial cell activation, migration, network formation, tubulogenesis, and ends with anastomosis and blood flow.

In recent years there has been a focus on understanding the process of vascular morphogenesis, and the mechanisms by which endothelial cells form tube networks with defined lumens (5). There is a distinct difference between the processes of lumen formation and tubulogenesis. Lumen formation is a local event that involves a small number of cells opening up a space between them, while tubulogenesis is the formation of a continuous lumen that spans the entire length of a vessel (6). The formation of these contiguous tubes via tubulogenesis is required for subsequent blood flow, and for tissue growth and viability.

4.1 MECHANISM FOR TUBULOGENESIS IN VIVO: CORD HOLLOWING

A proposed mechanism of tubulogenesis *in vivo* occurs via cord hollowing (6; **Figure 4.2**). Prior to lumen morphogenesis, blood vessels consist of coalesced cords of endothelial cells that lack apicobasal polarity. Luminal space is generated extracellularly between endothelial cells as they remain tethered peripherally. A possible mechanism for creating extracellular space between endothelial cells is the clearance of adhesions at the cord center. Clearance at the cord center can occur either by de-adhesion at the

apical/luminal membrane, and/or by redistribution of junctional molecules away from the cord center. Finally, luminal expansion occurs as a result of adhesion junction rearrangements until a single lumen spans the entire vessel.

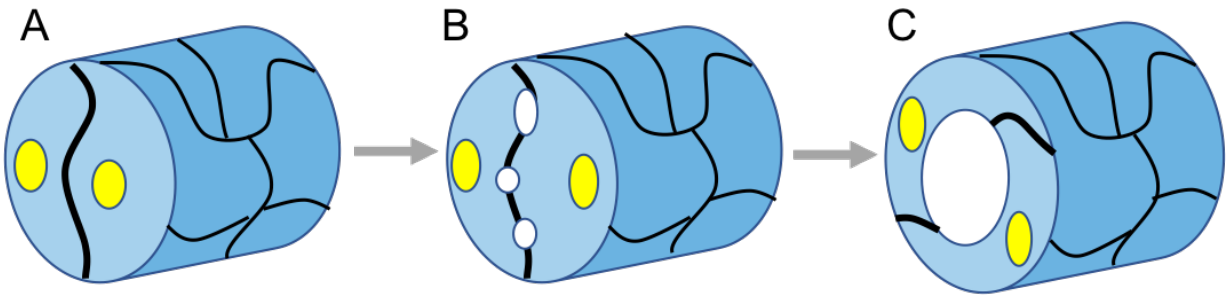

Figure 4.2. Proposed cord hollowing mechanism. (A) Prior to lumen formation, blood vessels consist of coalesced cords of endothelial cells that lack apicobasal polarity. (B) Lumenal space is generated extracellularly between adjacent endothelial cells as they remain tethered peripherally. (C) Lumenal expansion occurs as a result of endothelial-endothelial cell junctional rearrangements until a single lumen spans the vessel.

Adherens junctions provide strong cell-cell contacts mediated by the cadherin-catenin complex and its interaction with the actin cytoskeleton (12). Cadherins are transmembrane glycoproteins that regulate calcium-dependent cell-cell junctions (11). Cadherins have important roles in establishing cell growth, migration, and polarity, as well as regulating tissue morphology and cell differentiation (9,11). Adherens junctions located at homotypic endothelial cell-cell contacts regulate endothelial cord permeability, and play an essential role in cord hollowing (8). These junctions are involved in the activation of many subsequent signaling cascades depending on the complexes formed.

There are two primary cadherins expressed in the endothelium: Vascular endothelial cadherin (VE-Cadherin) and Neural cadherin (N-Cadherin). These adherens junctions have distinct functions in vascular maintenance. VE-Cadherin is the principal

endothelial-specific adherens junction molecule present in all vascular beds, and is essential for vascular morphogenesis (9). Its expression in endothelial cells is localized to homotypic cell-cell contacts, while N-cadherin is distributed throughout the entire cell membrane (11). This dispersion of N-cadherin to extra-junctional regions of the endothelial cell is regulated by VE-cadherin expression, and is proposed to be involved in vessel stabilization that occurs through interactions between endothelial and mural cells, such as pericytes and vascular smooth muscle cells, which helps stabilize vessels by anchoring the endothelium (9,11).

Catenin recruitment to adherens junctions, specifically, the p120-catenin regulates cadherin turnover by regulating their entry into the degradation endocytic pathway (13). N-cadherin controls the levels and cellular distributions of p120-catenin in human endothelial cells, and thereby regulates VE-cadherin. Luo, et. al. did studies in Human umbilical vascular endothelial cells (HUVEC) and showed that a knockdown of N-cadherin resulted in loss of VE-cadherin in endothelial cell-cell junctions, and that levels of junctional and non-junctional p120-catenin were significantly reduced (12). Therefore, both of these cadherins play critical roles in vasculogenesis and tubulogenesis by modulating adherens junctional components, and subsequent endothelial cell behavior.

In response to angiogenic stimuli *in vivo,* endothelial cells undergo dynamic rearrangements of cell-cell junctions, while simultaneous maintaining their barrier function (8). This coordinated response is dominantly regulated by the adhesion molecules located at intercellular junctions. Specifically, Vascular Endothelial Growth Factor-A signaling is of interest for inducing lumen formation, and subsequent

tubulogenesis, in the SPEC because it regulates the levels of VE-cadherin at endothelial cell-cell junctions (7,8,10).

4.2 Vascular Endothelial Growth Factor-A (VEGFA) Signaling

Vascular Endothelial Growth Factor-A (VEGFA) is the most critical regulator of vasculogenesis and angiogenesis (7,8,10,15). VEGFA signaling mediates immediate responses, like vascular permeability, and long-term responses, such as endothelial cell survival, migration, and proliferation (10). Reduced production of VEGFA results in decreased angiogenesis, and is thought to contribute to impaired tissue repair. VEGFA and their receptors are critical regulators of new vessel development and the remodeling of existing ones (10). Blood vessel homeostasis is regulated by VEGFA, which in turn controls endothelial cell functions within the vessels.

There are three receptors, VEGFR1, VEGFR2, and VEGFR3, that VEGFA can interact with. These receptors are regulated on numerous levels: the receptor expression levels, availability and affinity for binding to its different ligands, the presence of co-receptors, the rate of cellular uptake, and extent of degradation and speed of recycling (10). VEGFR2 is the major signaling receptor in vascular endothelial cells, and is the main transducer of VEGFA effects on these cells differentiation, proliferation, migration, and formation of the vascular tube (10). VEGFR1 is expressed by monocytes and macrophages, and is not required for endothelial cell functions. VEGFR1 actually binds to VEGFA with a ten-fold higher affinity than VEGFR2, however it has poor kinase activity, and may act as a negative regulator of VEGFR2 by capturing VEGFA in order to spatially regulate VEGFR2 signaling and the formation of angiogenic sprouts (10).

VEGFR1 is majorly involved in regulating monocyte migration during inflammation. VEGFR3 is expressed by lymphatic endothelial cells and does not play a major role in tube-formation, *in vivo* (10).

Of specific interest to us, VEGFR2 regulates VE-cadherin expression at intercellular junctions through VEGFA-VEGFR2-activated SRC signaling. Upon VEGFA-VEGFR2 binding, the receptor gets dimerized and then stabilized through interactions between membrane-proximal Ig-like domains, which allows trans/autophosphorylation of intracellular tyrosine residues. Specifically, the Y951 residue, located in the kinase inert domain of the VEGFR2 receptor, gets phosphorylated, which binds to the SH2 of Tsad that in turn recruits and binds to the SH3 domain of Src, activating Src (**Figure 4.3)**. Src activation is dependent on the phosphorylation of residue Y951, and regulates vascular permeability, cell-matrix components, and cell adhesion (10). The activated Src phosphorylates VE-cadherin at the Y658 residue of the cytoplasmic domain, which disrupts the binding of p120-catenin (13). This dissociation of p120-catenin results in VE-cadherin endocytosis and results in opening paracellular junctions and increases vascular permeability (8,13).

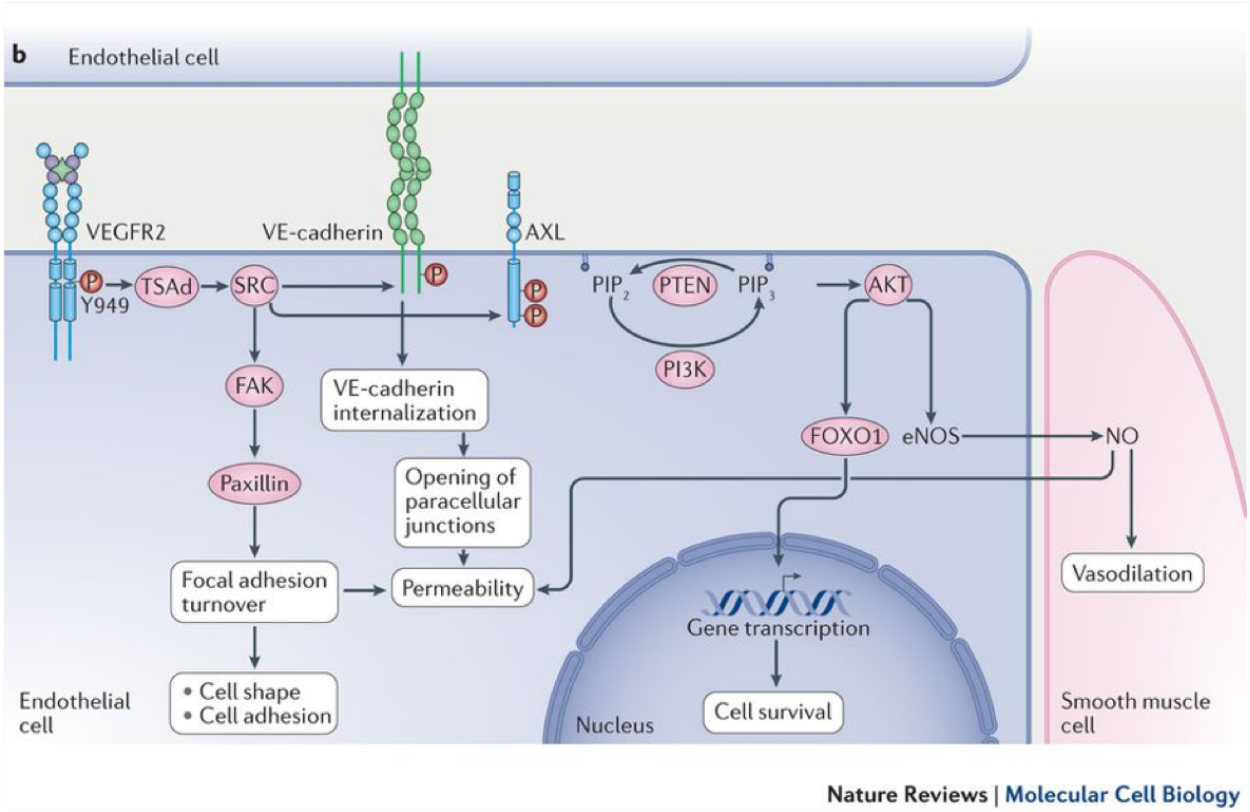

Figure 4.3. Schematic representation of VEGF-activated VEGFR2–SRC–AKT signaling. Figure adapted from ref Simons, M., et. al. (2016). Nature Reviews **17**:611-625.

4.3 Sphingosine-1-Phosphate (S1P) Signaling

Sphingosine-1-phosphate (S1P) is a bioactive lipid that stimulates both endothelial cells and fibroblasts. *In vitro,* Sphingosine-1-Phosphate (S1P) stimulates endothelial cell proliferation and survival, migration, capillary-like tube formation, and regulates the endothelial barrier permeability (14,15). *In vivo,* S1P binds to its receptor (S1P1) on endothelial cells to stimulate angiogenesis, and promotes the coverage of nascent vessels with mural cells for stabilization. S1P has also been reported to be involved in the stabilization of N-cadherin-mediated endothelial cell-mural cell interactions (12). S1P has been indicated as a key player in stabilizing N-cadherin-

mediated endothelial cell-mural cell interactions both *in vitro* and *in vivo* (12). The maturating and barrier-protecting actions of S1P inhibit tissue edema and is predicted to produce synergistic therapeutic effects with other angiogenic factors, like VEGF (14,15).

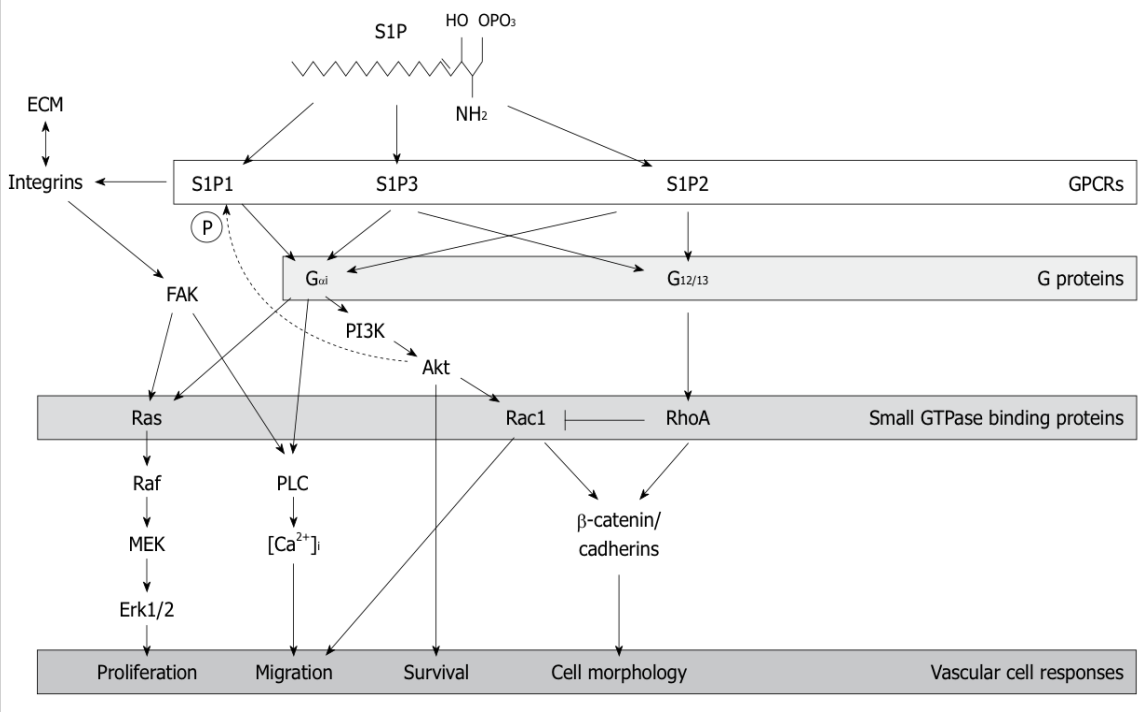

Figure 4.4. Sphingosine-1-phosphate receptor signaling. The figure shows aspects of the signaling cascades that are mediated by three members of the S1P receptor family, S1P1-3. Fig adapted from ref Argraves, K.M. et. al. (2010). *World J Biol Chem* **1**(10):291-297.

Due to the known pro-angiogenic effects of and potential crosstalk between these factors, exogenous administration of VEGF or S1P into the SPEC is predicted to accelerate *in vitro* angiogenesis. We hypothesize this dosing regimen will initiate lumen formation via cell-cell junctional rearrangements, which stimulates endothelial cell polarity and in turn recruits essential components of the tubulogenesis machinery to the site of lumen formation (7).

4.4 MATERIALS AND METHODS

SPEC Formation

The scaffold-free prevascularized endothelial-fibroblast constructs were created as described previously in chapter 3. Briefly, a high-density cell suspension of 1:4 human adipose microvascular endothelial cells (HAMEC, ScienCell) and normal human dermal fibroblasts (NHDF, Lonza) were seeded in a non-adherent agarose mold and cultured for three days. The rod-shaped SPEC with dimensions of 1 mm wide by 6 mm long, required $9x10^5$ total cells.

Preparation of Vascular Endothelial Growth Factor-A and Sphingosine-1-Phosphate

Vascular endothelial growth factor-A (VEGFA, R&D Systems Cat#293-VE-010) was prepared following manufacturer's instructions. Sphingosine-1-phosphate (Sigma-Aldrich Cat#S9666) was also prepared following the provided protocol.

Dosing Regimen of SPECs with exogenous growth factors

We decided to treat our SPECs at different time points during their formation, while they are undergoing the process of self-assembly. We seeded the cells in the non-adherent agarose molds at D.0. After 24 hours, we treated our constructs with VEGF as a D.1 treatment by incorporating either VEGFA or S1P in the media. We harvested these constructs on D.3. As a second treatment group, we treated our SPECs 48 hours after seeding them into the molds, as a D.2 treatment. These constructs were also harvested on D.3.

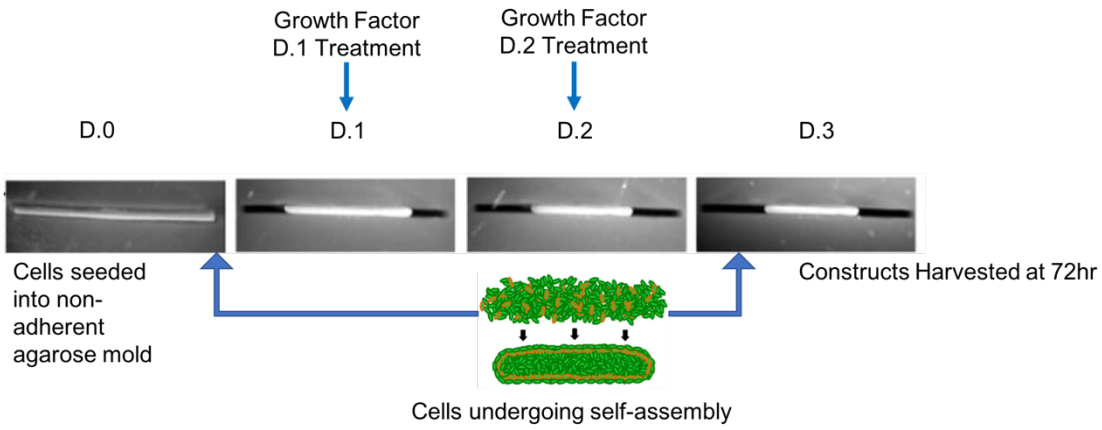

Figure 4.5. Dosing regimen of SPEC constructs during their formation

Immunohistochemistry Analysis of SPECs

Tissue sections were fixed in 4% paraformaldehyde solution for thirty minutes and subjected to hematoxylin and eosin staining, direct or indirect immunofluorescence labeling. Tissue sections were directly labeled with Hoescht 33342 nuclear stain (Molecular Probes, 1:10,000), and Alexa Fluor™ phalloidin 488 (ThermoFisher Scientific A12379, 1:500) for F-actin. Selected sections were stained with primary antibodies to human CD31 (monoclonal antibody) (R&D Systems BBA7, 1:25). Primary antibodies were fluorescently tagged with the secondary antibodies Alexa Fluor™ goat anti-mouse 488, goat anti-rabbit 546, goat anti-mouse 546, and goat anti-rabbit 633 (ThermoFisher Scientific, A-11001,11035,11030,21070, 1:500). Sections were mounted on Colormark Plus microscope slides in Prolong Gold antifade reagent (Molecular probes P36934).

Western Blot Analysis

Treated SPECs were collected after their appropriate culture times in the 2% linear agarose molds as previously described. Samples were snap frozen, and mechanically

homogenized in RIPA lysis buffer with protease inhibitor cocktail. Samples were maintained in constant agitation for 2h at 4°C, centrifugated for 20 min at 16,000 g at 4°C. Supernatant was stored in fresh tube at -20°C. Pierce™ BCA Protein Assay kit (Thermofisher Scientific 23227) was used to estimate protein concentration for samples as per manufacturer's instructions. Prior to gel electrophoresis, samples were diluted in RIPA buffer to attain 20 ug of protein in 20 uL solution, and further diluted 1:1 in 2x Laemmli Sample buffer to attain 40 uL loading volumes. Samples were loaded onto Any kD™ Mini-Protean® TGX™ Precast Protein Gels. Following protein separation and overnight transfer onto PVDF membranes, western blots were performed using antibodies towards GAPDH (loading control) (CalBioChem CB1001, 1:1000), VEGFR2 (Abcam ab39256, 1:900), vWF (Abcam, ab6994, 1:500), DLL4 (Abcam ab7280, 1:1000), Laminin (Abcam ab11575, 1:200), N-cadherin (Abcam ab98952, 1:200), VEGFA (Abcam ab46154, 1:200), Cdc42 (Abcam ab187643, 1:100), and Podocalyxin (PODXL, Abcam ab150358, 1:300). GAPDH was used as a loading control for all samples.

4.5 RESULTS

Immunohistochemistry Analysis of Treated SPECs

VEGF-treated SPECs

There were distinct differences between the untreated SPEC control, the D.1 VEGF-treated SPEC, and the D.2 VEGF-treated SPEC. There was no lumen present at the interior of the untreated SPEC (**Figure 4.6A**). A singular, small central lumen was present in the D.1 VEGF-treated SPECs that was surrounded by organized endothelial

cells (CD31, red; **Figure 4.6B**). The D.2 VEGF-treated SPECs had a very large central lumen with densely packed endothelial cells surrounding the luminal area (**Figure 4.6C**). This could be attributed to the high pro-angiogenic potential of the SPEC at this time point during its normal formation *in vitro*, as indicated in the previous chapter by high DLL4 expression at this time point. Due to this, we believe the SPEC is most responsive to growth factor treatments at this time point during its formation.

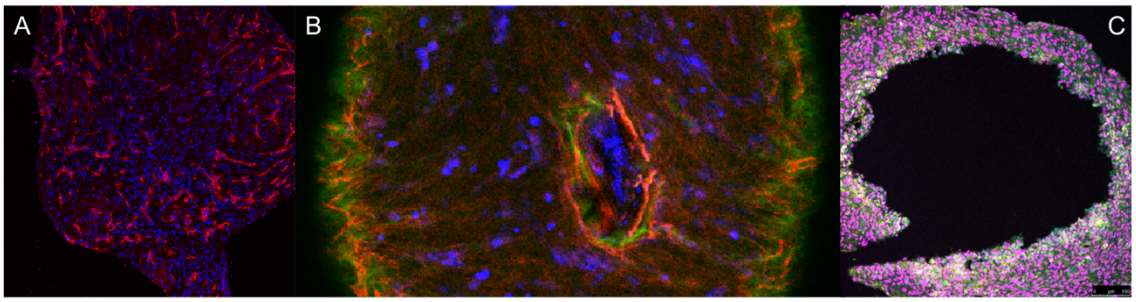

Figure 4.6. VEGF-treated SPECs have lumens present. (A) Untreated SPEC control showing no lumen present at interior of construct. (B) D.1 VEGF-treated SPEC with small, central lumen surrounded by dense endothelial network (CD31, red). (C) D.2 VEGF-treated SPEC with large, central lumen surrounding by densely packed endothelial cells (CD31, yellow)

We also analyzed these constructs to see if there were endothelial cell-cell junction rearrangements in response to the VEGF treatment by looking at the expression and density of these networks (CD31, red; **Figure 4.7**). The untreated SPEC controls have endothelial networks that span across the entirety of the constructs, including the most central interior regions (**Figure 4.7A**). The VEGF-treated SPECs, however, have an obvious disruption of these networks at the interior of the constructs. This is indicative of VE-cadherin, the major endothelial cell-cell junction regulator, internalization, which follows the proposed process of cord hollowing.

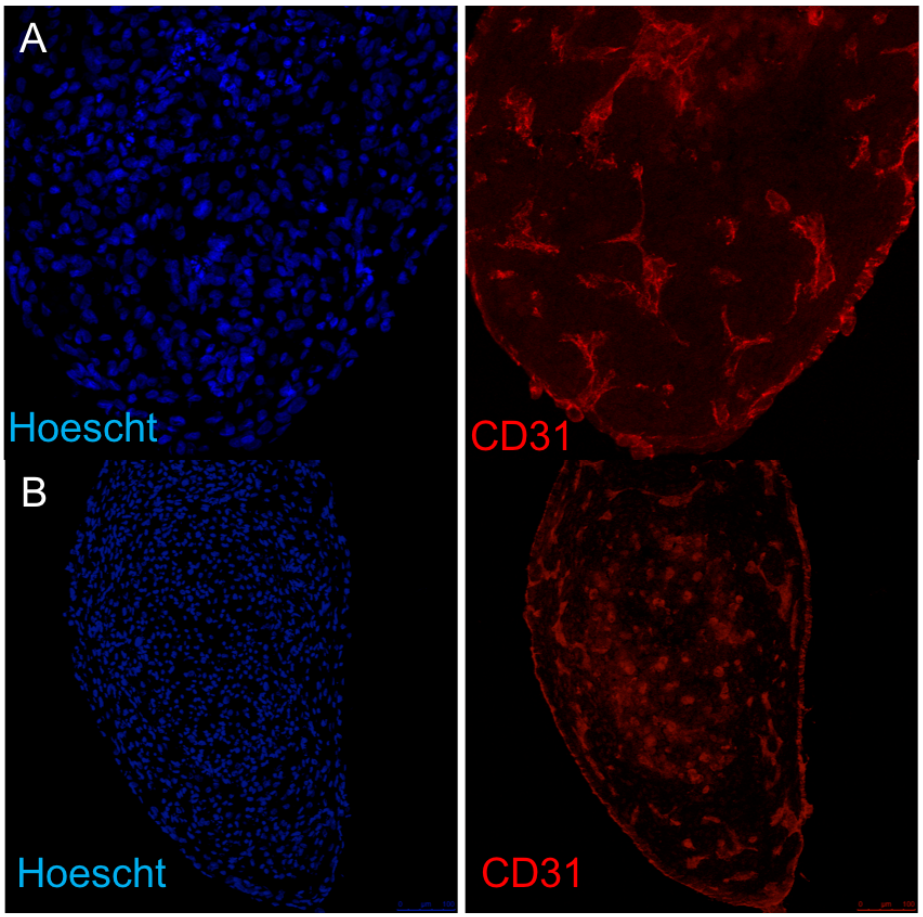

Figure 4.7. Assessment of endothelial networks (CD31, red) in (A) untreated SPEC controls and (B) VEGF-treated SPECs. There is an evident disruption of the endothelial networks at the interior of the treated SPECs, indicating cell-cell junctional rearrangements occurred as a response to treatment.

S1P-treated SPECs

In contrast to the single, central lumen found in both of the VEGF-treated SPECs, we found multiple smaller lumens present at the center region of the S1P-treated SPECs (**Figure 4.8**).

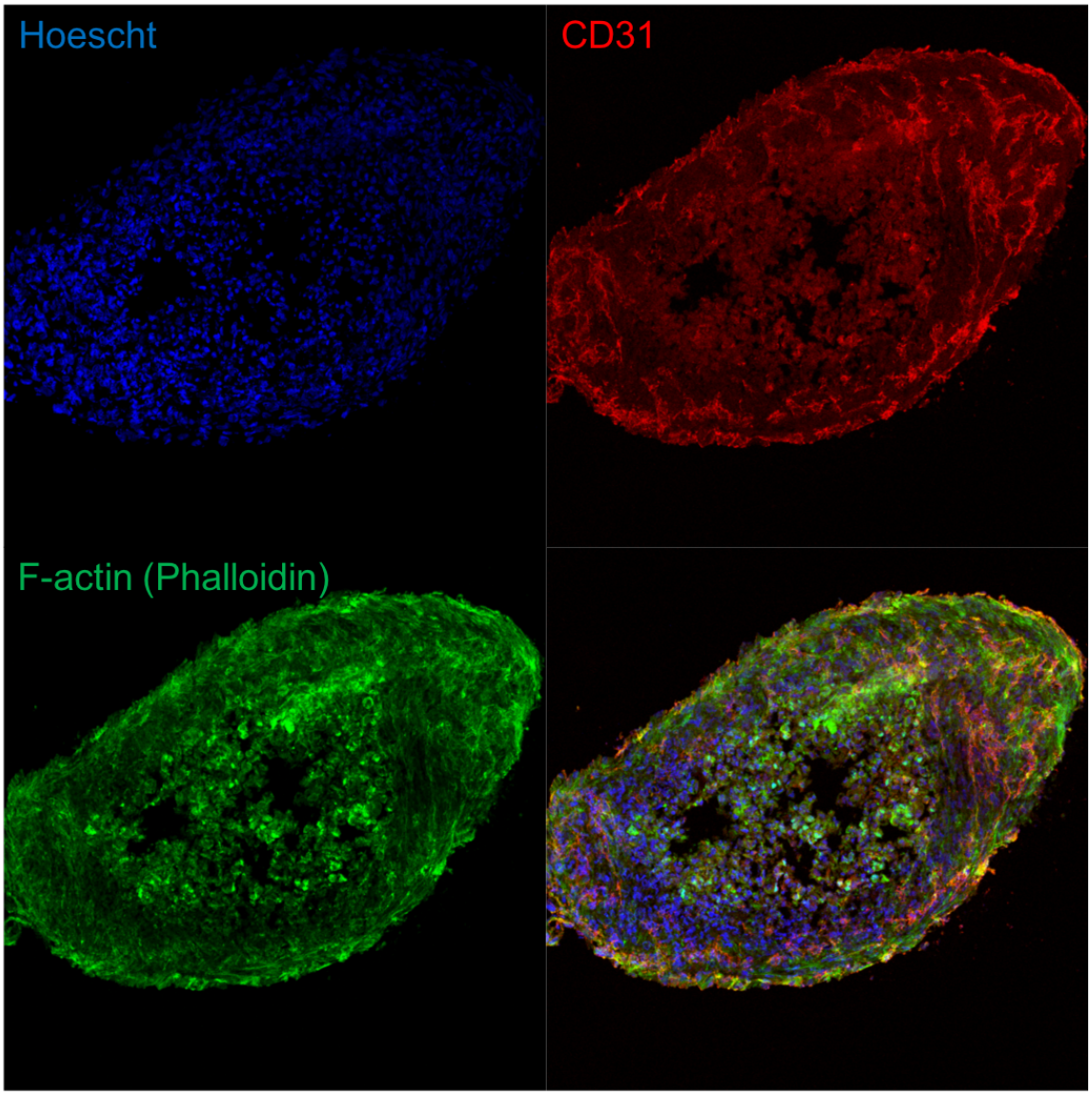

Figure 4.8. S1P-treated SPEC analysis where nuclei are indicated by Hoescht (blue), endothelial networks indicated by CD31 (red), and F-actin indicated by phalloidin staining (green).

We also compared the expression of F-actin (indicated by phalloidin staining) of the S1P-treated SPECs to the untreated SPEC control. We found that there was a much more dense F-actin network surrounding the luminal areas of the S1P-treated SPECs that was

not as dense as the untreated controls (**Figure 4.9**). This indicates the fibroblasts began secreting more extracellular matrix in response to the S1P treatment.

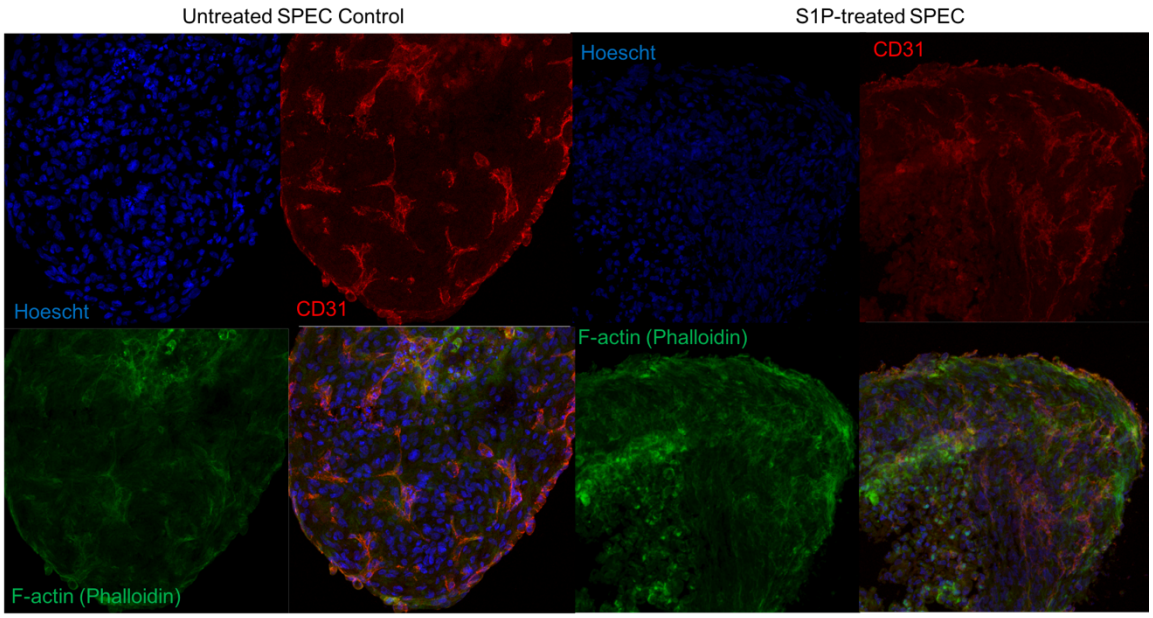

Figure 4.9. Comparison of untreated SPEC control (left) to S1P-treated SPECs. There is an obviously more dense F-actin network (green), secreted by the stimulated fibroblasts in response to S1P treatment. The F-actin fibers and endothelial networks (red) in the S1P-treated SPEC appear more directionally aligned around the luminal area.

Additionally, the F-actin fibers (green) and endothelial networks (red) in the S1P-treated SPEC appear more directionally aligned around the luminal area (**Figure 4.9**).

Western Blot Analyses of VEGF-treated SPECs

Podocalyxin (PODXL) is a marker of the early luminal surface. This molecule gets shuffled to the interior surface of the forming lumen. It is a charged molecule, and it's presence at the interior luminal wall of newly-forming vessels is indicative of established polarity and the indictment of luminal expansion. Notably, we found that PODXL expression was upregulated in the VEGF-treated SPECs, indicating these constructs have established polarity and the cells at the interior are beginning to rearrange to permit luminal expansion through the entirety of the constructs (**Figure 4.10**).

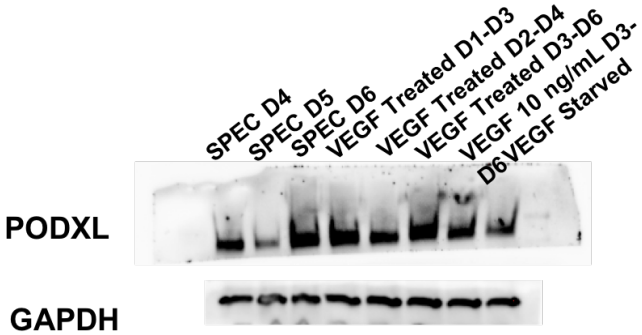

Figure 4.10. Western Blot analysis for Podocalyxin (PODXL) expression in VEGF-treated SPECs.

In our analysis for vWF, we found that the VEGF-treated SPECs had a significant increase in expression, as compared to the untreated controls (**Figure 4.11**). This finding was surprising, and may be due to the densely packed endothelial cells surrounding the luminal region. The cells in this area serve to maintain the endothelial barrier integrity, while the interior cells undergo rearrangements to form a luminal space. Cdc42 is a small GTPase that induces vesicle formation and the formation of a luminal area. We found its expression was also increased in VEGF-treated SPECs. The expression of Cdc42 could indicate another mechanism participating in the formation of lumens in these treated constructs: vesicle fusion. Further investigation will be done in future work. We additionally found that N-cadherin expression was increased in only one of our treated constructs, which could be due to the disruption of VE-cadherin junctions, therefore cell-cell adhesions rely on N-cadherin. This presence of N-cadherin could also be due to the incorporated fibroblasts, as this is not an endothelial-specific junctional molecule.

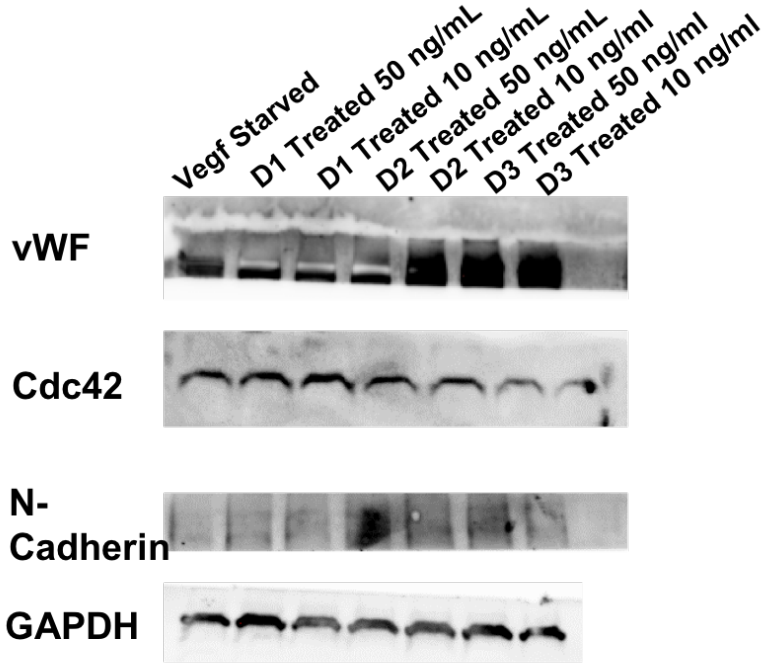

Figure 4.11. Western Blot analyses for vWF, Cdc42, N-cadherin, and loading control (GAPDH) in VEGF-treated SPECs and untreated controls.

Finally, we analyzed the expression of laminin in our VEGF-treated SPECs. Laminin is an extracellular matrix component that is expressed on the abluminal walls of blood vessels. We found that it was uniformly expressed in all constructs, regardless of treatment.

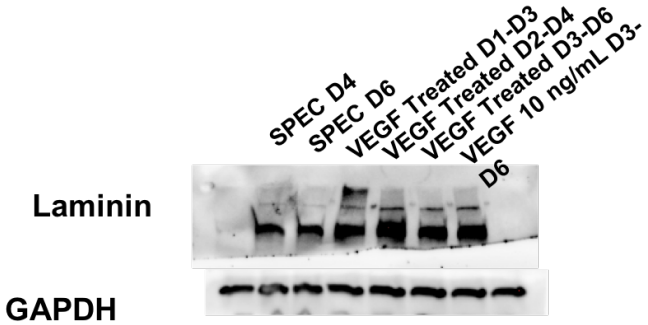

Figure 4.12. Western Blot analysis for Laminin expression.

4.6 DISCUSSION

We have looked at how to modify the capabilities of the SPEC to create different types of vascular patterns using growth factors. We were encouraged from our previous *in vivo* data that the SPEC had reached this later stage of vessel maturation in the pipeline by 72 hours. With our recent *in vitro* data, incorporating the VEGFA and S1P during the formation of the SPEC constructs, and seeing network remodeling and lumen formation, we are excited to get these in vivo studies going in future work. We believe that SPECs treated with exogeneous growth factors *in vitro* are tailorable to application-specific demands, due to the obvious differences seen between the treatment groups. In our future work, we plan to analyze the S1P-treated SPECs using the same markers as described here to assess the VEGF-treated SPECs. We also want to investigate the possible synergistic effects of these two factors by treating SPECs with both of them during the culture period. Varying the ratio of endothelial:fibroblast cells used to create the SPEC constructs, could elicit different results from what is reported here, so we plan to investigate that possibility by including more endothelial cells at the time of seeding. Finally, we plan to implement the same animal model as described in chapter three to determine if they get perfused more quickly than the untreated SPECs once implanted.

4.7 REFERENCES

1. Park, K.M. and Gerecht, S. Harnessing Developmental Processes for Vascular Engineering and Regeneration. *Development.* **141**(14):2760-2769, (2014).
2. Czajka, C.A., et. al. Scaffold-free tissue engineering: organization of the tissue cytoskeleton and its effects on tissue shape. *Ann Biomed Eng* **42**(5):1049-1061, (2014).
3. Calder, B., et. al. Implanted scaffold-free prevascularized constructs promote tissue repair. *Ann Plast Surg* **74**(3):371-375, (2015).
4. Pattanaik, S., Dennis, S.G., et. al. (in submission).

5. Norden, P.R., Kim, D.J., Barry, D.M., Cleaver, O.B., and Davis, G.E. Cdc42 and k-Ras Control Endothelial Tubulogenesis through Apical Membrane and Cytoskeleton Polarization: Novel Stimulatory Roles for GTPase Effectors, the Small GTPases, Rac1 and Rap1b, and Inhibitory Influence of Arhgap31 and Rasa1. *PLoS ONE*. **11**(1):e0147758, (2016).
6. Xu, K. and Cleaver, O. Tubulogenesis during blood vessel formation. *Sem Cell & Dev Biol* **22:**993-1004, (2011).
7. Herbert, S.P. and Strainier, D.Y.R. Molecular control of endothelial cell behavior during blood vessel morphogenesis. *Nature Reviews* **12:**551-564, (2011).
8. Murakami, M. Signaling Required for Blood Vessel Maintenance: Molecular Basis and Pathological Manifestations. *Int J Vasc Med.* **2012**(6): 293641, (2012).
9. Gentil-dit-Maurin, A., Oun, S., Almagro, S., Bouillot, S., Courcon, M., Linnepe, R., Vestweber, D., Huber, P., and Tillet, E. Unraveling the Distinct Distributions of VE- and N-cadherins in Endothelial Cells: A Key Role for p120-catenin. *Experimental Cell Res.* **316**(16):2587-2599, (2010).
10. Simons, M, Gordon, E., and Claesson-Welsh, L. Mechanisms and Regulation of Endothelial VEGF Receptor Signaling. *Nature Reviews* **17**:611-625, (2016).
11. Navarro, P., Ruco, L., and Dejana, E. Differential Localization of VE- and N-cadherins in Human Endothelial Cells: VE-cadherin Competes with N-cadherin for Junctional Localization. *J Cell Biol.* **140**(6):1475-1484, (1998).
12. Luo, Y and Radice, G.L. N-cadherin Acts Upstream of VE-cadherin in Controlling Vascular Morphogenesis. *J Cell Biol.* **169**(1): 29-34, (2005).
13. Davis, M.A., R.C. Ireton, and A.B. Reynolds. A core function for p120- catenin in cadherin turnover. *J. Cell Biol.* **163**:525–534, (2003).
14. Argraves, K.M., Wilkerson, B.A., and Argraves, W.S. Sphingosine-1-phosphate signaling in vasculogenesis and angiogenesis. *World Journal Biol Chem* **1**(10):291-297, (2010).
15. Ryu Y, Takuwa N, Sugimoto N, Sakurada S, Usui S, Okamoto H, Matsui O, Takuwa Y: Sphingosine-1-phosphate, a platelet- derived lysophospholipid mediator, negatively regulates cellular rac activity and cell migration in vascular smooth muscle cells. *Circ Res* **90**:325-332, (2002).

CHAPTER FIVE

THE SMART WOUND DRESSING

From these promising findings described in the previous chapters, we started thinking about different applications we could apply these different technologies to. The Yost lab has been investigating wound healing for many years and through our collaboration with surgeons here at MUSC, we became interested in what goes wrong during this healing process, which results in a non-healing wound. We define these non-healing wounds as chronic wounds.

In the United States, chronic wounds account for more than $25 billion annually in health care expenses and affect over 6.5 million people, with 85% of these patients being 65 years and older (1-5, 34). Separate from direct healthcare expenses, an additional $15 billion is spent on wound care products, as well as another $12 billion on scar treatment, reaching almost $60 billion spent annually on chronic wound treatment. Additionally, these financial estimates do not include the morbidities facing these patients including lost work time, decreased productivity, disability payments, nor rehabilitation costs (34).

5.1 NORMAL WOUND HEALING OF ACUTE WOUNDS

Acute wounds affect over 11 million people in the United States every year (Singer). These wounds undergo a well-organized process of normal wound healing that leads to predictable tissue repair. Normal wound healing is a complex, highly regulated process that progresses through a cascade of events consisting of four temporally and

spatially regulated phases, including coagulation, inflammation, proliferation, and remodeling and scar formation (Demidova-Rice) (**Figure 5.1**).

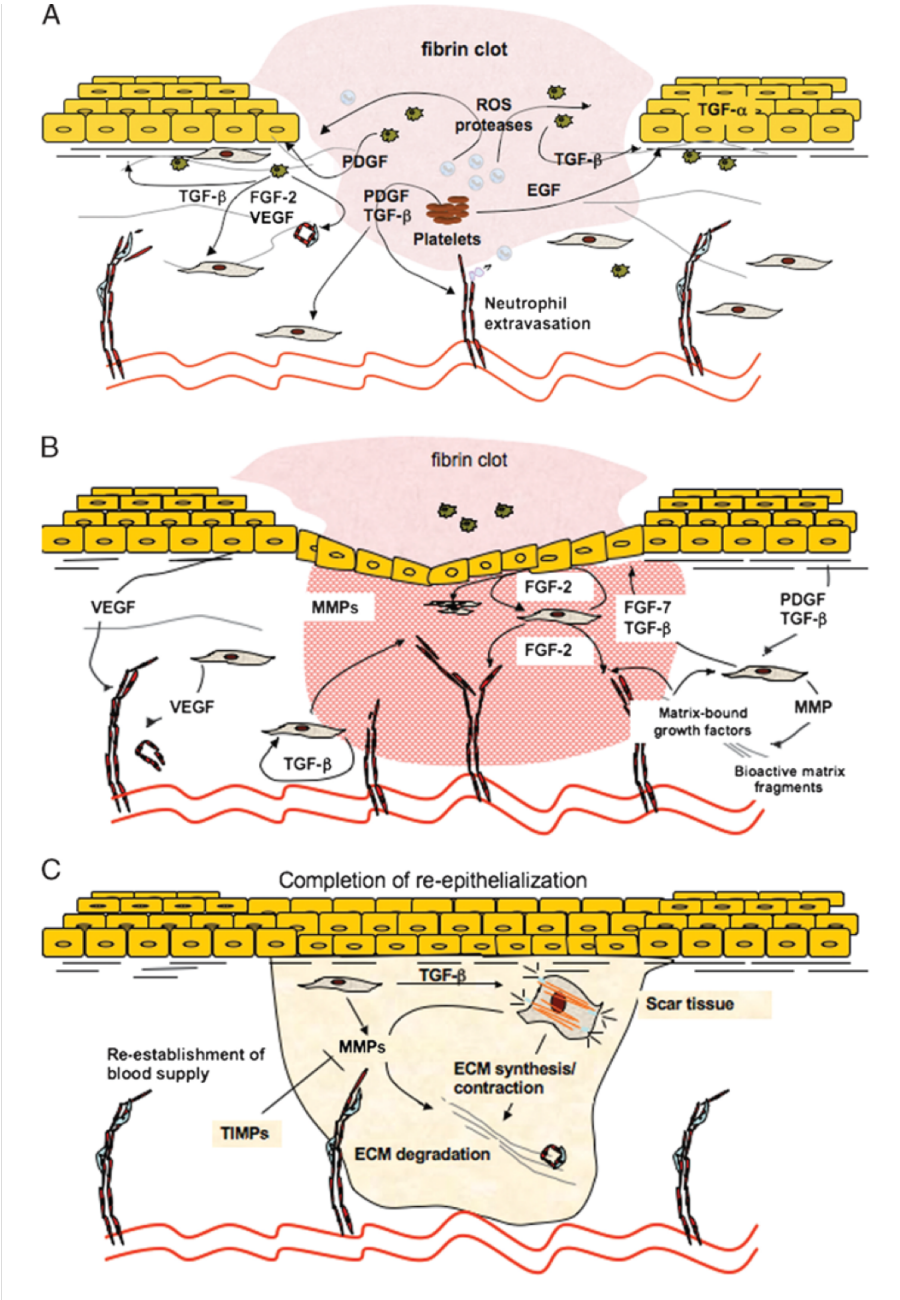

Figure 5.1. Stages of normal wound healing. Normal wound healing processes can be divided into 4 overlapping phases: coagulation (not shown), inflammatory phase (A), proliferative phase/granulation tissue formation (B), and remodeling phase (C). Fig adapted from ref Demidova-Rice, T.N., et al. Adv Skin Wound Care **25**(7):304-314, (2012).

Immediately after the injury occurs, platelets are activated and recruited to the injury site where they adhere to the damaged blood vessel. When the platelets adhere to the damaged vessel they release signaling factors, such as platelet-derived growth factor (PDGF) and transforming growth factors A1 and A2 (TGFA1,TGFA2), that initiate a blood-clotting cascade to prevent excess bleeding and the resultant clot provides temporary protection for the wounded area (**Figure 5.1A**). The released factors stimulate inflammatory cells, including leukocytes, neutrophils, and macrophages that then get recruited to the wounded area and begin clearing out foreign bodies and bacteria through the release of reactive oxygen species (D-R). This is the inflammatory phase of wound healing, which gets resolved upon the gradual apoptosis of these inflammatory cells over the span of a few days.

As the inflammatory phase is being resolved, the proliferative phase of tissue repair is initiated (**Figure 5.1B**). The remaining inflammatory cells present at the wounded area begin to release growth factors, as well as migratory epidermal and dermal cells. The epidermal and dermal cells "act in an autocrine, paracrine, and juxtacrine fashion to induce and maintain cell proliferation while initiating cellular migration" to the site. All of these events are essential for forming granulation tissue and supporting epithelialization of the wound area (D-R). To sustain these incoming cells an angiogenic response is initiated to provide an adequate blood supply, which carries nutrients and oxygen, and allows for metabolite exchange. Angiogenesis in wound healing is initiated almost immediately after the injury occurs as the wound area becomes hypoxic. Initially, the activated platelets release proangiogenic growth factors including vascular

endothelial growth factor (VEGF), fibroblast growth factor-2 (FGF-2), and PDGF. After the inflammatory phase, the infiltrated cells also secrete these factors, which in turn regulate the angiogenic **induction**. Endothelial cells degrade their surrounding basement membranes, so they can "migrate toward the wound site where they proliferate, form new cell-cell contacts, and eventually new blood vessels" (D-R).

Once the new blood vessels have been formed and normal blood supply is provided to the wounded area, epidermal and dermal cells migrate and proliferate within this area (**Figure 5.1C**). The wound epithelium gets restored by the epidermal cells, while the dermal cells, i.e. fibroblasts, secrete extracellular matrix to form granulation tissue, mainly consisting of collagen type I, that gets perfused with the previously formed vessels. As this occurs, a new provisional matrix consisting of collagen type III, fibrin, fibronectin, and hyaluronic acid gradually replaces this granulation tissue. The next, and final, phase of wound healing is wound contraction and matrix remodeling (**Figure 5.1C**). Wound contraction is mediated by fibroblasts that respond to platelet-released TGFA, tissue tension, and matrix protein presentation. The fibroblasts generate actin-containing stress fibers that induces contractile forces, which are transmitted to the surrounding extracellular matrix through focal adhesion complexes comprised of integrins. Additionally, the matrix is continuously reorganized through slow cycles of extracellular matrix generation and degradation, which occurs in a fibroblast-depdendent manner (D-R). Matrix degradation occurs via matrix metalloproteases (MMPs), which are critical regulators of the local matrix microenvironment and allow for cellular migration, proliferation, and angiogenic induction. Once the matrix has been sufficiently

remodeled, the fibroblasts begin to undergo apoptosis, which results in the formation of a relatively acellular fibrotic scar (**Figure 5.1C**). However, even when normal wound healing is successful, the resultant tissue can be disfigured and non-functional (35). For example, **Figure 5.2** is of a patient treated at the Medical University of South Carolina Hospital with traditional therapies that left this patient with a non-functional tissue associated with reduced mobility and increased morbidity for this patient.

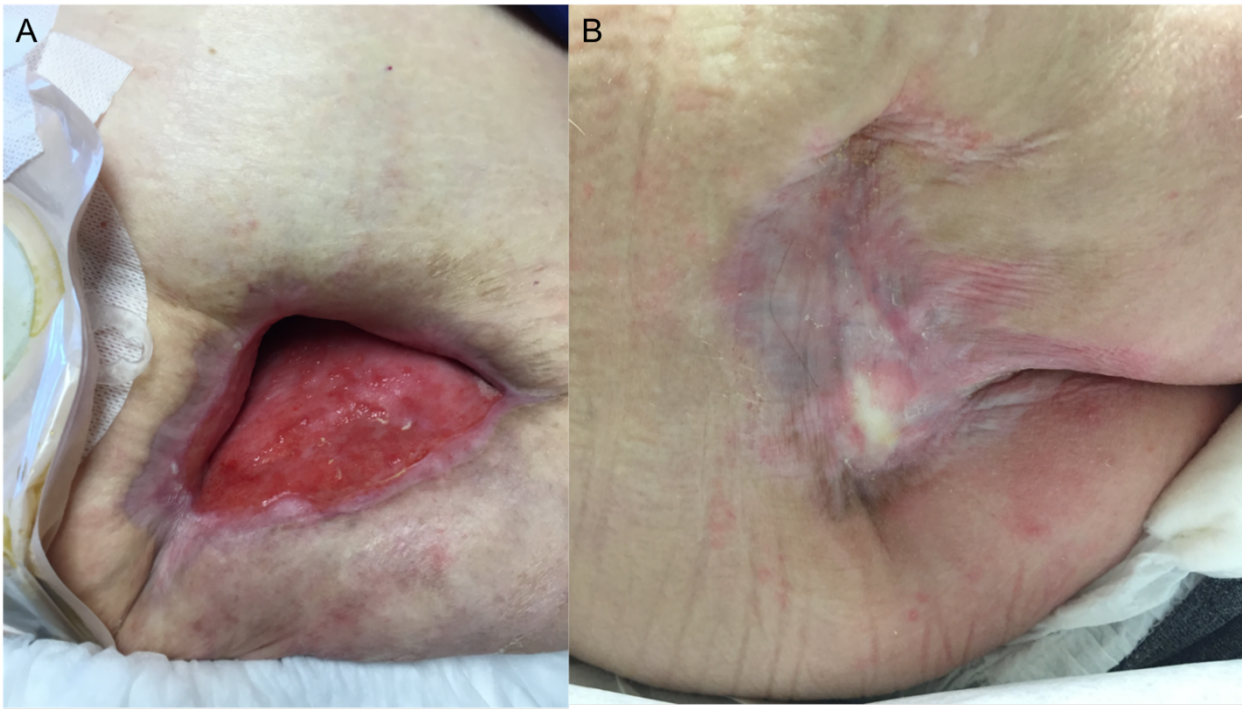

Figure 5.2. (A) Before and (B) after images of a patient treated at the Medical University of South Carolina, where the wound healed but the resultant tissue was non-functional and disfigured.

5.2 THE CHRONIC WOUND ENVIRONMENT

Chronic wounds are wounds that have failed to progress through the normal stages of wound healing (**Figure 5.3**). These wounds characteristically have an accumulation of metabolic waste products, proteins, and enzymes in the affected area,

leading to excess wound exudate. Chronic wound exudate inhibits fibroblast proliferation and contains proteases that degrade extracellular matrix and growth factors.

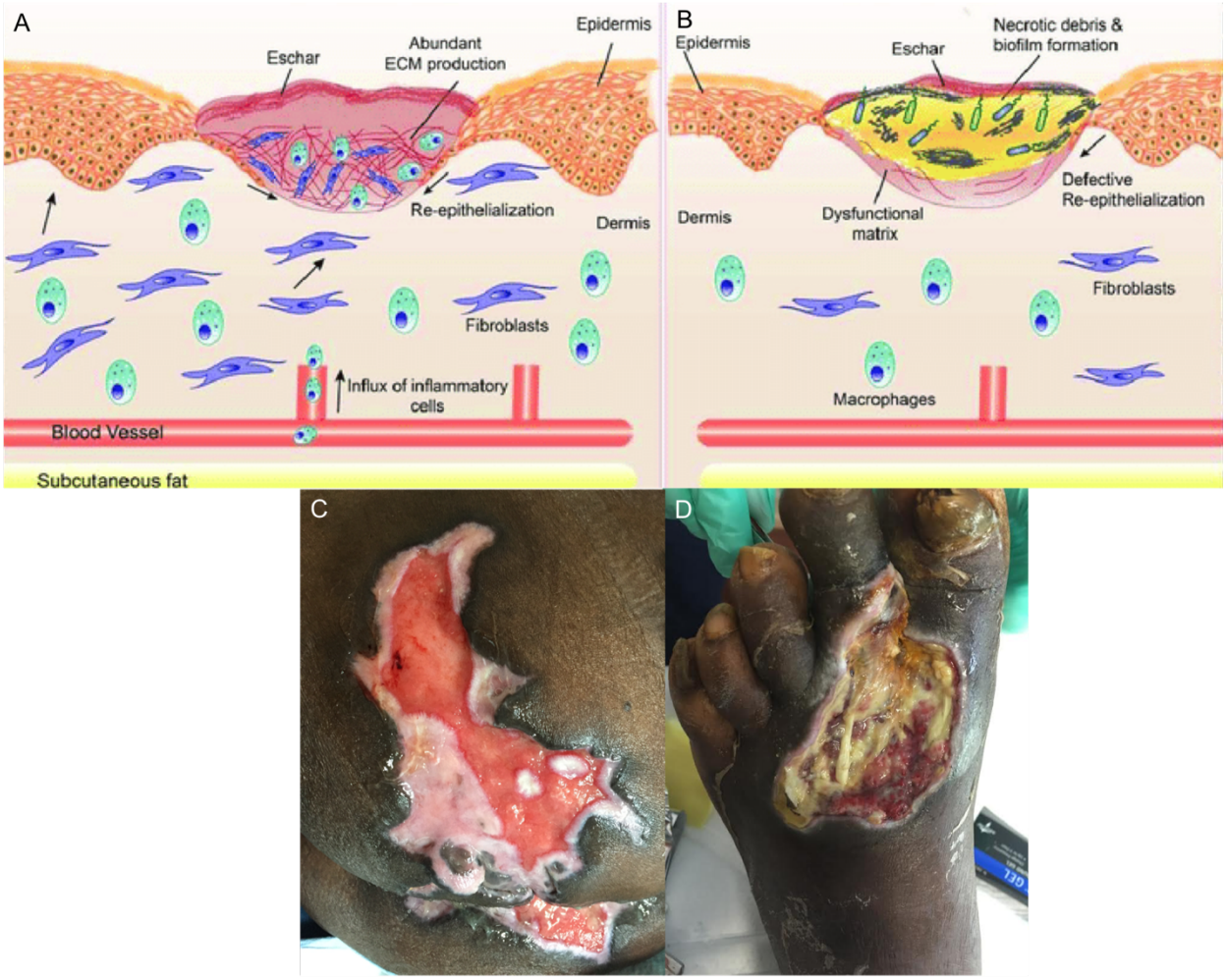

Figure 5.3. (A) Normal-healing wound microenvironment. (B) Chronic, non-healing wound microenvironment. (A,B) from ref Pandya, UM, Gold, LI. *J Dermatolog Clin Res* **4**(5):1083 (2016). (C) Image of a gluteal wound closing by secondary intention from a patient at MUSC. (D) Image of a diabetic foot wound infected with C. gas gangrene that later required amputation.

Chronic wounds are also associated with high levels of pro-inflammatory cytokines, which have been shown to inhibit growth and induce morphological changes in normal skin fibroblasts, as well as arrest the healing process in the inflammatory state (4). Fibroblasts in chronic tissue appear larger and polygonal, tend to be non-responsive

to growth factor stimulation, and have reduced mobility and migration as compared to normal healing tissues. The irregularities of the predominant extracellular matrix-producing cells lead to a compositional change in the structural environment, such as decreased production of laminin, fibronectin, collagen, as well as others, and inadequate matrix reorganization. Chronic inflammation can lead to endothelial cell dysfunction and impaired blood vessel regeneration. Bacteria are present on virtually all open wounds. Bacterial colonization occurs when the growth and death of microbes are kept in balance by the host immune system. When host defenses can no longer maintain this balance, the wound enters a non-healing, infected state. If the infection goes untreated, and turns systemic, the infected area may have to be amputated for patient survival. For example, the C. gas gangrene infection shown in **Figure 5.3D** of a patient treated at the Medical University of South Carolina hospital resulted in a lower right limb amputation due to the extent of the infection. From our literature search, we came up with a list of the major players contributing to impaired wound healing in these chronic wounds (**Figure 5.4**).

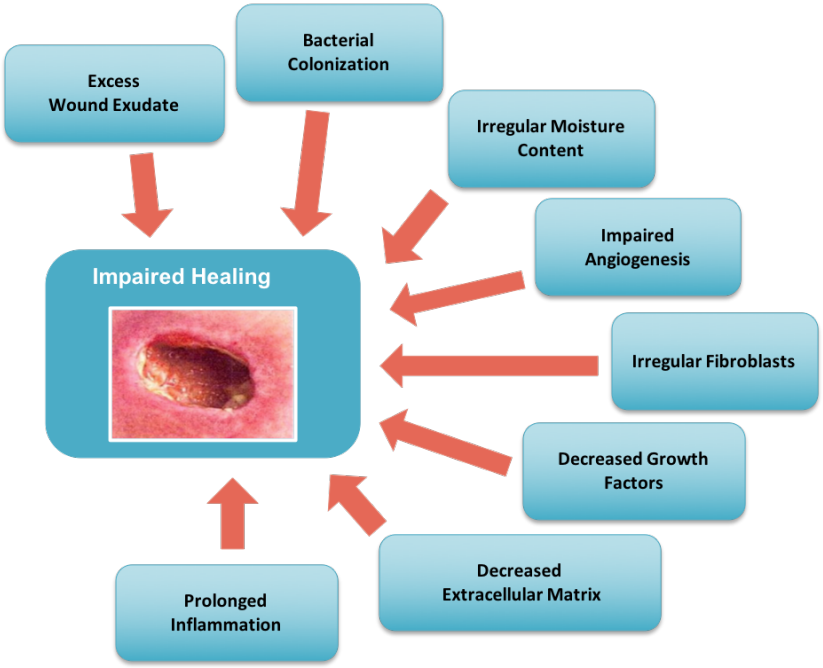

Figure 5.4. The key players contributing to impaired wound healing.

5.3 PRESSURE ULCERS

Pressure ulcers, one of the most frequently observed chronic wounds in clinics, develop when an area of skin is placed under constant pressure for an extended period of time resulting in tissue ischemia, depletion of nutrients and oxygen supply to site, and eventually tissue necrosis (Osuala). When an area of skin is exposed to prolonged pressure, blood vessels within the distorted tissue are occluded and blood is unable to flow. While ischemia is the initiator of pressure ulcer formation, there are other underlying factors involved in the failure of these wounds to heal.

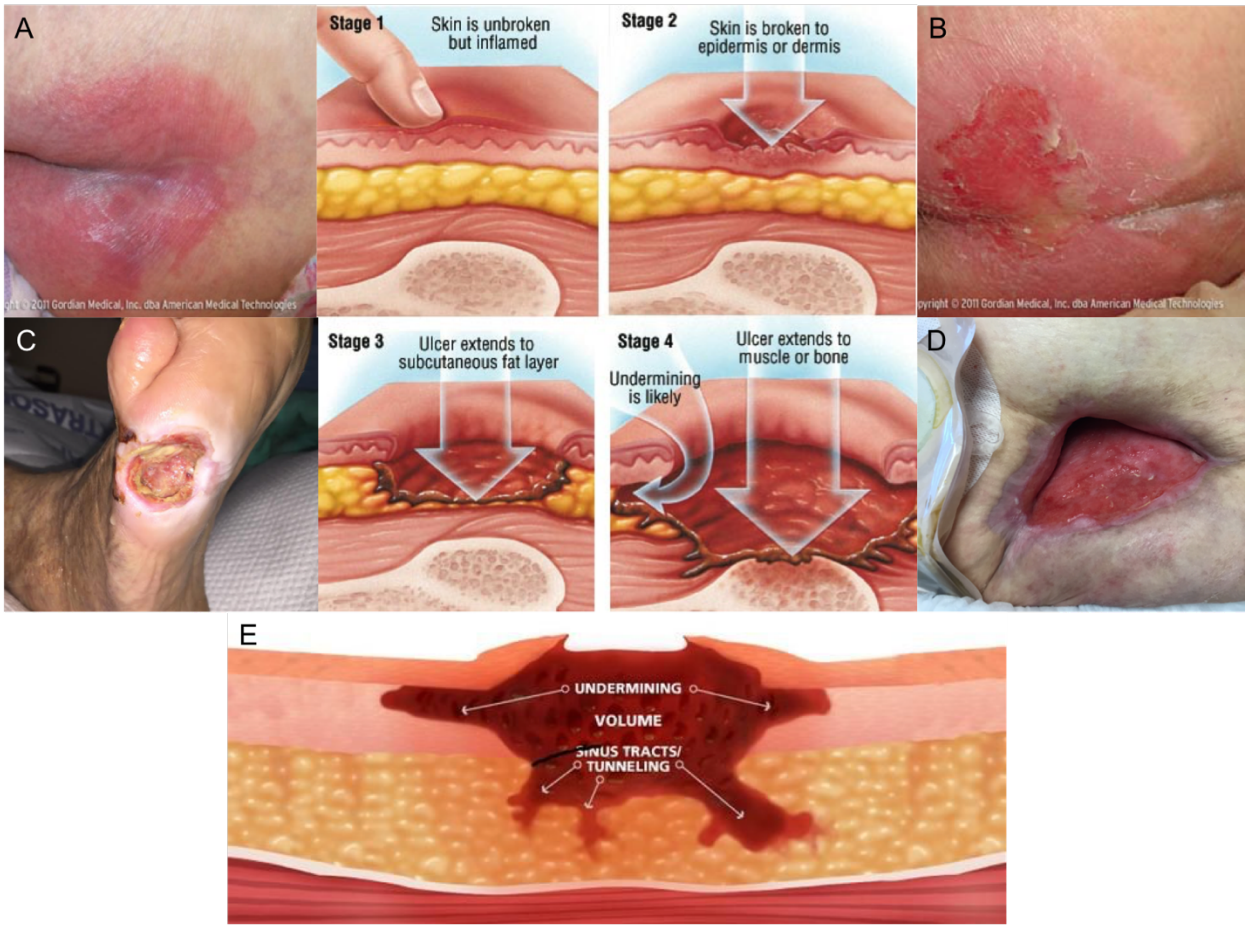

Figure 5.5. Progression and classification of pressure ulcers where (A) is a Stage I, (B) Stage II, (C) Stage III, and (D) Stage IV pressure ulcers. Patient images in (A) and (B) were adapted from ref National Pressure Ulcer Advisory Panel (NPUAP, www.npuap.org). Images shown in (C) and (D) are of patients treated at the Medical University of South Carolina Hospital. (E) Undermining and tunneling that can occur with later stage (i.e. Stage III and IV) pressure ulcers. Fig adapted from ref North Country Nursing: Wound Care Summit 2015.

Pressure ulcers are classified as Stage 1 if the skin remains unbroken, but there is evident inflammation at the site with the area appearing red and warm (**Figure 5.5A**). Stage 2 pressure ulcers have partial-thickness loss of the epidermis, the outermost layer of the skin, and some of the dermis, however no slough is present (**Figure 5.5B**). Slough is soft, moist, avascular, dead tissue. Stage 3 ulcers are characterized by full-thickness skin loss, including epidermis and dermis, and necrosis of subcutaneous tissue (**Figure**

5.5C). Slough and necrotic tissue, as well as undermining and tunneling, may be visible, however, no underlying muscle, bone, or tendon is exposed (**Figure 5.5E**). Undermining is caused by erosion under the wound edges, resulting in a large wound with a small opening. Tunneling is a secondary wound caused by a high volume of pressure being forced upon many tissue layers, which can prompt the layers to become less voluminous than surrounding tissues, creaking a sinkhole-like effect in the skin. Pressure ulcers progress to Stage 4 when there is full-thickness skin loss including the epidermis, dermis, and subcutaneous tissue (**Figure 5.5D**). Underlying muscle, bone, and tendon may be visible, as well as slough, undermining, and tunneling.

5.4 TRADITIONAL WOUND TREATMENT

Wound dressing devices are a vital component in the treatment of chronic, non-healing wounds. The traditional dressings predominantly used in clinics are shown in **Figure 5.6.** Plain dry gauze has historically been one of the most popular wound dressings. Gauzes have good absorptive properties, but can completely dehydrate the wound, which is detrimental to wound healing. They also tend to adhere to the wound surface and removal can be painful and traumatic. Due to their absorptive properties, they have limited ability to provide an effective barrier against bacterial invasion. Hydrocolloids are adhesive, occlusive (do not permit gas or fluid flow) dressings that absorb wound exudate to form a hydrophilic gel that helps maintain a moist healing environment. They provide protection against shear force at the skin surface. However, these dressings have risk of periwound maceration and, if the site gets too moist, may separate from the wound bed, requiring frequent dressing changes. Maceration occurs

when the healthy tissues surrounding the wound bed, i.e. the periwound, are exposed to excess moisture and begin to degrade, which can further impede wound healing, as well as lead to increased deterioration of the wound bed (31). Hydrogels are water-based materials that help maintain a moist environment. They can be applied and removed without causing pain or further trauma. Additionally, patients have reported pain relief with these dressings, likely due to their cooling effects. Foams are semi-occlusive dressings that provide thermal insulation and protect against shear. They are non-adhesive, so there is no tissue injury or pain associated with dressing changes. However, foams have no protective barrier to prevent bacterial contamination and, like hydrocolloids, may promote development of excessive wound exudate requiring frequent dressing changes.

Figure 5.6. Traditional Wound Dressings including (A) Gauze, (B) Hydrocolloids, (C) Hydrogels, (D) Foams, and (E) Topical Antibiotics.

Traditional dressings fall short in addressing the three main issues that impede healing: preventing bacterial infection, ineffective inducement of cell migration and neovascularization, as well as maintenance of wound moisture balance and control of wound exudate. Additionally, standard of care techniques, for example wet-to-dry dressings, are labor intensive and can induce secondary injury and pain to the patient.

5.5 MODERN WOUND TREATMENT

Advanced wound dressings such as TriTech Silver and Apligraf®, a bi-layered cultured skin substitute, require numerous applications and have been unsuccessful in adequately closing chronic wounds (7,15,18-19). Tritec Silver® is a bi-layered device comprised of a Protective Layer and a Transfer Layer (**Figure 5.7**).

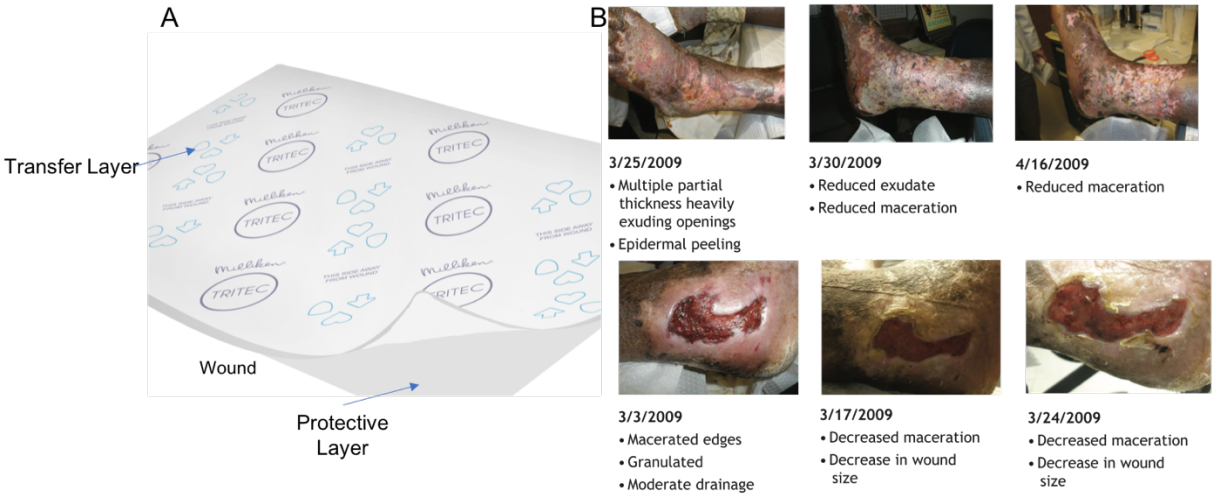

Figure 5.7. TriTec Silver by Milliken wound treatment option. (A) Schematic of tritec where the bottom of the dressing, or the layer adjacent to the wound surface is the protective layer, and the top layer is the transfer layer. Figure adapted from Milliken website. (B) Clinical trial results with TriTec Silver dressing. Figure adapted from ref Smith, A. and Garoufalis, M. Case Study. Milliken Healthcare Products, LLC. (2013).

The layer proximal to the wound is the Protective Layer, which supports two critical functions: regulating moisture and protecting surrounding healthy skin and underlying

tissues. The layer is designed with unidirectional fibers that only wick moisture vertically through the dressing and away from the wound bed. The top or transfer layer is composed of highly hydrophilic fiber that pulls exudate through the protection layer, away from the wound, and into a secondary dressing (i.e. gauze). This layer prevents accumulation of wound exudate. In addition, this dressing has a silver antimicrobial technology that releases silver ions when exposed to sodium-containing fluid, like wound exudate. While this product targets some of the contributors of wound healing, it has been met with limited success in case studies, and must be used in combination with other treatments, like compression therapy (15).

Apligraf is a bi-layered skin substitute comprised of cells and collagen (**Figure 5.8**). It is currently the only FDA-approved cell-based treatment for venous and diabetic ulcers (18).

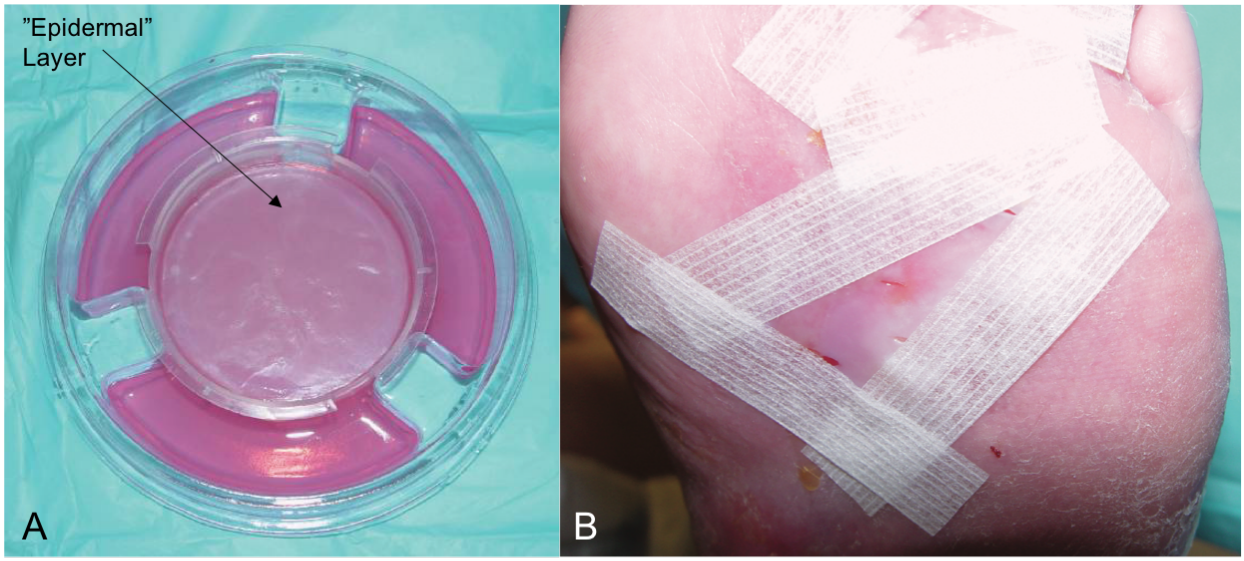

Figure 5.8. Apligraf wound dressing. (A) Apligraf® as it is received from the manufacturer with the epidermal-side (dull) facing upwards. (B) Apligraf® that has been applied directly to a wound bed. Fig adapted from ref Zaulyanov, L. and Kirsner, R.S. *Clinical Interventions in Aging* **2**(1): 93-98 (2007).

The dermal layer combines a type I collagen matrix and human fibroblasts, which secrete additional matrix produces. The epidermal layer is formed from keratinocytes, which proliferate and differentiate to replicate the *in vivo* architecture. While Apligraf has shown promising results for the healing of acute wounds (**Figure 5.8B**), studies in chronic wounds found the graft did not persist long enough for therapeutic effects (18,19). This dressing also must be used with a secondary dressing, and is not a single-application treatment option.

5.6 THE SMART WOUND DRESSING (SWOD)

When we started thinking about how to design a single device that can address all of the major players contributing to impaired wound healing, we reverted back to what the ancient Egyptians were doing in ~2000 B.C. They created combinatorial devices comprised of lint to address the excess wound exudate, animal grease to provide a hydrophobic barrier and protect the wound bed from the external environment, and honey, which has inherent antibacterial properties due to its osmolarity. In doing so, we realized there was no single material that could successfully provide all of these features (**Figure 5.4**), and began developing a multi-layered wound dressing, the Smart Wound Dressing (SWOD). The SWOD is a multi-component device made up of three separate layers that individually address different facets of the chronic wound environment (**Figure 5.9**).

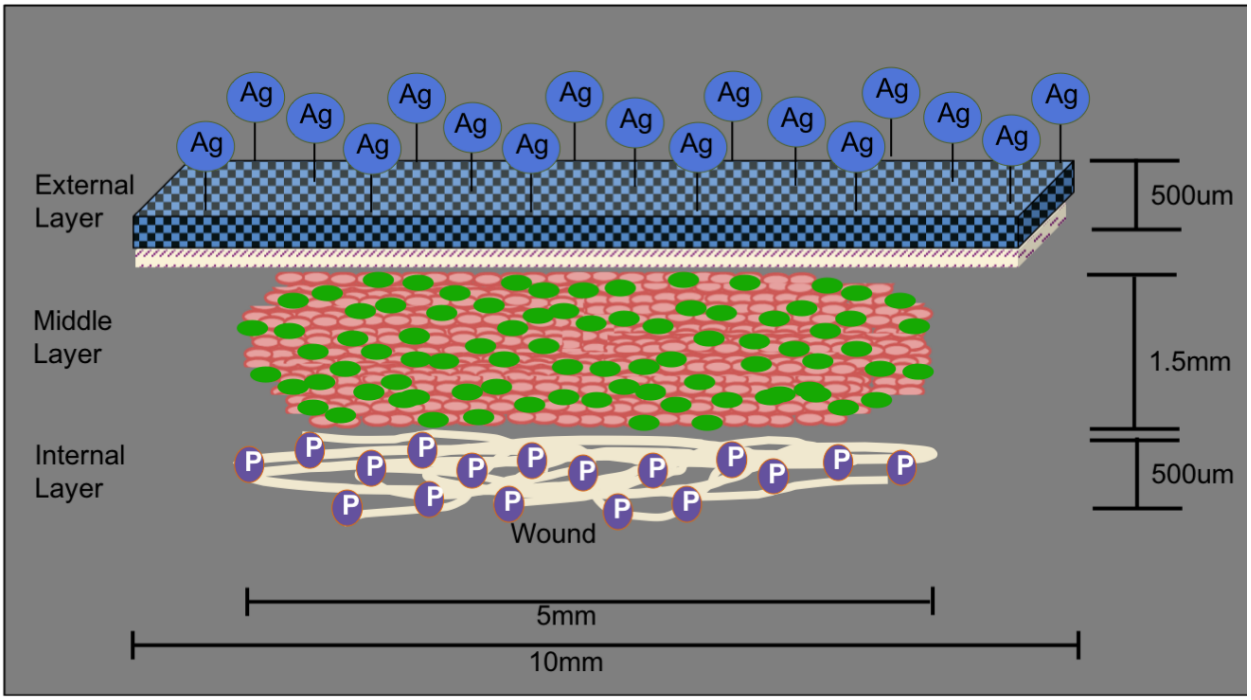

Figure 5.9. The Smart Wound Dressing (SWOD) schematic. The external layer is comprised of: woven polyester coated in silver, and hydrophilic PTFE. The middle layer is made up of scaffold-free prevascularized endothelial-fibroblast constructs. The internal layer is made up of reaction electrospun collagen fibers with or without a drug, "P".

The bottom layer of the SWOD, the anti-inflammatory layer, serves a dual function, first providing a provisional matrix to host cell migration, and second to regulate moisture balance in the wound bed. This layer was designed to address the deficiency in extracellular matrix proteins and provisional matrix in chronic wounds, and act as a scaffold for cell adherence and subsequent matrix deposition. Electrospun collagen was chosen because it has previously been reported to improve wound healing (27). The reaction electrospun collagen fibers are created using a novel technique developed in the Yost Lab at the Medical University of South Carolina. This technique produces a superior fibrous scaffold that is unique in its resistance to trypsin digestion,

and as produced, these fibers can donate or absorb water from the wound bed to maintain a moisture content equivalent to that found in healthy skin (22).

The middle layer of the SWOD, the living component, has been incorporated to promote revascularization and angiogenesis at the wound site. This layer incorporates endothelial cells and fibroblasts to overcome the irregularities associated with these cell types in chronic wounds. These constructs have been engineered to contain a prevascular bed and supply reparative fibroblasts (21,28). This layer serves to provide cues to encourage migration and repopulation of the wound bed with viable host cells and promote revascularization to the site. Additionally, when implanted into the hind limb of a rat, the SPEC was shown to rapidly integrate with the surrounding host vasculature within 6 hours of implantation. **Figure 5.10** shows that there is distinct overlap of the implanted cells, shown in Cell Tracker+ blue, coinciding with vasculature marker (vWF) that is labeling both the human implanted and the host rat vascular components.

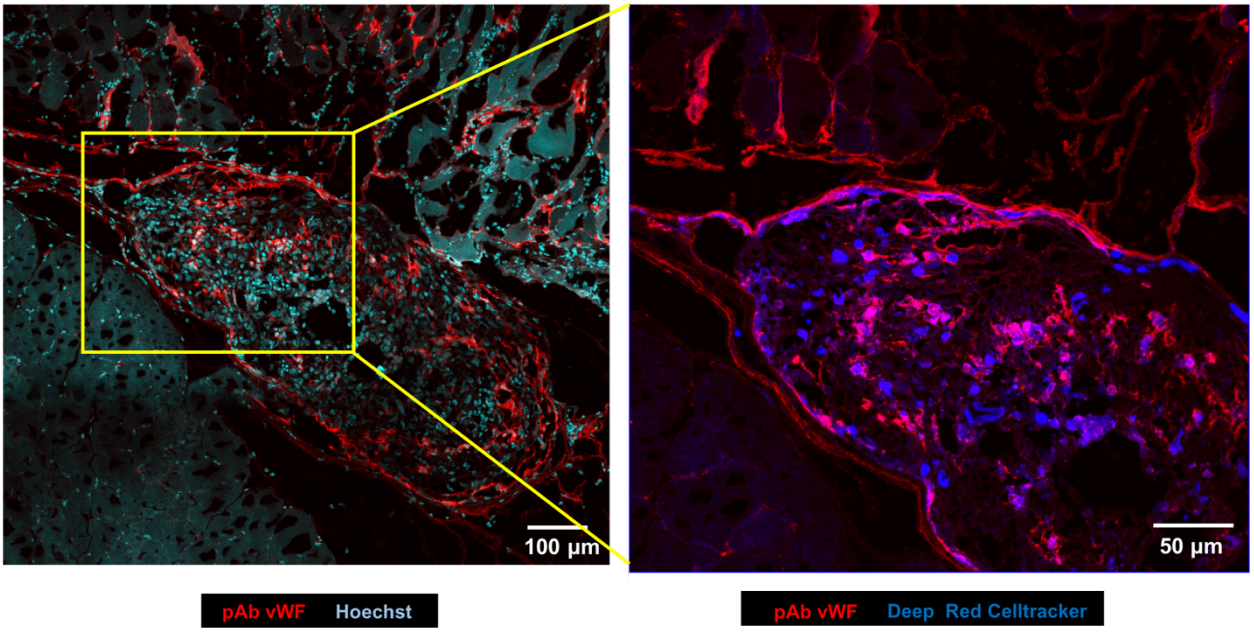

Figure 5.10. Scaffold-free prevascularized endothelial-fibroblast constructs explants from hind limb of a rat at 6 hours post-implantation.

Finally, the external side is composed of hydrophobic silver coated woven polyester and an internal membrane of 0.1μm pore size, hydrophilic polytetrafluoroethylene (PTFE). The amphipathic nature of this layer creates a unidirectional flow of exudate out of the wound bed, thereby creating an appropriate environment that promotes regeneration, while preventing accumulation of excess wound exudate. In addition, the hydrophobic outer silver coating kills invading pathogens and provides an added layer of protection against infection (23). During the development of this layer many materials were investigated including regenerated cellulose, polysulfone, polycarbonate membranes, among others. Hydrophilic PTFE proved to be the best option for the SWOD, and has been widely used in medical applications, such as vascular grafts and surgical meshes (24-26). Its hydrophilic nature prevents protein binding, and subsequent cell or bacteria adherence, while

permitting the filtration of fluid. The combination of these product features specifically targets the issues encountered in treating and closing these difficult wounds.

The Smart Wound Dressing (SWOD) is unique in its multifaceted approach which minimizes bioburden, while reviving normal wound healing mechanisms by increasing cellular migration, facilitating angiogenesis, and controlling moisture balance in the wound bed. The scientific premise of this project is that the overlapping functions of these layers combine to create a superior treatment by attenuating the multiple contributors to failed healing as compared to standard of care. The SWOD is a single application device, and its development will accelerate closure, shorten hospital stays, and reduce costs associated with chronic wounds. We believe that this combinatorial approach, which actively targets all of the contributors to impaired wound healing, will provide an exciting new option for the treatment of chronic wounds.

5.7 METHODS

Electrospinning Apparatus and Methods

The electrospinning technology was developed and previously described by the Yost Lab at the Medical University of South Carolina (**Figure 5.11**; Patent Filed; 22).

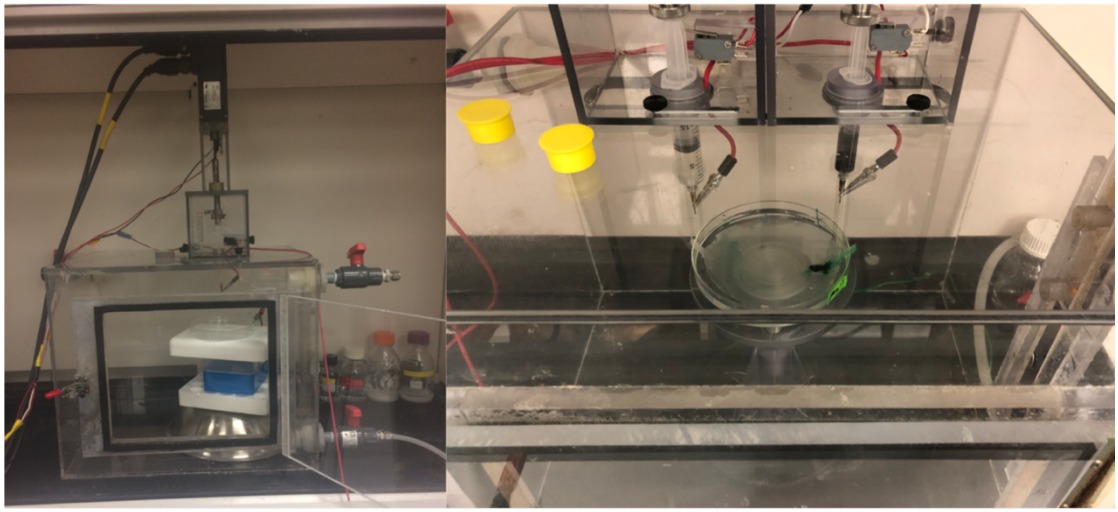

Figure 5.11. Electrospinning apparatus developed by the Yost Lab at the Medical University of South Carolina.

Sputter-coating of Woven Polyester Membranes

The top portion of the external layer comprises a woven polyester material with one side sputter-coated with silver using a Cressington 180 Auto/SE apparatus. In preliminary work we determined the optimal parameters for silver deposition across the entirety of the sample to be 30mA for 150 seconds for uniform coating.

Total Silver-Loading Measurements

Sputter-coated samples were analyzed for silver concentration using flame atomic absorption spectrometry (FAAS). Total ash from each membrane was measured and reported as a percentage of the starting weight of the material. Both the silver-coated woven polyester and the hydrophilic 0.1μm PTFE membranes were imaged with scanning electron microscopy.

Hydrophobicity of Silver-coated Woven Polyester

The hydrophobicity of silver sputter-coated samples will be determined by contact angle measurements. Each side (A,B) of the polyester material was sputter-coated in silver for

one cycle (30mAmps for 150 seconds). The samples were placed on a level surface and a 12μL drop of distilled water was deposited on top of it. Side-view images of the drops and a length reference scale were captured. The measurements required for analyzing the contact angles were taken and recorded in CellSens. Drop shape analysis was performed using the formula: $\text{Contact Angle} = 2\tan^{-1}(\frac{\text{height}}{0.5\text{ base}})$ for quantifying the contact angles.

Bulk Absorption

The bulk absorption properties of the top layer of the SWOD was measured following the standard method (31). Silver-coated or plain woven polyester samples were cut into 22 mm discs and the initial weight of each dressing was recorded. The samples were then be placed in a cup of simulated wound fluid ($142\text{mM NaCl}, 2.5\text{mM } CaCl_2$ in DI H_2O) and incubated at 37℃ in humidity for 30 minutes. Two marketed products, Gauze and CVS non-stick pads, were used as controls. The samples were removed from the solution and hung vertically for 30 seconds to remove any excess fluid. Finally, the sample was weighed to determine the final weight. Bulk absorption was calculated as:

$\text{Bulk Absorption} = \frac{\text{Final Weight} - \text{Initial Weight}}{\text{Area of Sample}} (\frac{\text{g}}{\text{m}^2})$. This was performed in triplicate.

Antimicrobial Properties of Silver-coated Woven Polyester Membrane

Ubiquitous opportunistic microorganisms readily occupy the site of an open wound. The presence of these microorganisms above a specific bacterial load exacerbates the already unresolved inflammatory response. An antibacterial layer that preemptively excludes these organisms will improve our ability to accelerate closure. To assess the antimicrobial properties of our silver-coated woven polyester membrane, we performed a Kirby-Bauer

assay using three frequently seen bacteria in clinics, including MSSA, MRSA, and E. Coli.

Cytotoxicity of SWOD Components

The woven polyester membrane with and without a silver-coating were analyzed separately to assess cytotoxicity of the material. Samples were submerged in supplement-free Endothelial Growth Medium (EGM) and incubated for 2, 8, or 14 days. Human adipose microvascular endothelial cells were cultured to confluence in a 96-well plate, and a 1:1 supernatant extract to EGM-2 volume (i.e. 100μL supernatant and 100μL EGM-2 per well) was added to the endothelial cells for 24 hours. At 24 hours, AlamarBlue was added at 10% total volume and incubated for 3 hours. During this incubation, the cells metabolize the blue non-fluorescent dye to red fluorescent resorufin. A microplate reader was used to measure fluorescence at an excitation length of 535 nm and emission of 590 nm.

Moisture Content of Reaction Electrospun Collagen Fibers

A piece of aluminum foil was weighed. Reaction electrospun collagen fibers were added to the aluminum foil, and excess water was removed using a Kim Wipe. The wet weights of the fibers were recorded, and the fibers were placed in an oven overnight. The dry weights of the collagen fibers were recorded, and the moisture content was determined from the amount of protein: $\text{Protein}(\%) = \frac{\text{Dry Weight}}{\text{Wet Weight}} \times 100\%$.

Formation of Scaffold-free Prevascularized Endothelial-fibroblast Constructs and Fibroblast-only Spheroids (FOS)

The scaffold-free prevascularized endothelial-fibroblast constructs were created as described previously in chapter 3. Briefly, a high-density cell suspension of 1:4 human adipose microvascular endothelial cells (HAMEC, ScienCell) and normal human dermal fibroblasts (NHDF, Lonza) were seeded in a non-adherent agarose mold and cultured for three days. The rod-shaped SPEC with dimensions of 1 mm wide by 6 mm long, required $9x10^5$ total cells. For controls, fibroblast-only spheroids (FOS) were formed from $9x10^5$ NHDF.

Incorporation of Reaction Electrospun Collagen Fibers with SPEC

Crosslinked collagen fibers were placed in the bottom of the SPEC agarose mold. $7.2e^5$ Normal Human Dermal Fibroblasts (NHDF) and $1.8e^5$ Human Adipose Microvascular Endothelial Cells (HAMEC) were seeded onto the fibers, and cultured for 3 days in order to validate that the SPEC will incorporate the collagen fibers when cultured together, and that the SPEC will retain its prevascular networks with surrounding matrix deposition.

Drug Incorporation in Reaction Electrospun Collagen Fibers and Drug (JM-2) Release Kinetics

The JM-2 peptide, denoted "P" in **Figure 5.9**, targets the microtubule-binding domain of connexin 43 hemichannels and was shown to prevent the release of cytoplasmic ATP into extracellular space, resulting in reduced inflammation and improved wound healing (**Figure 5.12**; Calder). We wanted to investigate the possibility of using the reaction electrospun collagen fibers as a drug delivery mechanism to improve wound healing in chronic wounds.

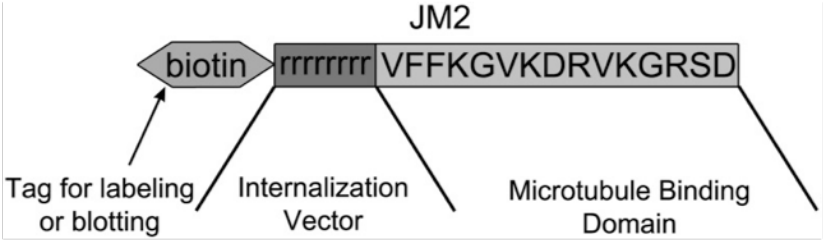

Figure 5.12. JM-2 Peptide. Fig adapted from ref Calder, B., et. al. (2015). Tiss Eng A **21**(11-12): 1752-62.

The 1% collagen fibers (wet) were UV-crosslinked with $6.3e^5 \frac{\mu j}{cm^2}$. The JM-2 peptide was incorporated by dip coating 1.5 g crosslinked collagen fibers (wet) in buffer containing 180μM of JM2 in a 12-well plate, and shaking for two hours at 4℃. The supernatant was removed and the fibers were placed in Eppendorf tubes, and stored in the -20℃ freezer. 1 mL Dulbecco's phosphate-buffered saline (+Ca, +Mg) was added to each well, and the fibers were incubated for 1 hour at 37℃. After 1 hour, the supernatant was removed and placed in Eppendorf tube, and stored in the -20℃ freezer. A fresh 1 mL PBS (+Ca, +Mg) was added. This was repeated at times 1, 2, 5, 17, 20, and 24 hours. The supernatants were then in -20℃ freezer until ready for use. We hypothesize that the UV-crosslinking will not impact drug release from the reaction electrospun collagen fibers, and that these fibers will serve as an adequate vehicle for drug delivery for our application.

Invasion Assay

A zone of exclusion was created in each well of a 12-well plate by placing a sterile 5 mm silicone disc on the bottom center of a culture well and seeding a monolayer of 5,000 normal human dermal fibroblasts. After 3 days, and once the surrounding, perimeter fibroblasts had reached ~75% confluence, they were stained with Cell Tracker Deep Red following the kit instructions. The silicone discs were removed, and a SPEC was placed

in the center of the excluded area (**Figure 5.13**). An avascular fibroblast-only spheroid (FOS) was used as a control to determine the effects of having a prevascularized structure present on recruiting cell migration. The BioTek LionHeart FX Automated Live Cell Imaging Microscope was used to record cell migration over 7 days. This was performed in triplicate and analyzed using regression analysis for the time series data.

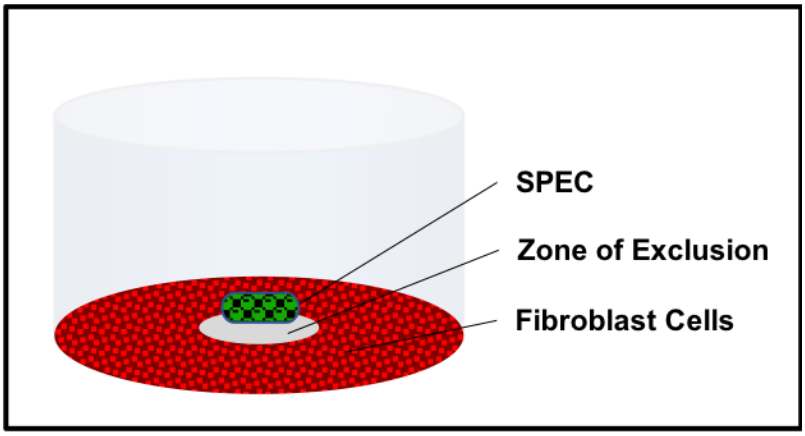

Figure 5.13. Invasion assay setup for mock wound assay.

Development of an in vivo Murine Pressure Wound Model

For future *in vivo* studies to assess the functionality of the SWOD to heal pressure wounds, the Yost lab has created a murine pressure wound model by compressing full thickness tissue between a magnet and steel plate for 48 hours.

5.8 RESULTS

Reaction Electrospun Collagen Fibers

Electrospinning, a technique developed at the Yost lab, is capable of recreating collagen fibers that closely resemble the *in vivo* niche (22; **Figure 5.14**). Here we have demonstrated that the collagen fibers produced with this technique retain the native

collagen molecular structure and mechanical properties that are tunable to the *in vivo* elastic modulus (**Figure 5.14;** 22).

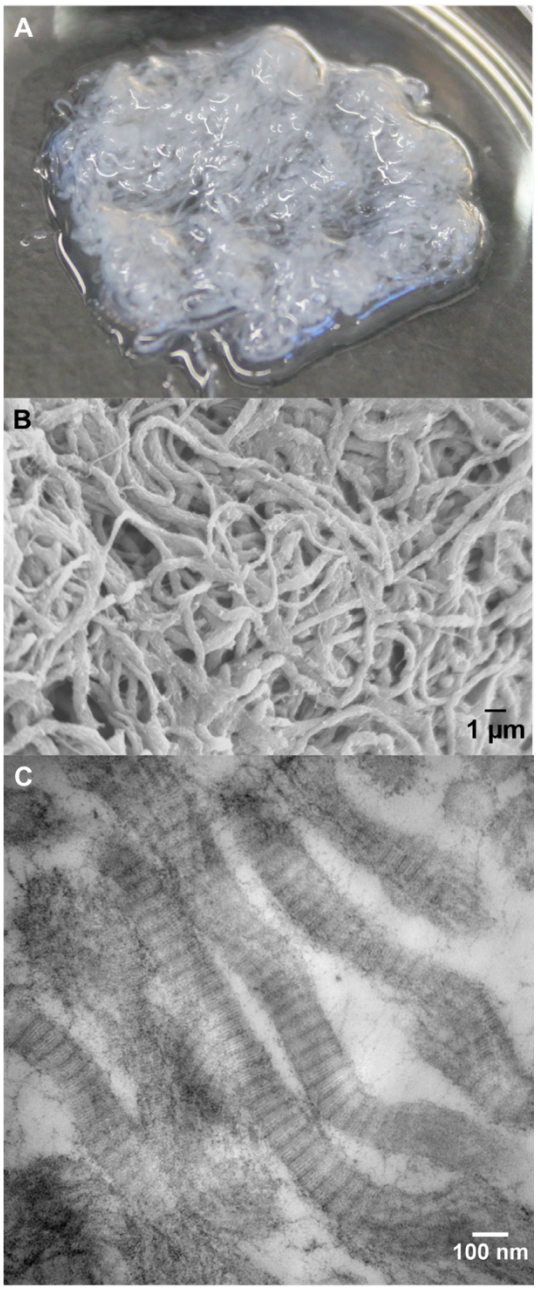

Figure 5.14. (A) 1.5% Reaction Electrospun (RES) collagen fibers. (B) Scanning Electron Microscopy (SEM) image of RES collagen fibers. (C) Transmission Electron Microscopy (TEM) image of RES collagen fibers showing banding patterns characteristic of the *in vivo* environment.

Total Silver-Loading Measurements

The total amount of silver deposited on the woven polyester membranes using Cressington 180 Auto/SE apparatus at 30 mAmp for 150 seconds was 0.12%. **Figure 5.15** shows scanning electron microscopy images of the silver-coated woven polyester and the hydrophilic 0.1μm PTFE membranes.

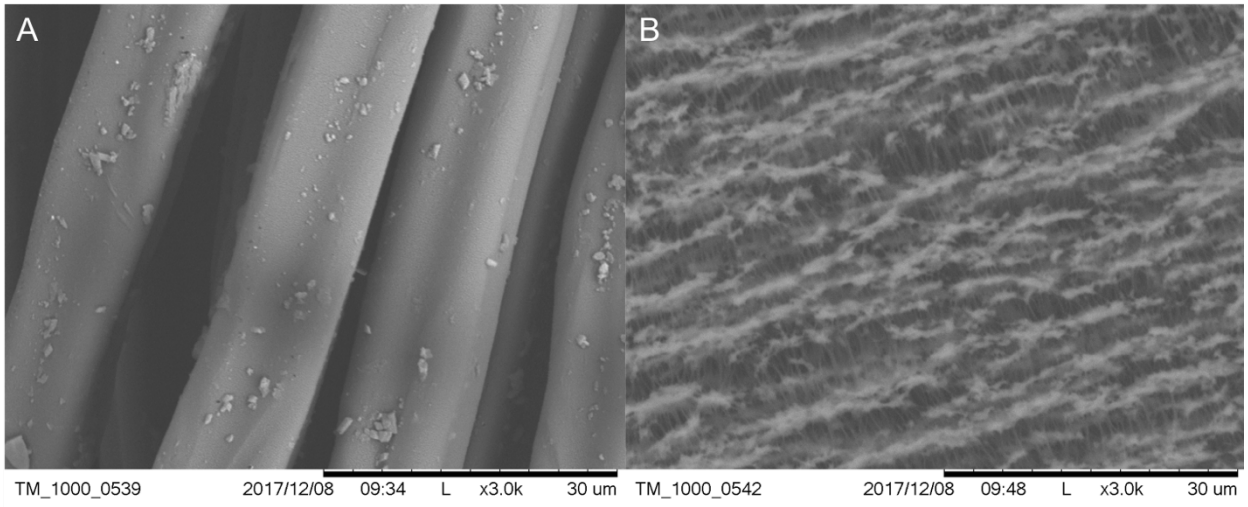

Figure 5.15. Scanning Electron Microscopy (SEM) images of (A) Woven Polyester sputter-coated with silver, and (B) hydrophilic 0.1μm PTFE membranes taken at 3,000X.

Hydrophobicity of Silver-coated Woven Polyester

The contact angles were measured for each side (n=8). The average contact angles were $133.37 \pm 6.62°$ and $134.45 \pm 4.48°$ for side A and B, respectively, with no significant difference between the two sides (**Figure 5.16**, P>0.5). Both sides were sufficiently hydrophobic for our application, as indicated by contact angles greater than $90°$.

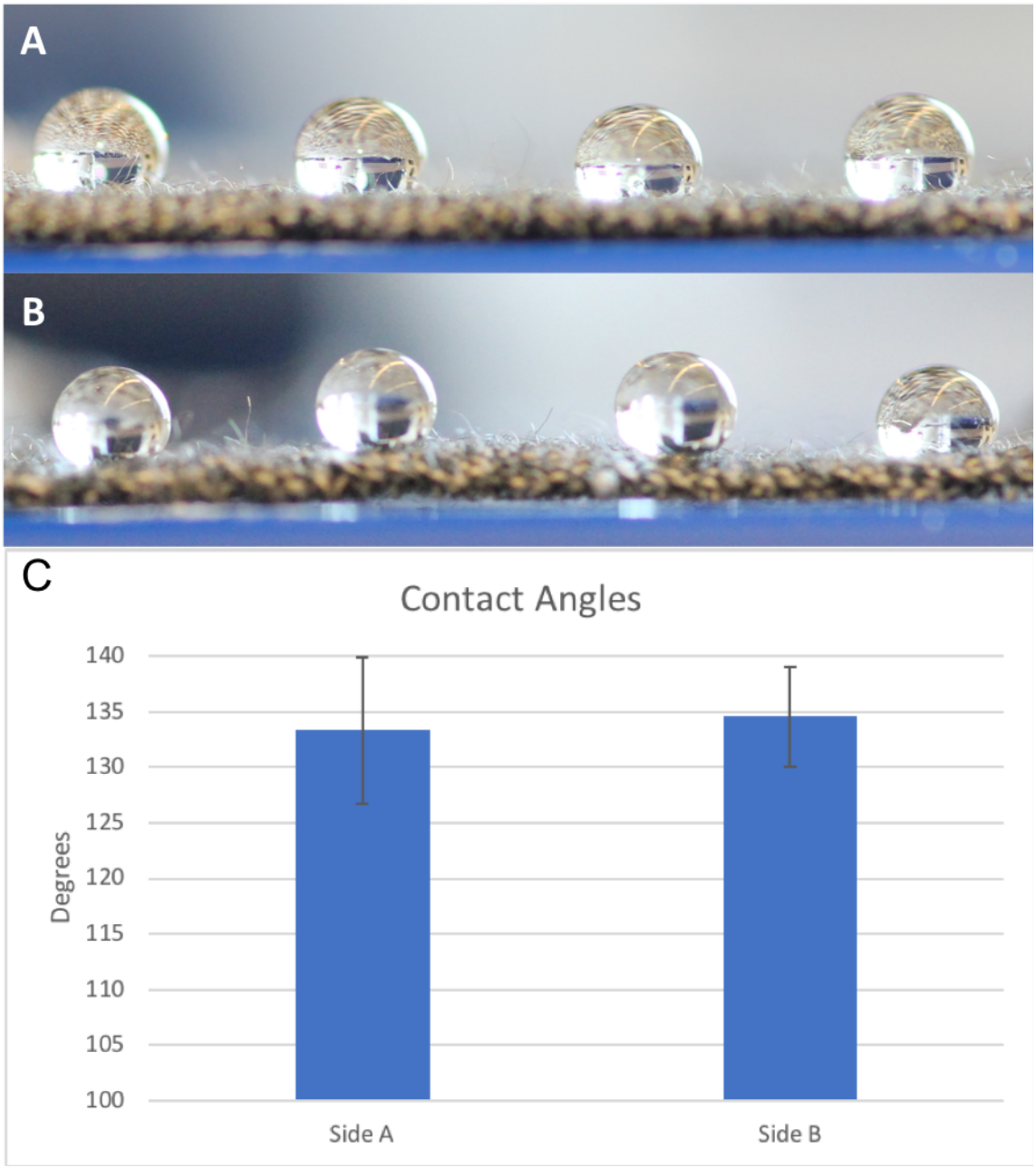

Figure 5.16. Deposited drops on side (A) top and (B) bottom of silver-coated woven polyester membrane. (C) Measured contact angles for either side of membrane.

Bulk Absorption

The bulk absorption of the standard 12-ply gauze and the CVS Non-stick pads were significantly higher than the woven polyester with and without silver-coating (**Figure 5.17**). The woven polyester materials were still able to absorb $500\,\frac{g}{m^2}$ of simulated wound fluid. While our materials absorbed less fluid than the marketed products, this may actually be advantageous because the other products can actually become to moist and induce maceration, the degradation of healthy surrounding tissues due to excess fluid exposure, which could actually increase the size of the wound and lead to more trauma.

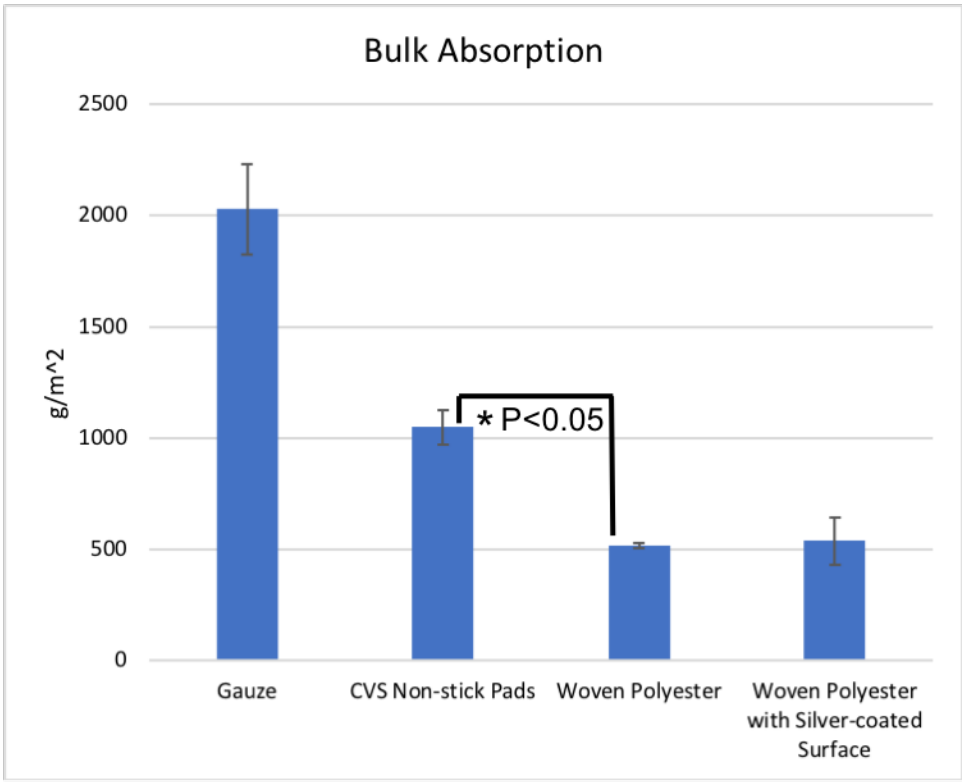

Figure 5.17. Bulk Absorption of Various Materials. There was a significant difference between the CVS non-stick pads and woven polyester (P<0.05).

Antimicrobial Properties of Silver-coated Woven Polyester Membrane

To determine if the top layer is actively antimicrobial, we ran a bacterial colonization assay. We determined its bacterioscidal and had a zone of exclusion of 150 microns. We were very happy to see these results specifically with MRSA as this is an antibiotic-resistant type of bacteria often seen in clinical settings.

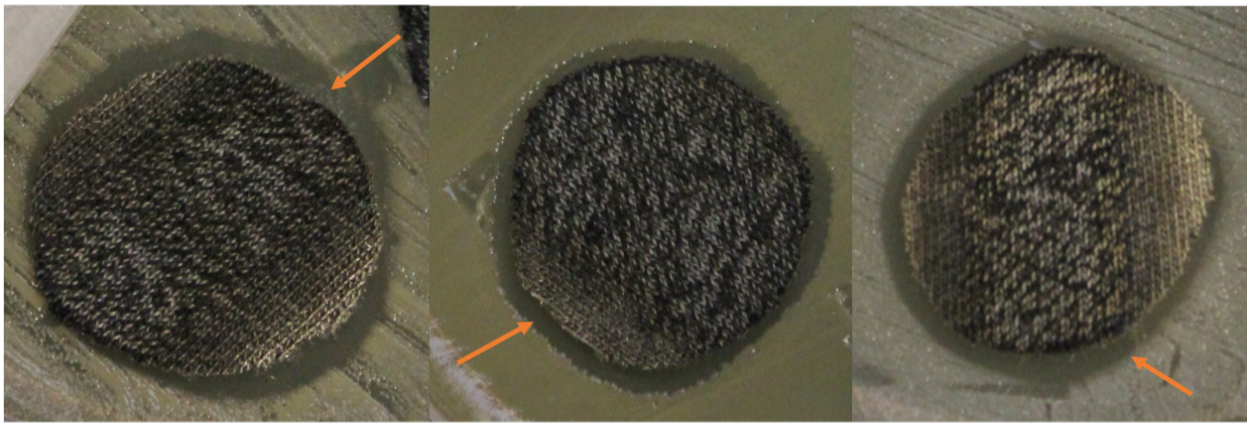

A) MRSA B) E. Coli C) MSSA

Figure 5.18. Silver-coated woven polyester membrane on (A) Methicillin-resistant Staphylococcus aureus (MRSA), (B) Escherichia coli (E.Coli), and (C) Methicillin-sensitive Staphylococcus aureus (MSSA), which are three types of bacteria frequently seen in clinics. The arrows indicate the evident zones of exclusion surrounding the silver-coated woven polyester membranes.

Cytotoxicity of SWOD Components

Our analysis of cell toxicity indicated that the woven polyester was not toxic to endothelial cells (**Figure 5.19**). Importantly, the silver-coating did not hinder their viability, which was a concern during the development of this layer. Therefore, we believe we have the appropriate material, and have determined the appropriate silver-loading, to act as an antibacterial, while permitting endothelial cell survival and functionality.

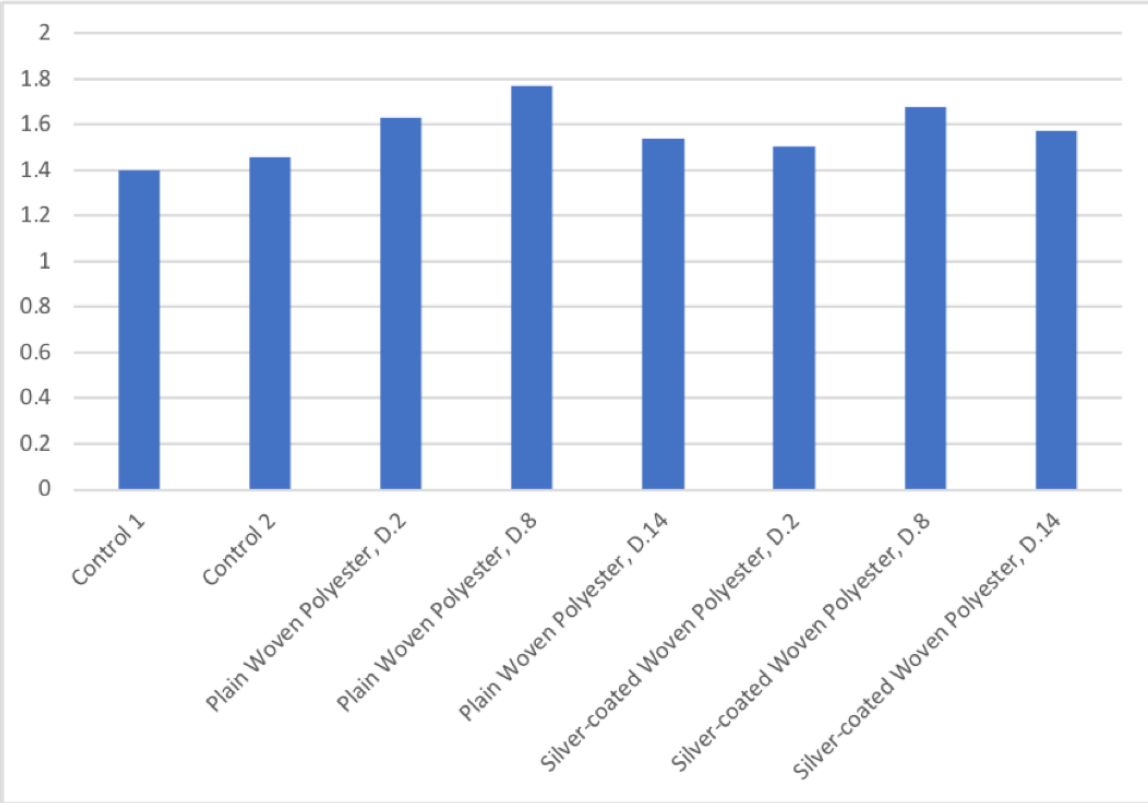

Figure 5.19. Cell toxicity analysis of woven polyester membrane with and without silver-coating on days 2, 8, and 14.

Moisture Content of Reaction Electrospun Collagen Fibers

We theorize that it will also help maintain a moist wound environment by donating or absorbing water molecules to the wound surface. The moisture content of reaction electrospun collagen fibers was found to be $97.59 \pm 0.33\%$ and $97.50 \pm 0.58\%$ for 0.75% and 1.5% collagen fibers, respectively ($0.5<P<0.2$, not significant; **Figure 5.20**). As produced, these fibers have an average moisture content of 97.54% with the water bound to the collagen. As there were no significant differences between these two collagen concentrations, we are not limited to a specific collagen concentration, and a variety of collagen fibers could be used for the treatment of these wounds.

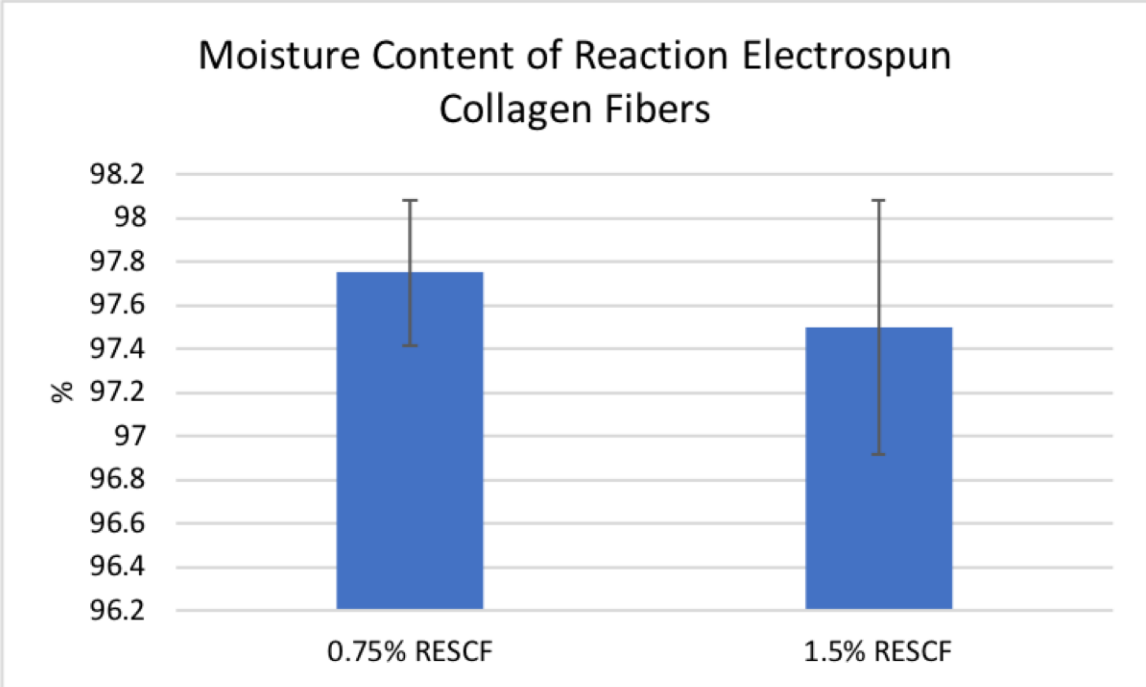

Figure 5.20. Moisture content of Reaction Electrospun Collagen Fibers of varying concentrations (n=3). There were no significant differences between the two groups ($p<0.2$).

Incorporation of Reaction Electrospun Collagen Fibers with SPEC

SPECs were fixed and labeled with F-actin (Phalloidin, green), endothelial networks (CD-31, red), and nuclei (Hoescht, blue) to validate the formation of prevascular networks when reaction electrospun collagen fibers were incorporated during the incubation period (**Figure 5.21**). The SPEC cultured with the collagen fibers retained the prevascular network, as well as adequate extracellular matrix production, indicating successful integration with one another. This data also suggests that the reaction electrospun collagen fibers will provide a scaffold for cell migration.

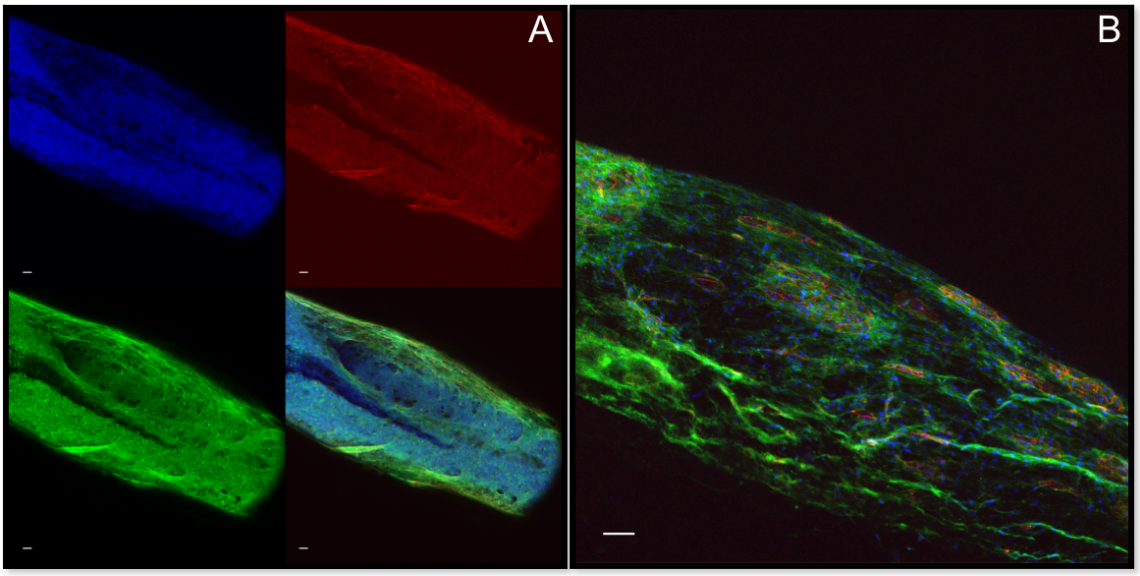

Figure 5.21. Confocal image projection of whole mount rod-shaped SPEC in 1.4% collagen. A) 5x magnification, Nuclei labeled with Hoescht (blue), Endothelial cells labeled with CD31 in (red), Fibroblast cells labeled with Phalloidin (green). B) 10x magnification.

Drug Incorporation in Reaction Electrospun Collagen Fibers and Drug (JM-2) Release Kinetics

Our Western Blot analysis of the JM-2 released from the reaction electrospun collagen fibers demonstrated that the method of incorporating the drug, UV-crosslinking, did not affect its release, and showed that the majority of the drug was released within the first two hours (**Figure 5.22**). Therefore, we believe the reaction electrospun collagen fibers serve as adequate vehicles for drug delivery. A multitude of other drugs, such as vancomycin, etc., and/or signaling factors, i.e. VEGF, PDGF, etc., could be incorporated into the RES collagen fibers.

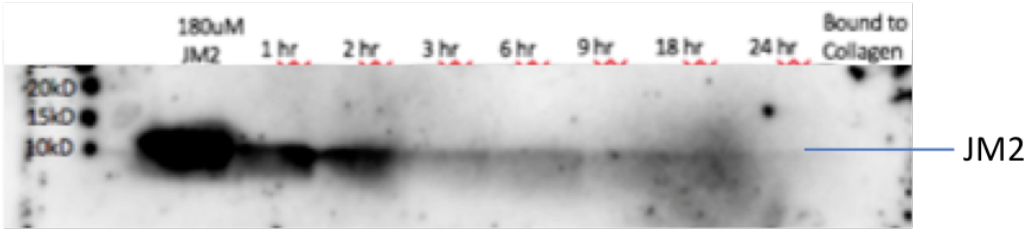

Figure 5.22. JM-2 Release Kinetics from Reaction Electrospun Collagen Fibers, where the majority of JM-2 was released within the first two hours.

Invasion Assay

By 24-48 hours cells are actively migrating out of both the SPEC and FOS into the surrounding exclusion zone. By day 4 the surrounding healthy fibroblasts (indicated by yellow staining) had migrated across the zone of exclusion and integrated with both the SPEC and FOS constructs. By day 10 (not pictured) we had a monolayer of cells remaining. This was really exciting because it indicates the SPEC can re-establish cell communication and migration across wound area. Additionally, the SPEC provides endothelial cells, which can contribute to angiogenesis and new blood vessel formation, as well as fibroblasts that will secrete extracellular matrix and help stabilize newly formed vessels in the area.

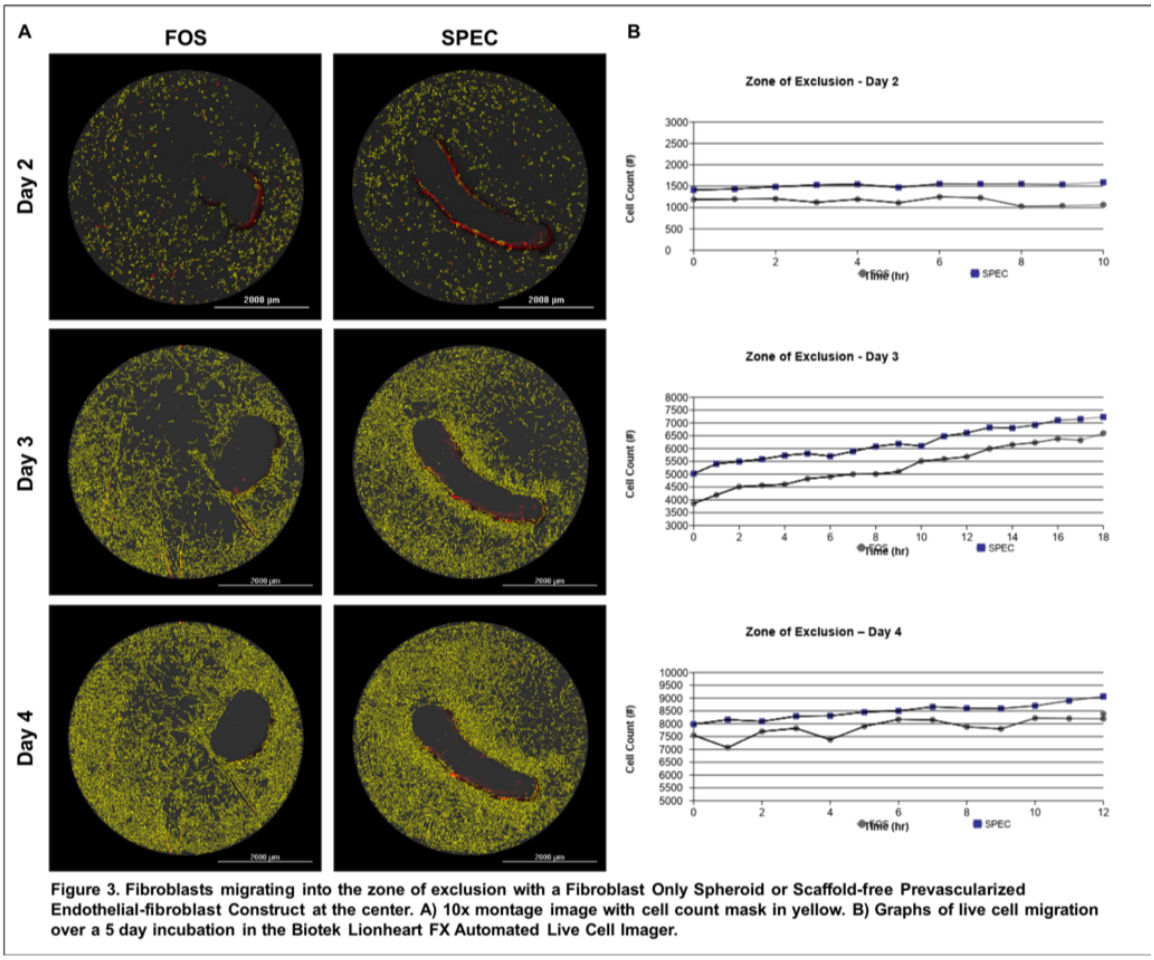

Figure 3. Fibroblasts migrating into the zone of exclusion with a Fibroblast Only Spheroid or Scaffold-free Prevascularized Endothelial-fibroblast Construct at the center. A) 10x montage image with cell count mask in yellow. B) Graphs of live cell migration over a 5 day incubation in the Biotek Lionheart FX Automated Live Cell Imager.

Figure 5.23. Invasion Assay, where perimeter fibroblasts (yellow) migrated across the zone of exclusion, and began integrating with both SPEC and FOS controls by day 4.

SWOD Assembly

To ensure all of the components of the SWOD can be successfully integrated and assembled into a single device, we have developed the prototype shown in **Figure 5.24.** We were able assemble all of the components, and in the future will be able to tailor the device depending on wound depth and the presence of tunneling and undermining in order to treat the entire wound area.

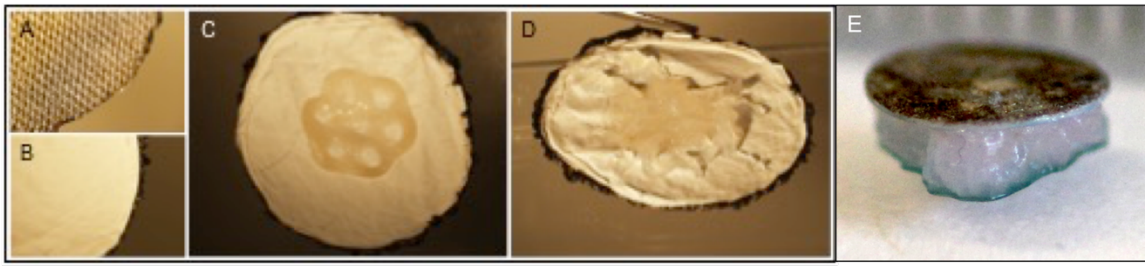

Figure 5.24. Assembled Smart Wound Dressing Prototype. Components shown in (A-B) make up the bi-layered top portion of the SWOD where (A) is the silver-coated woven polyester membrane and (B) is the hydrophilic PTFE membrane. The living SPEC layer shown in (C) has been assembled with the top layer of the SWOD and is adjacent to the hydrophilic PTFE. Reaction electrospun collagen fibers have been additionally assembled in (D) and are placed on top of the SPEC. Depending on wound depth more collagen fibers may be required, as shown in (E).

Development of an in vivo Murine Pressure Wound Model

Figure 5.25A shows the successful creation of a pressure wound created by compressing full thickness tissue between an implanted steel plate and a magnet for 48 hours. The wound is approximately 8 mm on the long axis and 1.5 mm deep. There is an eschar in the wound that will be removed and the wound debrided prior to application of wound care technology. **Figure 5.25B** shows a hematoxylin and eosin stained section of the same wound in A, which highlights the loss of skin tissue, the necrotic muscle tissue and a fragment of the eschar. **Figure 5.25C** is an image of a full-thickness acute wound created using an 8mm biopsy punch, and **Figure 5.25D** is a hematoxylin and eosin-stained section of the wound from C, showing the loss of tissue from the creation of the wound. We believe that these two models will serve as useful platforms for testing the SWOD *in vivo.*

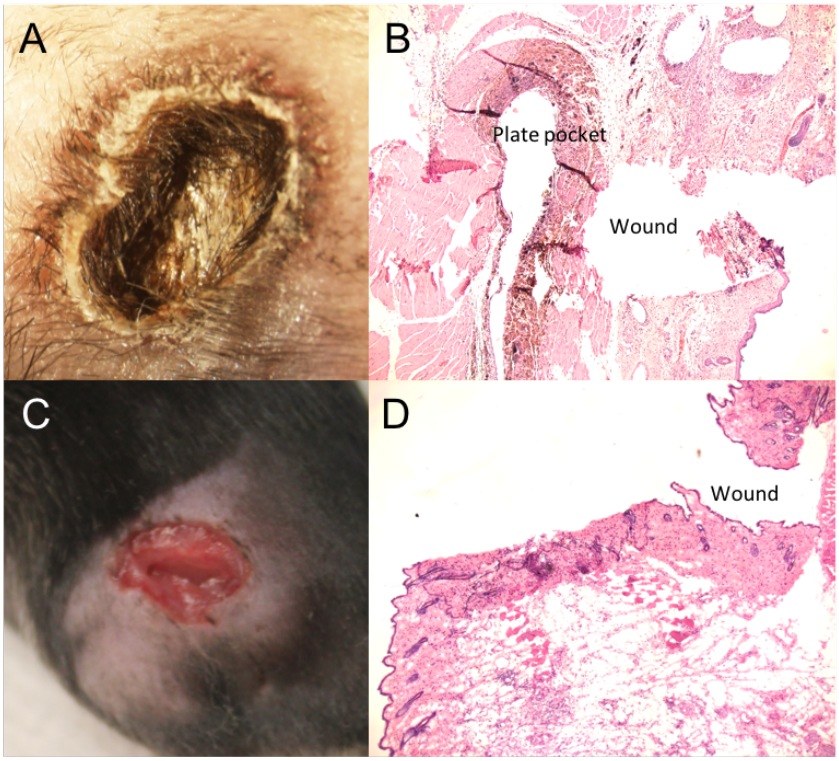

Figure 5.25. Two wound models being investigated in our laboratory for assessing the properties of the Smart Wound Dressing *in vivo*. (A) is a gross image (7 days) of the pressure wound created by compressing full thickness tissue between an implanted steel plate and a magnet for 48 hours. (B) Hematoxylin and Eosin staining of the wound in A. (C) Full thickness acute wound created using an 8mm biopsy punch. (D) Hematoxylin and Eosin staining of the wound in C.

5.9 DISCUSSION

Described here is a novel wound healing device that successfully targets all facets contributing to the impaired wound healing observed in chronic wounds. We have demonstrated in *in vitro* studies that the woven polyester layer sputter-coated for 100s at 150 mAmp, applying 0.12 wt% silver, is bactericidal to S. aureus MSSA and MRSA, E. coli, and E. faecalis and also non-toxic to cultured endothelial cells. Additionally, we have shown that the reaction electrospun collagen fibers have the appropriate moisture content for the wound area, and that they can serve as a provisional matrix for cells. The

reaction electrospun collagen fibers were able to be incorporated into the cellular component of the SWOD, the SPEC layer, during the three-day culture period, and were shown to be adequate vehicles for drug delivery, specifically JM-2, for this application. We were able to successfully assemble all of the components of the SWOD to create a prototype, and developed adequate animal models for testing this product *in vivo* for future studies. We believe the SWOD will perform superiorly to other marketed devices, and accelerate the time it takes chronic wounds to heal. Finally, the SWOD is novel in that it is a single-application device, which will reduce healthcare costs and morbidity associated with dressing changes seen with other devices.

Future Possibilities of Generating a Patient-Specific SWOD

Current treatments for chronic wounds, including pressure ulcers, are standard-sized gauzes, films, and casts. There is no product that comes in patient-derived sizes, as even Apligraf® comes in standard sizes. During the treatment of these wounds, it is essential for a clinician to consistently check the wound progression, which is often done with imaging. 3D ultrasound (3D-US) has previously been used to image pressure ulcers as a prognostic indicator (41). These images can be used to produce volume-rendered 3D images for determination of the volume of a wound area. The MakerBot Replicator 2, a plastic 3D printer, can generate scaffolds with a resolution of 400μm. With this technology, it is possible to take patient images and reproduce a 3D model. We have previously obtained CT images from a pediatric patient at MUSC suffering from craniosynostosis. Amira was used to convert the patient CT scans into CAD designs for use in surgical planning. The architecture of the models rendered were measured and

compared to the original scans to assess the resolution of this method. The plastic skulls were mimetic of the *in vivo* condition (**Figure 5.26, Table 5.1**).

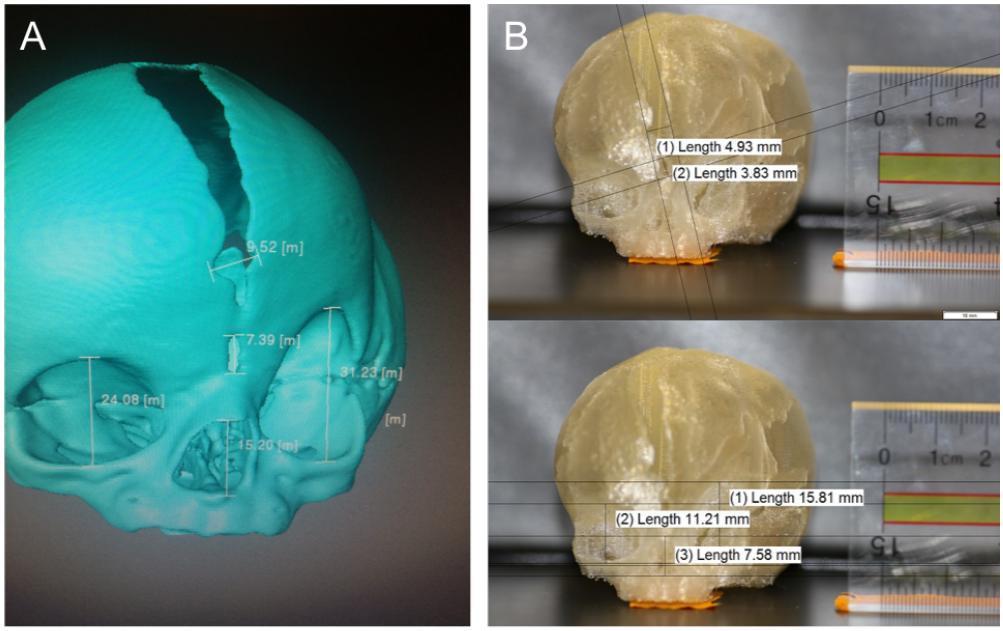

Figure 5.26. (A) AMIRA reconstruction of an infant patient's skull suffering from craniosynostosis. (B) Model of skull printed using a MakerBot Replicator 2 with dimensions measured using CellSens.

	Scans (mm)	Reconstruction (mm)
Left orbit	15.615	15.81
Right orbit	12.04	11.21
Nose	7.6	7.58
Hole between orbits	3.695	3.83
Gap above orbits	4.76	4.93

Table 5.1. Measurements taken from the scans of an infant patient suffering from craniosynostosis and of the model created using the MakerBot Replicator 2.

We can also incorporate these patient scans for use with the Palmetto Printer as discussed in chapter two to create patient-mimetic constructs. **Figure 5.27** shows reaction electrospun collagen fibers serving as a substrate for cell printing, as could be used for creating the SWOD.

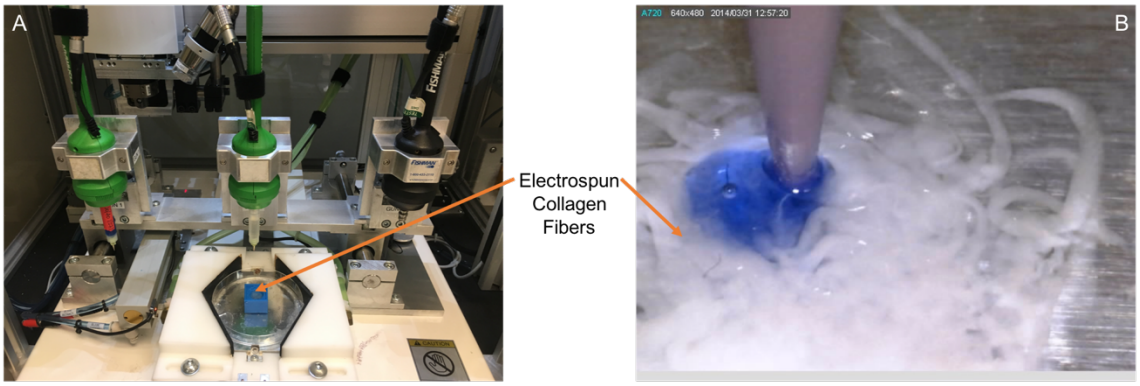

Figure 5.27. Utilizing the Palmetto Bioprinter to develop patient-specific wound dressings. (A) Bioprinter setup with electrospun fibers in the blue reservoir. (B) Image of cells, shown in blue for visualization, being deposited onto electrospun collagen fibers.

We have further expanded on methods for developing patient-specific dressings through the use of a novel imaging technique we have patented. The scanner is a multi-camera system that uses structured light to calculate the dimensions and architectures of three-dimensional soft objects (**Figure 5.28A**). We are unique in having the capability of being able to recapitulate soft tissue areas with high fidelity, as demonstrated by this scan of an abdominal wound of an MUSC patient (**Figure 5.28B**). This technology can help us determine the depth of the wound, and how much collagen we would need, as well as the overall size of the SWOD dressing, allowing us to determine the number of SPEC constructs needed, as well as the other components. Additionally, these scans could be converted into bioprinter-compatible software and we could mimic a deficit as needed. This technology it is not limited to the creation of Smart Wound Dressings, but could also be used for many other tissue engineering applications.

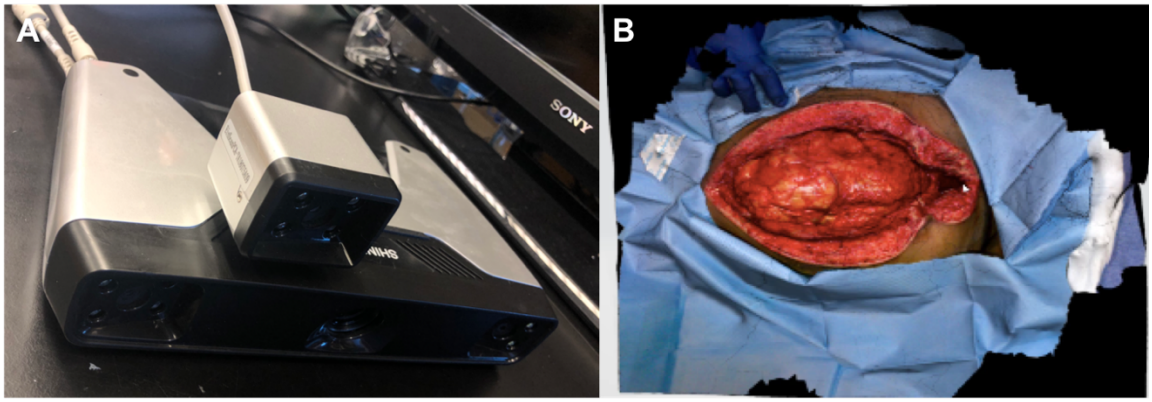

Figure 5.28. Patented (A) imaging and scanner technology for recapitulating the wound architecture for the future development of patient-specific wound dressings. (B) Scanned recapitulation of the tissues in a MUSC patient undergoing an abdominal wall reconstruction. The image in B is the CAD-designed colorimetric scanned projection.

In addition to developing patient-mimetic wound scaffolds with respect to structure, we have the technology to produce autologous cellular constructs (i.e. the SPEC component). In clinic, autologous cells could be harvested from the patient's adipose tissue, and grown in culture. To generate patient-specific constructs, the wound scaffold could be created from patient images rendered into computer-aided design software and fabricated using a 3D bioprinter, specifically the Palmetto Printer, and subsequently seeded with cells (i.e. indirect bioprinting). The Palmetto Printer has three dispensers and is able to concurrently deposit heterogeneous materials and cell types. We have previously characterized the bioprinter for cell viability, reproducibility, and its ability to generate constructs in complex architectures.

The most critical aspect of developing these novel technologies, especially those including cellular components, is the translational feasibility of actually being able to implement them in clinics. The following SWOD production timeline has been

developed, and has promising translatability due to the availability of the required cell types, as well as the short culture time periods.

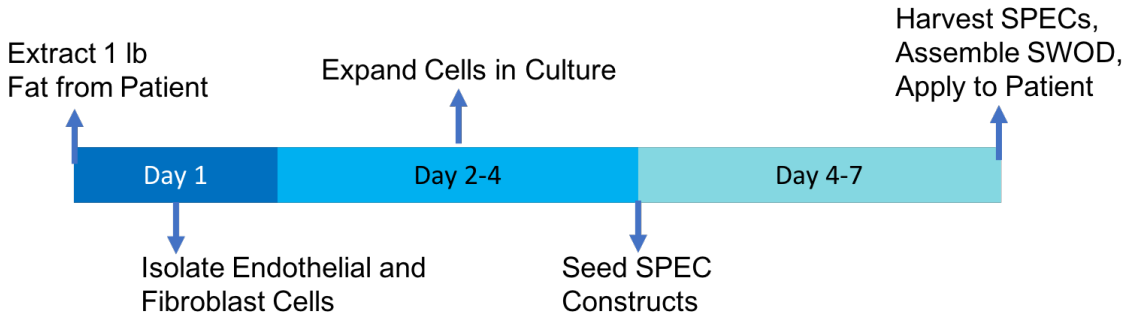

Figure 5.29. The Smart Wound Dressing Production Timeline.

5.10 REFERENCES

1. Golinko MS, Clark S, Rennert R, Flattau A, Boulton AJ, Brem H. (2009). "Wound emergencies: the importance of assessment, documentation, and early treatment using a wound electronic medical record." Ostomy/wound management **55**(5):54-61.
2. Brem, H. et. al. (2007). "Molecular Markers in Patients with Chronic Wounds to Guide Surgical Debridement." Mol Med **13**(1-2): 30-39.
3. Teixeira PG, Inaba K, Dubose J, Salim A, Brown C, Rhee P, Browder T, Demetriades D. (2009). Enterocutaneous fistula complicating trauma laparotomy: a major resource burden. The American surgeon." **75**(1):30-2.
4. Sen CK. (2009). "Wound healing essentials: let there be oxygen." Wound repair and regeneration **17**(1):1-18.
5. Valencia IC, Falabella A, Kirsner RS, Eaglstein WH. (2001). "Chronic venous insufficiency and venous leg ulceration." Journal of the American Academy of Dermatology **44**(3):401-21.
6. McDaniel JC, Browning KK. (2014). "Smoking, chronic wound healing, and implications for evidence-based practice. Journal of wound, ostomy, and continence nursing." WOCN **41**(5):415-23.
7. Gordon MD, Gottschlich MM, Helvig EI, Marvin JA, Richard RL. (2004). "Review of evidenced-based practice for the prevention of pressure sores in burn patients." The Journal of burn care & rehabilitation **25**(5):388-410.
8. Brem H, Maggi J, Nierman D, Rolnitzky L, Bell D, Rennert R, Golinko M, Yan A, Lyder C, Vladeck B. (2010). "High cost of stage IV pressure ulcers." American journal of surgery **200**(4):473-7.
9. Russo CA, Steiner C, Spector W. (2006). "Hospitalizations Related to Pressure Ulcers Among Adults 18 Years and Older.": Statistical Brief #64. Healthcare Cost and Utilization Project (HCUP) Statistical Briefs. Rockville (MD): Agency for Health Care Policy and Research (US). PubMed PMID:21595131

10. Bauer, K., Rock, K., Munier, N., Jones, O., and Qu, W. (2016). "Pressure Ulcers in the United States' Inpatient Population from 2008 to 2012: Results of a Restrospective Nationwide Study." Ostomy Wound Management **62**(11):30-38.
11. Demidova-Rice, T.N., Hamblin, M.R., and Herman, I.M. (2012). "Acute and Impaired Wound Healing: Pathophysiology and Current Methods for Drug Delivery, Part 1: Normal and Chronic Wounds: Biology, Causes, and Approaches to Care." Adv Skin Wound Care **25**(7):304-14.
12. Fonder, M.A., et. al. (2008). "Treating the chronic wound: A practical approach to the care of nonhealing wounds and wound care dressings." J Am Acad Dermatol **58**(2): 185-206.
13. Lazic T, Falanga V. (2011). "Bioengineered skin constructs and their use in wound healing." Plastic and reconstructive surgery **127**(Suppl 1):75S-90S.
14. Baltzis, D. E., I.; Veves, A. (2014). "Pathogenesis and Treatment of Impaired Wound Healing in Diabetes Mellitus: New Insights." Adv Ther **31**: 817-36.
15. Smith, A. and Garoufalis, M. (2013). "Addressing Periwound Maceration and Exudate Bioburden in Venous Insufficiency Ulcerations Using a Unique Active Fluid Management Silver Dressing." Case Study. Milliken Healthcare Products, LLC. (http://healthcare.milliken.com/en-us/literature/Documents/Addressing%20Periwound%20Maceration_Smith%20TRITECCS10r01.pdf)
16. Hu, S., et al. (2006). "Evaluation of Apligraf persistence and basement membrane restoration in donor site wounds: a pilot study." Wound Repair Regen **14**(4): 427-33.
17. Griffiths, M., Ojeh, N., Livingstone, R., Price, R., and Navsaria, H. (2004). "Survival of Apligraf in Acute Human Wounds." Tissue Eng **10**(7/8): 1180-95.
18. Phillips T.J., et. al. (2002). "The longevity of a bilayered skin substitute after application to venous ulcers." Arch Dermatol **138**: 1079–81.
19. Zaulyanov, L. and Kirsner, R.S. (2007). "A review of bi-layered living cell treatment (Apligraf) in the treatment of venous leg ulcers and diabetic foot ulcers." Clinical Interventions in Aging **2**(1): 93-98.
20. Fivenson, D.P., Scherschun, L., Choucair, M., Kukuruga, D., Young, J., Shwayder, T. (2003). "Graftskin therapy in epidermolysis bullosa. J Am Acad Dermatol **48**: 886-92.
21. Czajka CA, Calder BW, Yost MJ, Drake CJ. (2015). "Implanted scaffold-free prevascularized constructs promote tissue repair." Annals of plastic surgery **74**(3):371-5.
22. Rodriguez-Rivera V, Weidner JW, Yost MJ. Reaction Electrospinning: A Novel Technique for the Fabrication of Collagen Scaffolds. Unpublished manuscript - Submitted to Biomedical Materials research October 2017.
23. Ip M, Lui SL, Poon VK, Lung I, Burd A. (2006). "Antimicrobial activities of silver dressings: an in vitro comparison." Journal of medical microbiology **55**(Pt 1):59-63.
24. Klinge, U. and Klosterhalfen, B. (2012). "Modified classification of surgical meshes for hernia repair based on the analyses of 1,000 explanted meshes." Hernia **16**:251-58.

25. Redbord, K.P. and Hanke, C.W. (2008). “Expanded polytetrafluoroethylene implants for soft-tissue augmentation: 5-year follow-up and literature review.” American Society for Dermatologic Surgery **34**:735-44.
26. Maitz, M.F. (2015). “Applications of synthetic polymers in clinical medicine.” Biosurface and Biotribology **1**:161-76.
27. Rho, K.S., et. al. (2006). “Electrospinning of Collagen Nanofibers: Effects on the behavior of normal human keratinocytes and early-stage wound healing.” Biomat **27**:1452-61.
28. Czajka CA, Drake CJ. (2015) “Self-assembly of prevascular tissues from endothelial and fibroblast cells under scaffold-free, nonadherent conditions.” Tissue engineering Part A.**21**(1-2):277-87.
29. Benbow, M. (2008). “Exploring the concept of moist wound healing and its application in practice.” British Journal of Nursing **17**(15):S4-16.
30. Okan, D., et. al. (2007). “The role of moisture balance in wound healing.” Clinical Management **20**:39-53.
31. Kang, P., Perry, K.M., and Bockstiegel, N. (2015). “Assessing Periwound Moisture Using a Novel In Vitro Test Method.” Wounds **27**(1):E1-E6.
32. Kloeters, O., et. al. (2016). “Prospective and randomised evaluation of the protease-modulating effect of oxidized regenerated cellulose/collagen matrix treatment in pressure sore ulcers.” International Wound Journal **13**(6): 1231-36.
33. Wassermann, E., van Griensven, M., Gstaltner, K., et al. (2009). “A chronic pressure ulcer model in the nude mouse.” Wound Repair Regen **17**:480–484.
34. Menke, N.B., Ward, K.R., Witten, T.M., Bonchev, D.G., and Diegelmann, R.F. (2007). “Impaired Wound Healing.” Clinics in Dermatology **25**:19-25.
35. Rhett, M.J., Ghatnekar, G.S., Palatinus, J.A., O’Quinn, M., Yost, M.J., and Gourdie, R.G. (2008). “Novel Therapies for Scar Reduction and Regenerative Healing of Skin Wounds.” Trends in Biotechnol **26**(4):173-180.
36. Osuala, E. O. (2014). "Innovation in prevention and treatment of pressure ulcer-Nursing implication." Trop J Med Res **17**: 61-68.
37. Fullana, M. J. and G. E. Wnek (2012). "Electrospun collagen and its applications in regenerative medicine." Drug Deliv Transl Res **2**(5): 313-322.
38. Calder, B. W., et al. (2015). "Inhibition of connexin 43 hemichannel-mediated ATP release attenuates early inflammation during the foreign body response." Tissue Eng Part A **21**(11-12): 1752-1762.
39. Demidova-Rice, T.N., Hamblin, M.R., and Herman, I.M. (2012). “Acute and Impaired Wound Healing: Pathophysiology and Current Methods for Drug Delivery, Part 1: Normal and Chronic Wounds: Biology, Causes, and Approaches to Care.” Adv Skin Wound Care **25**(7):304-314.
40. Singer AJ, Dagum AB. Current management of acute cutaneous wounds. *N Engl J Med.* **359**:1037–46, (2008).
41. Yabunaka, K., Iizaka, S., Nakagami, G., Fujioka, M., and Sanada, H. “Three-dimensional ultrasound imaging of the pressure ulcer. A case report.” *Med Ultrason* **17**(3):404-406, (2015).